THÈSE POUR OBTENIR LE GRADE DE DOCTEUR DE L'UNIVERSITÉ DE MONTPELLIER

En Chimie et Physico-chimie des Matériaux

École doctorale Sciences Chimiques Balard

Unité de recherche Institut Charles Gerhardt Montpellier (ICGM) - Equipe D3

En partenariat international avec Istanbul Technical University, Turkey

OLEFIN/PARAFFIN SEPARATION IN POLYMER/MOF MIXED-MATRIX MEMBRANES

Présentée par Elif Begum DOGAN

Le 22 Décembre 2023

Sous la direction de Guillaume MAURIN Directeur de thèse
et de Mehmet Goktug AHUNBAY Co-Directeur de thèse

Devant le jury composé de

Prof. Sacide Alsoy ALTINKAYA, Professeur, Izmir Institute of Technology	Présidente de jury, Rapporteuse
Prof. Yunus ZORLU, Professeur, Gebze Technical University	Rapporteur
Prof. Serife Birgul TANTEKİN-ERSOLMAZ, Professeur, Istanbul Technical University	Examinatrice
Dr. Sadiye VELIOGLU, Maître de Conférences, Gebze Technical University	Examinatrice
Dr. Sabine DEVAUTOUR-VINOT, Maître de Conférences, ICGM, Université de Montpellier	Examinatrice
Prof. Guillaume MAURIN, Professeur, IGCM, Université de Montpellier	Directeur de thèse
Prof. Mehmet Goktug AHUNBAY, Professeur, Istanbul Technical University	Co-Directeur de thèse

UNIVERSITÉ DE MONTPELLIER

ACKNOWLEDGEMENTS

First, I would like to express my heartfelt gratitude to my advisor, Prof. Mehmet Goktug AHUNBAY, for his patience, guidance and support throughout this doctoral journey. His dedication to helping me to learn molecular simulation has been instrumental in my academic development. I am also very thankful to him for introducing me to my advisor Prof. Guillaume MAURIN. I would like to specially thank Prof. Guillaume MAURIN for his time, patience and invaluable scientific guidance. It is through his support and expertise that this international joint PhD program have become possible.

I would like to extend my appreciation to Prof. Birgül TANTEKIN-ERSOLMAZ and Assoc. Dr. Sadiye VELIOGLU for their extensive knowledge and valuable feedbacks during my thesis.

I would also like to express my gratitude to all of the jury members, first, Prof. Sacide Alsoy ALTINKAYA and Prof. Yunus ZORLU, for their time to read my work as reviewers. I would also like to extend my thanks to Prof. Birgül TANTEKIN-ERSOLMAZ, Assoc. Dr. Sabine DEVAUTOUR-VINOT and Assoc. Dr. Sadiye VELIOGLU for their participation as members of my doctoral dissertation jury.

Special thanks to my current and former colleagues at DAMP: Alejandro, Shanping, Dong, Wahid, Cecilia, Valentin, Gopal, Supriyo, Pedro, BeiBei, Patrick, Inderdip, Carla, Kamal and Ezgi. I would also like to thank to the ITU group members: Marcel and Aysa, for their scientific discussions.

Furthermore, I want to thank my close friends Berrak and Nevinur, for their support throughout my life since high-school.

Finally, I want to thank my parents, Leyla and Selahattin, as well as my brother Berkay, for their unconditional support. I am extremely grateful for my mother for always being there for me, believing in me and providing me with the extra strength when I needed the most.

This thesis was supported by the Scientific and Technological Research Council of Turkey-TUBITAK (Grant #1059B142000368) for the international doctoral research fellowship program and the 100/2000 Council of Higher Education (YÖK) PhD Scholarship program.

TABLE OF CONTENTS

ACKNOWLEDGEMENTS ..... **iii**

TABLE OF CONTENTS ..... **v**

ABBREVIATIONS ..... **ix**

SYMBOLS ..... **xiii**

LIST OF TABLES ..... **xv**

LIST OF FIGURES ..... **xvii**

GENERAL INTRODUCTION **1**

1. Significance of the Thesis 3

2. Research Purposes and Organization of the Thesis 5

REFERENCES **8**

1. POTENTIAL OF MOFS, POLYMERS AND MOF/POLYMER MIXED MATRIX MEMBRANES FOR C2 &C3 SEPARATION **11**

1.1 Introduction 13

1.2 Propylene/Propane and Ethylene /Ethane Separation 14

1.2.1 Existing separation technology 15

1.2.2 Current commercial sorbents/membranes for gas separation 21

1.3 Polymers 25

1.3.1 PIMs 26

1.3.2 Polyimides 32

1.4 Metal Organic Frameworks 37

1.4.1 General presentation 38

1.4.2 ZIFs for C2/C3 separation 41

1.4.3 Other MOFs for C2/C3 separation 46

1.5 Mixed Matrix Membranes 52

1.5.1 General introduction on MMM 53

1.5.2 MOFs-based MMM for gas separation 57

1.5.3 MOFs-based MMM for C2/C3 separation 69

1.5.4 Macroscopic Models of MOFs-based MMMs 76

1.5.5 Atomistic Models of MOFs-based MMMs 77

REFERENCES **80**

2. MOLECULAR SIMULATION 115
2.1 Introduction 117
2.2 Statistical Ensembles 118
2.3 Microscopic models for MOFs, polymers and MOF/polymer composites 122
2.4 Force fields 123
2.5 Molecular Dynamics Simulations 130
2.6 Monte Carlo Simulations 136
2.7 Quantum Calculations 140
2.7.1 Geometry optimization 144
2.7.2 Charge calculations 145
REFERENCES 146
3. CONSTRUCTION OF ATOMISTIC MODELS OF MOFS, POLYMERS AND THEIR COMPOSITES AND EXPLORATION OF THEIR SORPTION PROPERTIES 153
3.1 Introduction 155
3.2 ZIF-67 Surface Models 155
3.3 Polymer Models 159
3.4 MOF/polymer MMM Models 164
3.5 Analysis of the ZIF-67/6FDA-DAM MMM Interface 166
3.6 Effect of IDip-functionalized MOF Surface on ZIF-67/6FDA-DAM MMM Interface 169
3.6.1 ZIF67-IDip surface models 170
3.6.2 Analysis of the ZIF-67-IDip/6FDA-DAM MMM interface 175
3.7 Impact of Polymers on ZIF-67-based MMM Interfaces 179
3.7.1 ZIF-67/PIM-1 vs ZIF-67/6FDA-DAM MMM interfaces 179
3.7.2 ZIF-67-IDip/PIM-1 vs ZIF-67-IDip/6FDA-DAM MMM interfaces 182
3.8 Adsorption Studies on ZIF-67-based MMMs 186
3.8.1 Impact of polymers on the adsorption properties of ZIF-67-based MMMs 186
3.8.2 Impact of IDip-functionalized MOF surface on the adsorption properties of ZIF-67-based MMMs 190
3.8.3 Impact of MOF loading on the adsorption properties of ZIF-67-based MMMs 198
3.9 Conclusion 200
REFERENCES 201

ARTICLE 207

4. IMPACT OF MOF SURFACE FUNCTIONALIZATION AND SOLVENT-DRIVEN TERMINATIONS ON THE STRUCTURING & PROPERTIES OF ZIF-67-BASED MMMs 221

4.1 Introduction 223

4.2 ZIF67-IPD/Polymer MMM Models 226

4.2.1 ZIF67-IPD surface models 227

4.2.2 ZIF-67-IPD/6FDA-DAM and ZIF-67-IPD/PIM-1 MMM models 230

4.2.3 Analysis of the ZIF-67-IPD/6FDA-DAM and ZIF-67-IPD/PIM-1 MMM interfaces 231

4.2.4 Adsorption properties of ZIF-67-IPD/6FDA-DAM and ZIF-67-IPD/PIM-1 MMMs 238

4.3 ZIF67/Polymer MMM Models with MOF Surfaces Terminated by Methanol 240

4.3.1 ZIF67 surface models 240

4.3.2 ZIF-67/6FDA-DAM and ZIF-67/PIM-1 MMM models 243

4.3.3 Analysis of the ZIF-67/6FDA-DAM and ZIF-67/PIM-1 MMM interfaces 244

4.3.4 Adsorption properties of ZIF-67/6FDA-DAM and ZIF-67/PIM-1 MMMs 252

4.4 Conclusion 254

REFERENCES 254

5. ASSESSMENT OF THE ENERGY BARRIERS FOR PROPYLENE/PROPANE TO CROSS THE WINDOWS 259

5.1 Introduction 261

5.2 Free Energy Profiles for Propylene/Propane in ZIF-67 262

5.3 Free Energy Profiles for Propylene/Propane in ZIF67-IDip 269

5.4 Free Energy Profiles for Propylene/Propane in ZIF67-IPD 273

5.5 Free Energy Profiles for Propylene/Propane in ZIF67 with MOF Surfaces Terminated by Methanol 276

5.6 Conclusion 279

REFERENCES 280

CONCLUSIONS AND PERSPECTIVES 285

Abstract 291

Résume 292

Özet 293

ABBREVIATIONS

1D : One-dimensional

2D : Two-dimensional

3D : Three-dimensional

4D : Four-dimensional

6FDA : 4,4-(Hexafluoroisopropylidene)diphthalic anhydride

Abtc : 3,3′,5,5′azo benzene –tetracarboxylates

ADC : Acetylenedicarboxylate

AIMD : Ab initio molecular dynamics

Atz : 3-amino-1,2,4-triazole

BbIm : Bromobenzimidazole

BDC : Terephthalic acid

BFGS : Broyden-Fletcher-Goldfarb-Shanno

Bim : Benzimidazole

BMDA : Dimethylbenzylamine

BPDA : Biphenyl tetracarboxylic diandhydride

CAGR : Compound annual growth rate

CGD-MD : Concentration gradient-driven molecular dynamics

CH_2Cl_2 : Methylene chloride

CHARMM : Chemistry at HARvard Macromolecular Mechanics

$CHCl_3$: Chloroform

CMS : Carbon Molecular Sieve

COF : Covalent Organic Framework

COMPASS : Condensed-phase Optimized Molecular Potentials for Atomistic Simulation Studies

CuBTC : Copper benzene-1,3,5-tricarboxylate

DABA : 3,5- diaminobenzoic acid

DAM : 2,4,6-trimethyl-1,3-diaminobenzene

DDBT : Dimethyl-3,7-diaminodibenzothiophene5,5-dioxide

DEF : Diethylformamide

DFT **:** Density Functional Theory

DMA **:** Dimethylammonium

DMAc **:** Dimethylacetamide

DMDB : 2,2′-dimethyl-4,4′-diaminobiphenyl

DMF **:** Dimethylformamide

DMSO **:** Dimethyl sulfoxide

DOPA **:** 1,2-dioleoyl-sn-glycero-3-phosphate

DPX **:** 2,5-dimethyl-p-phenylenediamine

EMD **:** Equilibrium molecular dynamics simulations

ESP **:** Electrostatic potential

FFV **:** Fractional Free Volume

GAFF **:** General AMBER force field

GCMC **:** Grand Canonical Monte Carlo

GEMC **:** Gibbs ensemble Monte Carlo

GME **:** Gmelinite

GPU **:** Gas permeation units

Hmim **:** 2-methylimidazole

HTCS **:** High-throughput computational screening

IAST **:** Ideal adsorbed solution theory

Ica **:** 2 imidazolecarboxaldehyde

IDip **:** 1,3-bis(2,4,6-diisopropylphenyl)imidazole-2-ylidene

ILs **:** Ionic liquids

IMMP **:** Interfacial microfluidic membrane processing

IPD **:** Isophthalic dihydrazide

IPDA **:** 4,4′ -(4,4′ -isopropylidenediphenoxy) bis(phthaltic anhydride)

IRMOF-1 **:** Isoreticular metal organic framework

LIPS **:** Ligand-induced permselectivityation

LJ **:** Lennard Jones

LPSQ **:** Ladder-type polysilsesquioxane

MC **:** Monte Carlo

MD **:** Molecular Dynamics

MeOH : Methanol

MOF : Metal Organic Framework

NEMD : Non-equilibrium molecular dynamics simulations

NHC : N-heterocyclic carbene

NMP : N-Methyl-2-pyrrolidone

NPs : Nanoparticles

NPT : The isothermal-isobaric ensemble

NVE : The microcanonical ensemble

NVT : The canonical ensemble

ODA : 4, 4′-oxydianiline

OPLS : Optimized Potentials for Liquid Simulations

PAA : Polyacrylic acid

PBC : Periodic boundary conditions

PBI : Polybenzimidazole

PBO : Polybenzoxazoles

PCFF : Polymer Consistent Force Field

PCP : Porous coordination polymers

PDFT : Periodic Density Functional Theory

PDMS : Polydimethylsiloxane

PEI : Polyethylenimine

PES : Polyethersulfone

PIM : Polymers of Intrinsic Microporosity

PIM-PIs : Polyimides of Intrinsic microporosity

PMA : Phosphomolybdenum heteropoly acid

PMDA : Pyromellitic dianhydride

PMF : Potential of mean force

POC : Porous organic cages

PPPM : Particle−particle particle−mesh

Psf : Polysulfone

PSLE : Postsynthetic ligand exchange

QM : Quantum mechanics

RC : Reaction coordinate

RDF **:** Radial Distribution Function

RESP **:** Restrained electrostatic potential

SBS-g-POEM: Poly (styrene-b-butadiene-b-styrene)-g-poly(oxyethylene methacrylate)

SC **:** Steam cracking

SCC **:** Fluid-catalytic cracking

SDA **:** Structure Directing Agents

SOD **:** Sodalite

SRCs **:** Sorption-relaxation cycles

TeMPD **:** 2,3,5,6-tetramethyl-1,4-phenylene-diamine

THF **:** Tetrahydrofuran

TraPPE **:** Transferable Potentials for Phase Equilibria Force Field

TrMPD **:** 2,4,6-trimethylbenzene-1,3-diamine

UA **:** United Atom

UFF **:** Universal Force Field

UMN **:** University of Minnesota

US **:** United States

US **:** Umbrella sampling

VdW **:** Van der waals

WHAM **:** Weighted histogram analysis method

XRD **:** X-ray diffraction

ZIF **:** Zeolitic imidazolate frameworks

ZIF-67 **:** $Co(Hmim)_2$

ZIF-8 **:** $Zn(Hmim)_2$

β-CD **:** Beta-cyclodextrin

***μ*VT** **:** The Grand Canonical ensemble

SYMBOLS

A	**:** Helmholtz function
cmHg	**:** Centimeters of Mercury
D	**:** Diffusivity
e	**:** Partial charge
esu	**:** Electrostatic unit of charge
f	**:** Fugacity
$\mathbf{F}_i$	**:** Force acting on atom i
g	**:** Total number of degrees of freedom
G	**:** Gibbs free energy
GPU	**:** Gas permeation units
$\boldsymbol{H}$	**:** Planck constant
K	**:** Temperature
$\boldsymbol{K_s}$	**:** Kinetics energy
$\mathbf{K_r}$, $\mathbf{K_z}$	**:** Spring constant
l	**:** Length
L	**:** Lagrangian of the system
m	**:** Number of system states
$\mathbf{M_\mu}$	**:** Mass of the nuclei
$\boldsymbol{N}$	**:** Number of molecules
$\boldsymbol{N_A}$	**:** Avogadro's number
nm	**:** Nanometer
$\boldsymbol{P}$	**:** Pressure
P	**:** Permeability
q	**:** Partial charge
Q	**:** Effective mass
$\mathbf{r_{ij}}$	**:** Separating distance between atoms
S	**:** Sorption coefficient
S	**:** Entropy
STP	**:** Standard temperature and pressure

t	**:** Time
$\boldsymbol{T}$	**:** Temperature
U	**:** Total energy
$\boldsymbol{V}$	**:** System volume
$\mathbf{V_i}$	**:** Van der Waals volume
$\mathbf{V_f}$	**:** Void fraction
$\boldsymbol{Z}$	**:** Atomic number of the nuclei
Z	**:** Compressibility factor
$\boldsymbol{a}$	**:** Selectivity
β	**:** Boltzman constant
$\boldsymbol{\eta}$	**:** Boltzmann density probability
$\boldsymbol{\epsilon_{ij}}$	**:** Well depth of energy
$\boldsymbol{\varepsilon}$	**:** Molar energy
$\langle \boldsymbol{E} \rangle$	**:** Average energy
γ	**:** Phase angle
$\widehat{\boldsymbol{H}}$	**:** Hamiltonian operator
ħ	**:** Reduced Plank constant
Λ	**:** Broglie thermal wavelength
$\boldsymbol{n}$	**:** Multiplicity
$\boldsymbol{\mu_i}$	**:** Chemical potential of molecular type *i*
$\boldsymbol{p_k}$	**:** Generalized momenta
$\boldsymbol{p_s}$	**:** Momentum
ρ(r)	**:** Electron density
ρN	**:** Atomic density
Ψ	**:** Wave function
φ	**:** Torsional angle distribution
$\boldsymbol{\sigma_{kt}}$	**:** Molecule kinetic diameter
$\boldsymbol{\sigma_{LJ}}$	**:** Lennard–Jones parameter
$\boldsymbol{s^N}$	**:** Scaled coordinates
$	**:** Dollar

LIST OF TABLES

Page

Table 1.1 : Physical properties of C2 and C3 olefin and paraffin [26]. **17**
Table 1.2 : The physical properties of several olefins and paraffins [45]..... **24**
Table 1.3 : Summary of the gas separation performance of MOFs-based MMMs. **66**
Table 1.4 : Summary of the gas separation performance of MOFs-based MMMs for C2/C3 separation..... **75**
Table 2.1 : Statistical ensembles [1]……**118**
Table 3.1 : The atomic partial charges for ZIF-67……**157**
Table 3.2 : Description of the 21-steps equilibration method [12]. **162**
Table 3.3 : Comparison between the simulated properties for the three polymer models and the corresponding data available in the literature..... **163**
Table 3.4 : Atom types and charges for ZIF-67-IDip **173**
Table 3.5 : FFV increase in 6FDA-DAM and MOF/6FDA-DAM composites at T=35°C and P=8 bar, induced by the single component adsorption of C_3H_6 and C_3H_8. ..... **194**
Table 4.1 : Atom types and charges for ZIF-67-IPD…… **229**
Table 4.2 : The atomic partial charges for ZIF-67 NP terminated by methanol..... **242**

LIST OF FIGURES

Page

Figure 1. Overall strategy of the PhD work **7**
Figure 1.1 : (a) Global consumption of base chemicals in 2019. (b) Current and estimated market values of ethylene and propylene [23]. **15**
Figure 1.2 : Different techniques employed for light olefin/paraffin separations [5]..... **17**
Figure 1.3 : Schematic diagrams of kinetic separation and molecular sieving mechanisms [23]. **20**
Figure 1.4 : Schematic diagrams of various structures of membranes [38]. **21**
Figure 1.5 : Schematic representation of a gas separation membrane [39]. **22**
Figure 1.6 : Schematic representation of most common possible mechanisms for gas separation with membrane [40]. **23**
Figure 1.7 : Schematic representation of the Robeson upper bounds (trade-off curves) from 1991 and 2008 [48]..... **26**
Figure 1.8 : Rigid, randomly contorted fragment of PIM-1 structure [50]..... **27**
Figure 1.9 : Structural classification of PIMs based on building blocks [53]. **28**
Figure 1.10 : Comparison of propylene/propane gas separation performance of different polymeric materials [61]..... **29**
Figure 1.11 : Chemical structure of (a) acid anhydrides and (b) diamines used in the synthesis of polyimides [1]..... **33**
Figure 1.12 : Representation of the polymer structures explored in this thesis (a) 6FDA-DAM (b) 6FDA-DABA [79] and (c) PIM-1 [80]. **37**
Figure 1.13 : A common MOF structure consists of a metal based cluster and an organic linker, with the yellow sphere representing “open space” [95]..... **38**
Figure 1.14 : Growth of the CSD and MOF entries from 1990 to 2020 [117]. **39**
Figure 1.15 : A concise timeline highlighting key advancements in the field of MOFs and MOF membranes [129]. **41**
Figure 1.16 : Scheme showing the structural diversity of zeolites and MOFs [138]. **42**
Figure 1.17 : The structure of NbOFFIVE-1-Ni, with a focus on the arrangement of building blocks, and a comparison with the parent SIFSIX-3-Ni. (a) Illustration of a 3D MOF with primitive cubic topology, showcasing the square-shaped arrangement in the Ni-pyrazine (4,4′) square grid, pillared by inorganic blocks [$(NbOF_5)^{2-}$ or $(SiF_6)^{2-}$] (b) Crystal structure of NbOFFIVE-1-Ni, displaying the titling of pyrazine molecules. (c) Crystal structure of SIFSIX-3-Ni. Simulation of the maximum open structure of (d) NbOFFIVE-1-Ni and (e) SIFSIX-3-Ni, displaying a theoretical window sizes [155]. **47**
Figure 1.18 : Representation of the MOF structures explored in this thesis (a) ZIF-67 [168] and (b) UTSA-280 [5]. **52**
Figure 1.19 : Schematic of MMM concept [2]. **53**
Figure 1.20 : MOFs-based MMM [202]. **58**
Figure 1.21 : Typical MOFs employed as fillers in MMMs [216]. **59**

Figure 1.22 : Propylene/propane separation performance of channel-based and carrier-based membranes. The grey, light pink and light blue oval areas highlight the separation performance of membranes with network structures, membranes with framework structures, and other kinds of channel-based membranes, respectively [26]. **73**
Figure 1.23 : Ethylene/ethane separation performance of channel-based and carrier-based membranes. The grey and light blue oval areas highlight the separation performance of membranes with network structures and other kinds of channel-based membranes, respectively [26]..... **74**
Figure 2.1 : Illustration of the use of MC and MD simulations to build a reliable statistical ensemble and extract the desired properties [2]. ……**122**
Figure 2.2 : Representation of the Lennard-Jones potential to describe the interactions between two atom pairs. [7]. **125**
Figure 2.3 : Schematic representation of the periodic boundary conditions [19]..... **129**
Figure 3.1 : Representative ZIF-67 super-cell. Color code: C (gray), N (blue), Co (steel blue), and H (white).……...**155**
Figure 3.2 : Schematic representation of the ZIF-67 external surface. Color code: C (gray), O (red), N (blue), Co (steel blue), and H (white). **156**
Figure 3.3 : ZIF-67 crystal, terminated by OH and ligand groups. **157**
Figure 3.4 : MD-simulated aperture size distribution of ZIF-67 NP at 308 K. **158**
Figure 3.5 : ZIF-67 model validation using propane (solid) and propylene (open) adsorption isotherms obtained with experimental [43] (red line) and computational data (black) at 308 K up to 1 bar..... **159**
Figure 3.6 : Schematic representation of the 6FDA-DAM, 6FDA-DABA and PIM-1 repeat units with their charges. Color code: C (gray), O (red) and N (blue)..... **160**
Figure 3.7 : 6FDA-DAM model validation comparing experimental [43] propane (red line with solid markers) and propylene (red line with open markers) adsorption isotherms to the simulated data (black) at 308 K up to 1 bar. **164**
Figure 3.8 : Representative atomistic model for the (a) ZIF-67/6FDA-DAM composite containing 34.5 wt.% ZIF-67 and (b) its resulting MOF/polymer interface. ZIF-67 atoms are represented as ball and stick atoms and polymer chains in light blue lines. Color code: O (red), C (grey), H (white), N (blue) and Co (steel blue). . **166**
Figure 3.9 : Calculated radial atomic density distribution **of** (a) 6FDA-DAM (black) in the unfunctionalized ZIF-67/6FDA-DAM composite with respect to the center of the nanoparticle (r = 0), (b) Representative snapshot of the unfunctionalized ZIF-67/6FDA-DAM interface showing the presence of microvoids. Color scheme: 6FDA-DAM, grey wireframe; ZIF-67, ball and stick; O, red; C, gray; H, white; Co, blue..... **167**
Figure 3.10 : Calculated radial distribution functions between oxygen atoms of 6FDA-DAM and – H(OH) of the ZIF-67 along with illustration of the preferential site-to-site interactions for the ZIF-67/6FDA-DAM composite. **168**
Figure 3.11 : Diamine–dianhydride linkage of torsional angle $\varphi_{C-N-C-C}$ in 6FDA-DAM... **168**
Figure 3.12 : Torsional angle Distributions ($\varphi_{C-N-C-C}$) in the 6FDA-DAM for the ZIF-67/6FDA-DAM at the interface (black) and at the bulk phase (red) and neat 6FDA-DAM (blue)..... **169**

Figure 3.13 : Schematic representation of the IDip molecule. Color code: C (gray), N (blue), and H (white). **170**
Figure 3.14 : Schematic representation of the ZIF-67-IDip surface. Color code: C (gray), O (red), N (blue), Co (steel blue), and H (white) **171**
Figure 3.15 : Schematic representation of the clusters used to calculate charges for the ZIF-67 imidazolate linkers and IDip at the DFT-level. **172**
Figure 3.16 : Schematic representation of the atom types for the charges. **172**
Figure 3.17 : ZIF-67-IDip crystal, terminated by OH and ligand groups. Color code: C (gray), O (red), N (blue), Co (steel blue), and H (white). **174**
Figure 3.18 : Calculated radial atomic density distribution of (a) 6FDA-DAM (black) in the functionalized ZIF-67-IDip/6FDA-DAM composite with respect to the center of the nanoparticle (r = 0), (b) Representative snapshot of the functionalized ZIF-67-IDip/6FDA-DAM interface where MOF/polymer overlap is marked by a dashed circle. The interfacial MOF/polymer overlap regions are marked by the dashed area. Color scheme: 6FDA-DAM, grey wireframe; ZIF-67-IDip, ball and stick; O, red; C, gray; H, white; Co, blue. **176**
Figure 3.19 : Calculated radial distribution functions in the composites (a) between oxygen atoms of 6FDA-DAM and –H(OH) of the ZIF-67 functionalized (black) and unfunctionalized (red) surface in the corresponding composites along with illustration of the preferential site-to-site interactions for the ZIF-67/6FDA-DAM composite and (b) between oxygen atoms (red curve) and $–CF_3$ groups (black curve) of 6FDA-DAM and carbon atoms of the IDip functional groups attached at the ZIF-67 surface along with illustration of the preferential site-to-site interactions of the ZIF-67-IDip/6FDA-DAM composite. **177**
Figure 3.20 : Torsional angle Distributions ($\varphi_{C–N–C-C}$) in the 6FDA-DAM for the ZIF-67-IDip/6FDA-DAM at the interface (black) and at the bulk phase (red). **178**
Figure 3.21 : Torsional angle ($\varphi_{C–N–C-C}$) distributions in the 6FDA-DAM for the ZIF-67/6FDA-DAM (black) and ZIF-67-IDip/6FDA-DAM (blue) composites at the interface. **178**
Figure 3.22 : Calculated radial atomic density distribution of (a) 6FDA-DAM (black) in the ZIF-67/6FDA-DAM composite with respect to the center of the nanoparticle (r = 0), (b) Representative snapshot of the ZIF-67/6FDA-DAM interface showing the presence of microvoids, (c) PIM-1 (black) in the ZIF-67/PIM-1 composite with respect to the center of the nanoparticle (r = 0), (d) Representative snapshot of the interface of ZIF-67/PIM-1 showing the presence of microvoids. The interfacial MOF/polymer overlap regions are marked by black dashed shaded areas. Color scheme: 6FDA-DAM and PIM-1, grey wireframe; ZIF-67, ball and stick; O, red; C, gray; H, white; Co, blue. **181**
Figure 3.23 : Torsional angle of $\varphi_{C–C–O-C}$ (green colored) and $\varphi_{C–N–C-C}$ (red colored) for PIM-1. ..... **182**
Figure 3.24 : Torsional angle distributions in the PIM-1 for the ZIF-67/PIM-1 composite (a) $\varphi_{C–C–O-C}$ angle at the interface (black) and at the bulk phase (red) (b) $\varphi_{C–C–C-C}$ angle at the interface (black) and at the bulk phase (red). **182**

Figure 3.25 : Calculated radial atomic density distribution of (a) 6FDA-DAM (black) in the functionalized ZIF-67-IDip/6FDA-DAM composite with respect to the center of the nanoparticle (r = 0), (b) Representative snapshot of the functionalized ZIF-67-IDip/6FDA-DAM interface showing the presence of microvoids, (c) PIM-1 (black) in the functionalized ZIF-67-IDip/PIM-1 composite with respect to the center of the nanoparticle (r = 0), (d) Representative snapshot of the interface of functionalized ZIF-67-IDip/PIM-1 showing the presence of microvoids. The interfacial MOF/polymer overlap regions are marked by black dashed shaded areas. Color scheme: 6FDA-DAM and PIM-1, grey wireframe; ZIF-67-IDip, ball and stick; O, red; C, gray; H, white; Co, blue. **184**

Figure 3.26 : Torsional angle distributions in the PIM-1 for the functionalized ZIF-67-IDip/PIM-1 composite (a) $\varphi_{C-C-O-C}$ angle at the interface (black) and at the bulk phase (red) (b) $\varphi_{C-C-C-C}$ angle at the interface (black) and at the bulk phase (red). **185**

Figure 3.27 : Gas adsorption of (a) Propane uptakes (b) Propylene uptakes in PIM-1 (blue), 6FDA-DAM (red) and 6FDA-DABA (black) at 308 K up to 8 bar. (Dashed lines are to guide the eye). **187**

Figure 3.28 : Gas adsorption of (a) Propane uptakes in 34.5 wt % ZIF-67/PIM-1 (blue), ZIF-67/6FDA-DAM (red) and ZIF-67/6FDA-DABA (black) (b) Propylene uptakes in 34.5 wt % ZIF-67/PIM-1 (blue), ZIF-67/6FDA-DAM (red) and ZIF-67/6FDA-DABA (black) (c) Propane uptakes in ZIF-67(red), 6FDA-DAM (blue), 34.5 wt % ZIF-67/6FDA-DAM (black solid) and volume additive 34.5 wt % ZIF-67/6FDA-DAM (black empty) (d) Propylene uptakes in ZIF-67(red), 6FDA-DAM (blue), 34,5 wt % ZIF-67/6FDA-DAM (black solid) and volume additive 34.5 wt % ZIF-67/6FDA-DAM (black empty) at 308 K up to 8 bar. (Dashed lines are to guide the eye). **188**

Figure 3.29 : Radial distribution functions (a) Favored MOF/polymer interactions between the – O (blue and black) of and – H(OH) of ZIF-67 surface for 6FDA-DAM and 6FDA-DABA and – N (red) of PIM-1 and – H(OH) of ZIF-67 surface. (b) Selected sorption sites are in red colors for the 6FDA-DAM, 6FDA-DABA and PIM-1 repeat units. 189

Figure 3.30 : Simulated propane (solid symbols) and propylene (open symbols) sorption isotherms for the composites. 34.5 wt. % ZIF-67/6FDA-DAM (black) and ZIF-67-IDip/6FDA-DAM (red) at 308 K up to 8 bar and comparison with pure 6FDA-DAM (blue) (dashed lines are to guide the eyes). **190**

Figure 3.31 : Calculated radial atomic density distribution of functionalized ZIF-67-IDip/6FDA-DAM composite of 6FDA-DAM (black) when exposed to (a) propylene and (b) propane molecules, unfunctionalized ZIF-67/6FDA-DAM composite of 6FDA-DAM (black) when exposed to (c) propylene and (d) propane molecules with respect to the center of the nanoparticle (r = 0)..... **192**

Figure 3.32 : Calculated radial atomic density distribution of functionalized ZIF-67-IDip/PIM-1 composite of PIM-1 (black) when exposed to (a) propylene and (b) propane molecules, unfunctionalized ZIF-67/ PIM-1 composite of PIM-1 (black) when exposed to (c) propylene and (d) propane molecules with respect to the center of the nanoparticle (r = 0). **193**
Figure 3.33 : Simulated propane and propylene sorption isotherms for 34.5 wt. % ZIF-67-IDip/PIM-1 (blue), ZIF-67-IDip/6FDA-DAM (red) and ZIF-67-IDip/6FDA-DABA (black) at 308 K up to 8 bar, with an inset up to 1 bar at logarithmic scale (dashed lines are to guide the eye): (a) Propane and (b) Propylene (c) Comparison of propane (solid) and propylene (blank) uptakes in 34.5 wt. % ZIF-67-IDip/6FDA-DAM (black) and ZIF-67/6FDA-DAM (red)..... **195**
Figure 3.34 : Torsional angle ($\varphi_{C-N-C-C}$) distributions in the 6FDA-DAM for the unfunctionalized ZIF-67/6FDA-DAM at the interface (black) and at the bulk phase (red) when exposed to (a) propylene and (b) propane molecules, functionalized ZIF-67-IDip/6FDA-DAM at the interface (black) and at the bulk phase (red) when exposed to (c) propylene and (d) propane molecules. **196**
Figure 3.35 : Torsional angle ($\varphi_{C-N-C-C}$) distributions in the PIM-1 for the unfunctionalized ZIF-67/PIM-1 at the interface (black) and at the bulk phase (red), when exposed to (a) propylene and (b) propane molecules, functionalized ZIF-67-IDip/PIM-1 at the interface (black) and at the bulk phase (red) when exposed to (c) propylene and (d) propane molecules..... **197**
Figure 3.36 : Torsional angle ($\varphi_{C-N-C-C}$) distributions in the PIM-1 for the ZIF-67/PIM-1 at the interface (black) and at the bulk phase (red), when exposed to (a) propylene and (b) propane molecules, functionalized ZIF-67-IDip/PIM-1 at the interface (black) and at the bulk phase (red) when exposed to (c) propylene and (d) propane molecules. **198**
Figure 3.37 : Gas adsorption of (a) Propane uptakes in 18 wt % ZIF-67/PIM-1 (blue), ZIF-67/6FDA-DAM (red) and ZIF-67/6FDA-DABA (black) (b) Propylene uptakes in 18 wt % ZIF-67/PIM-1 (blue), ZIF-67/6FDA-DAM (red) and ZIF-67/6FDA-DABA (black) at 308 K up to 8 bar. (c) Volume additive approach in propane (solid) and propylene (open) uptakes in 34.5 wt % ZIF-67/6FDA-DAM (red) and 18 wt % ZIF-67/6FDA-DAM (black) (dashed lines are guide to the eye)..... **199**
Figure 4.1 : Schematic representation of the IDip molecule. Color code: C (gray), N (blue), and H (white)..... **227**
Figure 4.2 : Schematic representation of the ZIF-67-IPD surface. Color codes for the atoms are the same as in Figure 4.1. ..... **227**
Figure 4.3 : Schematic representation of clusters used to calculate the charges for ZIF-67 and IPD at the DFT-level. Color codes for the atoms are the same as in Figure 4.1. ..... **228**
Figure 4.4 : Schematic representation of the atom types for the charges. **228**
Figure 4.5 : ZIF-67-IPD crystal, terminated by OH and ligand groups. Color code: C (gray), O (red), N (blue), Co (steel blue), and H (white). **230**
Figure 4.6 : Representative atomistic model for the ZIF-67-IPD/6FDA-DAM composite containing 34.5 wt.% ZIF-67-IPD. ZIF-67 atoms are represented as ball and stick atoms and polymer chains in light blue lines. Color code: O (red), C (grey), H (white), N (blue) and Co (steel blue)..... **231**

Figure 4.7 : Calculated radial atomic density distribution of (a) 6FDA-DAM (black) in the unfunctionalized ZIF-67/6FDA-DAM composite with respect to the center of the nanoparticle (r = 0), (b) Radial atomic density distribution of 6FDA-DAM (black) in the functionalized ZIF-67-IPD/6FDA-DAM composite with respect to the center of the nanoparticle (r = 0). The interfacial MOF/polymer overlap regions are marked by black dashed shaded areas. **233**

Figure 4.8 : Calculated radial distribution functions in the composites (a) between oxygen atoms of 6FDA-DAM and – H(OH) of the ZIF-67-IPD (blue) and ZIF-67-IDip functionalized (black) and unfunctionalized (red) surface in the corresponding composites along with illustration of the preferential site-to-site interactions for the ZIF-67/6FDA-DAM composite and (b) between $–CH_3$ groups (orange curve) and $–CF_3$ groups (green curve) of 6FDA-DAM and Carbon atoms of the IPD functional groups attached at the ZIF-67 surface along with illustration of the preferential site-to-site interactions of the ZIF-67-IPD/6FDA-DAM composite..... **234**

Figure 4.9 : Calculated radial atomic density distribution of (a) PIM-1 (black) in the unfunctionalized ZIF-67/PIM-1 composite with respect to the center of the nanoparticle (r = 0), (b) Radial atomic density distribution of PIM-1 (black) in the functionalized ZIF-67-IPD/PIM-1 composite with respect to the center of the nanoparticle (r = 0), The interfacial MOF/polymer overlap regions are marked by black dashed shaded areas. **236**

Figure 4.10 : Torsional angle ($\varphi_{C–N–C-C}$) distributions in the 6FDA-DAM for the ZIF-67-IPD/6FDA-DAM at the interface (black) and at the bulk phase (red). **237**

Figure 4.11 : Torsional angle distributions in the PIM-1 for the ZIF-67-IPD/PIM-1 composite (a) $\varphi_{C–C–O-C}$ angle at the interface (black) and at the bulk phase (red) (b) $\varphi_{C–C–C-C}$ angle at the interface (black) and at the bulk phase (red). **238**

Figure 4.12 : Simulated propane (solid symbols) and propylene (open symbols) sorption isotherms for the composites. 34.5 wt. % ZIF-67/6FDA-DAM (blue) and ZIF-67-IPD/6FDA-DAM (orange) at 308 K up to 8 bar and comparison with ZIF-67 NP (red) and ZIF-67-IPD NP (black). **239**

Figure 4.13 : Simulated propane (solid symbols) and propylene (open symbols) sorption isotherms for the composites. 34.5 wt. % ZIF-67-IPD/6FDA-DAM (black) and ZIF-67-IPD/PIM-1 (blue) at 308 K up to 8 bar. **240**

Figure 4.14 : Schematic representation of the ZIF-67 surface terminated by methanol. Color code: C (gray), O (red), N (blue), Co (steel blue), and H (white) **241**

Figure 4.15 : Schematic representation of cluster to obtain charges for ZIF-67 NP terminated by methanol. **242**

Figure 4.16 : ZIF-67 crystal, terminated by $–C(H_3)O$ groups and −H. Color code: C (gray), O (red), N (blue), Co (steel blue), and H (white). **243**

Figure 4.17 : Representative atomistic model for the ZIF-67/ PIM-1 composite with containing 34.5 wt.% ZIF-67 with $–C(H_3)O$ termination. PIM-1 atoms are represented as ball and stick atoms and polymer chains in light blue lines. Color code: O (red), C (grey), H (white), N (blue) and Co (steel blue). **244**

Figure 4.18 : Calculated radial atomic density distribution of (a) 6FDA-DAM (black) in the ZIF-67/6FDA-DAM composite with –OH termination with respect to the center of the nanoparticle (r = 0), (b) Representative snapshot of the interface of ZIF-67/6FDA-DAM showing the presence of microvoids (c) Radial atomic density distribution of 6FDA-DAM (black) in ZIF-67/6FDA-DAM composite with –C(H_3)O terminations with respect to the center of the nanoparticle (r = 0), (d) Representative snapshot of the interface of ZIF-67/6FDA-DAM with –C(H_3)O terminations where MOF/polymer overlap is marked by a dashed circle. The interfacial MOF/polymer overlap regions are marked by black dashed shaded areas. Color scheme: 6FDA-DAM, grey wireframe; ZIF-67, ball and stick; O, red; C, gray; H, white; Co, blue..... **245**

Figure 4.19 : Calculated radial distribution functions in the composites (a) between oxygen atoms of 6FDA-DAM and – H(CH_3O**H**) of the ZIF-67 (red) and –H(O**H**) of the ZIF-67 (black) surface (b) between –CH_3 groups of 6FDA-DAM and –O(CH_3**O**H) of the ZIF-67 (red) and –O(**O**H) of the ZIF-67 (black) surface in the corresponding composites. 246

Figure 4.20 : Calculated radial atomic density distribution of (a) PIM-1 (black) in the ZIF-67/PIM-1 composite with –OH termination with respect to the center of the nanoparticle (r = 0), (b) Radial atomic density distribution of PIM-1 (black) in the ZIF-67/PIM-1 composite with –C(H_3)O termination with respect to the center of the nanoparticle (r = 0), The interfacial MOF/polymer overlap regions are marked by black dashed shaded areas. **247**

Figure 4.21 : Representative snapshot of the interface of (a) ZIF-67/6FDA-DAM where 6FDA-DAM perfectly covers ZIF-67 surface (b) ZIF-67/PIM-1 where PIM-1 plug into the troughs of MOF surface. Color scheme: 6FDA-DAM and PIM-1, grey wireframe; ZIF-67, wireframe; O, red; C, gray; H, white; Co, blue. **248**

Figure 4.22 : Torsional angle ($\varphi_{C-N-C-C}$) distributions in the 6FDA-DAM for the (a) ZIF-67/6FDA-DAM at the interface (black) and at bulk phase (red) with –C(H_3)O terminated (b) ZIF-67/6FDA-DAM at the interface (black) and at the bulk phase (red) with –OH terminated composites. **249**

Figure 4.23 : Torsional angle distributions in the PIM-1 for the ZIF-67/PIM-1 composite with –C(H_3)O termination (a) $\varphi_{C-C-O-C}$ angle at the interface (black) and at the bulk phase (red) (b) $\varphi_{C-C-C-C}$ angle at the interface (black) and at the bulk phase (red). **250**

Figure 4.24 : General summary of MOF/polymer overlap (black) and interfacial (red) lengths of composites with ZIF-67 (-OH termination), ZIF-67 (–C(H_3)O termination), ZIF-67-IDip and ZIF-67-IPD fillers in (a) 6FDA-DAM and (b) PIM-1 polymer matrices in bar charts. **251**

Figure 4.25 : Binding energies per atoms of ZIF-67 with polymers in 34.5 wt. % ZIF-67/6FDA-DAM and 34.5 wt. % ZIF-67/PIM-1 composites with –C(H_3)O (MeOH) and –OH terminations in bar charts. **252**

Figure 4.26 : Simulated propane (solid symbols) and propylene (open symbols) sorption isotherms for the composites. 34.5 wt. % ZIF-67/6FDA-DAM (black) with –OH terminations and ZIF-67/6FDA-DAM (red) with –C(H_3)O terminations at 308 K up to 8 bar and comparison with pure 6FDA-DAM (blue). **253**

Figure 4.27 : Simulated propane (solid symbols) and propylene (open symbols) sorption isotherms for the composites. 34.5 wt. % ZIF-67/6FDA-DAM (black) and ZIF-67/PIM-1 (blue) with –C(H_3)O terminations at 308 K up to 8 bar. **253**
Figure 5.1 : Schematic representation of the computational procedure applied to ZIF-67 NP……..**263**
Figure 5.2 : Calculated free energy profile for propane (black line) and propylene (red line) molecules plotted as a function of the distance from the aperture center to the ouside of the cage for ZIF-67 NP. **265**
Figure 5.3 : Calculated free energy profile for propane (black line) and propylene (red line) molecules as a function of the distance from the aperture center to the ouside of the cage for ZIF-67 NP along with selectively preserving the rigidity of specific Co-N bonds within the ZIF-67 NP. **267**
Figure 5.4 : Aperture size calculation of ZIF-67 obtaining from the mean values of distances of r_1 , r_2 and r_3 (red dashed lines). **268**
Figure 5.5 : Distribution of ZIF-67 aperture sizes upon heating (black line, 308 K; red line, 500 K; green line, 600 K). **269**
Figure 5.6 : Schematic representation of the computational procedure applied to ZIF-67-IDip NP. **270**
Figure 5.7 : Calculated free energy profile of propane (black line) and propylene (red line) molecules plotted as a function of the distance from the aperture center to the outside of the cage for ZIF-67-IDip NP. **272**
Figure 5.8 : The effective diameter for (a) ZIF-67 aperture size (black line) and ZIF-67-IDip aperture size (red line) (b) ZIF-67-IDip aperture sizes upon heating (black line, 308 K; red line, 500 K; green line, 600 K). **273**
Figure 5.9 : Schematic representation of how umbrella sampling is performed in ZIF-67-IPD cage. **274**
Figure 5.10 : Calculated free energy profile of propane (black line) and propylene (red line) molecules plotted as a function of the distance from the aperture center to the outside of the cage for ZIF-67-IPD NP. **275**
Figure 5.11 : Schematic representation of (a) propane and (b)propylene passage through the gate of ZIF-67-IPD cage. ZIF-67-IPD atoms are represented as stick atoms and guests in orange CPK atoms. Color code: O (red), C (grey), H (white), N (blue) and Co (steel blue). **276**
Figure 5.12 : Calculated free energy profile of propane (black line) and propylene (red line) molecules plotted as a function of the distance from the aperture center to the outside of the cage for ZIF-67 NP NP with –C(H_3)O terminations. **278**
Figure 5.13 : Distribution of ZIF-67 aperture sizes with methanol (black line) and water (red line) terminations at 308 K. **279**

Figure 1. UTSA-280 crystal, terminated by OH and H groups, (b) Representation of 6FDA-DAM:DABA(3:2) structure, (c) Illustration of the constructed UTSA-280/6FDA-DAM:DABA model, (d) Atomic density profile for the UTSA-280/6FDA-DAM:DABA in the direction perpendicular to the surface slab (i.e. along the z direction), (e) Calculated radial distribution functions in the UTSA-280/6FDA-DAM:DABA between O (red curve), $–CH_3$ groups (blue curve) and C (black curve) of 6FDA-DAM:DABA and H(OH) of the UTSA-280, (f) Pore size distribution of UTSA-280/6FDA-DAM:DABA. UTSA-280 atoms are represented as ball and stick atoms. Color code: O (red), C (grey), H (white) and Ca (green)……..……. **290**

GENERAL INTRODUCTION

1. Significance of the Thesis

Since the development of the chemical and petroleum industry in the 1920s, light olefins like ethylene and propylene have played a crucial role in petrochemical industries, serving as essential raw materials for various chemical and consumer products [1]. At present, the feedstocks for olefin production include oil (naphtha and light paraffin), natural gas and coal. In the petroleum industry, processes like fluid catalytic cracking, gas oil thermal cracking, or thermal decomposition are commonly employed for olefin production. However, high-purity olefins are essential for the downstream processes in the olefin industry. Hence, a suitable separation process is necessary to extract the olefins from the product mixtures [2]. The traditional separation methods, particularly cryogenic distillation, are energy-intensive, primarily because of the similar molecular sizes and boiling points of propane/propylene and ethylene/ethane molecules, which make their separation challenging [3].

In this context, membrane-based-separation has gained popularity as an attractive alternative technology due to its cost-effectiveness, continuous operation, and superior energy efficiency, while offering a significant reduction in energy consumption [4]. In large-scale commercial gas separation processes, polymeric membranes are typically favored over inorganic membranes due to their processability, scalability, and mechanical strength, whereas these membranes suffer a tradeoff between permeability and selectivity due to the tendency of condensable gases such as C_3H_6 and C_3H_8 cause swelling of the polymer chains [5]. Hybrid mixed-matrix membranes (MMMs), offer an efficient alternative to overcome the disadvantages of polymer-based membranes by combining a continuous organic polymer phase with a dispersed inorganic/organic fillers. Among the various fillers available, Metal Organic Frameworks (MOFs) have attracted significant attention due to their tunable pore structures and versatile chemical functionality. Establishing strong interfacial adhesion between MOF and polymers is crucial for fabricating continuous and mechanically stable membranes, allowing for high MOF loading and ensuring the uniform dispersion of MOF nanoparticles within the polymer matrices [6].

In this thesis, even though there are numerous MOFs reported for various separations, the primary focus is on ZIF-67 ($Co(Hmim)_2$, Hmim = 2-methylimidazole)), for propylene/propane separation and UTSA-280 ($Ca(C_4O_4)(H_2O)$) for ethylene/ethane separation. ZIF-67, Cobalt-substituted ZIF-8 is a sub family of the zeolitic imidazolate frameworks (ZIFs), has gained significant attention due to its remarkable stability, selective architecture, and its efficacy in propylene/propane separation [7]. On the other hand, UTSA-280 is exceptionally well-suited for ethylene/ethane separation due to its molecular sieving properties [8]. These findings encouraged the incorporation of ZIF-67 and UTSA-280 as fillers in a range of polymeric matrix for the fabrication of propylene/propane and ethylene/ethane selective MMMs.

Molecular simulation methods are powerful tools employed to simulate molecular behavior and interactions, operating at both the atomistic level (classical calculations) and electronic level (quantum calculations). To investigate the mechanical properties of polymers, Molecular Dynamics (MD) methods are used, whereas the modeling of sorption isotherms in membranes employs a combination of Monte Carlo (MC) and MD methods. Although computer simulations are powerful tools for comprehending the interfacial dynamics in MMMs, researches on the polymer/nanoparticle interface within MMMs have been limited.

To investigate the impact of the MOF/polymer interface morphology on MMM separation performance, atomistic simulations initially aimed to gain a deep understanding of the MOF/polymer interfacial structure by systematically varying nature of the polymer. This approach enabled the identification of key features in both MOFs and polymers that influence the adhesion between the two components in the MMMs. Subsequently, to fully exploit the potential of MOF/polymer composites, enhancing MOF/polymer interfacial interactions through ZIF-67 surface modification can significantly improve adhesion between the two components. For this purpose, NHC-based surface functionalized group of IDip [9] is chosen due to its potential high affinity to unsaturated metal sites, along with its similar chemistry to the imidazole linker present in ZIF-67. Simultaneously, isophthalic dihydrazide (IPD) [10] is explored due to its dual polar sides, making it suitable for adsorption on the MOF surface. While recent studies have suggested an improvement in MOF/polymer

adhesion through functionalization of the MOF, direct evidence confirming this effect remains limited.

When generating surface models of ZIF-67, it is important to consider that under-coordinated sites on its outer surface may be susceptible to reactions with the solvents employed during the synthesis process. To achieve this, the outer surface terminations of ZIF-67 are evaluated with two solvents, water, and methanol, while considering the dissociative adsorption of both water and methanol.

2. Research Purposes and Organization of the Thesis

The main objective of this PhD is to gain microscopic insight into the propylene/propane separation performances of MOF-based MMMs using a combination of force field- Monte Carlo and Molecular Dynamics simulations and quantum calculations.

Conducting computational studies instead of real experiments offers clear advantages, as experimental studies demand extensive efforts, resources, and a significant amount of time. Molecular simulations provide a rapid and precise evaluation of the gas separation potential of MOFs-based MMMs membranes under various operational conditions, a task that may pose challenges in experimental setups. Computational modeling, particularly high-throughput screening studies, offers a time-efficient means to evaluate the performance of MOF membranes, providing insightful molecular-level understanding of gas permeation in MOFs. HTCS studies predict the gas separation performance of MMMs, assuming perfect adhesion between the MOF filler and polymer matrix. However, these studies often neglect MOF/polymer incompatibility and focus exclusively on the atomistic-level description of the MOF particle, overlooking the influence of the polymer [11]. For this purpose, employing full atomistic simulations that integrate both MOF and polymer components to provide insights into the interactions at the MOF/polymer interface becomes the primary computational approach for this study. The exploration of atomic-level compatibility in MOF/polymer interactions through computational studies is limited; thus, further investigation in this area holds significant potential for designing high-performing

membranes. To achieve this highly ambitious objective, several steps are required with specific key target achievements:

a) Construction of atomistic model for the selected polymers such as PIM-1, 6FDA-DAM, 6FDA-DABA and the explored MOFs NPs ZIF-67 via DFT and force-field based Molecular Dynamics simulations,

b) Generation of the MOF/polymer interface models and understanding the interfacial structuring as well as the interactions in play that drive the compatibility between the two components and hence the feasibility of MMMs with well dispersed MOFs into the polymeric matrix,

c) Functionalization of the outer surface of the MOF with either carbene groups or coordinated solvent to tune the MOF/polymer compatibility,

d) Modulation of the polymer nature with the consideration of rigid and more flexible polymers to impact the MOF/polymer compatibility,

e) Exploration of the thermodynamic adsorption/separation of propane/propylene in this series of composites using Monte Carlo simulations combined with Molecular Dynamics relaxation steps,

f) Investigating of the kinetics of propane and propylene via potential of mean force (PMF) simulations

The overall strategy implemented over the PhD can be summarized as follows:

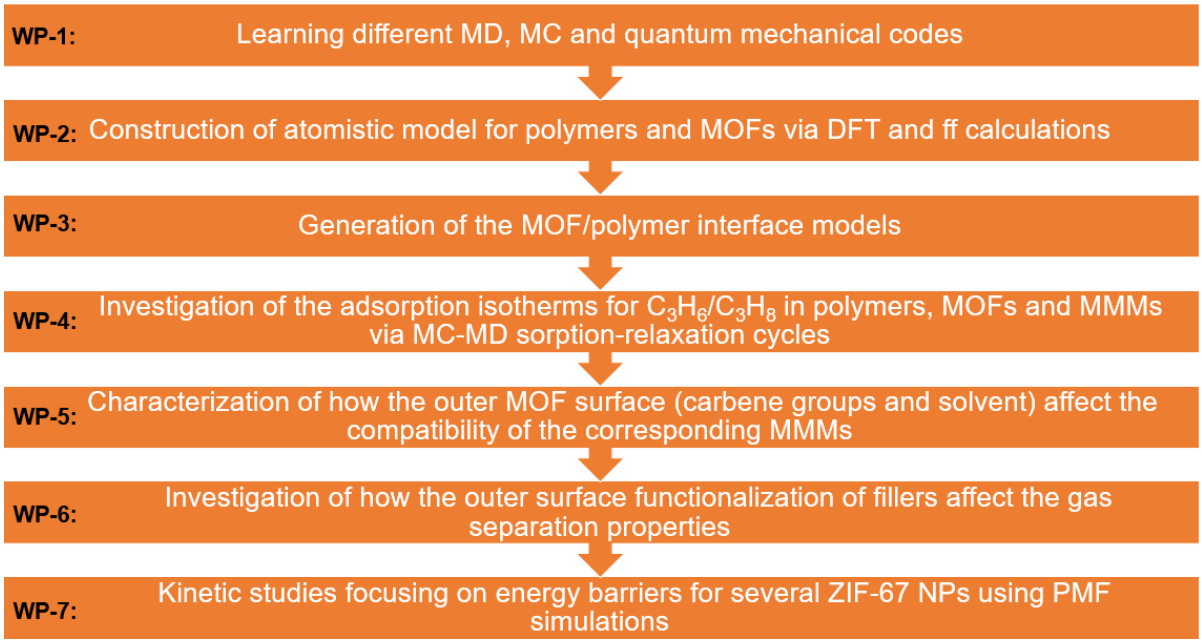

Figure 1. Overall strategy of the PhD work

The manuscript is constructed as follows:

Chapter 1 delivers an overview of the fields of MOFs, polymers and their resulting MMMs, with a special attention paid on their properties especially in the context of gas separation processes, particularly for the C2/C3 separation. The computational approaches commonly used to investigate the MOF-based MMMs are discussed along with their limitations.

Chapter 2 provides a brief summary of the basics of the molecular simulation approaches used in this PhD including statistical ensembles, force fields, Monte Carlo and Molecular Dynamics methods, quantum mechanical approaches, aiming to provide insight by using minimal number of mathematical equations.

Chapter 3 focuses on the computational methodology tailored for modeling MOFs, polymers and their resulting composites to reveal the microscopic origin of the improved adhesion of ZIF-67 and 6FDA-DAM in the resulting composites by functionalizing the MOF by carbene groups, as well as understanding how the MOF functionalization affects the propane and propylene adsorption performance of the composites. Furthermore, a systematic

assessment of the impact of the nature of the polymers (6FDA-DAM, 6FDA-DABA, PIM-1) on the ZIF-67/polymer adhesion in the corresponding composites and their subsequent impact on adsorption properties is described.

Chapter 4 details the microscopic models of IPD functionalized ZIF-67 with 6FDA-DAM and PIM-1, along with exploring the impact of terminal solvent of ZIF-67 on the ZIF-67/polymer adhesion in the corresponding composites as well as their sorption properties.

Chapter 5 describes the kinetics study, primarily focusing on evaluating the energy barrier required for the diffusion of propane and propylene throughout the pore entrance of ZIF-67 as well as functionalized ZIF-67 using PMF simulations implementing the umbrella sampling technique.

Finally, General Conclusions and Perspectives provides a comprehensive summary of the main findings of this PhD work and outlines future directions for further development. This includes the exploration of alternative MOF/Polymer composites, such as UTSA-280/6FDA-DAM:DABA for ethylene/ethane separation.

REFERENCES

[1] S. Najari, S. Saeidi, F. Gallucci, E. Drioli, Mixed matrix membranes for hydrocarbons separation and recovery: A critical review, Rev. Chem. Eng. 37 (2019) 363–406. https://doi.org/10.1515/revce-2018-0091.

[2] Y. Ren, X. Liang, H. Dou, C. Ye, Z. Guo, J. Wang, Y. Pan, H. Wu, M.D. Guiver, Z. Jiang, Membrane-Based Olefin / Paraffin Separations, 2001398 (2020) 1–29. https://doi.org/10.1002/advs.202001398.

[3] R. Lin, L. Ge, H. Diao, V. Rudolph, Z. Zhu, Propylene/propane selective mixed matrix membranes with grape-branched MOF/CNT filler, J. Mater. Chem. A. 4 (2016) 6084–6090. https://doi.org/10.1039/c5ta10553f.

[4] D.S. Sholl, R.P. Lively, Seven chemical separations, Nature. 532 (2016) 435–437.

[5] L.M. Robeson, The upper bound revisited, J. Memb. Sci. 320 (2008) 390–400. https://doi.org/10.1016/j.memsci.2008.04.030.

[6] D. Fan, A. Ozcan, O. Shekhah, R. Semino, M. Eddaoudi, G. Maurin, Engineering MOF surface defects in mixed matrix membranes: An effective strategy to enhance MOF/polymer adhesion and control interfacial gas transport, J. Membr. Sci. Lett. 2 (2022) 100029. https://doi.org/10.1016/j.memlet.2022.100029.

[7] P. Iacomi, G. Maurin, ResponZIF Structures: Zeolitic Imidazolate Frameworks as Stimuli-Responsive Materials, ACS Appl. Mater. Interfaces. 13 (2021) 50602–50642. https://doi.org/10.1021/acsami.1c12403.

[8] R.B. Lin, L. Li, H.L. Zhou, H. Wu, C. He, S. Li, R. Krishna, J. Li, W. Zhou, B. Chen, Molecular sieving of ethylene from ethane using a rigid metal–organic framework, Nat. Mater. 17 (2018) 1128–1133. https://doi.org/10.1038/s41563-018-0206-2.

[9] A. Knebel, A. Bavykina, S.J. Datta, L. Sundermann, L. Garzon-Tovar, Y. Lebedev, S. Durini, R. Ahmad, S.M. Kozlov, G. Shterk, M. Karunakaran, I.D. Carja, D. Simic, I. Weilert, M. Klüppel, U. Giese, L. Cavallo, M. Rueping, M. Eddaoudi, J. Caro, J. Gascon, Solution processable metal–organic frameworks for mixed matrix membranes using porous liquids, Nat. Mater. 19 (2020) 1346–1353. https://doi.org/10.1038/s41563-020-0764-y.

[10] Y. Shi, S. Wu, Z. Wang, X. Bi, M. Huang, Y. Zhang, J. Jin, Mixed matrix membranes with highly dispersed MOF nanoparticles for improved gas separation, Sep. Purif. Technol. 277 (2021) 119449. https://doi.org/10.1016/j.seppur.2021.119449.

[11] S. Keskin, S.A. Altinkaya, A Review on Computational Modeling Tools for MOF-Based Mixed Matrix Membranes, Computation. 7 (2019).

CHAPTER 1

POTENTIAL OF MOFS, POLYMERS AND MOF/POLYMER MIXED MATRIX MEMBRANES FOR C2 &C3 SEPARATION

1.1 Introduction

Light unsaturated hydrocarbons, such as propylene and ethylene, play a crucial role in petrochemical industries as they serve as essential raw materials for producing a wide range of chemicals and products used in both industrial and domestic applications [1,2]. The primary application of light olefins is in the polymerization industry, where they serve as the main raw materials for producing polypropylene from propylene and polyethylene from ethylene. In addition to polymers, light olefins are used in the production of various specialty chemicals, while light paraffins are primarily used as fuels [3]. In the petroleum industry, olefins are typically produced through processes such as fluid catalytic cracking, gas oil thermal cracking or thermal decomposition. The recent technology for dehydrogenation of paraffins to produce olefins encounters thermodynamic constraints, limiting the equilibrium conversion to 20–40%.[4]. Hence, a suitable separation process is necessary to extract the olefins from the reaction mixtures containing unreacted paraffins. However, the separation propylene/propane and ethylene/ethane separation is highly challenging due to the similarities in molecular size and boiling points of these molecules [5,6]. Existing separation techniques, primarily dominated by cryogenic distillation, pose challenges as they are energy-intensive processes. Membrane-based-separation has become an appealing alternative technology due to its cheaper operating costs, continuous operation and energy efficiency [6–8] with a use of 90% less energy compared to distillation [9].

For large scale commercial gas separation processes, polymeric membranes are generally preferred over inorganic membranes due to their ease of processability, scalability and mechanical strength. However, these membranes suffer from a permeability–selectivity tradeoff, known as Robeson upper bound and they can undergo plasticization issues when operating at high gas pressure [6,10–12]. Mixed-matrix membranes (MMMs) provide an effective alternative solution to address the drawbacks of polymer-based membranes by incorporating a continuous polymer phase with dispersed inorganic or inorganic/organic fillers [13]. Incorporating fillers, e.g. zeolites and Metal Organic Frameworks (MOFs) among

others, into polymers, allows the combination of the high gas selectivity of the fillers with the good processability of polymeric membranes [14–22].

The objective of this chapter is to introduce an overview of MOFs, polymers and MOF/polymer based MMMs for C2/C3 gas separation. Throughout this work, various MOFs, polymers, and MMMs, as well as alternative materials have been examined and discussed to explain their distinct properties and potential applications in gas separation processes.

1.2 Propylene/Propane and Ethylene /Ethane Separation

In the past century, rapid advancements in technology and industrialization have propelled human society to extraordinary levels of development. This progress has led to significant increases in the global population and improved living standards, leading to an exponential demand for an array of products that are predominantly manufactured using raw materials and base chemicals. Among these essential base chemicals, ethylene and propylene stand out, contributing to over 50% of the global base chemical consumption (Figure 1.1a) [23].

Light olefins, such as ethylene and propylene, play a crucial role as essential feedstocks for various downstream chemical industries. Their significance is evident from their massive global annual production, exceeding 200 million tons. This substantial output translates into a substantial market value, amounting to US$254.6 billion in 2016. Moreover, industry experts predict that the market value will surge even further, reaching an impressive US$475.8 billion by the end of 2023. Specifically, the ethylene market is projected to experience consistent growth, with an estimated increase from $113 billion in 2021 to reach $159 billion by 2026, reflecting a compound annual growth rate (CAGR) of 6.6%. Similarly, the propylene market is also expected to exhibit substantial progress, rising from $96.47 billion to approximately $123 billion at a CAGR of 4.6% (Figure 1.1b) [5].

Moreover, 80% of ethylene production is used for the manufacture of ethylene oxide, a crucial component in surfactant and detergent production, as well as for the production of ethylene dichloride and polyethylene. On the other hand, propylene finds numerous applications, including the production of polypropylene, which is extensively used in

packaging, laboratory equipment. Additionally, propylene plays a vital role in the production of acrylonitrile and propylene oxide, further highlighting its significance in the chemical industry [1].

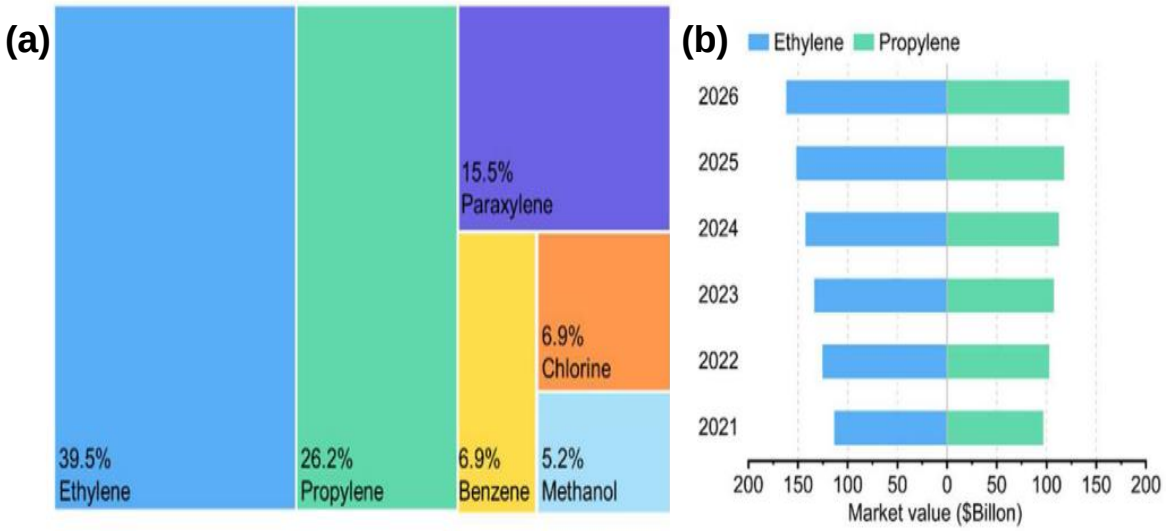

Figure 1.1 : (a) Global consumption of base chemicals in 2019. (b) Current and estimated market values of ethylene and propylene [23].

1.2.1 Existing separation technology

There have been many processes such as steam cracking (SC), fluid-catalytic cracking (SCC), or catalytic dehydrogenation of paraffins to produce light olefins. Among these processes, SC and SCC account for more than 90% of olefin production. The feedstocks for ethylene and propylene vary from paraffins (ethane, propane) to petroleum liquids (naphtha and distillate fuel oil). During SC process, naphtha and paraffins, along with high pressure steam are heated to temperatures ranging from 750–900 °C (up to 1000 °C) to produce light olefins and paraffins. Additionally, small amounts of H_2, CH_4, C_2H_2, benzene, toluene, xylene, and other by-products are generated during the process [5]. Despite advancements in cracking technology, the current yields are still not sufficiently high, resulting in products containing only about 5–30% paraffin. Unfortunately, this falls far below the olefin purity requirement of the downstream industry. A purity of 95 mol% is necessary for chemical-grade olefin production. For polyolefin production at the monomer grade level, a purity of 99.9 wt% and 99.5 wt% is required for ethylene and propylene respectively. These

demanding specifications necessitate sophisticated separation processes to achieve the target purity levels [23].

In order to achieve a polymer-grade purity of 99.9% for light olefins, it is crucial to separate them from undesired components like paraffins. Currently, cryogenic distillation stands as the state-of-the-art technology for light olefin/paraffin separations, and it is widely utilized in many separation processes and techniques [24]. Due to the similarities in size and close volatilities of the C_2H_4/C_2H_6 and C_3H_6/C_3H_8 gas pairs, cryogenic distillation becomes operationally demanding [5]. Physical properties of C2 and C3 olefin and paraffin can be seen in Table 1.1. It requires temperatures of 183−258 K, pressures of 7−28 bar, and involves high tray numbers (>100) and reflux ratios (2.5–4 for ethylene/ethane and 12–20 for propylene/propane) to achieve polymer-grade purity specifications [9]. The utilization of cryogenic distillation systems demands significant capital investment due to the high cost of equipment and operational complexity. As a result, these systems are economically viable primarily for processing highly olefin-rich streams, such as those obtained from large refinery catalytic crackers [1,25]. The energy consumption in a typical process is considerable, amounting to roughly the equivalent of Singapore's annual energy consumption. Considering the vast market for light olefins, even minor improvements in the quality of separation can lead to significant reductions in operating costs and carbon footprint [5].

Due to (i) the increasing demand for pure hydrocarbons, (ii) growing environmental concerns, and (iii) the high costs associated with conventional separation processes, there is a rising interest in the development of more effective separation techniques. Various processes have been explored for hydrocarbon separation, including extractive distillation, absorption, adsorption and membrane since the 1990s [2]. Different separation processes, including energy-consuming conventional techniques and alternative methods, can be observed in Figure 1.2.

Table 1.1 : Physical properties of C2 and C3 olefin and paraffin [26].

Component	Boiling Point [K]	Critical Temperature [K]	Kinetic diameter [nm]	Polarizability $\times 10^{25}$[cm]	Dipole moment$\times 10^{18}$ [esu cm]
Ethylene	169.5	282.3	0.423	42.5	0
Ethane	184.5	305.3	0.442	44.3	0
Propylene	225.5	364.9	0.468	62.6	0.366
Propane	231.1	369.8	0. 506	63.3	0.084

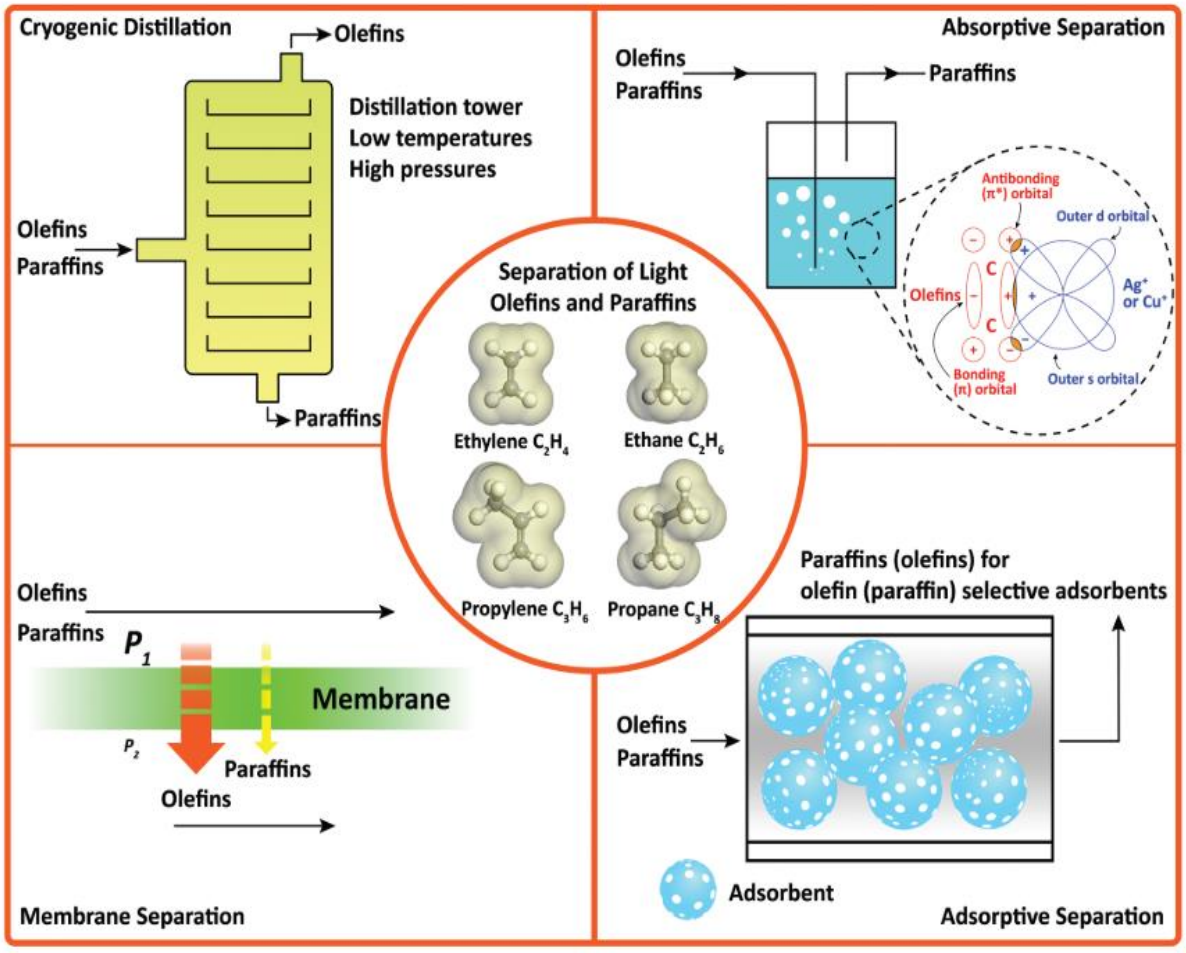

Figure 1.2 : Different techniques employed for light olefin/paraffin separations [5].

Extractive distillation, in particular, has been a subject of intense study to evaluate its potential advantages over traditional distillation. However, research has shown that the economic viability of extractive distillation largely depends on the thermodynamic properties of the solvent used. Thus, while alternative separation techniques hold promise for improving energy efficiency and reducing carbon footprint, their economic feasibility must be thoroughly assessed in conjunction with solvent selection and other factors [27].

Absorption-based separation involves preferential transportation of certain components into the bulk absorbent phase, while the remaining components become enriched in the gas phase. The key to its energy efficiency lies in the absorption regeneration process, making it a promising option for separating olefins from paraffins, with the potential to significantly reduce energy consumption and operational costs [28,29]. Due to the strong interaction between olefins and Ag^+ and Cu^+ species, the design of absorption-based separation systems becomes straightforward using liquid absorbents containing these cations. These systems can be comprised of aqueous solutions of $AgBF_4$ or $AgNO_3$, or organic solutions of $CuAlCl_4$ or $CuCF_3COO$. In recent times, absorption systems utilizing ionic liquids (ILs) have attracted increasing attention. These IL-based systems offer several advantages over traditional solvent systems, such as ultra-low vapor pressure, excellent thermal stability, and high solubility of silver and copper complexing agents. As a result, they significantly reduce solvent loss in the processes without compromising gas absorption capacity [30,31]. Moreover, some ILs demonstrate moderate olefin/paraffin absorption selectivity, and their interactions with chemicals and complexing agents can be finely tuned by engineering the cationic and anionic components. However, it is worth noting that impurities present in gas streams such as H_2, C_2H_2 and H_2S may deactivate the complexing agents, potentially reducing the overall separation performance of π-complexation-based absorption systems [31].

Another alternative gas separation technique is adsorption (also called physisorption) which is a spontaneous process that gas molecules adhere to the surface of solids. Adsorptive gas separation processes rely on the distinct adsorption properties of target gases in adsorbents. These adsorbents, often in the form of powder or pellets, are designed to have large internal surface areas, maximizing the gas adsorption sites and, consequently, their adsorption capacities [32]. The separation mechanisms of adsorptive olefin/paraffin systems can be

broadly classified into two categories: equilibrium separation and non-equilibrium separation which includes kinetic separation and molecular sieving.

In the equilibrium separation process, the separation is achieved by leveraging the varying affinities of olefins and paraffins to the adsorbents. For instance, olefins, being more polar than their paraffin counterparts, can be selectively enriched in polar adsorbents like 4A zeolite due to their stronger interactions with the adsorbent materials [33]. Therefore, materials with porous structures containing charged frameworks and counter ions could serve as potential adsorbents with olefin selectivity, whereas adsorbents with less polar building blocks may preferentially adsorb paraffins over olefins [34].

On the other hand, for non-equilibrium separation, the separation is achieved by the diffusion rate of olefins and paraffins in adsorbents. Kinetic separation involves gas adsorption processes that have not reached equilibrium. In this case, olefins, with higher diffusion rates, tend to have higher concentrations in the adsorbents compared to slower-diffusing paraffins. The diffusion rates are determined by diffusion constants, which can be obtained by fitting time-dependent gas uptake curves of the adsorbents to known solutions of the diffusion equation for adsorbents with varying crystalline geometries. Kinetic separation occurs when certain components in a gas mixture cannot enter the narrow pore aperture of an adsorbent, resulting in a zero-adsorption rate for these components. This process is known as steric separation, molecular sieving, or size-selective separation. By carefully selecting adsorbents with pore apertures smaller than the kinetic diameters but larger than the smallest cross-sectional area of the molecules, both kinetic and molecular sieving separation (mechanisms in Figure 1.3) can be utilized for effective olefin/paraffin separations [35].

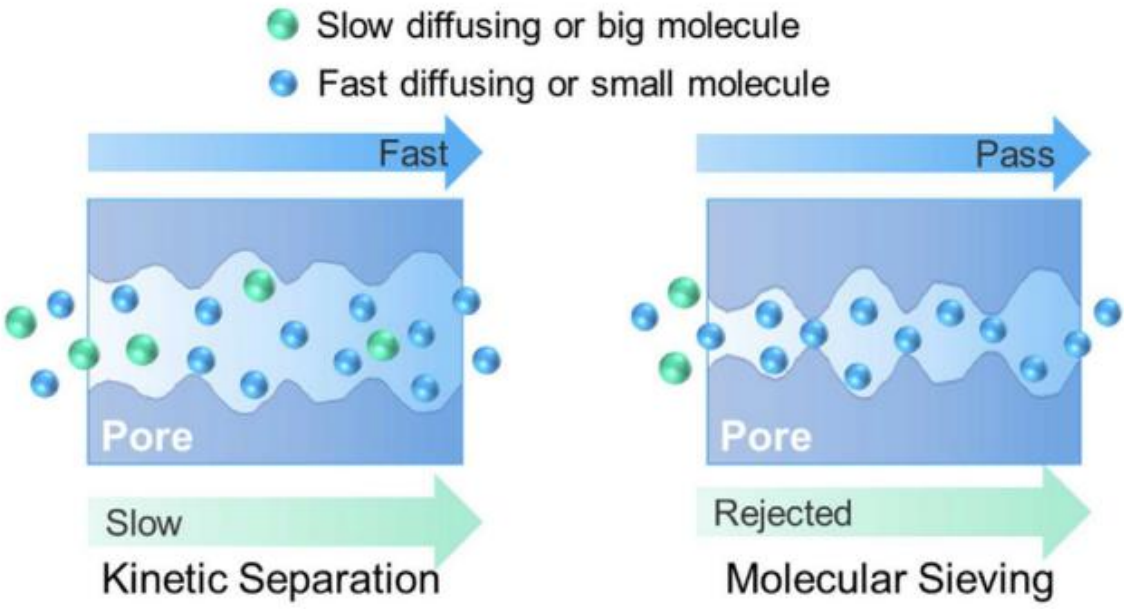

Figure 1.3 : Schematic diagrams of kinetic separation and molecular sieving mechanisms [23].

In the upcoming sections, the recent advancements in olefin/paraffin separations achieved using various porous adsorbents, such as zeolites, MOFs, porous COFs, and porous carbons derived from different carbon sources, are presented.

Traditional separation methods like distillation and adsorption-regeneration processes are resource-intensive, with distillation alone accounting for approximately 50% of total industrial separation energy consumption. However, membrane separation technology, which is based on molecular size and chemical affinity rather than thermal forces and adsorbents, offers numerous advantages [36]. Therefore, membrane-based gas separation has become an appealing alternative technique due to its lower capital and operating costs, energy efficiency, scalability, smaller carbon footprint and effective utilization to separate gaseous mixtures such as CO_2/H_2, CO_2/N_2, or CO_2/CH_4 [25,37]. With recent developments, membrane-based gas separation has gained popularity in various applications, including food processing, water treatment, biotechnology, pharmaceuticals, and petrochemical processing [37].

1.2.2 Current commercial sorbents/membranes for gas separation

Membrane is a thin barrier that selectively separates two phases and limits the transport of several components. The membrane's structure can be symmetric or asymmetric, and it can be homogenous or heterogeneous, carrying a positive or negative charge. Transport through the membrane occurs when a driving force such as concentration, pressure, temperature or electrical potential difference applied to the feed components. The membrane thickness, which depends on the application's purpose, may vary from 10 microns to few hundred micrometers [38]. The types of membranes could be seen in Figure 1.4.

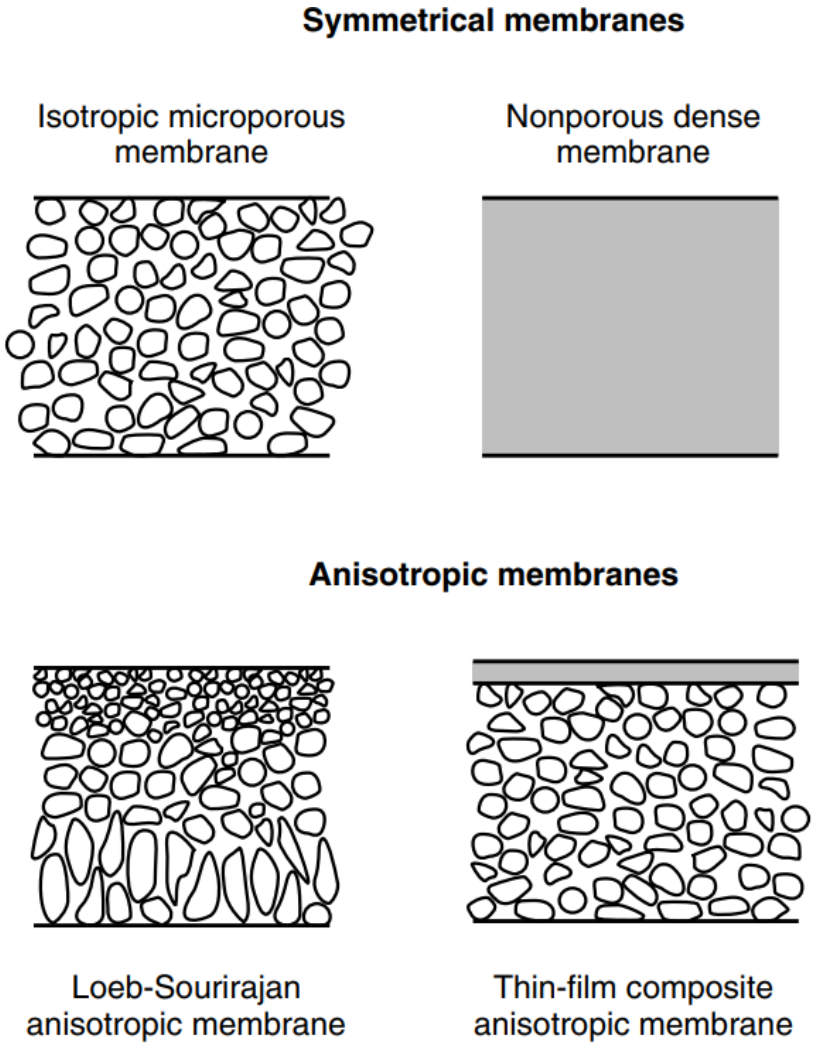

Figure 1.4 : Schematic diagrams of various structures of membranes [38].

For gas separation membranes act as barriers that separate one or more gases from a feed mixture and produce specific gases. The gas that passes through the membranes is called the permeate, whereas the one that does not pass through is called the retentate [39]. A schematic representation of membrane gas separation could be seen in Figure 1.5.

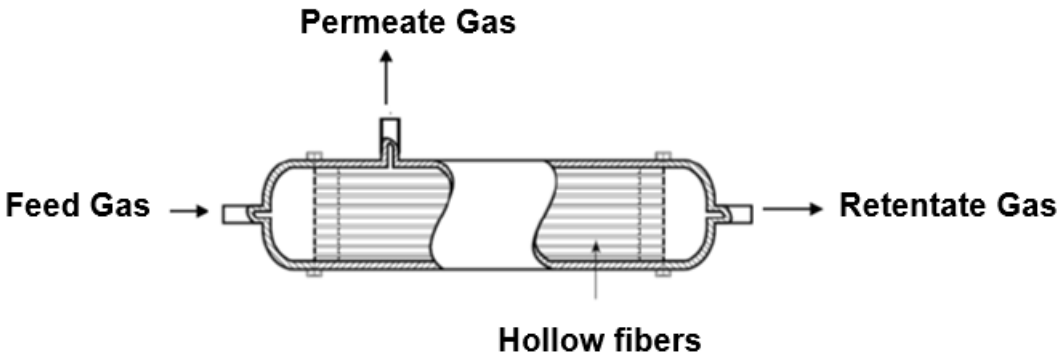

Figure 1.5 : Schematic representation of a gas separation membrane [39].

Different gas separation membranes employ various effective mechanisms, such as Knudsen diffusion, molecular sieving, solution-diffusion, surface diffusion, and capillary condensation, depending on the gas/membrane system. These mechanisms play a vital role in the transport of gaseous species within membranes. Membranes can be categorized into polymeric membranes, inorganic membranes, and composite membranes, each exhibiting different transport mechanisms based on their composition and structure. For example, Knudsen diffusion is prevalent in porous inorganic membranes, while dense membranes are more suitable for the solution-diffusion mechanism. Composite membranes may showcase different mechanisms depending on their membrane components, and glassy polymers commonly adhere to the dual-mode sorption theory [37].

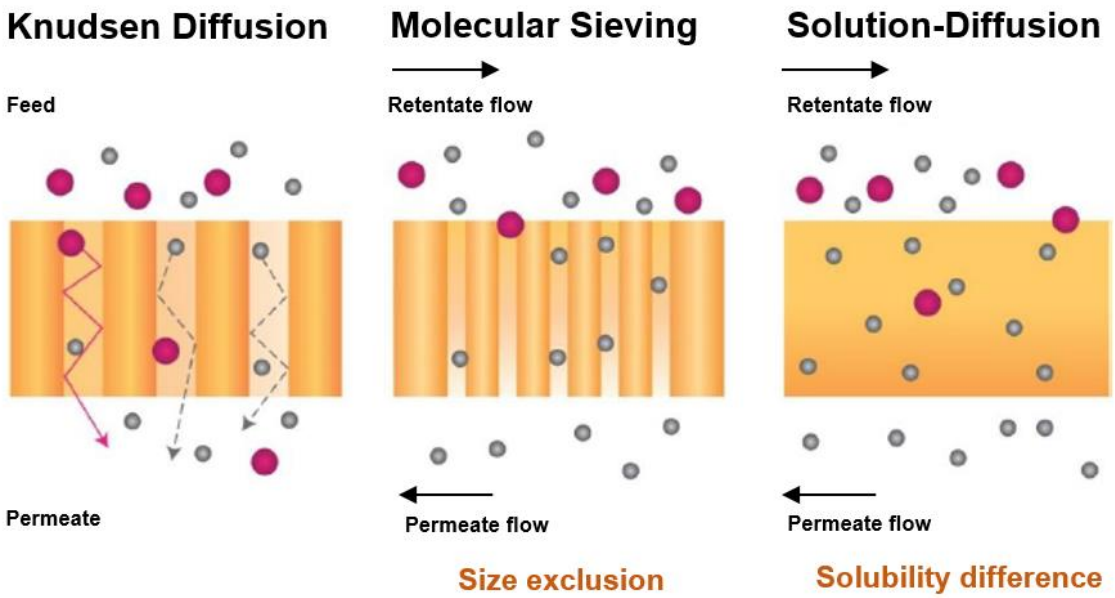

Figure 1.6 : Schematic representation of most common possible mechanisms for gas separation with membrane [40].

Knudsen diffusion occurs in porous inorganic membranes when membrane pores are small enough to prevent bulk diffusion. The separation is based on the difference in the mean free path of gas molecules, which is related to their molecular weight and their collisions with the pore walls. On the other hand, in dense membranes, the gas permeation process follows the solution-diffusion mechanism proposed by Sir Thomas Graham. The solution-diffusion mechanism can be divided into three steps. First, the penetrant comes into contact with the membrane and is absorbed and dissolved into the membrane surface from the upstream feed. Then, it diffuses through the membrane thickness driven by factors such as concentration, pressure, and temperature. Finally, the molecules desorb into the low activity downstream feed [21,41].

Permeability (P) of a gas membrane can be expressed with an arrangement of Fick's 1st law, which is equal to the product of the effective diffusivity (D) and sorption coefficient (S):

$$P = S\ x\ D \tag{1.1}$$

Permeability values are commonly expressed in Barrers, $10^{-10}\ \frac{ss\ (STP).cm}{cm^2.cmHg.s}$.

The ratio of permeability to the average membrane thickness is defined as the gas permeance and is commonly stated in gas permeation units (GPU) where 1 GPU= 3.35×10^{-10} (mol/m^2/s/Pa). Depending on some studies, the permeability unit is expressed as GPU [42–44].

Diffusivity (D), which is related to the capability of the polymeric matrix to transmit molecules through, relies on both the polymer structure, such as polymer packing and rigidity of the macromolecular ensemble, and the motion of the polymer segments. Gas properties, such as size and shape, also affect the gas that passes through the membranes. The molecular size of light olefins and paraffins hydrocarbons are related to van der Waals volume, V_i, collision diameter calculated by the Lennard–Jones parameter, σ_{LJ}, and the molecule kinetic diameter, σ_{kt}, determined from molecular sieves [1]. The physical properties of several light hydrocarbons are listed in Table 1.2.

Table 1.2 : The physical properties of several olefins and paraffins [45].

Adsorbate	Boiling Point [K]	Kinetic diameter [Å]	Dipole moment [$\times10^{18}$ esu cm]	Polarizability [$\times10^{25}$cm^3]
CH_4	111.6	3.8	0	25.9
C_2H_6	184.6	4.4	0	44.3
C_2H_4	169.4	4.2	0	62.5
C_3H_8	231.0	4.3-5.1	0. 084	62.9
C_3H_6	225.5	4.7	0.366	62.9
n-C_4H_{10}	272.7	4.7	0.05	82.0
i-C_4H_{10}	261.3	5.3	0.132	81.4-82.9
n-C_4H_8	266.9	4.5	0.359-0.438	79.7-85.2
i-C_4H_8	266.3	4.8	0.501	78.9
C_4H_6	268.6	5.2	0	86.4

As, the size and shape of molecules is important, olefins exhibit a smaller kinetic diameter than paraffins, with containing shorter C=C (double bond) distance of 1.337 Å compared

with longer C−C (single bond) distance of 1.534 Å found in paraffins, have higher diffusivity selectivity. Moreover, due to olefins have lower critical temperature and condensability compared to paraffins, they have higher solubility in the absence of specific interactions [1,2].

Membranes have found significant success in several industrial applications, representing about 80-90% of the current $1.0−1.5 billion/year membrane market. These applications include nitrogen production, natural gas treatment, hydrogen recovery, and vapor recovery, among others. Currently, polymer membranes dominate the industrial capacity, but the emergence of MOFs and their successful formation into crystalline films and composite materials, such as MMMs, has opened new possibilities for membrane researchers to create materials with enhanced properties. Although challenges remain in transforming lab-scale innovations into commercial products, there is promising evidence suggesting that a breakthrough is on the horizon [46].

1.3 Polymers

For large-scale commercial gas separation processes, polymeric membranes are generally preferred over inorganic membranes due to their easy processability, scalability and mechanical strength. Even though, polymeric membranes have been utilized in gas separation applications in the industry since the 1980s, they encounter challenges due to the trade-off between gas permeability and selectivity as well as plasticization issues (swelling) under high pressure working conditions. Membrane materials generally suffer from a trade-off, with either having high selectivity and low permeability or vice versa. This phenomenon can be explained by the well-known Robeson plot, as shown in Figure 1.7, where the selectivity of gas pairs is logarithmically plotted against the permeability of the faster permeating gas. Therefore polymers hardly exhibit both high selectivity and permeability simultaneously for a given mixture separation. Enormous, ongoing efforts have been made to create membrane materials to meet this challenge. Based on different application cases, an appropriate combination of permeability and selectivity must be applied. Such that, a higher permeability coupled with high selectivity enables the use of less polymeric material, leading

to the cost reduction, while emphasizing high selectivity ensures greater purity of the treated gas [20,47].

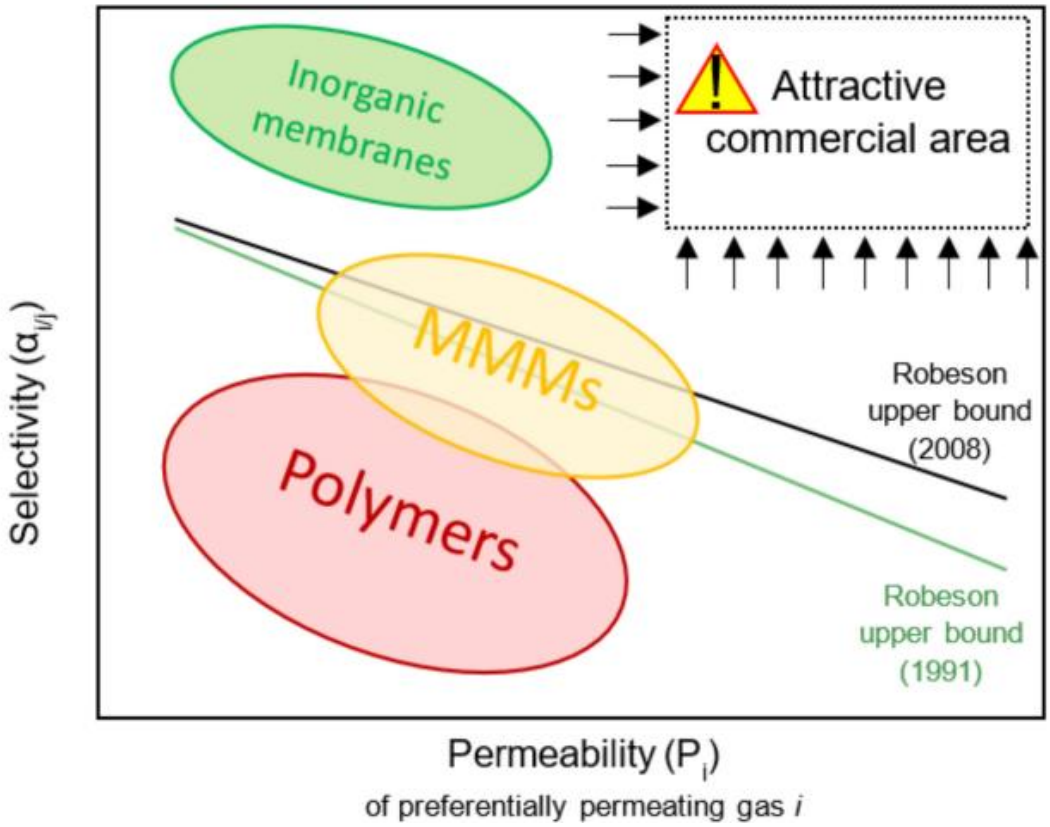

Figure 1.7 : Schematic representation of the Robeson upper bounds (trade-off curves) from 1991 and 2008 [48].

1.3.1 PIMs

In 2002, the groups of Budd and McKeown developed polymers of intrinsic microporosity (PIMs) which have rigid and contorted macromolecular backbones [41]. According to the IUPAC classification [49], PIMs are considered microporous materials as they have less than 2 nm in width micropores and they do not exhibit rotational freedom along the polymer backbone. These polymers are typically synthesized using a ladder-type monomer consisting of two aromatic rings connected by a single tetrahedral carbon atom and tetrafluoroterephthalonitrile. PIM-1 is typically synthesized using 5,5′,6,6′-tetrahydroxy-3,3,3′,3′-tetramethyl-1,1′-spirobisindane and tetrafluoroterephthalonitrile [50], is an example of such synthesis. Due to their rigid and ladder-type structure, PIMs exhibit bulky polymer backbones that prevent efficient space packing of the polymer chains [51]. This leads to the

formation of pores between the polymer chains, which could be exploited as gas transport pathways (fractional free volume).

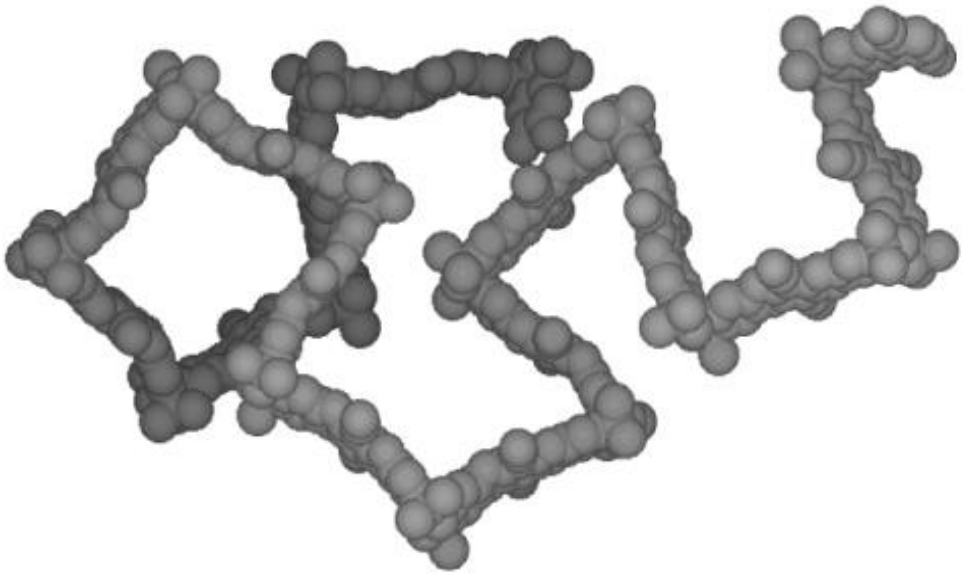

Figure 1.8 : Rigid, randomly contorted fragment of PIM-1 structure [50].

PIM materials can be classified into two categories: ladder PIMs and polyimides of intrinsic microporosity (PIM-PIs). In 2018, Ghanem et al. developed linear-chain PIM-PIs (PIM-PI-1 to PIM-PI-8), which consist of polyimide backbones with rigid bulky contortion sites. Depending on the placement of the contortion site in either the dianhydride or diamine monomer, PIM-PIs can be manipulated in various ways. Such that, in certain instances, PIM-PIs incorporate sterically restricted groups in both the dianhydride and diamine building blocks [52]. The categorization of PIMs based on their building block can be seen in Figure 1.9. Such that, ladder type of PIMs can be categorized based on its sterically hindered building blocks such as spirobisindane, phenazine, ethanoanthracene, triptycene, spirobifluorene, Tröger's base and tetraphenylethylene.

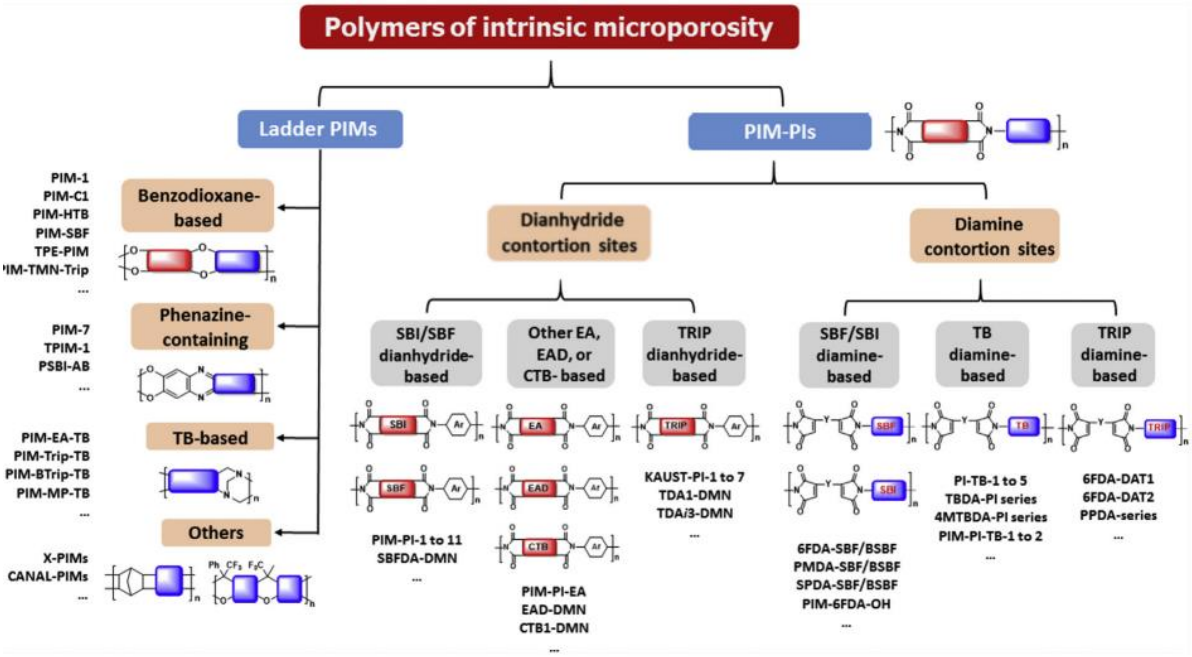

Figure 1.9 : Structural classification of PIMs based on building blocks [53].

PIMs are soluble in organic solvents such as THF, CH_2Cl_2, and $CHCl_3$ and NMP by heating, whereas they are insoluble in polar aprotic solvents such as DMAc, DMF and DMSO [54]. As PIMs are soluble in many solvents, they are processable by solution-casting method. It should be noted that the "intrinsic" term in relation to PIM-1 comes directly from its structure, rather than its processing protocol. Compared to glassy polymers, PIM-1 provides high gas permeability with 100-fold enhancement without any unfavorable effects on selectivity. Hence, this type of behavior of PIMs can be related to its high solubility coefficient values combined with modest diffusion coefficients [55]. Besides thermally rearranged (TR) polymers [56], PIMs in particular can demonstrate upper bound properties for numerous gas pairs and even surpass the upper bound performance for certain gas pairs such as O_2/N_2, CO_2/CH_4 and CO_2/CH_4. Robeson et al. investigated the upper bound performance of PIMs for specific gas pairs such as O_2/N_2 and CO_2/CH_4. They demonstrated that the upper bound performance of various PIMs is related to three factors: high diffusion selectivity, high diffusion coefficients, and high gas solubility coefficients compared to other glassy polymers. Upper bound performance of different polymeric materials for propylene/propane gas pairs can be seen in Figure 1.10. Additionally, the combination of high free volume and high glass transition temperature in PIMs lead to a significant dual

mode sorption, resulting high solubility coefficients [57]. As, PIMs consist of bulky rigid backbones with a high amount of free volume, it is expected that over time these polymer chains will relax towards a more thermodynamically stable state with loss of free volume, leading to a permeability loss. Such physical aging process is a major challenge common to glassy polymers and affects their applications in industry. Given the impact of the physical aging process, numerous researchers have directed their focus on developing strategies to stabilize polymeric membranes against it. So far, the first strategy consists of rigidifying the initial polymer structure with applications such as copolymerization [58] or crosslinking [59]. With these methods, it is possible to reduce the aging process at the expense of reduced permeability. A second strategy is using PIMs as polymer matrix for other porous materials such as MOFs and zeolites to form a MMM. Hence, these composites have the potential to outperform unfilled polymers and even exceed the upper bound performance [60].

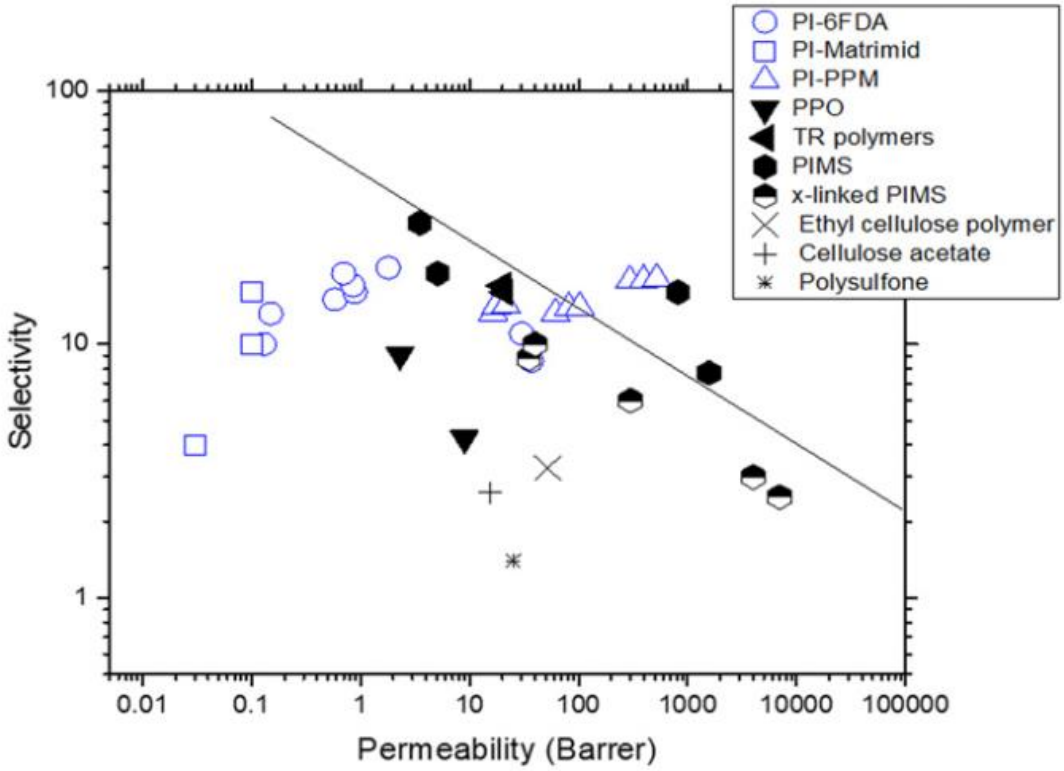

Figure 1.10 : Comparison of propylene/propane gas separation performance of different polymeric materials [61].

Budd et al worked with PIM-1 and PIM-7 membranes to demonstrate their superior performance, surpassing the previous upper bound of performance for commercially significant gas pairs such as O_2/N_2 (nitrogen generation) and CO_2/CH_4 (natural gas enrichment) PIM membranes, when initially produced and tested, exhibit remarkable CO_2 permeabilities of up to 6000 Barrer and moderate CO_2/CH_4 selectivities of 10−23. However, over time, permeability of these membranes decreases due to the aging process [62]. Li et al. studied the gas transport properties of PIM-1 membranes, including permeability, solubility and diffusion coefficients. The results demonstrated that the permeabilities and solubility coefficients of He, H_2, O_2, N_2, CH_4 and CO_2 increased by up to 10 atm with the dual-mobility model, while permeabilities of C_2H_4, C_2H_6, C_3H_6 and C_3H_8 exhibited a stronger increase with pressure due to the plasticization phenomena. The diffusion coefficients of all gases, as calculated from the measured permeability and solubility coefficients, increase with pressure; whereas, the diffusion coefficients of the hydrocarbon gases exhibit a more pronounced increase due to the plasticization phenomena [63].

Currently, there is limited knowledge regarding the separation of propylene and propane using PIM materials and PIM-derived CMS membranes. Swaidan et al. reported the pure- and mixed-gas propylene/propane separation properties of three highly permeable PIM-PIs namely triptycene based KAUST-PI-1, spirobisindane based PIM-PI-1 and 6FDA-TMPD. Among them, KAUST-PI-1 showed the highest pure-gas permeability for C_3H_6 of any polyimide reported to date, reaching 817 Barrer, with a propylene/propane selectivity of 16. However, due to the plasticization and competitive sorption effects, C_3H_6 permeability and C_3H_6/C_3H_8 selectivity decreased considerably during mixed-gas experiments with a 50:50 C_3H_6/C_3H_8 feed [64].

Another approach to achieve higher selectivity is to tailor the pore size distribution in PIM-1 by thermal annealing or by further heat treatment. Swaidan et al. conducted experiments to evaluate pure- and mixed-gas separation properties of C_3H_6/C_3H_8 using PIM-6FDA-OH and its derivatives of TR-PBO formation at 440 °C and CMS at 600 °C, after thermal annealing at 250 ˚C. The TR-PBO membrane showed a C_3H_6 permeability of 14 Barrer and a C_3H_6/C_3H_8 selectivity of 15, whereas compared to PIM–6FDA–OH, the CMS membrane demonstrated an approximately 15-fold increase in C_3H_6 permeability (3.5 vs 45 Barrer)

while maintaining a similar C_3H_6/C_3H_8 selectivity (30 vs 33). However, during mixed-gas experiments at 4 bar, the C_3H_6 permeability dropped from 45 to 31 Barrer with 50% decrease in C_3H_6/C_3H_8 selectivity (34 vs 17) at 4 bar. Despite that, both TR-PBO and CMS membranes surpassed the Robeson's upper bound for C_3H_6/C_3H_8 [65].

Various modification strategies have been developed to enhance the selectivity and plasticization resistance of PIM membranes. For instance, Liao et al. modified PIM-1 via hydrolysis and incorporating various metal ions such as Zn^{2+}, Mg^{2+} and Ag^{+} to improve their separation performance of C_3H_6/C_3H_8. The main idea behind their strategy is treating cPIMs as MOFs with unsaturated metal sites in their metal-carboxyl complexes and modify them accordingly. By adding metal ions into cPIM, larger free volume occurs as the ions facilating the hydrogen bonding between carboxylate and amide groups. Such that, based on different metals, the free volume properties decrease in the order of ZncPIM> AgcPIM> MgcPIM> cPIM, while the C_3H_6/C_3H_8 membrane selectivity decreases in the order of MgcPIM> AgcPIM> ZncPIM> cPIM> PIM-1. Hence, adding Zn^{2+} ions to the system increases the size of free volume, leading to higher permeability and better plasticization resistance, while Mg^{2+} ions offers affinity towards C_3H_6, resulting in a higher C_3H_6/C_3H_8 selectivity [66]. Liu et al. incorporated PIM-1 with beta-cyclodextrin (β-CD) through thermal treatment at temperatures ranging from 300 to 600 ˚C, resulting in 3D networks of PIM-CD membranes for propylene/propane separation properties. During the thermal treatment procedure, degragated β-CD components generated radicals that formed 3D cross-linking networks with narrow gates, resulting in highly C_3H_6/C_3H_8 selective membranes with slightly decreased C_3H_6 permeability by enhancing their molecular sieving capabilities [67]. Shin et al. investigated the C_3H_6/C_3H_8 separation performance of CMS membranes derived from the polymer blends of fluorinated polyimide of 6FDA-DAM: DABA (3:2) and a ladder-type polysilsesquioxane (PI/LPSQ). During the thermo-oxidative crosslinking of LPSQ, non-porous SiO_2 gases formed, which reduces gas diffusion and consequently decreases C_3H_6 permeability, while increasing the C_3H_6/C_3H_8 selectivity up to 67 due to the enhanced diffusivity selectivity. Even during mixed gas measurements at 2 bar for a 50:50 gas mixture, where permeability and selectivity decreased, the C_3H_6 permeability of 68 Barrer and mixed-

gas C_3H_6/C_3H_8 selectivity of 52, still demonstrate good potential for C_3H_6/C_3H_8 separation [68].

The literature is scarce regarding separation performance of PIM materials for C_2H_4/C_2H_6. Salinas et al. investigated the C_2H_4/C_2H_6 separation performance of PIM-1 based CMS membranes through heat treatment at temperatures ranging from 400 to 800 ˚C, under an inert N_2 atmosphere. The cross-linked PIM-1 structure, when heat treated at 400 °C, showed a 36% increase in pure-gas ethylene/ethane selectivity, from 1.8 to 2.4, while reducing the permeability of ethylene by 60% and of ethane by 200%. By carbonizing the films at 600 °C, the sorption capacity of both ethylene and ethane at lower pressures was enhanced, while cumulative surface increased by 30% compared to its cross-linked predecessor [69].

1.3.2 Polyimides

Polyimide membrane is a type of polymer formed by the condensation reaction between dianhydride and diamine monomers, known for their high chemical resistance, mechanical strength, and good thermal stability. Figure 1.11 displays the chemical structures of the acid anhydrides and diamines commonly utilized in the synthesis of polyimides. Many studies demonstrated that polyimide membranes outperform traditional polymers for olefin/paraffin separation. However, challenges such as physical and chemical ageing, plasticization and swelling still remain big challenges for preparing polyimide-based membranes for long-term industrial applications [41].

The configuration of polymer chains, interchain interactions, polymer chains stackings, and the network structure in polyimide membranes are all determined by the monomer structure. Hence, researchers have explored various monomers to regulate the twist structure of the main chains, main chains rigidity and flexibility, and the substituents in side chains. The rigidity of polyimides can be regulated by incorporating different groups into both the main chains and side chains, which influences segmental torsion and steric hindrance. Such that, polyimides that incorporate rigid aromatic rings into their main chains typically exhibit a higher amount of configuration-based free volume due to the hindrance of the segmental motion and dense packing of the polymer chains caused by the presence of aromatic rings. On the other hand, the incorporation of flexible segments, such as ether linkages, in the main

chains can lower the T_g, enhance stacking efficiency, and increase the cohesive energy density and conformation-based free volume. Additionally, the introduction of conjugated structures into the main chains results in a twisted polymer chain conformation, leading to the creation of additional voids and an increase in FFV [26].

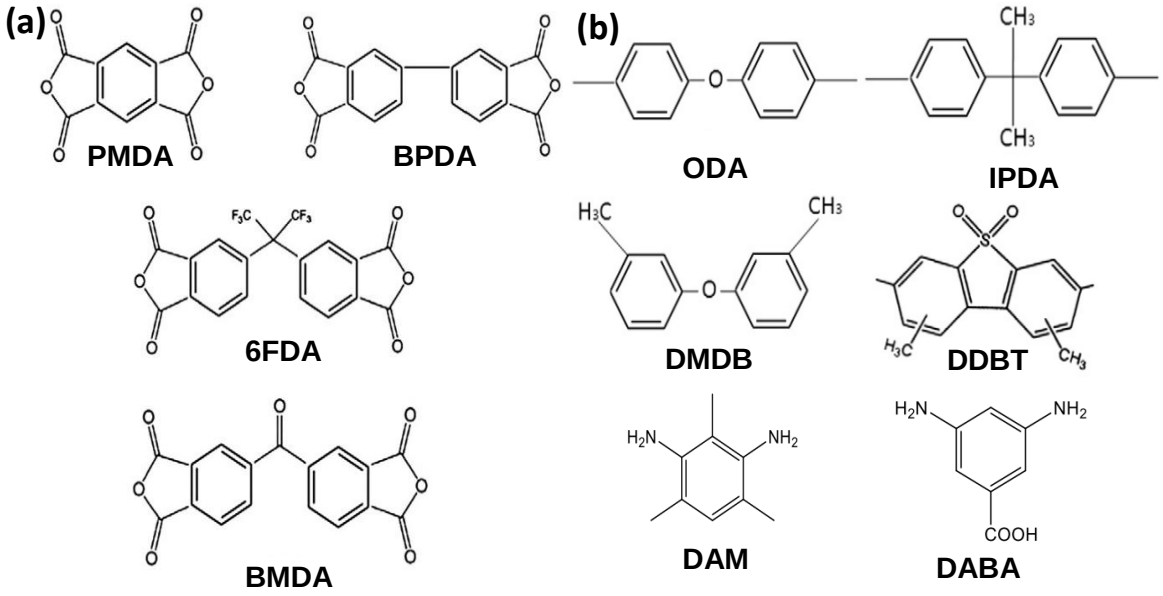

Figure 1.11 : Chemical structure of (a) acid anhydrides and (b) diamines used in the synthesis of polyimides [1].

Tanaka et al. conducted a study on propylene/propane separation using polyimide-based membranes prepared from BPDA and 6FDA acid anhydrides, in combination with various diamines including TeMPD, TrMPD, DDBT, and ODA. Due to the larger void fraction (V_f) in the 6FDA-based polyimides, they exhibit superior performance in propylene/propane separation compared to the BPDA-based polyimides. This is attributed to reduced molecular interactions and steric hindrance of CF_3 groups in the 6FDA polymer as compared to BPDA [70]. Likewise, polyimides containing methyl-substituted phenylene diamines, such as TeMPD and TrMPD, exhibit larger V_f compared to other diamines like ODA and DDBT. This can be attributed to the rigidity and non-polar nature of the polymer chains, as well as the bulkiness of the methyl groups, which leads to inefficient packing of the polymer chains [71]. Due to these factors, polyimide membranes prepared from 6FDA anhydride with

TrMPD or TeMPD diamines demonstrated superior performance compared to other polyimides. At the same operating conditions of 50 °C and 2 atm, the polyimide membranes prepared from 6FDA-TrMPD exhibited a permeability coefficient of 30 Barrer and an ideal selectivity of 11 for propylene. In contrast, the polyimide membranes prepared from 6FDA and DDBT showed a lower permeability of 0.8 Barrer and a higher permselectivity of 27. On the other hand, the BPDA-based polyimides demonstrated inferior performances for propylene/propane separation in comparison to the 6FDA-based polyimides. Staudt-Bickel and Koros conducted tests on polyimides based on 6FDA to evaluate their permeation and sorption properties for single gases of ethylene, ethane, propylene, and propane, as well as for 50:50 olefin/paraffin feed mixtures. At a feed pressure of 3.8 atm and 308 K, the investigated polyimides demonstrated ideal separation factors for ethylene/ethane ranging from 3.3 to 4.4 and for propylene/propane ranging from 10 to 16. On the other hand, in mixed gas permeation experiments, the selectivity for ethylene/ethane separation was found to be up to 20% lower, and the selectivity for propylene/propane separation was reduced by up to 50% compared to the ideal selectivity. Bickel and Koros encountered a limitation in conducting permeability measurements with membranes thicker than 10 μm. This is because the pressure increase resulting from the permeation of propane becomes comparable to the leak rate of the apparatus. Consequently, the confirmation of whether the membrane thickness is the main reason behind this discrepancy is still pending [72]. Experiments on propylene/propane separation were conducted by Burns and Koros using 6FDA-DMDB membranes at 1 atm and 35 °C. The pure gas permeability of propylene was measured to be 0.15 Barrer, with an ideal selectivity of 13.2. Additionally, the mixed propylene/propane selectivity was found to be 10.4 [73]. On the other hand, Shimazu et al. also investigated propylene/propane separation using 6FDA-DMDB membranes at different operating conditions of 1 atm and 25 °C. They found that propylene exhibited a pure gas permeability of 0.263 Barrer and an ideal selectivity of 39.4, while in mixed gas experiments, a higher selectivity of 45 was observed [74]. Yoshino et al. investigated propylene/propane separation through an asymmetric hollow fiber membrane of a 6FDA/BPDA(1/1)-DDBT copolyimide membrane. The gas permeability of the copolyimide film was similar to that of 6FDA–DDBT polyimide and significantly higher than that of BPDA–DDBT, with a high selectivity of 31 and an extremely propylene permeability of 1 Barrer [75]. Tanaka et al. also

investigated the separation properties of propylene/propane and ethylene/ethane using 6FDA based polyimides such as 6FDA-TrMPD and 6FDA-DDBT and BPDA-TeMPD membranes. They showed that 6FDA-TrMPD and 6FDA-TeMPD polyimides exhibited relatively high permeability ranging between 20 to 40 Barrer and selectivity of 8-11 at 323 K and 2 atm. However, 6FDA-DDBT polyimide displayed low permeability of 0.8 Barrer and high permselectivity at same operating conditions. On the other hand, 6FDA-TrMPD polyimides exhibited a higher ethylene permeability of 58 Barrer, but with a lower ethylene/ethane selectivity of 2.9 [76]. Moreover, Rungta et al. summarized the ethylene/ethane separation performance of various polymeric membranes using pure gases under standard conditions at 35–50 °C and feed pressure of 1–2 atm under vacuum. They demonstrated that the upper bound for ethylene/ethane separation, based on theoretical considerations, was comparable to that of other important gas pairs. In general, it could be said that the permeability of polyimide membranes is generally low and higher FFV membranes such as PIMs could improve both the permeability and selectivity.

Velioğlu et al. investigated the plasticization of 6FDA-based polyimides such as, 6FDA–ODA, 6FDA–DPX and 6FDA–DAM, due to the sorption of propane and propylene molecules using molecular simulation techniques. During propane induced plasticization, increasing the backbone flexibility of the polymers increases FFV and plasticization phenomena for all three polyimides, on the other hand during propylene plasticization for 6FDA–DPX it is the opposite as being highly polarizable of propylene resulting from π-electron complexation. The analysis of preferential sorption sites in single and binary gas adsorption indicates that site preferences are modified during binary gas adsorption as a result of the competition between propane and propylene molecules. In single gas adsorption, the dianhydride structure exhibits the most preferential sorption site, resulting in plasticization. However, in the case of binary sorption, particularly in more flexible polyimides like 6FDA-ODA, the most preferential sorption site shifts to the diamine structure. Therefore, the introduction of $–C(CF_3)_2–$ linkage in 6FDA-based polyimides hinders the rotation of phenyl rings, resulting in high gas permeabilities and low chain packing densities. Hence, the 6FDA-based polyimides exhibit high gas permeabilities and low chain packing densities as a result of the blockage of the rotation of phenyl rings by –

$C(CF_3)_2$– linkage and membranes with commercially attractive selectivities may be obtained by changing the diamine structure. By modifying the diamine structure, it is possible to obtain membranes with selectivities that are commercially appealing [77].

Even though there are limited experience with polyimide membranes prepared from 6FDA anhydride with DAM and DABA diamines, it is expected for bulky diamines to demonstrate superior performance compared to other polyimides. Liu et al. focused on the polymer chain packing and plasticization tendency of glassy 6FDA-DAM:DABA membranes while investigating their CO_2/CH_4 and H_2S/CH_4 separation performances. The incorporation of DAM moiety with bulky $-CH_3$ groups in the polymer backbone enhances the free volume and promotes high gas permeability by reducing polymer chain packing. On the other hand, the presence of DABA moiety with polar carboxyl groups offers crosslinking and functionalization sites, enabling control over the plasticization behavior of the polyimide membrane. By adding more DAM moieties into the polyimide backbone, the rigidity of the polyimide chains increases, as the presence of bulky methyl groups hinder localized and rotational mobilities of the polymer backbone, resulting in enhanced packing resistance and suppression of polymer chain packing. As a consequence, the membrane exhibits an increased free volume. On the other hand, the incorporation of DABA moieties into the polymer backbone can lead to tighter chain packing and a reduction in the free volume of the membrane. This is due to the ability of the carboxyl groups in the polyimide to form hydrogen bonds with the carbonyl and imide groups, facilitating stronger intermolecular interactions and reducing the available free space within the membrane [78].

This PhD work focuses on three polymers that exhibit distinct physical properties among the numerous polyimides and PIMs reported so far for the separation of C_3H_6/C_3H_8 and C_2H_4/C_2H_6. These polymers include 6FDA-DAM, known for its rigid backbone and inhibited polymer chain packing, 6FDA-DABA, which possesses plasticizing controlling capability through crosslinking due to the presence of polar –COOH groups, and PIM-1, characterized by its rigid contorted chains and relatively high porosity. Figure 1.12 shows the representation of the polymer structures explored in this thesis.

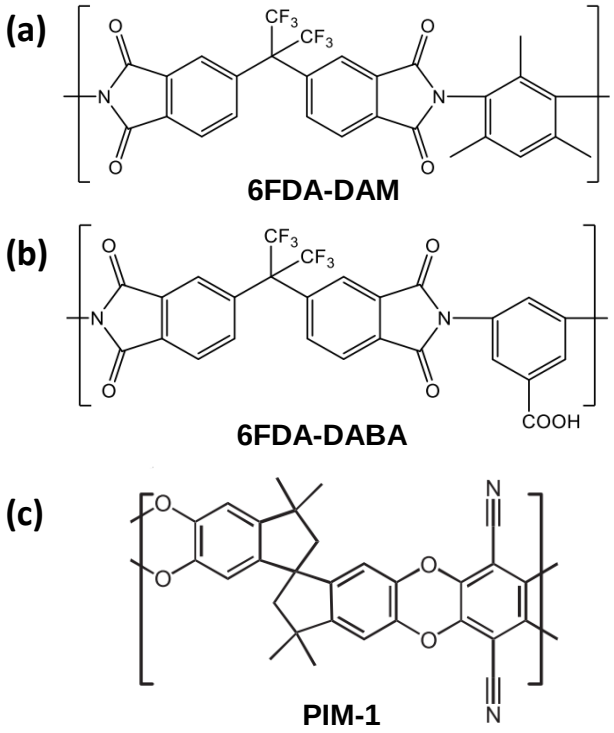

Figure 1.12 : Representation of the polymer structures explored in this thesis (a) 6FDA-DAM (b) 6FDA-DABA [79] and (c) PIM-1 [80].

1.4 Metal Organic Frameworks

Metal–organic frameworks (MOFs), also known as crystalline porous coordination polymers (PCPs), are captivating organic-inorganic hybrid solids [81,82]. These materials have attracted significant attention over the last two decades owing to their remarkable ability to design and control pores at the molecular length scale. MOFs are formed through the self-assembly of organic linkers coordinated to metal ions, creating open framework structures with potentially high micro/mesoporosity [82,83]. Through the various selection of molecular components, the MOF structure is highly tunable in terms of pore size, pore shape and/or pore chemistry [82,84]. Therefore, MOFs have enormous potential for a wide range of applications including gas storage and separation[85,86], chemical sensing [87–89], optical[90] , catalysis[91,92] and nanomedicine [93,94].

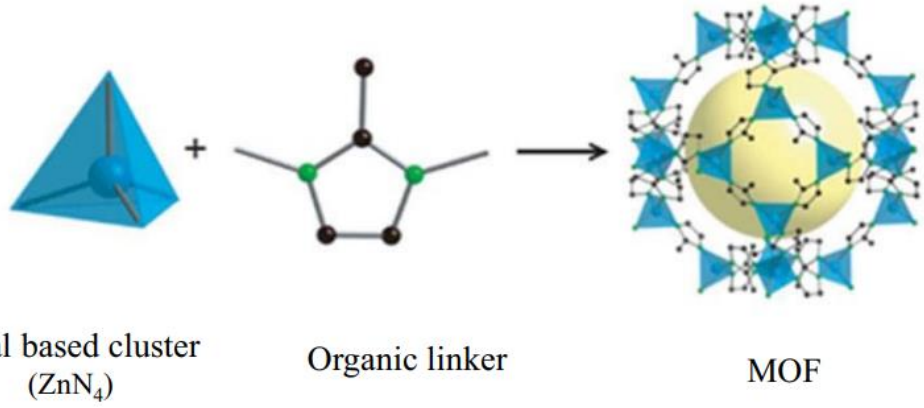

Figure 1.13 : A common MOF structure consists of a metal based cluster and an organic linker, with the yellow sphere representing "open space" [95].

1.4.1 General presentation

MOFs are a relatively new family of nanoporous materials constructed from metal ions/clusters and organic linking molecules. MOFs can be constituted by a variety of metal nodes, including divalent cations (Zn, Cu, Co, etc.), trivalent cations (Al, Cr, Fe, etc.) or tetra-valent cations (Zr, Ti, Hf, etc.), along with organic linking molecules such as carboxylates, phosphonates and imidizolates [96]. By carefully selecting suitable metal nodes and organic linkers along with the strategic design of topological structures and post synthetic modification of MOF skeletons, the framework structures and the functionality of MOFs can be finely adjusted [97]. MOFs are categorized into different dimensionalities, zero-dimensional (0D) MOFs manifest as hollow capsules, one-dimensional (1D) MOFs exist as nanorods or fibers, two-dimensional (2D) MOFs take the form of thin films and membranes, three-dimensional (3D) MOFs exhibit continuous and extended structures, and four-dimensional (4D) MOFs addressing the temporal evolution to characterize several spatiotemporal functions [82,98,99]. Based on differences in geometry, size and functionality, thousands of different MOFs being reported due to the altering the combination of organic linkers and metal complexes. All these MOFs deposited into the Cambridge Structural Database (CSD) (Figure 1.14) which has 119,927 synthesized MOF and MOF-type structures as of June 2023 [100]. Here is a list of several MOF membrane materials with increasing pore sizes: ZIF-7 [101] , ZIF-22 [102], ZIF-8 [103], ZIF-90 [104], ZIF-95 [105],

ZIF-71 [106], ZIF-78 [107], CAU-1 [108], MIL-53 [109], MOF-5 [110] , ZIF-69 [111] , HKUST-1 [112], SIM-1 [113], IRMOF-3 [114] and IRMOF-74 [115][116].

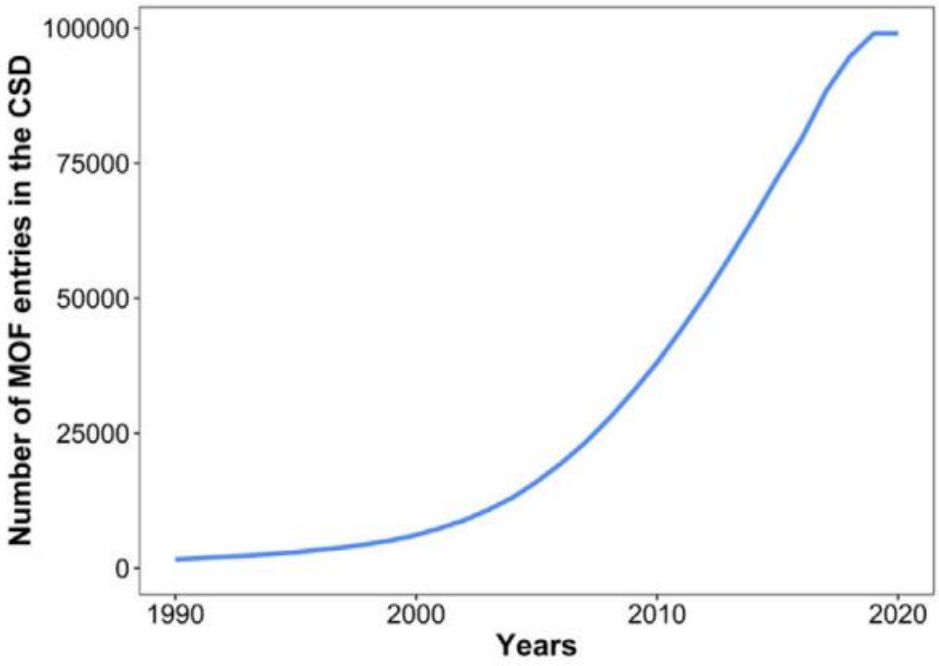

Figure 1.14 : Growth of the CSD and MOF entries from 1990 to 2020 [117].

Although thousands of MOF materials have been reported in the literature, only small amount of MOF membranes have been fabricated. Most of the membranes are fabricated using the same MOF materials such as MOF-5 (also known as IRMOF-1:isoreticular metal organic framework), CuBTC (Copper benzene-1,3,5-tricarboxylate, also known as HKUST1), ZIF-8 and ZIF-90 [37]. MOF-5, the first fabricated and extensively studied MOF membrane, is a zinc-based MOF known for its remarkable large surface area of 2900 $m^2\ g^{-1}$ [118]. Then Hermes et al. synthesized a thin film of MOF-5 particles by depositing them onto the carboxylate-terminated regions of the Self-Assembled Organic Monolayers [119]. In 2009, Liu and co-workers reported the synthesis of first continuous MOF-5 membrane on porous a-alumina supports [120], while $Cu_3(BTC)_2$ continuous thin film membrane was studied for several gas mixtures such as H_2/CO_2 showing high selectivity of hydrogen by Guo et al [121]. Caro et al. reported ZIF-8, one of the extensively studied ZIF membranes in the literature, obtained through a microwave-assisted solvothermal process. Despite the

narrow size of the six-membered ring pores (~3.4 Å), it has been observed that larger molecules like CH_4 (kinetic diameter ~3.8 Å) can pass through these pores, suggesting that ZIF-8 exhibits flexibility rather than a rigid nature [122]. The ZIF-8 membrane synthesized via secondary seeded growth on tubular a-alumina porous supports, exhibited a preference for the diffusion of CO_2 (kinetic diameter ≈ 3.3 Å) over CH_4 (kinetic diameter ≈ 3.8 Å). Notably, the ZIF-8 membrane displayed CO_2/CH_4 selectivities ranging from ~4-7 at 295 K and a high feed pressure of 139.5 KPa [123]. Pan and Lai achieved the fabrication of a ZIF-8 membrane for the first time in aqueous solution with seeded growth method, which demonstrated exceptional separation performance for C_2H_6/C_3H_8 and C_2H_4/C_3H_6. The membrane exhibited separation factors of 80 and 10, respectively, at 23 °C and 1 atm [124]. In 2012, Brown et al. fabricated a defect-free ZIF-90 membrane on a polymeric hollow fiber support with showing a possibility of a scale up high-surface-area membrane module [125]. In the same year Huang et al, designed a highly permselective ZIF-95 membrane, POZ topology ZIF featuring large 2.4 nm cavities, for the separation of H_2 from CO_2. As the temperature increases, the H_2/CO_2 gas selectivity of ZIF-95 shows an enhancement from 8.5 at 25 °C to 25.7 at 325 °C. This behavior can be attributed to the high affinity of ZIF-95 for CO_2 adsorption, resulting pore blockage at lower temperatures due to the highly adsorbed CO_2 in the ZIF-95, while at higher temperatures the reduced adsorption of CO_2, allows for an easier diffusion for H_2 [105]. ZIF-100, a MOF with MOZ topology and a pore-aperture size of 3.35 Å, was also fabricated as a membrane on polydopamine-modified support by the Caro group. The developed ZIF-100 membranes exhibited high H_2/CO_2 selectivity, attributed to the enhanced affinity of CO_2 which leads to the high CO_2 adsorption capacity within the MOF [126]. In 2016, Fu et al. synthesized the first COF-MOF composite membranes using $Zn_2(bdc)_2(dabco)$ and ZIF-8 membranes. They showed that the COF-MOF composite membranes exhibit higher separation selectivity for H_2/CO_2 gas mixtures compared to the individual COF and MOF membranes [127]. In 2020, a continuous MOF glass membrane of ZIF-62 was fabricated through the melt-quenching process, demonstrating high separation performance for H_2/CH_4, CO_2/N_2, and CO_2/CH_4 mixtures, along with superior long-term stability [128]. A brief timeline showcasing key advancements in the field of MOFs and MOF membranes are presented in Figure 1.15.

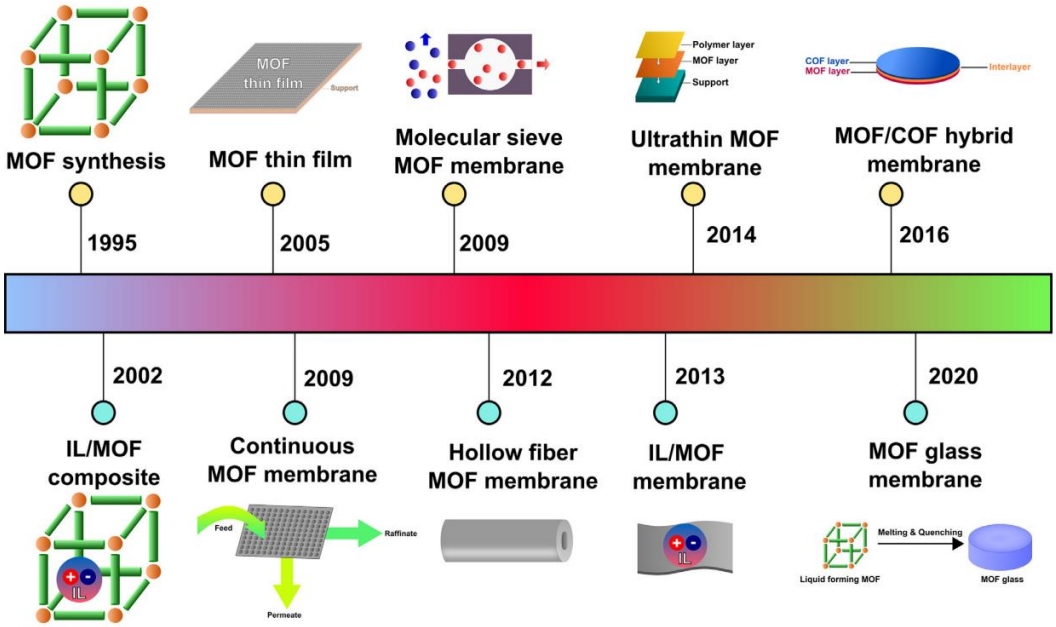

Figure 1.15 : A concise timeline highlighting key advancements in the field of MOFs and MOF membranes [129].

1.4.2 ZIFs for C2/C3 separation

Zeolitic imidazolate frameworks (ZIFs) are a sub-class of MOFs that derive their name from their similarity to zeolites. ZIF frameworks consist of transition metal cations (e.g. cobalt, zinc or indium) connected to organic linkers (e.g., methyl-/imidazolate), forming three dimensional networks. Given the resemblance between the M-Im-M bond angle of ZIFs and the Si-O-Si bond angle in zeolites, ZIFs have a tendency to adapt zeolitic topologies (e.g., MFI, SOD, MER, MOR, LTA, RHO, etc.), the reason why they are referred to as zeolitic imidazolate frameworks. ZIFs exhibit excellent thermal stability up to 550 °C and demonstrate chemical inertness in a wide range of solvents, including alkaline water and organic solvents. ZIFs with a sodalite (SOD) topology, including ZIF-7 [130], ZIF-8 [122], ZIF-9 [131], ZIF-67 [132], ZIF-90 [133,134], ZIF-91 [135], and ZIF-92 [135], have been extensively investigated for their gas separation applications (see Figure 1.16 for the structural diversity of MOFs). Their relatively small effective aperture sizes (approximately 3-5 Å) make them well-suited for the kinetic separation of small penetrant gases and light hydrocarbons. Hence, tunability, pore sizes and high stabilities make ZIFs the most widely

examined sub-group of MOFs for membrane applications as well as make them very attractive for C_2H_4/C_2H_6 and C_3H_6/C_3H_8 separation [136,137].

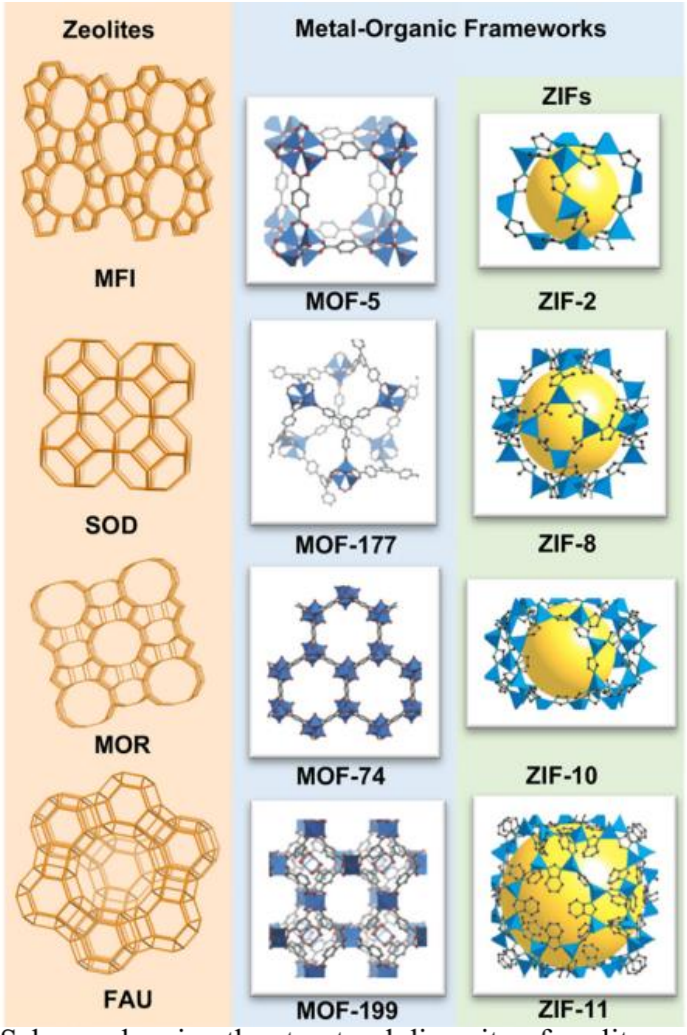

Figure 1.16 : Scheme showing the structural diversity of zeolites and MOFs [138].

ZIFs are known for their flexibility, enabling the diffusion of molecules with larger critical diameters than the pore window into their pores [139]. Despite the aperture size of ZIF-8 being 3.4 Å the flipping motion of the ligand under pressure or the presence of guest molecules allows for the adsorption of larger molecules, such as propane (kinetic diameter: 4.16 Å) and propylene (kinetic diameter: 4.03 Å) within the structure [140]. Li et al. studied the adsorption isotherms and kinetic separation of propylene and propane in ZIF-8 ([Zn(mIm)2]n, mIm = 2-methylimidazole). They found similar propane and propylene adsorption capacity along with similar isosteric heats of adsorption at zero loading. However, the diffusion rate coefficient was found to be 125 times higher than propane, indicating that

the separation mechanism is controlled by the effective sizes of the pore openings [141]. Zhang et al. calculated kinetic uptake rate measurements of propylene and propane and determined their respective diffusivities as 2.9×10^{-8} cm^2/s and 2.0×10^{-10} cm^2/s, respectively. Hence, the effective aperture size of ZIF-8 for molecular sieving is estimated to be in the range of 4.0 to 4.2 Å, which is considerably larger than the value derived from X-ray diffraction (XRD) measurements (3.4 Å) and between the molecular diameters of propylene and propane [142].

In 2012, Pan et al. conducted one of the earliest studies on ~2.0mm thick ZIF-8 membranes for the separation of C_3H_6/C_3H_8. They observed an average propylene permeance and C_3H_6/C_3H_8 separation factor of ~50 GPU up to 200 Barrers [42]. Then, Jeong and Kwon published a series of research articles describing propylene-selective ZIF-8 membranes with an average propylene permeance of ~90 GPU and a C_3H_6/C_3H_8 separation factor of around 50, respectively [43,44]. Eum et al. fabricated ZIF-8 membranes on PAI hallow fibers using the interfacial microfluidic membrane processing (IMMP) method. They observed an average propylene permeance and C_3H_6/C_3H_8 separation factor of 90 at 9.5 bar [143]. ZIF-8 membrane on ceramic hollow fibers and micromonoliths prepared by Huang et al., demonstrated a high C_3H_6/C_3H_8 separation factor of 139, while due to their thickness these membranes exhibited a low propylene permeance of 16 GPU [144].

Despite, membrane selectivity has shown significant improvements, reaching values of several tens to up to 300, membrane permeance remains limited, typically falling within the range of 30-60 GPU. This limitation can be attributed to the relatively thick nature of most ZIF-8 membranes, ranging from several micrometers to as much as 80 μm. Hence, current research efforts are concentrated on developing ultrathin MOF membranes to decrease the transport resistance [26]. Wei et al. prepared ~500 nm ultrathin thick ZIF-8 membranes on AAO disks using the cathodic deposition method. The membranes showed a propylene permeance of ~180 GPU and a C_3H_6/C_3H_8 separation factor of around 140, respectively [145]. Lee et al. further reduced the effective thickness of ZIF-8 membranes via postsynthetic ligand exchange (PSLE) method by exchanging 2-methylimidazole linkers (mIm) with 2 imidazolecarboxaldehyde(Ica). The Ica-exchanged ZIF-8 membranes displayed a propylene permeance of ~260 GPU and a C_3H_6/C_3H_8 separation factor of ~40 [146]. Recently, there

has been a growing research interest in the vapor-phase synthesis of ZIF membranes, which enables the formation of even thinner ZIF membranes. Ma. et al. utilized the ligand-induced permselectivityation (LIPS) technique the fabricate ZIF-8 membranes on a α-Al_2O_3 substrates coated with γ-Al_2O_3. They obtained a propylene permeance of ~480 GPU and a C_3H_6/C_3H_8 separation factor of 74 with a scalable and solvent-free environmentally method [147]. Li et al. used gel-vapor transformation technique to obtain nanometer-thick ZIF-8 membranes with a propylene permeance of ~830 GPU and a C_3H_6/C_3H_8 separation factor of ~70 for ~87 nm thin layers, while for thinner ~17 nm layer ZIF-8 membranes they obtained propylene permeance as 2500 GPU [148]. Most recently, Qiao et al. fabricated 45 nm thick, low-crystallinity-state MOF (LC-MOF) membranes on commercial polysulfone ultrafiltration PSF filters via interface layer polarization induction. They obtained a defective ZIF-8 (DZIF-8) membrane with a propylene permeance of ~3000 GPU and a high C_3H_6/C_3H_8 separation factor of ~90 which comes from the presence of abundant open metal sites that forms π bond interactions with propylene molecules [149].

ZIF-67 ($Co(Hmim)_2$, Hmim = 2-methylimidazole)), Cobalt-substituted ZIF-8 is also effective for propylene/propane separation due to having redox catalytic cobalt centers. Kwon et al. fabricated several types of membranes on α-Al_2O_3 discs through heteroepitaxial growth to prepare membranes such as ZIF-8/ZIF-67 and ZIF-67/ZIF-67 bilayer membranes. The resulting membranes outperformed almost all previously reported ZIF-8 membranes, with separation factors of ~190 and ~160 obtained for ZIF-8/ZIF-67 and ZIF-67/ZIF-67 membranes, respectively, while maintaining a similar propylene permeability of ZIF-67 to ZIF-8 membranes. They related this phenomena to the rigid Co-N connectivity, which limits the ligand flipping motion degree, resulting in a smaller effective pore aperture size and, consequently, greater selectivity [150]. Krokidas et al. supported their idea with molecular simulations, which demonstrated a significant increase in the ratio of C_3H_6/C_3H_8 corrected diffusivities compared to ZIF-8 [151]. Hence, the experimental and computational studies verify that ZIF-67 framework shows great potential as a candidate for propylene/propane separation due to suppressing the flexibility with more rigid framework. ZIF-67 membranes have some drawbacks arising from the poor grain boundary structure caused by the faster crystal nucleation and growth kinetics compared to ZIF-8. Hou et al. fabricated bimetallic

$Zn_{82}Co_{18}$-ZIF-8 membrane with a propylene permeance of ~60 GPU and a C_3H_6/C_3H_8 separation factor of 200 with a long term stability [152].

Separation of ethylene from ethylene/ethane mixtures using membranes are one of the most challenging separations. So far, there are only a limited number of studies for ethylene separation as there are not many ZIFs with suitable apertures and desirable transport properties. Bux et al. prepared 25 μm thick ZIF-8 membranes on asymmetric titania support with a C_2H_4/C_2H_6 separation factor of 4.2 and ~2.5 for single component and mixed gas permeation tests, respectively [153]. In single and binary gas separation tests conducted under several conditions, Li and co-workers obtained C_2H_4/C_2H_6 selectivities ranging between 1.5 and 3 for ZIF-8 membranes. As the diffusion activation energies for ethylene and ethane (11.7 and 13.2 kJ/mol) are lower than their respective heats of adsorption (16.2 and 17.1 kJ/mol), the permeability of ethylene and ethane decreased with increasing temperatures from 25 ˚C to 100 ˚C. On the other hand, single and binary permeation pressure dependence tests showed that with an increase in pressure, the ideal selectivity of C_2H_4/C_2H_6 increases while the ethylene diffusive selectivity decreases [154]. This could be related to the how ZIF-8 effective pore apertures of 4.0 Å is larger than both C_2H_4 (kinetic diameter: 3.59 Å) and C_2H_6 (kinetic diameter: 3.72 Å) molecules. Pure and hybrid ZIFs, such as ZIF-4 and ZIF-7, have been used as adsorbents for the separation of ethylene from ethane under kinetic or thermodynamic conditions. However, none of these have been developed as C_2H_4-selective membranes [136].

Furthermore, a slight reduction in the pore size of ZIF-8 is expected to enhance molecular sieving for ethylene and ethane, making ZIF-7 a promising candidate for C2 separation. ZIF-7 has a SOD topology consist of transition zinc ions connected to benzimidazole (bIM) ligands. The presence of bulky benzene rings in the ligand of ZIF-7 narrows its crystallographic aperture size to approximately ~3 Å, which is slightly smaller than that of ZIF-8 (~3.4 Å). Gücüyener et al. studied the adsorption isotherms of ethane over ethylene on ZIF-7 through a gate-opening effect. They showed that the interaction between the adsorbates and the benzene rings controls the selective adsorption mechanism with discriminating molecules of very similar size through a gate-opening effect. Adsorption

breakthrough experiments at lower pressures have demonstrated that ethane molecules can enter the pores of ZIF-7, highlighting its potential for outstanding ethane selectivity [130].

1.4.3 Other MOFs for C2/C3 separation

MOFs have demonstrated significant potential as adsorbents for C2/C3 separations based on different types of mechanisms such as an equilibrium-based mechanism, a gate-opening effect, and a kinetic-based mechanism. Currently, several materials have been reported that can demonstrate the capability of both kinetic and molecular sieving separation through adsorption studies. As a next step, new updates on recent developments in novel MOFs and their potential for membrane-based C2/C3 separations will be provided.

Cadiau et al. developed a fluorinated MOF material NbOFFIVE-1-Ni (also referred to as NbOFFIVE-1-N) to achieve molecular exclusion of propane from propylene under ambient conditions. This material is made of Ni(II)-pyrazine square-grid layers with $(NbOF_5)^{2-}$ pillars to obtain a 3-D MOF with square-shaped channels. The utilization of $(NbOF_5)^{2-}$ as the inorganic building block for pillaring, rather than $(SiF_6)^{2-}$, led to an increased metal-fluorine distance (1.95 Å) and subsequent tilting of pyrazine molecules in NbOFFIVE-1-Ni. Thus, the pore size of NbOFFIVE-1-Ni is found to be 3.0471 Å, which is significantly smaller than that of SIFSIX-3-Ni (4.965 Å) (Figure 1.17). These authors demonstrated that the separation of C3 occurs through a mechanism governed by the gate-opening effect, accompanied by additional tilting of the pyrazine molecules, allowing C_3H_6 molecules to pass into the pores and preventing C_3H_8 to do so. Breakthrough experiments provided further confirmation of the effective molecular sieving of C_3H_8 from a 50/50 C_3H_6/C_3H_8 mixture [155]. Wang et al. designed another microporous MOF, namely $Y_6(OH)_8(abtc)_3(H_2O)_6(DMA)_2$ (Y-abtc, abtc = 3,3′,5,5′azo benzene -tetracarboxylates; DMA = dimethylammonium) for propane/propylene separation through selective molecular exclusion mechanism. This Y-abtc MOF contains cage-like pores with an aperture size of 4.72 Å, which is in between the kinetic diameters of C_3H_6 (4.68 Å) and C_3H_8 (5.1 Å), enabling the fully exclusion of C_3H_8 molecules [156].

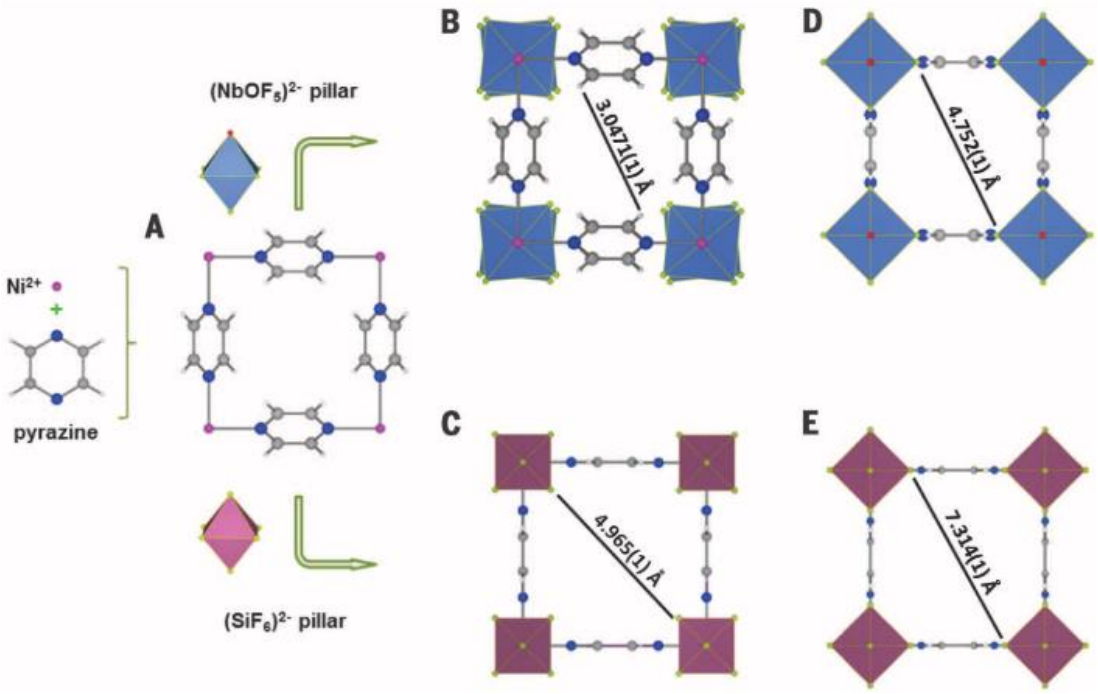

Figure 1.17 : The structure of NbOFFIVE-1-Ni, with a focus on the arrangement of building blocks, and a comparison with the parent SIFSIX-3-Ni. (a) Illustration of a 3D MOF with primitive cubic topology, showcasing the square-shaped arrangement in the Ni-pyrazine (4,4′) square grid, pillared by inorganic blocks [$(NbOF_5)^{2-}$ or $(SiF_6)^{2-}$] (b) Crystal structure of NbOFFIVE-1-Ni, displaying the titling of pyrazine molecules. (c) Crystal structure of SIFSIX-3-Ni. Simulation of the maximum open structure of (d) NbOFFIVE-1-Ni and (e) SIFSIX-3-Ni, displaying a theoretical window sizes [155].

Lee et al. synthesized four different MOFs, i.e. DTO, TO, DBTO, and BTO MOFs synthesized from 1,2,4,5-tetrakis(carboxyphenyl) benzene and trans-1,2-dipyridylethene struts ((L1 and L3, L4 and L1, L2 and L3, and L2 and L4, respectively) that enabled kinetic propylene/propane separation. These synthesized MOFs have two types of channels, I and II, whose apertures could be controlled by struts. DTO and TO MOFs have channel II apertures ranging from 4.26 - 5.70 Å and 4.88 - 6.03 Å, respectively, whereas DBTO and BTO MOFs have smaller apertures of 3.34 and 3.05 Å, respectively. On the other hand, channel I apertures are similar for all types. Time-dependent gas uptake profiles at 0.3 bar and 298 K for each MOFs showed that, DBTO and BTO MOFs exhibit higher kinetic selectivities (~12-fold) relative to the DTO and TO materials, as reduction in the apertures which comes from the Br atoms of the L2 ligands, increases the kinetic selectivity for the propylene. The shape of crystallites also has a role in kinetic separation such as the rectangular shaped MOF

crystals provide higher kinetic selectivities for propylene over propane. Hence, this early study highlights how the kinetic separation of propane and propylene can be achieved by the fine-tuning of MOF aperture through topology-directed ligand design and functionalization [157]. Li. et al. fabricated a microporous MOF ELM-12, with zig-zag 2D channels and appropriate pore apertures for the C_3H_6/C_3H_8 separation based on the kinetic separation mechanism. ELM-12 shows significantly faster adsorption of C_3H_6 compared to C_3H_8 at 298 K and 308 K, and C_3H_6 can reach the adsorption equilibrium very fast, indicating a high kinetic selectivity of C_3H_6 over C_3H_8. The kinetic selectivity of C_3H_6/C_3H_8 reaches up to 204 at 298 K and 971 at 308 K. In addition to it is high kinetic separation factor, the highly stable structure and ease of scaled-up production makes this material favorable for the industrial C_3H_6/C_3H_8 separation [158]. Two microporous MOFs, i.e. $Zn(ox)_{0.5}(trz)$ and $Zn(ox)_{0.5}(atrz)$ with 1D zig–zag shaped channels, developed by Peng et al., showed great performance for the kinetic separation of C_3H_6/C_3H_8. These two isoreticular MOFs demonstrated significantly faster adsorption of propylene over propane through a diffusion-controlled process across a wide temperature range, At some point, the kinetic separation factor reached 1565 at 323 K in $Zn(ox)_{0.5}(trz)$. Hence, these findings suggest that, these materials hold great potentials as candidates for the kinetic based separation of C_3H_6/C_3H_8 mixtures [159].

Wang et al. reported a porous MOF $[Zn_2(btm)_2)(btk)]$ (MAF-23-O) that improves the thermodynamic and kinetic adsorption selectivity of propylene/propane. MAF-23-O is obtained by heating $[Zn_2(btm)_2]$ (MAF-23) under oxygen flow, whereby half of the btm^{2-} ligands are selectively oxidized to form btk^{2-} leading to an improvement in the adsorption selectivity of C_3H_6/C_3H_8 as the oxidation reduces the framework flexibility. Breakthrough experiments show that after the oxidation procedure, C_3H_8 adsorption is largely reduced and C_3H_6 adsorption is improved, while the adsorption selectivity is increased from 1.5 to 15 at 298 K and 1 atm. Molecular Dynamics simulations showed that the kinetic selectivity of MAF-23-O is nearly one hundred times higher than that of MAF-23 (112.3 vs. 1.2) for the flexible MOF, while periodic density functional theory (PDFT) calculations revealed that MAF-23-O requires more energy for C_3H_6 diffusion compared to the unoxidized MOF. Hence, the oxidation procedure improved the thermodynamic selectivity while reducing the framework flexibility, which affects the kinetic selectivity [160].

Yang et al. investigated the kinetic separation of C_2H_4/C_2H_6 using a hydroxyl-functionalized Al-MOF, NOTT-300 with a comprehensive study that included computational modelling. The C_2H_4 and C_2H_6 adsorption uptakes in NOTT-300 at 293 K and 1 bar, are measured as 4.28 and 0.85 mmol g^{-1}, respectively, while the equimolar C_2H_4/C_2H_6 selectivity is found as 48.7 via ideal adsorbed solution theory (IAST) theory. DFT calculations showed that C_2H_6 poorly adsorb in NOTT-300 which leads to a high selectivity of C_2H_4/C_2H_6 mixtures [161]. [161]. Bachman et al. fabricated M_2(*m*-dobdc) type MOFs (M = Mg, Mn, Fe, Co, Ni, Zn), which are meta-substituted structural isomers of MMOF-74 (or CPO-27-M), for olefin/paraffin separations using single-component and multicomponent equilibrium gas adsorption and adsorption kinetics. Single-component gas adsorption measurements provide information about the thermodynamics of gas molecules, revealing higher adsorption of olefins over paraffins compared to their structural isomers with the Fe, Co, and Ni variants. Among them, Fe_2(m-dobdc) exhibits the highest olefin uptakes, with values exceeding 7 mmol g^{-1} and C_2H_4/C_2H_6 selectivity over 55 at 298 K and 1 bar. Single-crystal X-ray diffraction, along with differential enthalpy calculations, revealed that an increased charge density at the metal site enhances the metal–olefin interactions, resulting an improved separation performance. Further, breakthrough experiments indicate that Co_2(*m*-dobdc) can produce high purity olefins without a temperature swing, while transient adsorption experiments demonstrate fast adsorption kinetics, with > 90% of equilibrium reached within 30 s. Hence, the combination of high olefin/paraffin selectivity, large uptakes, fast adsorption kinetics and low cost makes the M_2(*m*-dobdc) frameworks promising adsorbents for olefin/paraffin separations in industrial processes [162].

Bereciartua et al. reported a flexible pure silica zeolite MOF, ITQ-55 which exhibits a tortuous monodirectional small-pore system with relatively large cavities. Due to the framework flexibility and the presence of large heart-shaped cages, ITQ-55 demonstrates the ability to kinetically separate ethylene from ethane with an extraordinary selectivity of~100. Ab initio molecular dynamics (AIMD) simulations provided insights into understanding the framework flexibility of ITQ-55. It was observed that when an ethylene molecule enters the pores, the mean window size expands from 2.38 Å to 3.08 Å with ethylene molecule effectively “braces the window open”. Single-component gas adsorption measurements

showed that, ethylene adsorption rate is much higher than that of ethane while only ethylene could only reach equilibrium kinetics. Hence, the separation mechanism in ITQ-55 is controlled by a preferential diffusion of ethylene over ethane [163]. Ding et al. prepared phosphate-anion pillared MOF $ZnAtzPO_4$ which exhibits a unique equilibrium kinetic synergetic effect for the C_2H_4/C_2H_6 separation. $ZnAtzPO_4$ (Atz = 3-amino-1,2,4-triazole) has a pore structure that decorated with electronegative functional groups, allowing for the entrapment of C_2H_4 molecules while hindering the diffusion of C_2H_6. Such that, the equilibrium-kinetic combined C_2H_4/C_2H_6 selectivity becomes 32.4 at 273 K, while at ambient temperature the selectivity is 12.4. With the aid of computational simulations to analyze the binding sites of the guest molecules and the recycling breakthrough experiments, researchers concluded that $ZnAtzPO_4$ could be a promising alternative for the separation of C_2H_4/C_2H_6 [164].

Wang et al. synthesized two zirconium-based MOFs, UiO-66-ADC and NUS-36, constructed from acetylenedicarboxylate (ADC) linkers and Zr_6 clusters. Compared to UiO-66-ADC, which has an fcu topology, NUS-36 possesses a bcu topology and ultramicropores smaller than 3.6 Å. The C_2H_4 adsorption isotherm of NUS-36 is 1.46 mmol g^{-1} which is comparable to UiO-66-ADC, while UiO-66-ADC exhibits higher C_2H_6 uptakes compared to NUS-36, 1.6 mmol g^{-1} and 1.01 mmol g^{-1}, respectively at 298 K and 105.8 kPa. IAST selectivity for C_2H_4 over C_2H_6 in an equimolar gas mixture is 4.1 for NUS-36 mixture, while it is much lower for UiO-66-ADC (1.8) at 298 K and 1 bar. The congested pores in NUS-36 provide a strong affinity for C_2H_4 over C_2H_6, which can be attributed to the synergistic enthalpic and entropic effects. Hence, the strategy of reducing pore size can be used for designing MOFs for challenging gas separation [165].

Bao et al. synthesized gallate-based MOFs comprising M-gallate (M = Ni, Mg, Co) with 3D zig–zag shaped channels, which exhibited pore apertures (3.47–3.69 Å) ideally suitable for the molecular sieving of ethylene (3.28 × 4.18 × 4.84 $Å^3$) and ethane (3.81 × 4.08 × 4.82 $Å^3$) based on their differential molecular cross-section sizes. Direct breakthrough experiments using equimolar C_2H_4/C_2H_6 mixtures have confirmed the high selectivity of ethylene for M-gallate, while Co-gallate shows an IAST C_2H_4/C_2H_6 selectivity of 52 and a C_2H_4 uptake of

3.37 mmol g^{-1} at 298 K and 1 bar. Additionally, these materials demonstrated high stability against water, making them a promising candidate for industrial applications [166].

The utilization of molecular sieves in gas separations offers the advantage of achieving ultrahigh selectivity, thereby enhancing the productivity of adsorption-based separation processes across diverse applications. An ultramicroporous MOF called UTSA-280 [$Ca(C_4O_4)(H_2O)$], synthesized from calcium nitrate and squaric acid, has been recently reported by Lin et al. UTSA-280 provides extremely high selectivity for C_2H_4/C_2H_6 separation due to their molecular sieving separation mechanism. UTSA-280 possesses rigid 1-D cylindrical channels with pore apertures of 3.2 × 4.5 Å and 3.8 × 3.8 Å, along with a similar cross sectional area of 14.4 $Å^2$. These dimensions make UTSA-280 ideally suitable for the molecular exclusion of ethane, as it's cross sectional area falls between that of ethylene (13.7 $Å^2$) and ethane (15.5 $Å^2$). On the other hand, UTSA-280 is very stable in water. Single-component equilibrium adsorption isotherms for ethylene and ethane showed that C_2H_4 uptake in UTSA-280 is 2.5 mmol $g^{-1,}$ while C_2H_6 uptake is very low 0.098 mmol g^{-1} for C_2H_6 at 298K and 1bar in line with a molecular exclusion of ethane. The IAST adsorption selectivities of C_2H_4/C_2H_6 for UTSA-280 exceed 10,000 at 298 K and 1 bar, which is significantly higher compared to other MOFs such as Fe-MOF-74 (13.6), NOTT-300 (48.7) and other comparable materials. Breakthrough experiments showed that C_2H_4 enriched from an equimolar C_2H_4/C_2H_6 mixture up to 1.86 mol kg^{-1}. Moreover, single-crystal X-ray diffraction measurements have demonstrated that the tilted C_2H_4 molecules can fit the narrow pore channels well. This favorable fit was attributed to the orientation of C_2H_4 molecules, which can minimize steric hindrance and electrostatic repulsion, allowing them to interact with aromatic ligands or coordinated water molecules through weak C–H···O hydrogen bonding (3.32–3.44Å), π···π stacking (3.31Å) and vdW interactions (shortest C–H···π distance of 3.32Å). Hence, the water-stability and ease of kilogram scale synthesis of UTSA-280 with an environmentally friendly method and excellent separation performance, makes them a promising candidate for energy-efficient chemical separation processes [167].

Among the numerous MOFs reported so far the separation of C_3H_6/C_3H_8 and C_2H_4/C_2H_6, the main focus of this study will be on ZIF-67 for C_3H_6/C_3H_8 separation, and UTSA-280 for

C_2H_4/C_2H_6 for future perspectives. Figure 1.18 shows the representation of the MOF structures explored in this thesis.

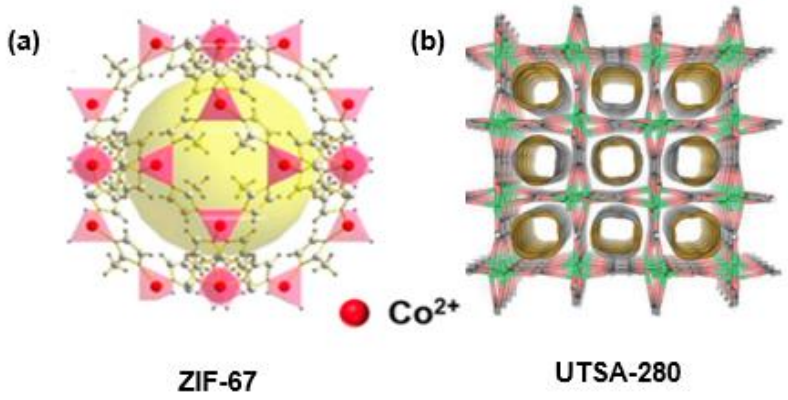

Figure 1.18 : Representation of the MOF structures explored in this thesis (a) ZIF-67 [168] and (b) UTSA-280 [5].

1.5 Mixed Matrix Membranes

Current commercial membrane materials especially pure polymeric membranes often suffer from the permeability–selectivity tradeoff. Most polymeric membranes, with a few exceptions in fluoropolymers, are vulnerable to severe plasticization and/or dilation when exposed to relatively high pressures of condensable gases such as C_3H_6 and C_3H_8. This is due to the tendency of these gases to cause swelling of the polymer chains. Hybrid mixed-matrix membranes (MMMs), which combine a continuous organic polymer phase with a dispersed inorganic phase, have become popular to overcome the disadvantages of membrane-based membranes. Such that, these membranes offer great potential for the fabrication of high-performance membranes [169]. MMMs offer the possibility of harnessing the advantages of both phases, combining the good processability and mechanical robustness of the polymer phase with the inherently high permeability and selectivity of the filler phase [2]. Various applications have utilized inorganic and organic filler particles, including sieving zeolites [163], silica membranes [170], alumina [171], MOFs [6], and porous organic cages (POCs) [172], to achieve enhanced energy-efficient separation of C_3H_6/C_3H_8. Despite the numerous advantages, challenges such as filler particle aggregation, sedimentation, and interfacial morphologies can arise in MMMs. Therefore, careful selection of the optimal filler and matrix scheme is crucial to achieve improvements in both permeability and selectivity [41].

Among the various fillers available, MOFs have attracted significant attention due to their tunable pore structures and versatile chemical functionality. A schematic for the MMM concept could be seen in Figure 1.19.

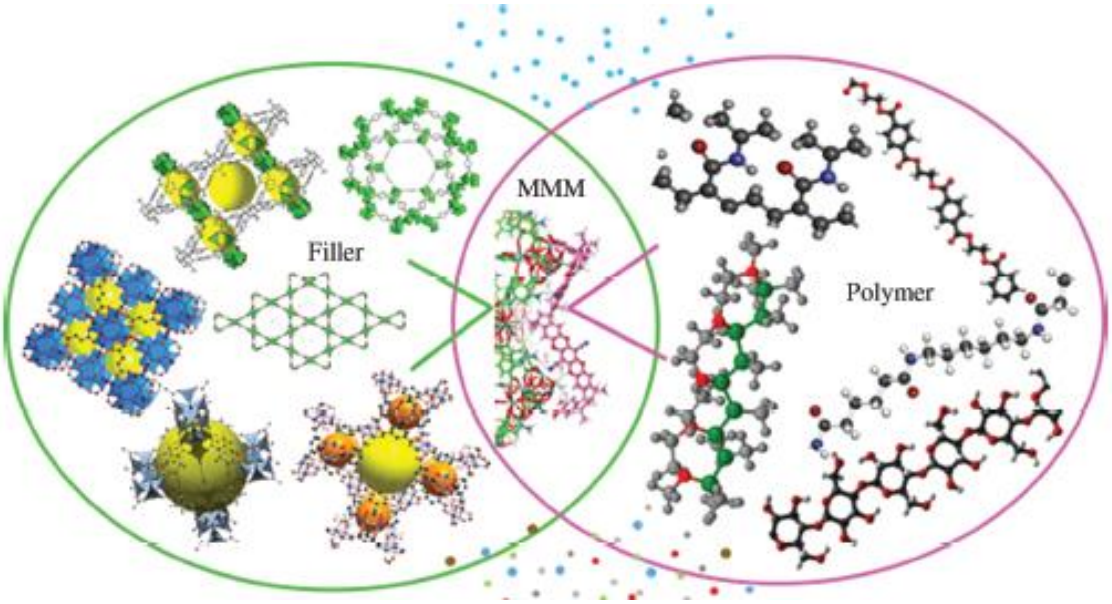

Figure 1.19 : Schematic of MMM concept [2].

1.5.1 General introduction on MMM

More than 50 years ago, Barrer and James used zeolite 13X and 4A to a resin matrix to produce ion exchange membranes, which have become the first application of MMMs [173]. Zeolites are a class of hydrated aluminosilicate materials known for their exceptional ion-exchange and sorption properties. Zeolites are primarily composed of SiO_4 and AlO_4 tetrahedra, which are interconnected through shared oxygen atoms. The AlO_4 units carry negative charges that are neutralized by specific cations within the zeolite pores. The architecture of zeolites is characterized by an abundance of channels, cavities, and pores. These zeolite structures feature uniform pore sizes at a molecular scale (ranging from 0.3 to 0.7 nm), granting them the ability to perform molecular sieving. Furthermore, the cations present within the pores can be substituted with different ions through exchange processes. With their rigid framework structure and remarkable molecular sieving capabilities, zeolites hold great promise as materials for effectively separating mixtures composed of molecules

with similar sizes, such as in olefin/paraffin separations [24]. The first performance study on MMMs for gas separation applications was conducted by UOP when developing zeolite/polymer composites in the 1980s [2]. Since then, various ion-exchanged molecular sieve zeolites have been developed for the purpose of separating light hydrocarbons. The majority of these zeolites exhibit olefin selectivity, a characteristic resulting from the robust adsorption caused by the unique interactions between the cationic sites within the zeolite micropores and the π-bonds of olefins [41]. ZSM-5 [174], SAPOs [175], A-Type [17], 13X [176], NaX [177], and silicates are among the zeolites that find extensive utilization in polymer matrices for gas separation applications. These zeolites are commonly employed for air separation, natural gas upgrading, as well as the recovery and separation of hydrocarbons. Further, several types of zeolites have been explored for olefin/paraffin separations, each exhibiting different pore sizes. For example, NaX has a pore size of 7.4 Å [178], ZSM-5 has a pore size of 5.5 Å [179], and ETS-10 has a pore size of 7.2 Å [180]. Zeolites have gained significant interest because of their superior permeability and selectivity values compared to polymers. This is primarily attributed to zeolites having larger porosities and specific pore sizes that enable the separation of gases based on their molecular size. Mahajan et al. prepared MMMs using zeolite 4A and Matrimid and Ultem type of various polymer matrices for O_2/N_2 separation. Despite the small pore aperture of zeolite 4A (3.8−4.0 Å), which resulted in a modest O_2 permeability of 0.8 Barrer, this membrane demonstrated an O_2/N_2 selectivity of 37. These material properties continue to generate significant interest within the membrane community [181]. Moreover, the utilization of zeolites in MMMs comes with several drawbacks:

(1) The preparation of defect-free zeolite crystals can pose challenges in terms of difficulty, time consumption, and cost.

(2) The available range of zeolite structures and compositions is limited.

(3) Expensive surface chemistries are frequently required to enhance adhesion to polymer matrices.

Overall, difficulties in scale up, complicated manufacturing processes, high manufacturing costs and low mechanical stability of zeolites issues create demand for new filler materials for MMMs [21,37].

An alternative filler material is COFs, which consist of pure organic polymers featuring strong covalent bonds formed by light elements such as B, C, N, O, and more [182]. Due to their composition of lightweight elements connected by robust covalent bonds, COFs exhibit low mass densities, exceptional thermal stabilities, and permanent porosity. COFs can be classified into two-dimensional (2D) or three-dimensional (3D) structures, depending on the dimensions of their building blocks. In the case of 2D COFs, individual 2D sheets are covalently bonded together to form a layered eclipsed structure with periodically aligned columns. This columnar stacking arrangement offers a distinct opportunity to construct ordered p-systems, which are challenging to achieve using traditional covalent or noncovalent methods. The presence of ordered columns in 2D COFs facilitates efficient charge carrier transport in the stacking direction. This suggests that 2D COFs hold promise for the development of novel p-electronic and photofunctional materials, which can find applications in fields such as optoelectronics and photovoltaics. On the other hand, 3D COFs differ by extending their framework in three dimensions using building blocks containing an sp^3 carbon or silane atom. These 3D COFs are known for their high specific surface areas, sometimes exceeding 4000 m^2g^{-1}, rich open sites, and low densities as low as 0.17 g cm^3. These distinctive characteristics make 3D COFs highly suitable for gas storage applications [183].

Over the past five years, research on COF-based membranes has progressed rapidly. However, the majority of research has focused on liquid-based separations due to the relatively large pore size (>1 nm) of these materials. Jiang et al., utilized COF-based composite membranes (CMs) to enable propylene/propane separation using a facilitated transport mechanism along with an asymmetric configuration of SCOF-Ag/PI CMs. This work represents the first instance of COF-based membranes being employed for olefin/paraffin separation. MMM composed of 15 wt% SCOF-Ag/PI CMs exhibits an impressive propylene permeability of 75.16 Barrer and a favorable propylene/propane selectivity of 35.45 [184]. Later, Liu et al. fabricated an electrochemical co-deposition

approach to fabricate MOF-COF alloy membranes. This method utilizes the Coulombic force between the quaternary-N of COF and pyridine-N of ZIF-8 to restrict the linker rotation of ZIF-8, resulting in a unique alloying effect. The optimized AMs with enhanced rigidity demonstrate an exceptional C_3H_6/C_3H_8 separation performance, achieving a separation factor of 203 and a remarkable C_3H_6 permeance of 168 GPU [185]. Therefore, COF membranes have thus far been shown to primarily serve as auxiliary components for enhancing olefin/paraffin separations, rather than serving as the intrinsic separation layer. Hence, COFs are not a good candidate as filler materials for gas separations.

Another inorganic filler that has attracted significant attention is silica. Silica particles can be classified into various types based on their pore and particle size, and each type imparts a different effect on the physical, chemical, and gas transport mechanisms of a polymeric membrane. Numerous studies have been conducted to investigate the combination of different glassy polymer properties with various types of silica particles. These investigations include combining glassy polymers with high chain packing density with nano-sized silica particles [186,187], high-density glassy polymers with fumed silica particles [188,189], hyperbranched glassy polymer with nano-sized silica particles [190,191], crosslinked glassy polymer with fumed silica particles [192], high density glassy polymers with mesoporous silica particles [193,194], glassy polymer with siloxane-type silica particles [195] and hyperbranched glassy polymer with mesoporous silica [196].

Fumed silica, typically ranging from 5 nm to 60 μm in particle size, is the primary nonporous silica utilized in MMM fabrication. It offers a specific surface area of 45–430 $m^2\ g^{-1}$ and a density of 2.20–2.81 g cm^{-3}. Fumed silica demonstrates higher hydrophilicity and surface energy due to its large surface area and the abundance of silanol groups on its surface. Hence, fumed silica can be incorporated into a wide range of polymers, such as glassy polymers, rubbery polymers, and block copolymers with two segments. For instance, the addition of fumed silica to glassy polymers like PIM1, polysulfone, polyvinylidene fluoride and polyvinyl alcohol as well as block copolymers such as polyether block amide and polyurethane, leads to an increase in the free volume of MMMs. Additionally, applying fumed silica to rubbery polymers with compatible functional groups enables the achievement of good matrix-filler interactions and uniform filler dispersion. Another form of mesoporous

silica is characterized by the presence of pores in the 2–50 nm range. It is often integrated into various glassy polymers, such as polyphenylene oxide, polyvinylidene fluoride, polyimide and polysulfone. These combinations result in a significant enhancement in gas selectivity, because of the mesopore structure and high surface area of the materials. On the other hand, microporous silicas such as tetraethyl orthosilicate and tetramethyl orthosilicate are commonly used in MMM fabrication in the form of silica sol. The synthesized microporous silica is commonly employed in glassy polymers such as polyamide, polysulfone/polyimide and polyphenylene oxide as similar approach of non-porous and mesoporous silicas [197].

In general, the incorporation of silica into MMMs results in higher gas permeability compared to pure polymeric membranes. This improvement can be attributed to an increase in the fraction of free volume within the MMMs and the interactions between the active sites of silica and the penetrant molecules. Despite the potential benefits of incorporating silica into MMMs, a trade-off relationship remains, and only a few combinations of hyperbranched polymer-silica membranes have been able to achieve gas separation performance that exceeds the Robeson's upper bound. Yamada et al. investigated the separation performance of CO_2/CH_4 with using hyperbranched polyimide and its silica hybrid membranes. They showed that with thermal treatment at 450 ˚C, gas permeability is enhanced with local deformation of molecular packing and rearrangement of molecular chains, as well as created around interfacial region between polymer and well-dispersed silica domains with a large surface area. Additionally, the adsorption reaction between the silica particles in the polymer matrix plays a role as barrier for penetrant gases to pass through membranes. Furthermore, the adsorption reaction occurring between the silica particles embedded in the polymer matrix serves as a barrier, hindering the passage of penetrant gases through the membranes [191].

1.5.2 MOFs-based MMM for gas separation

Among vast selections of filler materials, MOF-based MMMs offer several benefits over traditional MMMs that employ other types of porous materials as fillers [198]. Figure 1.20 illustrates the combination of the good processability of the polymer phase with the

inherently high permeability and selectivity of the MOF phase. Incorporating MOFs into MMMs offers distinct advantages over other inorganic fillers:

1. The pore structure and size of MOFs can be easily customized for specific applications by simply adjusting the nature of the inorganic node and the organic ligands [199].
2. MOFs typically exhibit better compatibility with polymeric matrices than zeolites due to the higher affinity between the organic linkers of MOFs and the polymer chains [200].

Despite the fact that a series of MOF-based MMMs have demonstrated improved gas separation performance compared to MMMs incorporating traditional fillers such as zeolites and metal oxides, the achieved membrane performance still falls short of the expected theoretical values based on material simulations [198,201].

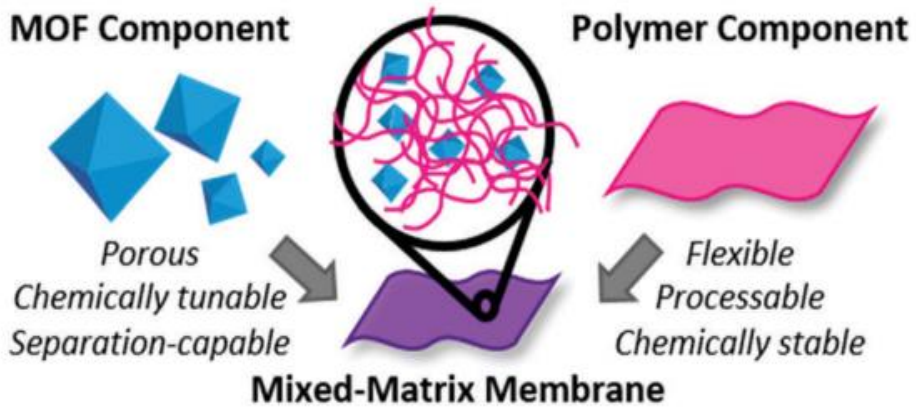

Figure 1.20 : MOFs-based MMM [202].

In addition to the concerns related to the membrane fabrication process, MOFs stability and cost, several engineering challenges arise when aiming to achieve the desired membrane morphology and optimized separation performance in MOF-based MMMs. These challenges include:

1. Selection of the appropriate MOF/polymer system based on fundamental considerations, rather than random selection.
2. Difficulties in achieving a uniform dispersion/distribution of the inorganic phase within the polymeric phase.

3. Control of the interfacial interactions between the MOF surfaces and the continuous polymeric phase to ensure the production of void-free MMMs.

Addressing these challenges is crucial to overcome potential limitations and maximize the performance of MOF-based MMMs in gas separation applications [201]. Various techniques have been developed to enhance the interfacial compatibility between MOFs and polymers in MMMs for gas separation. These techniques include increasing the interfacial surface area [19], adding MOFs into porous liquids to achieve good dispersion [203], MOF surface functionalization [204], MOF surface modification with oligomer or polymer brushes [205], polymer modification (e.g., functionalizing polymer matrix with specific groups [206]) and others (e.g., liquid MOFs [203], interfacial binders [207], defect engineering [208] and ionic liquid coating [209]) [210].

Typical MOFs commonly employed in MMMs include ZIFs, such as ZIF-8 and ZIF-67 [25,211], the University of Oslo-66 (UiO-66) series, such as UiO-66(Zr) and UiO-66(Nd) [212,213], and the Materials Institute Lavoisier (MIL) series, such as MIL-101(Cr) and MIL-125(Ti) [214,215] (Figure 1.21).

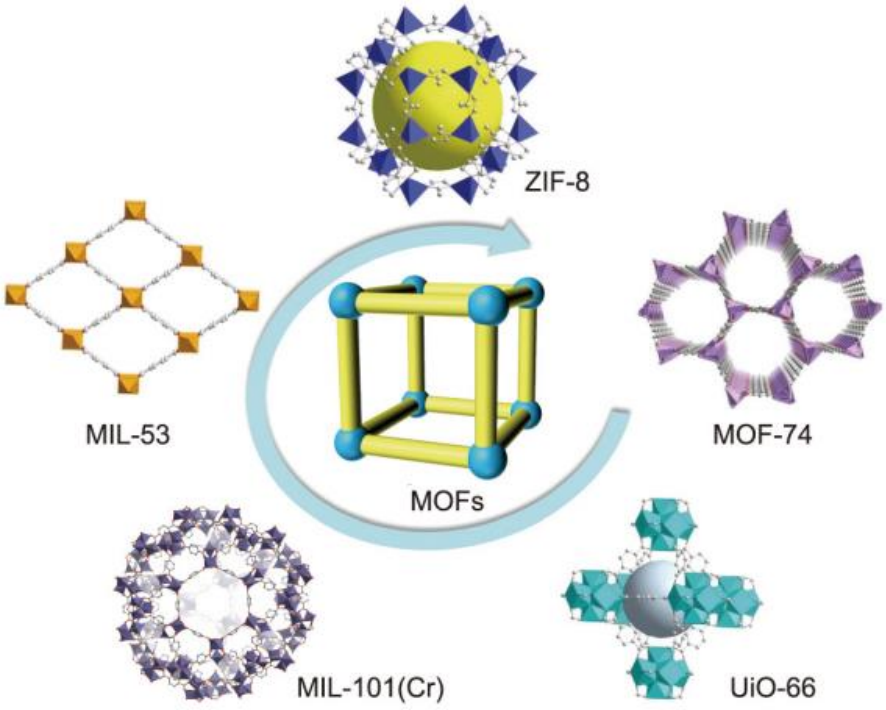

Figure 1.21 : Typical MOFs employed as fillers in MMMs [216].

UiO-66, composed of a terephthalic acid (BDC) linker, features octahedral and tetrahedral cavities, displaying remarkable stability in both aqueous solutions and various organic solvents [217]. Through the substitution of the linker with other BDC derivatives, researchers have successfully synthesized a series of UiO-66-type MOFs with diverse functional groups (e.g., -NH_2, -OH, -SO_3H) [218,219]. Marti et al. fabricated UiO-66/Matrimid MMMs using an in-situ MOF growth technique while simultaneously curing the polymer matrix. MMMs with MOF loadings of 2, 5, and 11 wt% were characterized and those with 11 wt% UiO-66 loading exhibited the most favorable gas separation performance, demonstrating CO_2 permeability and CO_2/N_2 selectivity values of 25 Barrer and 34, respectively [220]. Tahir et al. investigated sulfonic group functionalized UiO-66 grafted by silane coupling agent in polysulfone (PSf) to fabricate MMMs to prevent poor polymer-filler interaction and filler agglomeration for CO_2 capture. The results showed that increasing the sulfonic group concentration in UiO-66 led to higher selectivities due to their strong affinity towards CO_2 gas molecules. The permeabilities of UiO-66-SO_3H/PSf MMMs were slightly lower compared to UiO-66/PSf MMMs, due to the polymer rigidification caused by the increased filler concentration. At a filler loading of 30 wt% UiO-66-SO_3H, the CO_2 permeability was found as 19 Barrer, while CO_2/N_2 and CO_2/CH_4 selectivity were measured to be 53 and 48, respectively. With sulfonated functionalized UiO-66, the MMM exhibits a remarkable proximity to the Robeson upper bound, surpassing the performance of other MMMs [221]. Katayama et al. fabricated functionalized UiO-66 by covalently grafting it with polydimethylsiloxane (PDMS) to prepare PDMS-coated (termed here 'corona-MOF') defect-free MMMs. The UiO-66 particles were uniformly dispersed in the MMMs, exhibiting strong polymer-filler adhesion. Even at a high loading of 50 wt% corona-MOF particles, the MMMs achieved a CO_2 permeability of 4573 Barrer and a CO_2/N_2 selectivity of 10, thanks to the covalent linkages between the corona-MOF particles and the polymer matrix. Hence, the formation of covalent bonds between the MOF and the polymer matrix in corona-MOF MMMs significantly reduces particle aggregation during film curing, leading to a flexible, self-standing MMMs [222]. Wang et al. fabricated UiO-66-NH_2 fillers by grafting them with methoxysilane groups to prepare UiO-66-MS. These fillers were further incorporated into a silanol-terminated PDMS matrix, forming covalent crosslinks and leading to the formation of UiO-66-MS/PDMS MMMs. The solvent evaporation process effectively

prevented the aggregation and sedimentation of pristine MOF particles. Consequently, the resulting composites demonstrated good interfacial compatibility, even at high MOF loadings (60 wt%). The MMMs comprising 40 wt% UiO-66-MS particles exhibited excellent dispersion within the PDMS matrix, resulting in superior CO_2 permeability (2500 Barrer) and CO_2/N_2 selectivity (18) [223]. Thür et al. achieved a successful fabrication of Bipyridine (bpydc)-based UiO-67 incorporated in Matrimid 5218 for CO_2 capture applications, marking the first-time use of this composite. The excellent Lewis acid-base interaction between CO_2 and the bipyridine N sites in the MMM with 10 wt% UiO-67-33 resulted in a CO_2 permeability of 26 Barrer and a CO_2/CH_4 selectivity of 75. Despite experiencing interfacial defects at high filler loading (30 wt%), the MMMs still outperformed the pristine Matrimid membrane, demonstrating a 350% increase in CO_2 permeability without compromising selectivity [224].

On the other hand, MIL-series MOFs display fascinating properties, including flexibility, high surface area, and remarkable stability, opening up new possibilities when employed as fillers in MMM fabrication. For instance, MIL-53 is known for its "breathing" effect, wherein it undergoes a structural transformation from narrow pores to large pores when adsorbing guest molecules [225]. Fan et al. prepared nano-scale NH_2-MIL-53 (Al) fillers with Tröger's base (TB) polymer matrix to fabricate MMM membrane for CO_2/N_2 and CO_2/CH_4 separations. N-containing heterocyclic TB polymers demonstrate good interaction with NH_2-MIL-53 (Al), leading to the formation of transparent, robust, and plasticization-resistant hybrid membranes. These membranes exhibit the high CO_2 permeability of 187.6 Barrer, accompanied by CO_2/N_2 and CO_2/CH_4 selectivities of 21 and 20.2, respectively [226]. Loloei et al. produced flat-sheet membranes of MIL-53 (Al) and NH_2-MIL-53 (Al) on a 6FDA-ODA matrix using two different approaches for CO_2/CH_4 and CO_2/N_2 separations. In the first approach, the MOF was incorporated during the initial stages of the polyimide synthesis, with the 6FDA-ODA polymerization reaction occurring in the presence of the MOF. On the other hand, the second approach involved the traditional solution mixing technique for MMM preparation. In the first approach, improved particle distribution and reduced cluster agglomeration were observed, attributed to the H-bonding between the amine functionality of the MOF and the carbonyl group of the polymer at the MOF-polymer

interface. The best separation performance was achieved with 10 wt% NH_2-MIL-53, resulting in a 25% and 27% increase in CO_2/CH_4 mixed gas selectivity for the MMMs fabricated using the first and second techniques, respectively [227]. Lestari et al. fabricated MMMs by incorporating MIL-96(Al), which has a pore size at ~2.5-3.5 Å offering higher thermal stability, into polyethersulfone (PES) matrix using a conventional printing method combined with the wet phase inversion technique for CO_2 separation. The addition of 20% MIL-96(Al) resulted in the optimum selectivity of the membranes for the separation of CO_2/N_2 and CO_2/O_2 gases, showing increases of 155% and 86%, respectively [228]. Nuhnen et al. fabricated MMMs by incorporating MIL-101(Cr) fillers into a 6FDA-mPD matrix for CO_2/CH_4 separation. MIL-101(Cr) is known for its large pores, high surface area with a high pore volume of 1.32 $cm^3\ g^{-1}$. As a result, the CO_2 permeability of the 24 wt% MIL-101(Cr)@6FDA-mPD membrane increased from 10 (neat polymer) to 50 Barrer, while the CO_2/CH_4 selectivity increased from 54 to 89, respectively [229]. Suhaimi et al. fabricated MMMs by integrating NH_2-MIL-125(Ti) into a 6FDA-durene matrix for CO_2/CH_4 separation. Membrane loaded with 7.0 wt% of NH_2-MIL-125(Ti) in 6FDA-durene showed the highest CO_2 permeability of 1115.70 Barrer and CO_2/CH_4 selectivity of 37.10 due to the high porosity of nanofillers as well as the attraction of amine functional group towards CO_2 [230].

ZIFs as explained in the Chapter 1.3.2, are composed of transition metal cations (e.g. cobalt, zinc or indium) and neutral or organic linkers (e.g., methyl-/imidazolate), forming 3-D networks. By altering the anionic imidazolate linkers, a series of ZIFs with varying aperture sizes, including ZIF-8 (0.34 nm) and ZIF-90 (0.35 nm), have been synthesized and incorporated into polymeric matrices for MMM the fabrication of MMMs [231,232]. Tang et al. fabricated MMMs by integrating ZIF-8 into a PEBAX matrix for CO_2/N_2 separation while using dry-free processing method for the MOFs. Their study revealed that the dry-free processing method reduced the void volume at the interface between the MOF and the polymer, resulting in an improved gas separation efficiency for carbon dioxide and nitrogen. Hence, the 5 wt% ZIF-8@PEBAX membrane exhibited a CO_2 permeability of 195 Barrer, along with a CO_2/N_2 selectivity of 51.5 [233]. Kang et al. fabricated MMMs by dispersing solution-synthesized ZIF-8 nanoparticles into a rubbery amphiphilic copolymer matrix

known as poly(styrene-b-butadiene-b-styrene)-g-poly(oxyethylene methacrylate) (SBS-g-POEM) for CO_2/N_2 separation. The strong coordination interactions between Zn^{2+} ions of ZIF-8 and POEM, contributed to good interface contact and compatibility, effectively preventing interfacial defects. Such that, membrane loaded with 15% ZIF8/SBS-g-POEM demonstrated significant improvements in CO_2 permeability (increasing from 261.7 to 522.3 Barrer) and CO_2/N_2 selectivity (from 18.6 to 20.8) compared to the neat SBSg-POEM membrane. However, ZIF-8 loadings exceeding 30% had a negative impact on the separation performance of MMMs due to severe particle aggregation. This led to the formation of non-selective layers between the inorganic particles and a reduction in both CO_2 permeability and CO_2/N_2 selectivity [234]. On the other hand, Zhang et al. prepared MMMs for CO_2/N_2 separation by incorporating nickel (Ni)-substituted ZIF-8 into a polyether-block-amide (PEBA2533) polymer to achieve good interfacial compatibility between the Zn/Ni-ZIF-8 and PEBA. Due to the molecular sieving ability of ZIF-8, Zn/Ni-ZIF-8 exhibited a large surface area, micropore volume, high affinity, and adsorption capacity for CO_2. The MMM loaded with 10% Zn/Ni-ZIF-8 achieved optimum CO_2 permeability and selectivity of 408 Barrer and 51.8 at 5 bar, respectively. These results represent a significant increase of 60% and 64% compared to those of the pure PEBA membrane [235]. Gu et al. investigated CH_4/N_2 separation using ZIF-8@VR filler, which was synthesized with a high vacuum resistance sintering method (VRSM), incorporated into polyacrylic acid (PAA) to fabricate PAA/ZIF-8@VR MMMs. The MMMs showed good acid stability, good membrane-forming properties and excellent CH_4 adsorption capacity as well as high CH_4/N_2 separation performance. Hence, the 66.8 wt% ZIF-8@VR@PEBAX membrane exhibited a CH_4 permeance of ~1763 GPU along with a CO_2/N_2 selectivity of 3.1 [236]. Liu et al. fabricated MMMs by growing ZIF8 nanoparticles on one side of the PIM-1 membrane in methanol for O_2/N_2 separation properties. They showed that with the growth of ZIF-8 on the PIM-1 membrane, good thermal stability, a large surface area, and better adhesion could be achieved, resulting in enhanced O_2/N_2 separation performance. For instance, the PIM-1/ZIF-8-7 composite membrane showed an increase in diffusivity and solubility selectivity of O_2/N_2, resulting in an O_2/N_2 selectivity of 3.7 with an O_2 permeability of 1287 Barrer [237].

Gao et al. fabricated, three types of NH_2^-, OH^- and CH_3OH^- functionalized ZIF-7/PEBAX MMMs for CO_2 capture from flue gas, which mainly contains N_2. The CO_2 adsorption on each functionalized ZIF-7 was higher than that on unfunctionalized ZIF-7-based MMMs, demonstrating that the introduction of functional groups in the ZIF-7 framework was beneficial for CO_2 adsorption. The ZIF-7-OH-Pebax MMMs demonstrated the best performance for CO_2/N_2 separation among the three functionalized ZIF-7-based MMMs. The 14wt% ZIF-7-OH-Pebax MMM exhibited a high CO_2 permeability of 273 Barrer and a CO_2/N_2 separation factor of 38, which increased by 60% and 145%, respectively, compared to the unfunctionalized Pebax membrane [238]. Boroglu and Yumru prepared MMMs with various ZIF-11 percentages in the 6FDA-DAM matrix. They observed no agglomeration with different ZIF-11 percentages. The membrane loaded with 20.0 wt% of ZIF-11 in the 6FDA-DAM matrix at 30 ˚C and 4 bar exhibited H_2 and CO_2 permeabilities of 272 and 257 Barrer, respectively, while H_2/CO_2, H_2/CH_4, and CO_2/CH_4 selectivities were 1.06, 32.82, and 31.02, respectively [239]. Mubashir et al. prepared ZIF-62/CA MMMs to obtain high CO_2 permeation performance and CO_2 plasticization resistance. The composite membrane loaded with 8 wt% of ZIF-62 in CA exhibited the highest CO_2 permeability and CO_2/CH_4 ideal selectivity of 84.8 Barrer and 35.3, respectively. The mechanisms behind the materials stabilization and enhanced separation performance were attributed to the CO_2 affinity toward Zn^{2+} through electrostatic and π–π interactions, CO_2 adsorption on metal nodes, and the larger pore size [240].

Ye et al. synthesized nano-sized ZIF-67 and incorporated it into PIM-1 to fabricate a better compatible MMM without nonselective interfacial voids for biogas upgrading. The PIM-1/ZIF-S membranes with a 15 wt% loading of ZIF-S, showed H_2 and CO_2 permeabilities of 1500 and 2800 Barrier, and H_2/CH_4 and CO_2/CH_4 selectivities of 12, and 21, respectively [241]. Feng et al. successfully fabricated ZIF-67 into a Pebax matrix to obtain ZIF-67 NS/Pebax MMMs in an aqueous system. The exposed [211] crystal face exhibits higher stability due to a lower proportion of Co–N bond and higher surface atomic density. The MMM loaded with only 5.0% ZIF-67 NS achieved optimum CO_2 permeability and ideal selectivities of CO_2/N_2 and CO_2/CH_4, which were 139.4 Barrer, 73.2, and 17.6, respectively [242].

Van Essen et al. synthesized low aspect ratio and high aspect ratio ZIF-78 fillers and incorporated them into Matrimid with 10 and 20 wt% additive content for CO_2 and N_2 separation. ZIF-78, which possesses gmelinite (GME) topology, is constructed from nitrobenzimidazole (nbIm) and nitroimidazole (nIm) ligands. They showed that both low aspect and high aspect ZIF-78 MMMs exhibited similar sorption behavior, permeability, and selectivity. Thus, the aspect ratios were found to be insignificant to the gas separation performance, which contradicted previous observations in the literature [243]. Furthermore, Ilicak et al. prepared a series of defect-free membranes using the solution casting method with Matrimid®5218 and ZIF-95 for H_2/CH_4 and CO_2/CH_4 separation. The permeability and selectivity of CO_2, CH_4, and H_2 gases were found to increase with the increasing amount of ZIF-95 in the polymer matrix. The highest ideal separation factors for CO_2/CH_4 and H_2/CH_4 were 58.0 and 192.0, respectively, along with the corresponding selectivities of 58 and 192 [244]. Yuan et al. fabricated MMMs by incorporating ZIF-300 (composed of Zn, MeIm, and 5(6)-bromobenzimidazole (bbIm)) crystals into polyether block amide (PEBA) matrix for CO_2 capture. With a ZIF-300 loading of 30 wt%, the optimized ZIF-300-PEBA MMMs exhibited a high CO_2 permeability of 83 Barrer, along with a CO_2/N_2 selectivity of 84 [245]. Ghanem et al. prepared two types of MMMs: a dense MMM (ZIF-302/d-PI) and a spongy, self-consistent MMM (ZIF-302/s-PI), both without any asymmetry microvoids and exhibiting uniform disconnected pores. The spongy membrane demonstrated self-consistent and disconnected pores, leading to a reduction in overall membrane density and increased permeability for H_2, O_2, N_2, CO_2, and CH_4. On the other hand, ZIF-302/s-PI exhibited even better improvements in permeance with negligible effects on selectivity. Therefore, ZIF-302/s-PI exhibited ideal gas pair selectivities of 24.8 for CO_2/N_2, 42.3 for H_2/CH_4, and 62.6 for H_2/N_2 [246].

Datta et al. [22] fabricated $[Ni(AlF_5)(pyz)_2]_n$ (AlFFIVE-1-Ni) as known as KAUST-8 nanosheets based MMMs for $CO_2/H_2S/CH_4$ separation. They selected KAUST-8 for their research due to the size-sieving 1D channels and the [001] -oriented characteristics present in the AlFFIVE-1-Ni crystals. They explored AlFFIVE-1-Ni crystals in the 6FDA-DAM, 6FDA-DAT and 6FDA-DAM-DAT matrixes for $CO_2/H_2S/CH_4$ separation. Several MMMs exhibited experimentally observed enhancements in CO_2 permeability and CO_2/CH_4

selectivity compared to the pure (001)-AlFFIVE-1-Ni membrane. The presence of controllable pore apertures and distinctive pore functionalities provides MOFs with numerous selective transport nanochannels, thereby enabling the sorption and/or diffusion of gas molecules within the MMMs.

Table 1.3 summarizes the gas separation performance of MOF-based MMMs in recent studies.

Table 1.3 : Summary of the gas separation performance of MOFs-based MMMs.

MOF	Polymer	Gas Pair	Separation Performance	Ref
UiO-66	Matrimid	CO_2/N_2	$P_{CO_2} = 25\ Barrer$ $a_{CO_2/CH_4} = 34$	[220]
UiO-66	PSf	CO_2/N_2 CO_2/CH_4	$P_{CO_2} = 19\ Barrer$ $a_{CO_2/N_2} = 53\ a_{CO_2/CH_4} = 48$	[221]
UiO-66	PDMS	CO_2/N_2	$P_{CO_2} = 4573\ Barrer$ $a_{CO_2/N_2} = 10$	[222]
UiO-66-NH_2	PDMS	CO_2/N_2	$P_{CO_2} = 2500\ Barrer$ $a_{CO_2/N_2} = 18$	[223]
UiO-67-33	Matrimid	CO_2/CH_4	$P_{CO_2} = 26\ Barrer$ $a_{CO_2/CH_4} = 75$	[224]
NH_2-MIL-53	TB	CO_2/N_2 CO_2/CH_4	$P_{CO_2} = 187.6\ Barrer$ $a_{CO_2/N_2} = 21\ a_{CO_2/CH_4} = 20$	[226]
NH_2-MIL-53	6FDA-ODA	CO_2/N_2 CO_2/CH_4	$a_{CO_2/N_2} = 61.2\ a_{CO_2/CH_4} = 15$	[227]
NH_2-MIL-125(Ti)	6FDA-durene	CO_2/CH_4	$P_{CO_2} = 1115.7\ Barrer$ $a_{CO_2/CH_4} = 337.1$	[230]
MIL-96(Al)	PES	CO_2/N_2 CO_2/O_2	$P_{CO_2} = 25\ 531\ Barrer$ $a_{CO_2/N_2} = 1.6\ a_{CO_2/O_2} = 2.3$	[228]
MIL-101(Cr)	6FDA-mPD	CO_2/CH_4	$P_{CO_2} = 50\ Barrer$ $a_{CO_2/CH_4} = 89$	[229]

Table 1.3 (continued): Summary of the gas separation performance of MOFs-based MMMs.

MOF	Polymer	Gas Pair	Separation Performance	Ref
ZIF-8	PEBAX	CO_2/N_2	$P_{CO_2} = 195\ Barrer$ $a_{CO_2/N_2} = 52$	[233]
ZIF-8	SBS-g-POEM	CO_2/N_2	$P_{CO_2} = 522.3\ Barrer$ $a_{CO_2/N_2} = 20.8$	[234]
ZIF-8	PEBA2533	CO_2/N_2	$P_{CO_2} = 408\ Barrer$ $a_{CO_2/N_2} = 52$	[235]
ZIF-8	PAA	CH_4/N_2	$P_{CH_4} = 1763\ Barrer$ $a_{CO_2/CH_4} = 34$	[236]
ZIF-8-7	PIM-1	O_2/N_2	$P_{O_2} = 1287\ Barrer$ $a_{O_2/N_2} = 3.7$	[237]
ZIF-7-OH	Pebax	CO_2/N_2	$P_{CO_2} = 273\ Barrer$ $a_{CO_2/N_2} = 38$	[238]
ZIF-11	6FDA-DAM	H_2/CO_2 H_2/CH_4 CO_2/CH_4	$P_{H_2} = 272\ Barrer$ $P_{CO_2} = 257\ Barrer$ $a_{H_2/CO_2} = 1.06\ a_{H_2/CH_4} = 32.8$ $a_{CO_2/CH_4} = 31.02$	[239]
ZIF-62	CA	CO_2/CH_4	$P_{CO_2} = 84.8\ Barrer$ $a_{CO_2/CH_4} = 35.3$	[240]
ZIF-S (ZIF-67)	PIM-1	H_2/CH_4 CO_2/CH_4	$P_{H_2} = 1500\ Barrer$ $P_{CO_2} = 2800\ Barrer$ $a_{H_2/CO_2} = 12\ a_{H_2/CH_4} = 21$	[241]
ZIF-67	Pebax	CO_2/N_2 CO_2/CH_4	$P_{CO_2} = 139.4\ Barrer$ $a_{CO_2/N_2} = 73.2\ a_{CO_2/CH_4} = 17.6$	[242]

Table 1.3 (continued): Summary of the gas separation performance of MOFs-based MMMs.

MOF	Polymer	Gas Pair	Separation Performance	Ref
ZIF-71	6FDA-Durene	O_2/N_2	$P_{O_2} = 1713\ Barrer$ $a_{O_2/N_2} = 2.5$	[247]
ZIF-95	Matrimid 5218	H_2/CH_4 CO_2/CH_4	$P_{H_2} = 192\ Barrer$ $P_{CO_2} = 58\ Barrer$ $a_{CO_2/CH_4} = 58\ a_{H_2/CH_4} = 192$	[244]
ZIF-300	PEBA	CO_2/N_2	$P_{CO_2} = 83\ Barrer$ $a_{CO_2/N_2} = 84$	[245]
ZIF-302	s-PI	CO_2/N_2 H_2/CH_4 H_2/N_2	$P_{H_2} = 156\ Barrer$ $P_{CO_2} = 14\ Barrer$ $a_{CO_2/N_2} = 24.8\ a_{H_2/CH_4} = 42.3$ $a_{H_2/N_2} = 62.6$	[246]
Y-fum-fcu-MOF	6FDA-DAM	CO_2/CH_4	$P_{CO_2} = 1050\ Barrer$ $a_{CO_2/CH_4} = 136.4$	[248]
NUS-8	PIM-1	CO_2/CH_4	$P_{CO_2} = 6462\ Barrer$ $a_{CO_2/CH_4} = 29.8$	[249]
KAUST-7	6FDA-Durene	CO_2/CH_4	$P_{CO_2} = 1030\ Barrer$ $a_{CO_2/CH_4} = 33.2$	[250]
HKUST-1-IL	6FDA-Durene	CO_2/CH_4	$P_{CO_2} = 1101.6\ Barrer$ $a_{CO_2/CH_4} = 29.3$	[209]
Eu-naph-fcu-MOF	6FDA-DAM:DABA	CO_2/CH_4	$P_{CO_2} = 158.6\ Barrer$ $a_{CO_2/CH_4} = 46.6$	[251]
NbOFFIVE-1-Ni	6FDA-DAM	CO_2/CH_4	$P_{CO_2} = 547\ Barrer$ $a_{CO_2/CH_4} = 28.2$	[252]

Table 1.3 (continued): Summary of the gas separation performance of MOFs-based MMMs.

MOF	Polymer	Gas Pair	Separation Performance	Ref
AlFFIVE-1-Ni	6FDA-DAM	CO_2/CH_4	$P_{CO_2} = 599\ Barrer$ $a_{CO_2/CH_4} = 18.6$	[252]
MOF-74	PIM-1	CO_2/CH_4	$P_{CO_2} = 19000\ Barrer$ $a_{CO_2/CH_4} = 27.1$	[249]
JUC-62	Matrimid 5218	CO_2/CH_4	$P_{CO_2} = 30.5\ Barrer$ $a_{CO_2/CH_4} = 56.5$	[253]
$Cu_3(BTC)_2$	Matrimid 5218	CO_2/CH_4	$P_{CO_2} = 30.5\ Barrer$ $a_{CO_2/CH_4} = 56.5$	[254]
IRMOF-1	Matrimid 5218	CO_2/CH_4	$P_{CO_2} = 38.8\ Barrer$ $a_{CO_2/CH_4} = 29.2$	[255]
SAPO-34	Matrimid 5218	H_2/CH_4	$P_{CO_2} = 40.2\ Barrer$ $a_{H_2/CH_4} = 30$	[175]
MCM-41	PSf	H_2/CH_4	$P_{CO_2} = 24.5\ Barrer$ $a_{H_2/CH_4} = 30.6$	[256]
ETS-10	PSf	O_2/N_2	$P_{O_2} = 2.4\ Barrer$ $a_{O_2/N_2} = 4$	[257]

1.5.3 MOFs-based MMM for C2/C3 separation

Membranes with a C_3H_6/C_3H_8 selectivity higher than 10 and a C_3H_6 permeance of several hundred GPU are estimated to be competitive with distillation for C_3H_6/C_3H_8 separation in the industry. Some polymeric membranes can exhibit excellent C_3H_6/C_3H_8 separation performance with surpassing the upper bound during single gas tests which is explained in the previous sections. However, in mixed gas tests, C_3H_6 and C_3H_8 can easily dissolve in the

membrane, causing polymer chains to swell, leading to severe membrane plasticization and reduced selectivity. To address this issue, incorporating MOF fillers with favorable interactions with polymer chains can induce polymer chain rigidification at the filler surface, greatly enhancing the membrane's anti-plasticization performance [258]. Channel-based membranes and carrier-based membranes, have been widely investigated for propylene/propane and ethylene/ethane separation as shown in Figures 1.22 and 1.23.

Zhang et al (2012) indicated that ZIF-8 is a desired candidate as a filler for propylene/propane separation due to its effective pore aperture size is in the range of 4–4.2 Å. In their study, they incorporated 200 nm ZIF-8 nanocrystals into a 6FDA-based polymer, achieving a strong adhesion between the MOF and filler without requiring any surface-treatment of ZIF-8. They demonstrated that incorporating 48% of ZIF-8 into the 6FDA-DAM polymer resulted in a 258% increase in permeability and a 150% increase in selectivity. The MMM showed a C_3H_6 permeability of 56.2 Barrer and a C_3H_6/C_3H_8 ideal selectivity of 31.0 [211]. Liu et al. investigated MMMs by dispersing SAPO-34 particles with a pore size of 0.38 nm and ZIF-8 particles with an aperture size of 0.34 nm into 6FDA-mDAT and 6FDA-TrMPD matrices for CO_2 and CH_4 separation. The 6FDA-mDAT MMM with 40 wt% SAPO-34 zeolite exhibited a CO_2 permeability of 190 Barrer and a CO_2/CH_4 ideal selectivity of 60. On the other hand, the 6FDA-TrMPD based MMMs containing 20 wt% ZIF-8 showed a C_3H_6 permeability of 24 Barrer and a C_3H_6/C_3H_8 ideal selectivity of 17 [259]. Askari and Chung investigated the fabrication of MMMs with uniform morphology by incorporating ZIF-8 fillers into three 6FDA-based polyimides: 6FDA-Durene, 6FDA-Durene/DABA (9/1), and 6FDA-Durene/DABA (7/3). Among these, the MMM composed of 6FDA-Durene/DABA (9/1) and 40 wt % ZIF-8 showed a significant improvement in the ideal C_3H_6/C_3H_8 selectivity, increasing by 134% from 11.68 to 27.38. Additionally, the C_3H_6 permeability value for this MMM was measured at 47.3 Barrer [260].

Kwon et al. noticed a significant improvement in C_3H_6/C_3H_8 separation performance by heteroepitaxially growing ZIF-67 on ZIF-8 seed layers. They suggested that ZIF-67 might be intrinsically more efficient than ZIF-8 for C_3H_6/C_3H_8 separation due to the stiffer Co-N bond as compared to the Zn-N bond in ZIF-8. As a result, the membranes exhibited unprecedentedly high propylene/propane separation factors of ~200, possibly due to the

enhanced grain boundary structure [261]. Krokidas et al. further validated the higher efficiency of ZIF-67 for C_3H_6/C_3H_8 separation using their newly developed force fields and subsequent molecular dynamics simulations [262]. An et al. investigated the impact of ZIF-67 in MMMs for C_3H_6/C_3H_8 separations by successfully integrating them into 6FDA-DAM polymer matrix with excellent dispersion and good adhesion to the polymer matrix. The 6FDA-DAM/ZIF-67 MMMs with a weight ratio of 80/20 exhibited an ideal selectivity of 29.9 and a separation factor of 19 under both single gas and equimolar mixed gas conditions, at a temperature of 35 °C. The intrinsic C_3H_6/C_3H_8 separation performance of ZIF-67 was evaluated using the Maxwell model, revealing its superior C_3H_6/C_3H_8 selectivity of 251, which is twice that of ZIF-8, confirming the exceptional molecular sieving capacity of ZIF-67 in MMMs. Moreover, besides ZIF-67 containing MMMs exhibited excellent separation performance, the membranes displayed significantly improved physical aging resistance, which can be attributed to the buttress role of ZIF-67 between polymer chains within the large free volume elements [263]. Moghadam et al. successfully fabricated thermally annealed 6FDA-DAM-based MMMs containing 2D ZIF-67 decorated on the porous graphene oxide nanosheets exhibiting C_3H_6/C_3H_8 transport properties. By embedding a 20 wt% ZPGO67 filler in the polyimide matrix, they achieved an increase in C_3H_6 permeability from 19.5 Barrer to 58.8 Barrer at 2 bar and 35 °C while maintaining good plasticization resistance [100].

ZIF-71 is a rhombic MOF with an aperture size of 4.2 Å and a pore cavity of 16.5 Å. It contains zinc (II) as the metal center and 4, 5-dichloroimidazole as the organic linker. Its large pore cavity and aperture size, along with an aperture size between the kinetic diameters of propylene and propane, make ZIF-71 a promising candidate for incorporation into MMMs to enhance gas separation via the molecular sieving effect. Japip et al. conducted a study and found that MMMs with 20 wt% ZIF-71 exhibited a remarkable increase in C_3H_6 permeability from 57.6 Barrer to 371 Barrer. Interestingly, this enhancement in permeability did not significantly compromise the ideal C_3H_6/C_3H_8 selectivity, indicating the potential of ZIF-71-based MMMs for efficient C_3H_6/C_3H_8 separation [247].

Knebel and co-workers, worked with stable dispersions of 1,3-bis(2,4,6-diisopropylphenyl)imidazole-2-ylidene) (IDip) functionalized ZIF-67 (ZIF-67-IDip) blended

6FDA-DAM and newly developed copolymer 6FDA-DHTM-Durene to investigate the C_3H_6/C_3H_8 separation. Using ZIF-67-IDip with filler loadings up to 47.5 wt.% in 6FDA-DAM polymer while maintaining excellent physical resistance have been achieved with no agglomeration or sedimentation of ZIF-67-IDip nanocrystals throughout the membranes. The results showed that, compared to 6FDA-DAM, 6FDA-DHTM-Durene displayed a higher C_3H_6/C_3H_8 selectivity. Incorporation of ZIF-67 or ZIF-67-IDip in the polymer significantly increases C_3H_6 adsorption, but barely increases C_3H_8 adsorption compared to the pure polymer. Moreover, the separation performance of ZIF-67/6FDA-DAM and ZIF-67-IDip/6FDA-DAM membranes were evaluated in the separation of C_3H_6/C_3H_8 mixtures at 35 °C. In good agreement with the literature both C_3H_6 permeability and C_3H_6/C_3H_8 selectivity increase gradually upon increasing filler loading. Compared to ZIF-67/6FDA-DAM, ZIF-67-IDip/6FDA-DAM membranes exhibit a much better compatibility and denser arrangement between ZIF-67-IDip nanoparticles and polymer, and a homogeneous filler dispersion throughout the composite, which in the end for mixed gas mixtures enhancements in C_3H_6/C_3H_8 selectivity and C_3H_6 permeability were observed [203]. Further, Cheng et al. worked with IDip functionalized KAUST-7 (NbOFFIVE-1-Ni) fillers into 6FDA-DAM to investigate the C_3H_6/C_3H_8 separation. KAUST-7, which forms through coordination bonds involving Ni^{2+} cations, $(NbOF_5)^{2-}$ polyatomic anions, and pyrazine molecules, exhibits slender 1D channels featuring a window diameter of ~3.22 Å is a promising molecular sieve filler in MMMs, enabling the selective diffusion and/or transport of C_3H_6 over C_3H_8. At a high filler loading of 45 wt.%, KAUST-7-IDip-based MMMs exhibit remarkable performance with ~95 Barrer in C_3H_6 permeability and selectivity of C_3H_6/C_3H_8 selectivity of ~20, along with maintaining minimal nonselective defects at the interfaces between the polymer and filler [169].

Liu et al. conducted a study to explore MMMs by integrating Zr-fum-fcu-MOFs with trefoil-like pores into the 6FDA-DAM matrix to enhance the membrane's C_3H_6/C_3H_8 selectivity through a conformation-controlled molecular sieving effect. Their findings showed that MMMs with a 29 vol% Zr-fum-fcu-MOF loading exhibited a significant 73% increase in C_3H_6/C_3H_8 selectivity and an 8% increase in C_3H_6 permeability compared to the pure polymeric membrane. Moreover, Zr-fum-fcu-MOF exhibited a remarkable C_3H_6/C_3H_8

diffusivity selectivity of up to 1086, confirming its ability to effectively separate C_3H_6/C_3H_8 through the conformation-controlled molecular sieving effect. Plasticization was observed in MMMs when the testing pressure was increased to 483 kPa at 35°C. However, an increase in the testing temperature from 35°C to 55°C resulted in an improvement in the membrane's anti-plasticization ability [264].

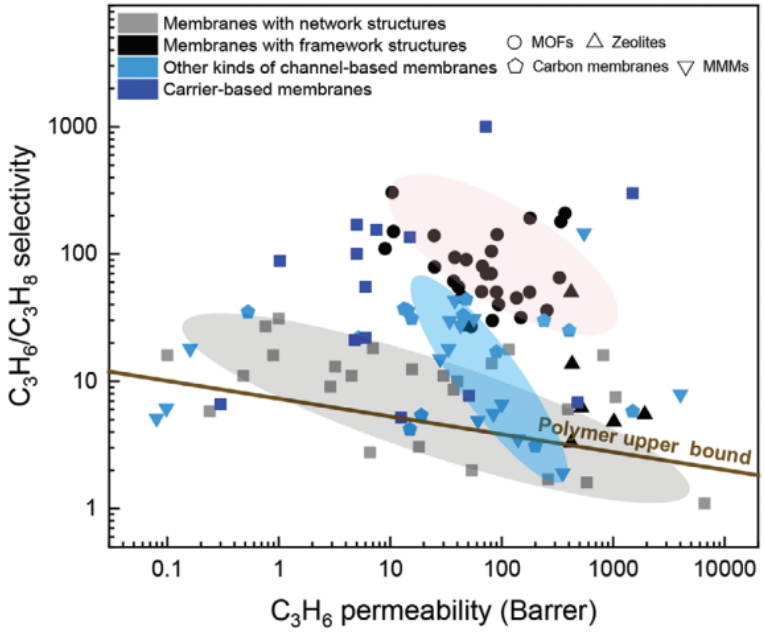

Figure 1.22 : Propylene/propane separation performance of channel-based and carrier-based membranes. The grey, light pink and light blue oval areas highlight the separation performance of membranes with network structures, membranes with framework structures, and other kinds of channel-based membranes, respectively [26].

Ploegmakers et al. successfully incorporated Cu_3BTC_2 particles into P84 for efficient ethylene/ethane separation. The material exhibited preferred dissolution of olefin over paraffin, thanks to the interaction between the exposed Cu(II) metal sites and the olefin. The resultant MMMs with a 20 wt% loading of Cu_3BTC_2, the separation factor was increased by 73% with similar permeability results [11]. Chen et al. achieved successful incorporation of M-gallate (M = Ni, Co, Mg) MOF particles into 6FDA-based polyimides for the first time and investigated their performance for C_2H_4/C_2H_6 separation. In comparison to the autoclave synthesis, which produced Ni-gallate particles of ≈7 μm in size, the flask synthesis method successfully reduced the particle size to ≈0.8 μm, facilitating the formation of uniform MMMs. Among all the M-gallate MMMs, Ni-gallate demonstrated the best compatibility

with the polymer primarily due to its restricted pore aperture, which allowed selective passage of C_2H_4 through molecular sieving. As a result, the MMMs with 20 wt% Ni-gallate demonstrated the best separation performance, with a C_2H_4/C_2H_6 selectivity of 3.5 and a C_2H_4 permeability of 90 Barrer [265].

Bachman et al. [266] fabricated MOFs with different metal ions (Mg, Mn, Co, Ni) within a 6FDA-DAM matrix for C_2H_4/C_2H_6 separation, while enhancing the membrane resistance to plasticization. Permeation studies with individual gases indicated that introducing MOF-74 series of MOF fillers into the 6FDA-DAM matrix significantly enhances the membrane performance for C_2H_4/C_2H_6 separation. Additionally, when considering the separation of the C_2H_4/C_2H_6 equimolar mixture, the pristine 6FDA-DAM membrane exhibited a plasticization pressure of ~ 10 bar, whereas MMMs containing MOF-74-Ni with a 25 wt% filler loading, exhibited a plasticization pressure exceeding 20 bar.

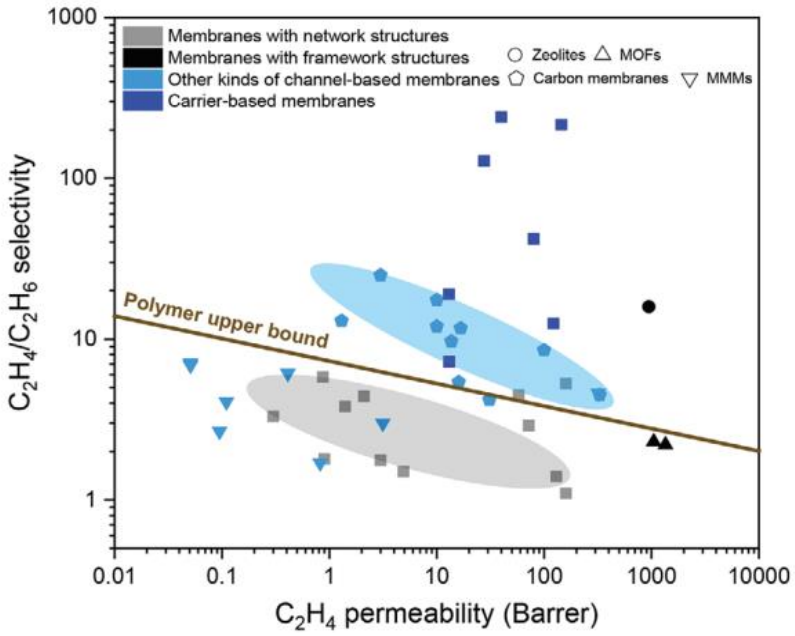

Figure 1.23 : Ethylene/ethane separation performance of channel-based and carrier-based membranes. The grey and light blue oval areas highlight the separation performance of membranes with network structures and other kinds of channel-based membranes, respectively [26].

Feng et al. prepared modified phosphomolybdenum heteropoly acid (PMA)@MIL-101/PIM-1 and MIL-101-SO_3Ag/PIM-1 composites. They achieved this by loading PMA guest molecules into MIL-101(Cr) and regulating the pore environment of MOF crystalline porous

fillers through the introduction of PMA and Ag(I), both of which exhibit strong interactions with olefins. As a result, the C_2H_4/C_2H_6 selectivity was increased to 2.88 (by 14%) and 3.47 (by 127%) for MIL-101/PIM-1 and MIL-101-SO_3Ag/PIM1, respectively. Moreover, the C_3H_6/C_3H_8 selectivity was enhanced by 46% (to 5.96) and 63% (to 3.89), respectively [267].

Table 1.4 summarizes the gas separation performance of MOF-based MMMs in recent studies for C2/C3 separation.

Table 1.4 : Summary of the gas separation performance of MOFs-based MMMs for C2/C3 separation.

MOF	Polymer	Gas Pair	Separation Performance	Ref
ZIF-8	6FDA-DAM	C_3H_6/C_3H_8	$P_{C_3H_6} = 56.2\ Barrer$ $a_{C_3H_6/C_3H_8} = 31$	[211]
ZIF-8	6FDA-TrMPD	C_3H_6/C_3H_8	$P_{C_3H_6} = 24\ Barrer$ $a_{C_3H_6/C_3H_8} = 17$	[259]
ZIF-8	6FDA-Durene/DABA	C_3H_6/C_3H_8	$P_{C_3H_6} = 47.3\ Barrer$ $a_{C_3H_6/C_3H_8} = 27.38$	[260]
ZIF-67	6FDA-DAM	C_3H_6/C_3H_8	$P_{C_3H_6} = 29.9\ Barrer$ $a_{C_3H_6/C_3H_8} = 19$	[263]
ZPGO67	6FDA-DAM	C_3H_6/C_3H_8	$P_{C_3H_6} = 18.2\ Barrer$ $a_{C_3H_6/C_3H_8} = 11.3$	[268]
ZIF-71	6FDA-DAM	C_3H_6/C_3H_8	$P_{C_3H_6} = 371\ Barrer$ $a_{C_3H_6/C_3H_8} = 8.38$	[247]
NbOFFIVE-1-Ni	6FDA-DAM	C_3H_6/C_3H_8	$P_{C_3H_6} = 95\ Barrer$ $a_{C_3H_6/C_3H_8} = 20$	[169]
Zr-fum-fcu-MOF	6FDA-DAM	C_3H_6/C_3H_8	$P_{C_3H_6} = 40\ Barrer$ $a_{C_3H_6/C_3H_8} = 1130$	[264]
Cu_3BTC_2	P84	C_3H_6/C_3H_8	$P_{C_2H_4} = 90\ Barrer$ $a_{C_2H_4/C_2H_6} = 3.5$	[11]
Ni-gallate	6FDA-DAM	C_2H_4/C_2H_6	$P_{C_2H_4} = 60\ Barrer$ $a_{C_2H_4/C_2H_6} = 2.5$	[265]
Ni-gallate	6FDA-DAM:DABA	C_2H_4/C_2H_6	$P_{C_2H_4} = 7\ Barrer$ $a_{C_2H_4/C_2H_6} = 4$	[265]
MIL-101/PIM-1	PIM-1	C_2H_4/C_2H_6 C_3H_6/C_3H_8	$a_{C_2H_4/C_2H_6} = 2.88$ $a_{C_3H_6/C_3H_8} = 5.96$	[267]
MIL-101-SO_3Ag	PIM-1	C_2H_4/C_2H_6 C_3H_6/C_3H_8	$a_{C_2H_4/C_2H_6} = 3.47$ $a_{C_3H_6/C_3H_8} = 3.89$	[267]

1.5.4 Macroscopic Models of MOFs-based MMMs

Designing MOFs-based MMMs present a significant challenge due to the vast selection of MOFs that can potentially use as fillers in polymer membranes. While the wide range and diversity of available materials offer a promising opportunity for choosing the appropriate MOF/polymer combinations for MMM fabrications, it is impractical to experimentally test all potential combinations of MOF/polymer MMMs. Therefore, computational studies that capable of predicting the selectivity and permeability of MOFs-based MMMs become instrumental in efficiently screening numerous MOFs before conducting experiments. Thus, this approach allows for a focused allocation of experimental efforts, resources and time toward the most promising MOF/polymer combination [269].

Most of the computational works reported so far for predicting the gas separation performances of MOF/polymer MMMs relies on the use of theoretical permeation model. This approach utilizes simulated gas permeability data for pure MOFs due to the lack of experimental information in the literature and integrates this data with experimental gas permeability values for polymers to anticipate the permeability of gases of MOF/polymer MMMs.

In 2010, Keskin and Sholl conducted an investigation into the pure gas permeation of CO_2, CH_4, H_2, and N_2 in MOF/Matrimid composite membranes utilizing two mathematical models such as Maxwell and Bruggeman which considers the ideal morphology of the mixed matrix membranes. The study, which involved six different MOFs, used simulated gas loadings and diffusivities for the MOFs. The results indicated the potential of this numerical simulation approach in identifying MMMs with exceptional properties for CO_2/CH_4 separations, which correlated with experimental data [271]. Subsequently, several research groups have investigated the separation of various gas pairs within numerous MOF/polymer MMMs. Hence, the development of high-throughput computational screening (HTCS) methods have enabled numerous MOFs customized for specific applications in a time-efficient manner, while enabling the identification of the most promising materials and guiding subsequent experimental endeavors [272]. Daglar et al. [277] employed GCMC and MD simulations along with the Maxwell model to calculate the permeability of CO_2, CH_4, O_2, N_2, H_2, and He gases, examining over 180,000 MOF/polymer MMMs to explore 11 distinct gas separation

scenarios at 1 bar and 298 K. It was shown that the incorporation of MOFs into different polymers could enhance gas permeabilities, this enhancement can be attributed to the highly permeable nature of largely porous MOF structures. Budhathoki et al. [274] conducted HTCS method to compute CO_2 permeabilities and CO_2/N_2 selectivities of 11 different MOF-based MMMs, employing the Maxwell Model and experimentally derived polymer properties. Their computational methodology was validated by the good agreement between the predicted and experimentally published gas permeabilities. It is essential to highlight that in HTCS studies, gas permeabilities of MOFs were predicted and subsequently combined with experimental polymer data using macroscopic permeation models, as discussed earlier, to predict the gas separation performance of MOF-based MMMs. However, HTCS studies such as using Maxwell models assume ideal morphology, with the assumption of perfect adhesion between the MOF filler and polymer matrix and neglecting the MOF/polymer interfacial study. For instance, not taking into account the polymer rigidity along with the compatibility between the MOF and the polymer could lead to irregularities at the MOF/polymer interface, potentially impacting the porous structure of the MMM and consequently affecting its separation performance [275].

While macroscopic models offer advantages such as analytical simplicity and the need for only a small number of input parameters, they tend to overlook the true complexity of molecular-level processes. Consequently, when an analytical macroscopic model diverges from experimental results, it offers limited insights into the underlying reasons for the discrepancy. In such cases, one can only conclude the model's invalidity for that scenario and seek alternatives. This underscores the necessity to develop computational models that accurately capture the structural complexity of MMMs, serving as a strong incentive for further research in this direction, with a particular focus on a comprehensive atomistic view [276].

1.5.5 Atomistic Models of MOFs-based MMMs

In this computational modeling approach for MOF/polymer MMMs, fully atomistic simulations are employed, integrating both MOF and polymer phases. Through this alternative approach, atomistic simulations offer insights into the MOF/polymer interface

interactions that govern the feasibility and stability of MOF/polymer MMMs. However, there is a limited number of computational studies on this topic [270]. Jiang's group [281] reported a pioneering fully atomistic simulation study, where both the MOF and polymer phases, specifically ZIF-7 and polybenzimidazole (PBI), were simulated at the atomistic level, to investigate H_2/CO_2 separation in the resulting MMMs. A newly developed force field was employed to model ZIF-7, while the polymer-consistent force field (PCFF) was utilized to mimic PBI in the computational study. The predicted glass transition temperature and density of PBI were found to be reasonably consistent with experimental measurements. Simulation results indicate that PBI/ZIF-7 membranes exhibit higher permeabilities for both H_2 and CO_2 compared to pristine PBI. Semino et al. [278] developed the first microscopic model for interactions between PIM-1 and ZIF-8. They employed a computational method that combines the density functional theory (DFT) calculations with force field-based MD simulations to study ZIF-8/PIM-1. Surface structures of ZIF-8 were constructed and geometry-optimized via DFT calculations, while polymer structures were constructed at the atomic level. This was followed by the utilization of force field-based MD simulations to generate robust models for the MOF/polymer interface. They demonstrated that polymer led to the formation of interfacial micro-voids at the vicinity of the MOF surface. Moreover, it was observed that the properties of the MOF/interface were minimally impacted by both the flexibility of the MOF surface and the polymer polydispersity [278]. This modelling approach has been applied to many future works to analyze MOF-polymer interface, in various MMMs featuring a diverse array of MOFs and polymers. However, it is crucial to highlight the necessity for a force field that accurately represents the MMM for successful application of this methodology to other MOF/polymer MMMs. Further, the same group [279] investigated the ZIF-8/PIM-1 compatibility in the presence of MOF surface defects via DFT calculations and force field-based MD simulations. Their computational findings illustrated that the presence of defects leads to variations in MOF/polymer interactions, although the microscopic morphology of the interfacial microvoids remained consistent. This discovery suggests that the structure of the MOF/polymer interface is primarily determined by properties like geometry and flexibility, with chemical interactions playing a relatively minor role [279]. Ozcan et al. investigated ZIF-8/PIM-1 composites via a concentration gradient-driven molecular dynamics (CGD-MD) simulations for H_2/CH_4 separation. The

results revealed that the H_2/CH_4 selectivity of ZIF-8/PIM-1 composite is lower (4.6) compared to the pure ZIF-8 (5.1) and PIM-1 (6.3) selectivities due to the presence of interfacial voids at the interface. Further, Fan et al. [281] conducted a study to investigate how the MOF/polymer interface affects the separation performance of NUS-8/PIM-1 MMM in CO_2/N_2 and CO_2/CH_4 separations. They employed molecular simulation techniques, including force field-based Monte Carlo (MC), as well as equilibrium and non-equilibrium molecular dynamics simulations (EMD and NEMD). The analysis of the interfacial study between NUS-8 and PIM-1 revealed the presence of newly identified microvoid porosities. NEMD simulations yielded permeabilities and selectivities that closely matched experimental values. The similarity between the CO_2/N_2 selectivity of the MMM and that of the polymer indicates that not all interfacial voids negatively impact selectivity. Balcik et al. [286] carried out an atomistic study on Matrimid 5218/ZIF-8 MMM to comprehend the interfacial dynamics, under high-pressure CO_2 exposure, aiming to study the plasticization effects. Performing atomistic CO_2 sorption simulations up to 30 bar enabled the analysis of the impact of CO_2 exposure on polymer chain dynamics, structural alterations at the interface, and interactions between MOF and polymer. An examination of the impact of CO_2 sorption on the interface revealed that, up to 10 bar CO_2 pressure, the interface showed no notable effect on sorption behavior, while it became the predominant sorption site at higher pressures. Recently, Dutta and Bhatia [287] investigated the interfacial properties of ZIF-8/6FDA-durene-PI MMMs for CO_2/CH_4 separation using a combined GCMC and EMD approach. To improve the interface compatibility between ZIF-8 and the polyimide, an IL was employed to fill the larger voids in the interface between ZIF-8 and 6FDA-durene-PI polymer. By incorporating the IL, the CO_2/CH_4 membrane selectivity MMM increased without a significant alteration in its permeability. The previous studies suggest that there is significant potential for computational methods to uncover how the properties of MOFs impact the compatibility at the MOF/polymer MMM interface and, in turn, influence the separation performance. Although atomically detailed simulations yield high-fidelity results, they come at the cost of being computationally expensive. Though there is a scarcity of computational studies examining the atomic-level compatibility of MOF/polymer interactions, further exploration in this area holds significant potential of designing high-performing membranes [284,285].

In this literature review, the focus is on highlighting the potential advantages of incorporating a molecular sieving MOF into a MOF/polymer composite for C2/C3 separation. Such integration has the potential to enhance the various properties of MOFs, including their gas adsorption and separation capabilities, by tailoring the interfacial interactions between MOF fillers and the polymer matrix. Therefore, as presented in Chapters 4, 5, and 6, the research has been driven by the goal of obtaining a microscopic understanding of the compatibility between the two components and understanding the separation mechanisms involved in C2/C3 separation. This involves a comprehensive analysis of the interactions between MOFs, including ZIF-67 in its pristine and functionalized forms, UTSA-280 in the future direction of this work, and three distinct polymers: 6FDA-DAM, 6FDA-DABA, and PIM-1, with the aim of acquiring fundamental insights into these composites at the atomistic level. Given the limited number of computational studies that focusing on C2/C3 separation at the microscopic level, it is believed that the atomistic insights obtained through this work can provide valuable guidance for experimental endeavors. This guidance extends to the selection of MOF/polymer combinations to create highly efficient MMMs, not only for hydrocarbon separation but also for a broad range of mixtures.

REFERENCES

[1] R. Faiz, K. Li, Polymeric membranes for light olefin/paraffin separation, Desalination. 287 (2012) 82–97. https://doi.org/10.1016/j.desal.2011.11.019.

[2] S. Najari, S. Saeidi, F. Gallucci, E. Drioli, Mixed matrix membranes for hydrocarbons separation and recovery: A critical review, Rev. Chem. Eng. 37 (2019) 363–406. https://doi.org/10.1515/revce-2018-0091.

[3] D. Saha, B. Toof, R. Krishna, G. Orkoulas, P. Gismondi, R. Thorpe, M.L. Comroe, Separation of ethane-ethylene and propane-propylene by Ag(I) doped and sulfurized microporous carbon, Microporous Mesoporous Mater. 299 (2020) 110099. https://doi.org/10.1016/j.micromeso.2020.110099.

[4] J.A. Moulijn, M. Makkee, A. van Diepen, Chemical Process Technology, 2nd ed., John Wiley & Sons, Chichester,England, 2001.

[5] Y. Wang, S.B. Peh, D. Zhao, Alternatives to Cryogenic Distillation: Advanced Porous Materials in Adsorptive Light Olefin/Paraffin Separations, Small. 15 (2019) 1–38. https://doi.org/10.1002/smll.201900058.

[6] R. Lin, L. Ge, H. Diao, V. Rudolph, Z. Zhu, Propylene/propane selective mixed matrix membranes with grape-branched MOF/CNT filler, J. Mater. Chem. A. 4 (2016) 6084–6090. https://doi.org/10.1039/c5ta10553f.

[7] M. Guo, M. Kanezashi, Recent progress in a Membrane-Based Technique for propylene/propane Separation, Membranes (Basel). 11 (2021) 310. https://doi.org/10.3390/membranes11050310.

[8] C.H. Park, J.H. Lee, J.P. Jung, J.H. Kim, Mixed matrix membranes based on dual-functional MgO nanosheets for olefin/paraffin separation, J. Memb. Sci. 533 (2017) 48–56. https://doi.org/10.1016/j.memsci.2017.03.023.

[9] D.S. Sholl, R.P. Lively, Seven chemical separations, Nature. 532 (2016) 435–437.

[10] M. Etxeberria-Benavides, O. David, T. Johnson, M.M. Łozińska, A. Orsi, P.A. Wright, S. Mastel, R. Hillenbrand, F. Kapteijn, J. Gascon, High performance mixed matrix membranes (MMMs) composed of ZIF-94 filler and 6FDA-DAM polymer, J. Memb. Sci. 550 (2018) 198–207. https://doi.org/10.1016/j.memsci.2017.12.033.

[11] J. Ploegmakers, S. Japip, K. Nijmeijer, Mixed matrix membranes containing MOFs for ethylene/ethane separation Part A: Membrane preparation and characterization, J. Memb. Sci. 428 (2013) 445–453. https://doi.org/10.1016/j.memsci.2012.11.014.

[12] L.M. Robeson, The upper bound revisited, J. Memb. Sci. 320 (2008) 390–400. https://doi.org/10.1016/j.memsci.2008.04.030.

[13] D. Liu, L. Xiang, H. Chang, K. Chen, C. Wang, Y. Pan, Y. Li, Z. Jiang, Rational matching between MOFs and polymers in mixed matrix membranes for propylene/propane separation, Chem. Eng. Sci. 204 (2019) 151–160. https://doi.org/10.1016/j.ces.2019.04.032.

[14] B. Zornoza, C. Tellez, J. Coronas, O. Esekhile, W.J. Koros, Mixed Matrix Membranes Based on 6FDA Polyimide with Silica and Zeolite Microsphere Dispersed Phases, AIChE J. 59 (2012) 215–228. https://doi.org/10.1002/aic.

[15] C. Klaysom, S. Shahid, Zeolite-based mixed matrix membranes for hazardous gas removal, Elsevier Inc., 2018. https://doi.org/10.1016/B978-0-12-814503-6.00006-9.

[16] T.S. Chung, L.Y. Jiang, Y. Li, S. Kulprathipanja, Mixed matrix membranes (MMMs) comprising organic polymers with dispersed inorganic fillers for gas separation, Prog. Polym. Sci. 32 (2007) 483–507. https://doi.org/10.1016/j.progpolymsci.2007.01.008.

[17] R. Surya Murali, A.F. Ismail, M.A. Rahman, S. Sridhar, Mixed matrix membranes of Pebax-1657 loaded with 4A zeolite for gaseous separations, Sep. Purif. Technol. 129 (2014) 1–8. https://doi.org/10.1016/j.seppur.2014.03.017.

[18] B. Zornoza, B. Seoane, J.M. Zamaro, C. Téllez, J. Coronas, Combination of MOFs and zeolites for mixed-matrix membranes, ChemPhysChem. 12 (2011) 2781–2785. https://doi.org/10.1002/cphc.201100583.

[19] T. Rodenas, I. Luz, G. Prieto, B. Seoane, H. Miro, A. Corma, F. Kapteijn, F.X. Llabrés I Xamena, J. Gascon, Metal-organic framework nanosheets in polymer composite materials for gas separation, Nat. Mater. 14 (2015) 48–55. https://doi.org/10.1038/nmat4113.

[20] J. Dechnik, J. Gascon, C.J. Doonan, C. Janiak, C.J. Sumby, Mixed-Matrix Membranes, Angew. Chemie - Int. Ed. 56 (2017) 9292–9310. https://doi.org/10.1002/anie.201701109.

[21] R. Adams, C. Carson, J. Ward, R. Tannenbaum, W. Koros, Metal organic framework mixed matrix membranes for gas separations, Microporous Mesoporous Mater. 131 (2010) 13–20. https://doi.org/10.1016/j.micromeso.2009.11.035.

[22] S.J. Datta, A. Mayoral, N. Murthy, S. Bettahalli, P.M. Bhatt, Rational design of mixed-matrix metal-organic framework membranes for molecular separations, 1087 (2022) 1080–1087.

[23] R. Wei, X. Liu, Z. Lai, MOF or COF membranes for olefin/paraffin separation: Current status and future research directions, Adv. Membr. 2 (2022). https://doi.org/10.1016/j.advmem.2022.100035.

[24] Y. Ren, X. Liang, H. Dou, C. Ye, Z. Guo, J. Wang, Y. Pan, H. Wu, M.D. Guiver, Z. Jiang, Membrane-Based Olefin/Paraffin Separations, Adv. Sci. 7 (2020) 1–29. https://doi.org/10.1002/advs.202001398.

[25] H. An, S. Park, H.T. Kwon, H.K. Jeong, J.S. Lee, A new superior competitor for exceptional propylene/propane separations: ZIF-67 containing mixed matrix membranes, J. Memb. Sci. 526 (2017) 367–376. https://doi.org/10.1016/j.memsci.2016.12.053.

[26] Y. Ren, X. Liang, H. Dou, C. Ye, Z. Guo, J. Wang, Y. Pan, H. Wu, M.D. Guiver, Z. Jiang, Membrane-Based Olefin / Paraffin Separations, 2001398 (2020) 1–29. https://doi.org/10.1002/advs.202001398.

[27] R. Faiz, K. Li, Olefin/paraffin separation using membrane based facilitated transport/chemical absorption techniques, Chem. Eng. Sci. 73 (2012) 261–284. https://doi.org/10.1016/j.ces.2012.01.037.

[28] D.J. Safarik, R.B. Eldridge, Olefin/paraffin separations by reactive absorption: a review, Ind. Eng. Chem. Res. 37 (1998) 2571–2581. https://doi.org/10.1021/ie970897h.

[29] R.B. Eldridge, Olefin/Paraffin Separation Technology: A Review, Ind. Eng. Chem. Res. 32 (1993) 2208–2212. https://doi.org/10.1021/ie00022a002.

[30] D. Han, K.H. Row, Recent applications of ionic liquids in separation technology, Molecules. 15 (2010) 2405–2426. https://doi.org/10.3390/molecules15042405.

[31] V. Mokrushin, D. Assenbaum, N. Paape, D. Gerhard, L. Mokrushina, P. Wasserscheid, W. Arlt, H. Kistenmacher, S. Neuendorf, V. Göke, Ionic liquids for Propene-Propane separation, Chem. Eng. Technol. 33 (2010) 63–73. https://doi.org/10.1002/ceat.200900343.

[32] Ralph T. Yang, Adsorbents: Fundamentals and Applications, Hobokoen, 2003.

[33] F.A. Da Silva, A.E. Rodrigues, Adsorption equilibria and kinetics for propylene and propane over 13X and 4A zeolite pellets, Ind. Eng. Chem. Res. 38 (1999) 2051–2057. https://doi.org/10.1021/ie980640z.

[34] K.A. Kovalenko, A.S. Potapov, V.P. Fedin, Micro- and mesoporous metal-organic frameworks for hydrocarbon separation, Russ. Chem. Rev. 91 (2022) RCR5026. https://doi.org/10.1070/rcr5026.

[35] Y. Wang, D. Zhao, Beyond Equilibrium: Metal-Organic Frameworks for Molecular Sieving and Kinetic Gas Separation, Cryst. Growth Des. 17 (2017) 2291–2308. https://doi.org/10.1021/acs.cgd.7b00287.

[36] Y. Duan, L. Li, Z. Shen, J. Cheng, K. He, Engineering Metal-Organic-Framework (MOF)-Based Membranes for Gas and Liquid Separation, Membranes (Basel). 13 (2023). https://doi.org/10.3390/membranes13050480.

[37] E. Adatoz, A.K. Avci, S. Keskin, Opportunities and challenges of MOF-based membranes in gas separations, Sep. Purif. Technol. 152 (2015) 207–237. https://doi.org/10.1016/j.seppur.2015.08.020.

[38] M. Takht Ravanchi, T. Kaghazchi, A. Kargari, Application of membrane separation processes in petrochemical industry: a review, Desalination. 235 (2009) 199–244. https://doi.org/10.1016/j.desal.2007.10.042.

[39] R.W. Baker, Membrane Technology and Applications, John Wiley & Sons, Menlo Park, California, 2004.

[40] S. Kentish, C. Scholes, G. Stevens, Carbon Dioxide Separation through Polymeric Membrane Systems for Flue Gas Applications, Recent Patents Chem. Eng. 1 (2008) 52–66. https://doi.org/10.2174/2211334710801010052.

[41] J. Hou, P. Liu, M. Jiang, L. Yu, L. Li, Z. Tang, Olefin/paraffin separation through membranes: From mechanisms to critical materials, J. Mater. Chem. A. 7 (2019) 23489–23511. https://doi.org/10.1039/c9ta06329c.

[42] Y. Pan, T. Li, G. Lestari, Z. Lai, Effective separation of propylene/propane binary mixtures by ZIF-8 membranes, J. Memb. Sci. 390–391 (2012) 93–98. https://doi.org/10.1016/j.memsci.2011.11.024.

[43] H.T. Kwon, H.K. Jeong, Highly propylene-selective supported zeolite-imidazolate framework (ZIF-8) membranes synthesized by rapid microwave-assisted seeding and secondary growth, Chem. Commun. 49 (2013) 3854–3856. https://doi.org/10.1039/c3cc41039k.

[44] H.T. Kwon, H.K. Jeong, In situ synthesis of thin zeolitic-imidazolate framework ZIF-8 membranes exhibiting exceptionally high propylene/propane separation, J. Am. Chem. Soc. 135 (2013) 10763–10768. https://doi.org/10.1021/ja403849c.

[45] Y.-S. Wang, X.-J. Zhang, Y.-Q. Ba, T.-Y. Li, G.-P. Hao, A.-H. Lu, Recent Advances in Carbon-Based Adsorbents for Adsorptive Separation of Light Hydrocarbons, Research. 2022 (2022). https://doi.org/10.34133/2022/9780864.

[46] Q. Qian, P.A. Asinger, M.J. Lee, G. Han, K. Mizrahi Rodriguez, S. Lin, F.M. Benedetti, A.X. Wu, W.S. Chi, Z.P. Smith, MOF-Based Membranes for Gas Separations, Chem. Rev. 120 (2020) 8161–8266. https://doi.org/10.1021/acs.chemrev.0c00119.

[47] S. Li, Y. Liu, D.A. Wong, J. Yang, Recent Advances in Polymer-Inorganic Mixed Matrix Membranes for CO 2 Separation, (2021).

[48] P. Fernández-Castro, A. Ortiz, D. Gorri, Exploring the potential application of matrimid® and ZIFs-based membranes for hydrogen recovery: A review, Polymers (Basel). 13 (2021). https://doi.org/10.3390/polym13081292.

[49] A.D. McNaught, A. Wilkinson, Compendium of Chemical Terminology: IUPAC recommendations, 2nd ed., Blackwell Science, Oxford, 1997.

[50] P.M. Budd, B.S. Ghanem, S. Makhseed, N.B. Mckeown, K.J. Msayib, E. Tattershall, Polymers of intrinsic microporosity (PIMs): robust , solution-processable , organic nanoporous materials, ChemComm. (2004) 230–231.

[51] K. Polak-Krasna, R. Dawson, L.T. Holyfield, C.R. Bowen, A.D. Burrows, T.J. Mays, Mechanical characterisation of polymer of intrinsic microporosity PIM-1 for hydrogen storage applications, (2017) 3862–3875. https://doi.org/10.1007/s10853-016-0647-4.

[52] B.B.S. Ghanem, N.B. Mckeown, P.M. Budd, J.D. Selbie, High-Performance Membranes from Polyimides with Intrinsic Microporosity **, (2008) 2766–2771. https://doi.org/10.1002/adma.200702400.

[53] Y. Wang, X. Ma, B.S. Ghanem, F. Alghunaimi, I. Pinnau, Y. Han, Polymers of intrinsic microporosity for energy-intensive membrane-based gas separations, Mater. Today Nano. 3 (2018) 69–95. https://doi.org/10.1016/j.mtnano.2018.11.003.

[54] M.D. Guiver, M. Yahia, M.M. Dal-cin, G.P. Robertson, S.S. Garakani, N. Du, N. Tavajohi, Gas Transport in a Polymer of Intrinsic Microporosity (PIM-1) Substituted with Pseudo-Ionic Liquid Tetrazole-Type Structures, (2020). https://doi.org/10.1021/acs.macromol.0c01321.

[55] M. Galizia, W.S. Chi, Z.P. Smith, T.C. Merkel, R.W. Baker, B.D. Freeman, 50th Anniversary Perspective: Polymers and Mixed Matrix Membranes for Gas and Vapor Separation: A Review and Prospective Opportunities, Macromolecules. 50 (2017) 7809–7843. https://doi.org/10.1021/acs.macromol.7b01718.

[56] H. Bum, S. Hoon, C. Ho, Y. Moo, A.J. Hill, Thermally rearranged (TR) polymer membranes for CO2 separation, J. Memb. Sci. 359 (2010) 11–24. https://doi.org/10.1016/j.memsci.2009.09.037.

[57] L.M. Robeson, M.E. Dose, B.D. Freeman, D.R. Paul, Analysis of the transport properties of thermally rearranged (TR) polymers and polymers of intrinsic microporosity (PIM) relative to upper bound performance, J. Memb. Sci. 525 (2017) 18–24. https://doi.org/10.1016/j.memsci.2016.11.085.

[58] G. Bengtson, S. Neumann, V. Filiz, Membranes of Polymers of Intrinsic Microporosity (PIM-1) Modified by Poly (ethylene glycol), (2017). https://doi.org/10.3390/membranes7020028.

[59] Q. Song, S. Cao, R.H. Pritchard, B. Ghalei, S.A. Al-muhtaseb, E.M. Terentjev, A.K. Cheetham, E. Sivaniah, Controlled thermal oxidative crosslinking of polymers of intrinsic microporosity towards tunable molecular sieve membranes, Nat. Commun. (2014). https://doi.org/10.1038/ncomms5813.

[60] T. Mitra, R.S. Bhavsar, D.J. Adams, P.M. Budd, A.I. Cooper, PIM-1 Mixed Matrix Membranes for Gas Separations using Cost- Effective Hypercrosslinked Nanoparticle, ChemComm. 52 (2016) 5581–5584. https://doi.org/10.1039/C6CC00261G.

[61] A. Roy, S.R. Venna, G. Rogers, L. Tang, T.C. Fitzgibbons, J. Liu, H. McCurry, D.J. Vickery, D. Flick, B. Fish, Membranes for olefin–paraffin separation: An industrial perspective, Proc. Natl. Acad. Sci. U. S. A. 118 (2021) 1–9. https://doi.org/10.1073/pnas.2022194118.

[62] N.B. Mc Keown, P.M. Budd, Polymers of intrinsic microporosity (PIMs): Organic materials for membrane separations, heterogeneous catalysis and hydrogen storage, Chem. Soc. Rev. 35 (2006) 675–683. https://doi.org/10.1039/b600349d.

[63] P. Li, T.S. Chung, D.R. Paul, Gas sorption and permeation in PIM-1, J. Memb. Sci. 432 (2013) 50–57. https://doi.org/10.1016/j.memsci.2013.01.009.

[64] R.J. Swaidan, B. Ghanem, R. Swaidan, E. Litwiller, I. Pinnau, Pure- and mixed-gas propylene / propane permeation properties of spiro- and triptycene-based microporous polyimides, J. Memb. Sci. 492 (2015) 116–122. https://doi.org/10.1016/j.memsci.2015.05.044.

[65] R.J. Swaidan, X. Ma, I. Pinnau, Spirobisindane-based polyimide as ef fi cient precursor of thermally-rearranged and carbon molecular sieve membranes for enhanced propylene / propane separation, J. Memb. Sci. 520 (2016) 983–989. https://doi.org/10.1016/j.memsci.2016.08.057.

[66] K. Liao, J. Lai, T. Chung, Metal ion modified PIM-1 and its application for propylene/propane separation, J. Memb. Sci. 515 (2016) 36–44. https://doi.org/10.1016/j.memsci.2016.05.032.

[67] J. Liu, Y. Xiao, T.S. Chung, Flexible thermally treated 3D PIM-CD molecular sieve membranes exceeding the upper bound line for propylene/propane separation, J. Mater. Chem. A. 5 (2017) 4583–4595. https://doi.org/10.1039/c6ta09751k.

[68] J.H. Shin, H.J. Yu, J. Park, A.S. Lee, S.S. Hwang, S.J. Kim, S. Park, K.Y. Cho, W. Won, J.S. Lee, Fluorine-containing polyimide/polysilsesquioxane carbon molecular sieve membranes and techno-economic evaluation thereof for C3H6/C3H8 separation, J. Memb. Sci. 598 (2020) 117660. https://doi.org/10.1016/j.memsci.2019.117660.

[69] O. Salinas, X. Ma, E. Litwiller, I. Pinnau, Ethylene/ethane permeation, diffusion and gas sorption properties of carbon molecular sieve membranes derived from the prototype ladder polymer of intrinsic microporosity (PIM-1), J. Memb. Sci. 504 (2016) 133–140. https://doi.org/10.1016/j.memsci.2015.12.052.

[70] K. Tanaka, H. Kita, K.I. Okamoto, Permeability and Permselectivity of Gases in Fluorinated Polyimides, Sen'I Gakkaishi. 46 (1990) 541–547. https://doi.org/10.2115/fiber.46.12_541.

[71] K. Tanaka, M. Okano, H. Toshino, H. Kita, K. -I Okamoto, Effect of methyl substituents on permeability and permselectivity of gases in polyimides prepared from methyl-substituted phenylenediamines, J. Polym. Sci. Part B Polym. Phys. 30 (1992) 907–914. https://doi.org/10.1002/polb.1992.090300813.

[72] C. Staudt-Bickel, W.J. Koros, Olefin/paraffin gas separations with 6FDA-based polyimide membranes, J. Memb. Sci. 170 (2000) 205–214. https://doi.org/10.1016/S0376-7388(99)00351-8.

[73] R.L. Burns, W.J. Koros, Defining the challenges for C3H6/C3H8 separation using polymeric membranes, J. Memb. Sci. 211 (2003) 299–309. https://doi.org/10.1016/S0376-7388(02)00430-1.

[74] A. Shimazu, T. Miyazaki, M. Maeda, K. Ikeda, Relationships between the Chemical Structures and the Solubility , Diffusivity , and Permselectivity of Propylene and Propane in 6FDA-Based Polyimides, (2000) 2525–2536.

[75] M. Yoshino, S. Nakamura, H. Kita, K.I. Okamoto, N. Tanihara, Y. Kusuki, Olefin/paraffin separation performance of asymmetric hollow fiber membrane of 6FDA/BPDA-DDBT copolyimide, J. Memb. Sci. 212 (2003) 13–27. https://doi.org/10.1016/S0376-7388(02)00434-9.

[76] K. Okamoto, K. Noborio, J. Hao, K. Tanaka, H. Kita, Permeation and separation properties of polyimide membranes to 1,3-butadiene and n-butane, J. Memb. Sci. 134 (1997) 171–179. https://doi.org/10.1016/S0376-7388(97)00128-2.

[77] S. Velioğlu, M.G. Ahunbay, S.B. Tantekin-Ersolmaz, Propylene/propane plasticization in polyimide membranes, J. Memb. Sci. 501 (2016) 179–190. https://doi.org/10.1016/j.memsci.2015.11.034.

[78] Z. Liu, Y. Liu, W. Qiu, W.J. Koros, Molecularly Engineered 6FDA-Based Polyimide Membranes for Sour Natural Gas Separation, Angew. Chemie - Int. Ed. 59 (2020) 14877–14883. https://doi.org/10.1002/anie.202003910.

[79] A. Jain, M.Z. Ahmad, A. Linkès, V. Martin-gil, R. Castro-muñoz, P. Izak, Z. Sofer, W. Hintz, V. Fila, 6FDA-DAM:DABA Co-Polyimide Mixed Matrix Membranes with GO and ZIF-8 mixtures for effective CO2/CH4 separation, Nanomaterials. 11 (2021) 1–16. https://doi.org/10.3390/nano11030668.

[80] A.F. Bushell, M.P. Attfield, C.R. Mason, P.M. Budd, Y. Yampolskii, L. Starannikova, A. Rebrov, F. Bazzarelli, P. Bernardo, J. Carolus Jansen, M. Lanč, K. Friess, V. Shantarovich, V. Gustov, V. Isaeva, Gas permeation parameters of mixed matrix membranes based on the polymer of intrinsic microporosity PIM-1 and the zeolitic imidazolate framework ZIF-8, J. Memb. Sci. 427 (2013) 48–62. https://doi.org/10.1016/j.memsci.2012.09.035.

[81] D. Zacher, R. Schmid, C. Wöll, R.A. Fischer, Surface chemistry of metal-organic frameworks at the liquid-solid interface, Angew. Chemie - Int. Ed. 50 (2011) 176–199. https://doi.org/10.1002/anie.201002451.

[82] S. Furukawa, J. Reboul, S. Diring, K. Sumida, S. Kitagawa, Structuring of metal-organic frameworks at the mesoscopic/macroscopic scale, Chem. Soc. Rev. 43 (2014) 5700–5734. https://doi.org/10.1039/c4cs00106k.

[83] H. Li, L. Li, R.B. Lin, W. Zhou, Z. Zhang, S. Xiang, B. Chen, Porous metal-organic frameworks for gas storage and separation: Status and challenges, EnergyChem. 1 (2019) 100006. https://doi.org/10.1016/j.enchem.2019.100006.

[84] B.V.K.J. Schmidt, Metal-Organic Frameworks in Polymer Science: Polymerization Catalysis, Polymerization Environment, and Hybrid Materials, Macromol. Rapid Commun. 41 (2020). https://doi.org/10.1002/marc.201900333.

[85] H. Wu, Q. Gong, D.H. Olson, J. Li, Commensurate adsorption of hydrocarbons and alcohols in microporous metal organic frameworks, Chem. Rev. 112 (2012) 836–868. https://doi.org/10.1021/cr200216x.

[86] Z. Bao, G. Chang, H. Xing, R. Krishna, Q. Ren, B. Chen, Potential of microporous metal-organic frameworks for separation of hydrocarbon mixtures, Energy Environ. Sci. 9 (2016) 3612–3641. https://doi.org/10.1039/c6ee01886f.

[87] L.E. Kreno, K. Leong, O.K. Farha, M. Allendorf, R.P. Van Duyne, J.T. Hupp, Metal-organic framework materials as chemical sensors, Chem. Rev. 112 (2012) 1105–1125. https://doi.org/10.1021/cr200324t.

[88] J.F. Olorunyomi, S.T. Geh, R.A. Caruso, C.M. Doherty, Metal-organic frameworks for chemical sensing devices, Mater. Horizons. 8 (2021) 2387–2419. https://doi.org/10.1039/d1mh00609f.

[89] W.-T. Koo, J.-S. Jang, I.-D. Kim, Metal-Organic Frameworks for Chemiresistive Sensors, Chem. 5 (2019) 1938–1963. https://doi.org/10.1016/j.chempr.2019.04.013.

[90] Y. Cui, Y. Yue, G. Qian, B. Chen, Luminescent functional metal-organic frameworks, Chem. Rev. 112 (2012) 1126–1162. https://doi.org/10.1021/cr200101d.

[91] A. García-Baldoví, R. Del Angel, G. Mouchaham, S. Liu, D. Fan, G. Maurin, S. Navalón, C. Serre, H. Garcia, Active site imprinting on Ti oxocluster metal-organic frameworks for photocatalytic hydrogen release from formic acid, Energy Environ. Sci. 16 (2022) 167–177. https://doi.org/10.1039/d2ee02258c.

[92] A. Bavykina, N. Kolobov, I.S. Khan, J.A. Bau, A. Ramirez, J. Gascon, Metal-Organic Frameworks in Heterogeneous Catalysis: Recent Progress, New Trends, and Future

Perspectives, Chem. Rev. 120 (2020) 8468–8535. https://doi.org/10.1021/acs.chemrev.9b00685.

[93] Y. Liu, Y. Zhao, X. Chen, Bioengineering of metal-organic frameworks for nanomedicine, Theranostics. 9 (2019) 3122–3133. https://doi.org/10.7150/thno.31918.

[94] W. Cai, C.C. Chu, G. Liu, Y.X.J. Wáng, Metal-Organic Framework-Based Nanomedicine Platforms for Drug Delivery and Molecular Imaging, Small. 11 (2015) 4806–4822. https://doi.org/10.1002/smll.201500802.

[95] S.R. Venna, M.A. Carreon, Metal organic framework membranes for carbon dioxide separation, Chem. Eng. Sci. 124 (2015) 3–19. https://doi.org/10.1016/j.ces.2014.10.007.

[96] T. Devic, C. Serre, High valence 3p and transition metal based MOFs, Chem. Soc. Rev. 43 (2014) 6097–6115. https://doi.org/10.1039/c4cs00081a.

[97] G. Cai, P. Yan, L. Zhang, H.C. Zhou, H.L. Jiang, Metal-Organic Framework-Based Hierarchically Porous Materials: Synthesis and Applications, Chem. Rev. 121 (2021) 12278–12326. https://doi.org/10.1021/acs.chemrev.1c00243.

[98] J. Annamalai, P. Murugan, D. Ganapathy, D. Nallaswamy, R. Atchudan, S. Arya, A. Khosla, S. Barathi, A.K. Sundramoorthy, Synthesis of various dimensional metal organic frameworks (MOFs) and their hybrid composites for emerging applications – A review, Chemosphere. 298 (2022) 134184. https://doi.org/10.1016/j.chemosphere.2022.134184.

[99] J.D. Evans, V. Bon, I. Senkovska, H.C. Lee, S. Kaskel, Four-dimensional metal-organic frameworks, Nat. Commun. 11 (2020). https://doi.org/10.1038/s41467-020-16527-8.

[100] P.Z. Moghadam, A. Li, X.W. Liu, R. Bueno-Perez, S.D. Wang, S.B. Wiggin, P.A. Wood, D. Fairen-Jimenez, Targeted classification of metal-organic frameworks in the Cambridge structural database (CSD), Chem. Sci. 11 (2020) 8373–8387. https://doi.org/10.1039/d0sc01297a.

[101] T. Xiao, D. Liu, Progress in the synthesis , properties and applications of ZIF-7 and its derivatives, Mater. Today Energy. 14 (2019) 100357. https://doi.org/10.1016/j.mtener.2019.100357.

[102] A. Huang, H. Bux, F. Steinbach, J. Caro, Zuschriften Molecular-Sieve Membrane with Hydrogen Permselectivity : ZIF-22 in LTA Topology Prepared with 3-Aminopropyltriethoxysilane as Covalent Linker **, (2010) 5078–5081. https://doi.org/10.1002/ange.201001919.

[103] Q. Song, S.K. Nataraj, M. V Roussenova, C. Tan, D.J. Hughes, W. Li, P. Bourgoin, M.A. Alam, A.K. Cheetham, S.A. Al-muhtaseb, E. Sivaniah, Zeolitic imidazolate framework (ZIF-8) based polymer nanocomposite membranes for gas separation†, Energy Environ. Sci. 5 (2012) 8359–8369. https://doi.org/10.1039/c2ee21996d.

[104] A. Huang, W. Dou, Steam-Stable Zeolitic Imidazolate Framework ZIF-90 Membrane with Hydrogen Selectivity through Covalent Functionalization, (2010) 15562–15564.

[105] A. Huang, Y. Chen, N. Wang, Z. Hu, J. Jiang, J. Caro, A highly permeable and selective zeolitic imidazolate framework ZIF-95 membrane for H2/CO2 separation, Chem. Commun. 48 (2012) 10981–10983. https://doi.org/10.1039/c2cc35691k.

[106] X. Dong, Y.S. Lin, Synthesis of an organophilic ZIF-71 membrane for pervaporation solvent separation†, Chem. Commun. 49 (2013) 1196–1198. https://doi.org/10.1039/c2cc38512k.

[107] X. Dong, K. Huang, S. Liu, R. Ren, W. Jin, Y.S. Lin, Synthesis of zeolitic imidazolate framework-78 molecular-sieve membrane: defect formation and elimination†, J. Mater. Chem. 22 (2012) 19222–19227. https://doi.org/10.1039/c2jm34102f.

[108] H. Yin, J. Wang, Z. Xie, J. Yang, J. Bai, J. Lu, Y. Zhang, D. Yin, J.Y.S. Lin, A highly permeable and selective amino- functionalized MOF CAU-1 membrane for CO2–N2 separation†, : : Chem. Commun. 50 (2014) 3699–3701. https://doi.org/10.1039/c4cc00068d.

[109] A. Ghoufi, K. Benhamed, L. Boukli-hacene, G. Maurin, E. Induced, Metal-Organic Framework To cite this version :, 53 (2018). https://doi.org/10.1021/acscentsci.6b00392.

[110] Z. Zhao, X. Ma, A. Kasik, Z. Li, Y.S. Lin, Gas Separation Properties of Metal Organic Framework (MOF-5) Membranes, (2013).

[111] A. Thomas, R. Ahamed, M. Prakash, Effect of functional group in the zeolitic imidazolate framework for selective CH 4 / CO and CO / N 2 separation : A theoretical study, Mater. Lett. 303 (2021) 130575. https://doi.org/10.1016/j.matlet.2021.130575.

[112] K.C. Chong, S.O. Lai, S.K. Mah, H.S. Thiam, W.C. Chong, S.H. Shuit, S.S. Lee, W.E. Chong, A Review of HKUST-1 Metal-Organic Frameworks in Gas Adsorption, OP Conf. Ser. Earth Environ. Sci. (2023). https://doi.org/10.1088/1755-1315/1135/1/012030.

[113] S. Aguado, C. Nicolas, V. Moizan-baslé, C. Nieto, Facile Synthesis of an Ultramicroporous MOF Tubular Membrane with Selectivity towards CO 2 1 . - Synthesis and characterization of SIM-1, (2010).

[114] T. Isobe, Y. Arai, S. Yanagida, S. Matsushita, A. Nakajima, Microporous and Mesoporous Materials Solvothermal preparation and gas permeability of an IRMOF-3 membrane, Microporous Mesoporous Mater. 241 (2017) 218–225. https://doi.org/10.1016/j.micromeso.2016.12.031.

[115] M. Gholami, S. Yeganegi, Adsorption of propylene , propane , ethylene and ethane in an isoreticular series of MOF-74 structures, Adsorption. 0 (2017) 0. https://doi.org/10.1007/s10450-017-9862-9.

[116] Y. Lin, Metal organic framework membranes for separation applications, Curr. Opin. Chem. Eng. 8 (2015) 21–28. https://doi.org/10.1016/j.coche.2015.01.006.

[117] A. Li, R.B. Perez, S. Wiggin, S.C. Ward, P.A. Wood, D. Fairen-Jimenez, The launch of a freely accessible MOF CIF collection from the CSD, Matter. 4 (2021) 1105–1106. https://doi.org/10.1016/j.matt.2021.03.006.

[118] O.M. Yaghi, G. Li, H. Li, Selective binding and removal of guests in a microporous metal–organic framework, Nature. 378 (1995) 703–706. https://doi.org/https://doi.org/10.1038/378703a0.

[119] S. Hermes, F. Schröder, R. Chelmowski, C. Wöll, R.A. Fischer, Selective nucleation and growth of metal-organic open framework thin films on patterned COOH/CF3-terminated self-assembled monolayers on Au(111), J. Am. Chem. Soc. 127 (2005) 13744–13745. https://doi.org/10.1021/ja053523l.

[120] Y. Liu, Z. Ng, E.A. Khan, H.K. Jeong, C. bun Ching, Z. Lai, Synthesis of continuous MOF-5 membranes on porous α-alumina substrates, Microporous Mesoporous Mater. 118 (2009) 296–301. https://doi.org/10.1016/j.micromeso.2008.08.054.

[121] H. Guo, G. Zhu, I.J. Hewitt, S. Qiu, Twin copper source" growth of metal-organic framework membrane: Cu3(BTC)2 with high permeability and selectivity for recycling H2, J. Am. Chem. Soc. 131 (2009) 1646–1647. https://doi.org/10.1021/ja8074874.

[122] H. Bux, F. Liang, Y. Li, J. Cravillon, M. Wiebcke, J. Caro, Zeolitic Imidazolate Framework Membrane with Molecular Sieving Properties by Microwave-Assisted Solvothermal Synthesis Helge, Chem. Mater. 131 (2009) 16000–16001. https://doi.org/10.1021/cm902032y.

[123] S.R. Venna, M.A. Carreon, Highly permeable zeolite imidazolate framework-8 membranes for CO 2/CH4 separation, J. Am. Chem. Soc. 132 (2010) 76–78. https://doi.org/10.1021/ja909263x.

[124] Y. Pan, Z. Lai, Sharp separation of C2/C3 hydrocarbon mixtures by zeolitic imidazolate framework-8 (ZIF-8) membranes synthesized in aqueous solutions, Chem. Commun. 47 (2011) 10275–10277. https://doi.org/10.1039/c1cc14051e.

[125] A.J. Brown, J.R. Johnson, M.E. Lydon, W.J. Koros, C.W. Jones, S. Nair, Continuous polycrystalline zeolitic imidazolate framework-90 membranes on polymeric hollow fibers, Angew. Chemie - Int. Ed. 51 (2012) 10615–10618. https://doi.org/10.1002/anie.201206640.

[126] N. Wang, Y. Liu, Z. Qiao, L. Diestel, J. Zhou, A. Huang, J. Caro, Polydopamine-based synthesis of a zeolite imidazolate framework ZIF-100 membrane with high H2/CO2 selectivity, J. Mater. Chem. A. 3 (2015) 4722–4728. https://doi.org/10.1039/c4ta06763k.

[127] J. Fu, S. Das, G. Xing, T. Ben, V. Valtchev, S. Qiu, Fabrication of COF-MOF Composite Membranes and Their Highly Selective Separation of H2/CO2, J. Am. Chem. Soc. 138 (2016) 7673–7680. https://doi.org/10.1021/jacs.6b03348.

[128] Y. Wang, H. Jin, Q. Ma, K. Mo, H. Mao, A. Feldhoff, X. Cao, Y. Li, F. Pan, Z. Jiang, A MOF Glass Membrane for Gas Separation, Angew. Chemie - Int. Ed. 59 (2020) 4365–4369. https://doi.org/10.1002/anie.201915807.

[129] H. Demir, G.O. Aksu, H.C. Gulbalkan, S. Keskin, MOF Membranes for CO2 Capture: Past, Present and Future, Carbon Capture Sci. Technol. 2 (2022) 100026. https://doi.org/10.1016/j.ccst.2021.100026.

[130] C. Gücüyener, J. Van Den Bergh, J. Gascon, F. Kapteijn, Ethane/ethene separation turned on its head: Selective ethane adsorption on the metal-organic framework ZIF-7 through a gate-opening mechanism, J. Am. Chem. Soc. 132 (2010) 17704–17706. https://doi.org/10.1021/ja1089765.

[131] S. Bendt, M. Hovestadt, U. Böhme, C. Paula, M. Döpken, M. Hartmann, F.J. Keil, Olefin/Paraffin Separation Potential of ZIF-9 and ZIF-71: A Combined Experimental and Theoretical Study, Eur. J. Inorg. Chem. 2016 (2016) 4440–4449. https://doi.org/10.1002/ejic.201600695.

[132] C. Wang, F. Yang, L. Sheng, J. Yu, K. Yao, L. Zhang, Y. Pan, Zinc-substituted ZIF-67 nanocrystals and polycrystalline membranes for propylene/propane separation, Chem. Commun. 52 (2016) 12578–12581. https://doi.org/10.1039/c6cc06457d.

[133] A. Huang, N. Wang, C. Kong, J. Caro, Organosilica-functionalized zeolitic imidazolate framework ZIF-90 membrane with high gas-separation performance, Angew. Chemie - Int. Ed. 51 (2012) 10551–10555. https://doi.org/10.1002/anie.201204621.

[134] Y. Xiao, Y. Chu, S. Li, F. Chen, W. Gao, J. Xu, F. Deng, Host-Guest Interaction in Ethylene and Ethane Separation on Zeolitic Imidazolate Frameworks as Revealed by Solid-State NMR Spectroscopy, Chem. - A Eur. J. 27 (2021) 11303–11308. https://doi.org/10.1002/chem.202101779.

[135] Y. Pan, X. Yu, Preparation of Zeolitic Imidazolate Framework-91 and its modeling for pervaporation separation of water/ethanol mixtures, Sep. Purif. Technol. 237 (2020). https://doi.org/10.1016/j.seppur.2019.116330.

[136] M.R. Abdul Hamid, T.C. Shean Yaw, M.Z. Mohd Tohir, W.A. Wan Abdul Karim Ghani, P.D. Sutrisna, H.K. Jeong, Zeolitic imidazolate framework membranes for gas separations: Current state-of-the-art, challenges, and opportunities, J. Ind. Eng. Chem. 98 (2021) 17–41. https://doi.org/10.1016/j.jiec.2021.03.047.

[137] D.T. Lee, P. Corkery, S. Park, H.K. Jeong, M. Tsapatsis, Zeolitic Imidazolate Framework Membranes: Novel Synthesis Methods and Progress Toward Industrial Use, Annu. Rev. Chem. Biomol. Eng. 13 (2022) 529–555. https://doi.org/10.1146/annurev-chembioeng-092320-120148.

[138] D. Shi, X. Yu, W. Fan, V. Wee, D. Zhao, Polycrystalline zeolite and metal-organic framework membranes for molecular separations, Coord. Chem. Rev. 437 (2021) 213794. https://doi.org/10.1016/j.ccr.2021.213794.

[139] A. Schneemann, V. Bon, I. Schwedler, I. Senkovska, S. Kaskel, R.A. Fischer, Flexible metal-organic frameworks, Chem. Soc. Rev. 43 (2014) 6062–6096. https://doi.org/10.1039/c4cs00101j.

[140] X. Ma, D. Liu, Zeolitic imidazolate framework membranes for light olefin/paraffin separation, Crystals. 9 (2019) 1–26. https://doi.org/10.3390/cryst9010014.

[141] K. Li, D.H. Olson, J. Seidel, T.J. Emge, H. Gong, H. Zeng, J. Li, Zeolitic imidazolate frameworks for kinetic separation of propane and propene, J. Am. Chem. Soc. 131 (2009) 10368–10369. https://doi.org/10.1021/ja9039983.

[142] C. Zhang, R.P. Lively, K. Zhang, J.R. Johnson, O. Karvan, W.J. Koros, Unexpected Molecular Sieving Properties of Zeolitic Imidazolate Framework-8, J. Phys. Chem. Lett. (2012) 8–12. https://doi.org/10.1021/jz300855a.

[143] K. Eum, C. Ma, A.A. Rownaghi, C.W. Jones, S. Nair, ZIF-8 Membranes via Interfacial Microfluidic Processing in Polymeric Hollow Fibers : Efficient Propylene Separation at Elevated Pressures, (2016). https://doi.org/10.1021/acsami.6b08801.

[144] K. Huang, B. Wang, Y. Chi, K. Li, High Propylene Selective Metal-Organic Framework Membranes Prepared in Confined Spaces via Convective Circulation Synthesis, 1800287 (2018) 1–8. https://doi.org/10.1002/admi.201800287.

[145] R. Wei, H. Chi, X. Li, D. Lu, Y. Wan, C. Yang, Z. Lai, Aqueously Cathodic Deposition of ZIF-8 Membranes for Superior Propylene / Propane Separation, 1907089 (2019) 1–7. https://doi.org/10.1002/adfm.201907089.

[146] M.J. Lee, H.T. Kwon, H. Jeong, High-Flux Zeolitic Imidazolate Framework Membranes for Propylene / Propane Separation by Postsynthetic Linker Exchange, (2017) 1–7. https://doi.org/10.1002/anie.201708924.

[147] X. Ma, P. Kumar, N. Mittal, A. Khlyustova, Zeolitic imidazolate framework membranes made by ligand-induced permselectivation, 1011 (2018) 1008–1011.

[148] W. Li, P. Su, Z. Li, Z. Xu, F. Wang, H. Ou, J. Zhang, G. Zhang, E. Zeng, production by gel – vapour deposition, Nat. Commun. (n.d.) 1–8. https://doi.org/10.1038/s41467-017-00544-1.

[149] Z. Qiao, Y. Liang, Z. Zhang, D. Mei, Z. Wang, M.D. Guiver, C. Zhong, Ultrathin Low-Crystallinity MOF Membranes Fabricated by Interface Layer Polarization Induction, Adv. Mater. 32 (2020) 1–6. https://doi.org/10.1002/adma.202002165.

[150] H.T. Kwon, H.K. Jeong, A.S. Lee, H.S. An, J.S. Lee, Heteroepitaxially Grown Zeolitic Imidazolate Framework Membranes with Unprecedented Propylene/Propane Separation Performances, J. Am. Chem. Soc. 137 (2015) 12304–12311. https://doi.org/10.1021/jacs.5b06730.

[151] P. Krokidas, M. Castier, S. Moncho, D.N. Sredojevic, E.N. Brothers, H.T. Kwon, H.K. Jeong, J.S. Lee, I.G. Economou, ZIF-67 Framework: A Promising New Candidate for Propylene/Propane Separation. Experimental Data and Molecular Simulations, J. Phys. Chem. C. 120 (2016) 8116–8124. https://doi.org/10.1021/acs.jpcc.6b00305.

[152] Q. Hou, S. Zhou, Y. Wei, J. Caro, H. Wang, Q. Hou, S. Zhou, Y. Wei, J. Caro, H. Wang, Balancing the Grain Boundary Structure and the Framework Flexibility through Bimetallic MOF Membranes for Gas Separation Balancing the Grain Boundary Structure and the Framework Flexibility through Bimetallic MOF Membranes for Gas, (2020). https://doi.org/10.1021/jacs.0c02181.

[153] H. Bux, C. Chmelik, R. Krishna, J. Caro, Ethene/ethane separation by the MOF membrane ZIF-8: Molecular correlation of permeation, adsorption, diffusion, J. Memb. Sci. 369 (2011) 284–289. https://doi.org/10.1016/j.memsci.2010.12.001.

[154] J.B. James, J. Wang, L. Meng, Y.S. Lin, ZIF-8 Membrane Ethylene/Ethane Transport Characteristics in Single and Binary Gas Mixtures, Ind. Eng. Chem. Res. 56 (2017) 7567–7575. https://doi.org/10.1021/acs.iecr.7b01536.

[155] A. Cadiau, K. Adil, P.M. Bhatt, Y. Belmabkhout, M. Eddaoudi, A metal-organic framework-based splitter for separating propylene from propane, Science (80-.). 353 (2016) 137–140. https://doi.org/10.1126/science.aaf6323.

[156] H. Wang, X. Dong, V. Colombo, Q. Wang, Y. Liu, W. Liu, X.L. Wang, X.Y. Huang, D.M. Proserpio, A. Sironi, Y. Han, J. Li, Tailor-Made Microporous Metal–Organic Frameworks for the Full Separation of Propane from Propylene Through Selective Size Exclusion, Adv. Mater. 30 (2018). https://doi.org/10.1002/adma.201805088.

[157] C.Y. Lee, Y.S. Bae, N.C. Jeong, O.K. Farha, A.A. Sarjeant, C.L. Stern, P. Nickias, R.Q. Snurr, J.T. Hupp, S.T. Nguyen, Kinetic separation of propene and propane in metal-organic frameworks: Controlling diffusion rates in plate-shaped crystals via tuning of pore apertures and crystallite aspect ratios, J. Am. Chem. Soc. 133 (2011) 5228–5231. https://doi.org/10.1021/ja200553m.

[158] L. Li, R.B. Lin, X. Wang, W. Zhou, L. Jia, J. Li, B. Chen, Kinetic separation of propylene over propane in a microporous metal-organic framework, Chem. Eng. J. 354 (2018) 977–982. https://doi.org/10.1016/j.cej.2018.08.108.

[159] J. Peng, H. Wang, D.H. Olson, Z. Li, J. Li, Efficient kinetic separation of propene and propane using two microporous metal organic frameworks, Chem. Commun. 53 (2017) 9332–9335. https://doi.org/10.1039/c7cc03529b.

[160] Y. Wang, N.Y. Huang, X.W. Zhang, H. He, R.K. Huang, Z.M. Ye, Y. Li, D.D. Zhou, P.Q. Liao, X.M. Chen, J.P. Zhang, Selective Aerobic Oxidation of a Metal–Organic Framework Boosts Thermodynamic and Kinetic Propylene/Propane Selectivity, Angew. Chemie - Int. Ed. 58 (2019) 7692–7696. https://doi.org/10.1002/anie.201902209.

[161] S. Yang, A.J. Ramirez-Cuesta, R. Newby, V. Garcia-Sakai, P. Manuel, S.K. Callear, S.I. Campbell, C.C. Tang, M. Schröder, Supramolecular binding and separation of hydrocarbons within a functionalized porous metal-organic framework, Nat. Chem. 7 (2015) 121–129. https://doi.org/10.1038/nchem.2114.

[162] J.E. Bachman, M.T. Kapelewski, D.A. Reed, M.I. Gonzalez, J.R. Long, M2(m-dobdc) (M = Mn, Fe, Co, Ni) Metal-Organic Frameworks as Highly Selective, High-Capacity Adsorbents for Olefin/Paraffin Separations, J. Am. Chem. Soc. 139 (2017) 15363–15370. https://doi.org/10.1021/jacs.7b06397.

[163] P.J. Bereciartua, Á. Cantín, A. Corma, J.L. Jordá, M. Palomino, F. Rey, S. Valencia, E.W. Corcoran, P. Kortunov, P.I. Ravikovitch, A. Burton, C. Yoon, Y. Wang, C. Paur, J. Guzman, A.R. Bishop, G.L. Casty, Control of zeolite framework flexibility and pore topology for separation of ethane and ethylene, Science (80-.). 358 (2017) 1068–1071. https://doi.org/10.1126/science.aao0092.

[164] Q. Ding, Z. Zhang, C. Yu, P. Zhang, J. Wang, X. Cui, C.H. He, S. Deng, H. Xing, Exploiting equilibrium-kinetic synergetic effect for separation of ethylene and ethane in a microporous metal-organic framework, Sci. Adv. 6 (2020) 1–7. https://doi.org/10.1126/sciadv.aaz4322.

[165] Y. Wang, S. Yuan, Z. Hu, T. Kundu, J. Zhang, S.B. Peh, Y. Cheng, J. Dong, D. Yuan, H.C. Zhou, D. Zhao, Pore Size Reduction in Zirconium Metal-Organic Frameworks for Ethylene/Ethane Separation, ACS Sustain. Chem. Eng. 7 (2019) 7118–7126. https://doi.org/10.1021/acssuschemeng.9b00062.

[166] Z. Bao, J. Wang, Z. Zhang, H. Xing, Q. Yang, Y. Yang, H. Wu, R. Krishna, W. Zhou, B. Chen, Q. Ren, Molecular Sieving of Ethane from Ethylene through the Molecular Cross-Section Size Differentiation in Gallate-based Metal–Organic Frameworks, Angew. Chemie. 130 (2018) 16252–16257. https://doi.org/10.1002/ange.201808716.

[167] R.B. Lin, L. Li, H.L. Zhou, H. Wu, C. He, S. Li, R. Krishna, J. Li, W. Zhou, B. Chen, Molecular sieving of ethylene from ethane using a rigid metal–organic framework, Nat. Mater. 17 (2018) 1128–1133. https://doi.org/10.1038/s41563-018-0206-2.

[168] S. Denning, A.A.A. Majid, J.M. Lucero, J.M. Crawford, M.A. Carreon, C.A. Koh, Methane Hydrate Growth Promoted by Microporous Zeolitic Imidazolate Frameworks ZIF-8 and ZIF-67 for Enhanced Methane Storage, ACS Sustain. Chem. Eng. 9 (2021) 9001–9010. https://doi.org/10.1021/acssuschemeng.1c01488.

[169] Y. Cheng, B. Joarder, S.J. Datta, N. Alsadun, D. Poloneeva, D. Fan, R. Khairova, A. Bavykina, J. Jia, O. Shekhah, A. Shkurenko, G. Maurin, J. Gascon, M. Eddaoudi, Mixed Matrix Membranes with Surface Functionalized Metal–Organic Framework Sieves for Efficient Propylene/Propane Separation, Adv. Mater. 2300296 (2023) 1–9. https://doi.org/10.1002/adma.202300296.

[170] N. Gholamipour, M. Sadeghi, M. Shafiei, Effect of Silica Nanoparticles on the Performance of Polysulfone Membranes for Olefin-Paraffin Separation, (2019) 2292–2301. https://doi.org/10.1002/ceat.201800147.

[171] A. Luna-Triguero, A. Slawek, R. Sánchez-de-Armas, J.J. Gutiérrez-Sevillano, C.. Ania, J.B. Parra, J.M. Vicent-Luna, S. Calero, π-Complexation for olefin/paraffin separation using aluminosilicates, Chem. Eng. J. 380 (2020). https://doi.org/10.1016/j.cej.2019.122482.

[172] Q. Zhang, H. Li, S. Chen, J. Duan, W. Jin, Mixed-matrix membranes with soluble porous organic molecular cage for highly efficient C 3 H 6 / C 3 H 8 separation, J. Memb. Sci. 611 (2020) 118288. https://doi.org/10.1016/j.memsci.2020.118288.

[173] R.M. Barrer, S.D. James, ELECTROCHEMISTRY OF CRYSTAL-POLYMER MEMBRANES. PART II. MEMBRANE POTENTIALS, J. Mater. Chem. 64 (1960) 421–427.

[174] I. Tirouni, M. Sadeghi, M. Pakizeh, Separation of C3H8 and C2H6 from CH4 in polyurethane-zeolite 4Å and ZSM-5 mixed matrix membranes, Sep. Purif. Technol. 141 (2015) 394–402. https://doi.org/10.1016/j.seppur.2014.12.012.

[175] D. Carter, F.H. Tezel, B. Kruczek, H. Kalipcilar, Investigation and comparison of mixed matrix membranes composed of polyimide matrimid with ZIF – 8, silicalite, and SAPO – 34, J. Memb. Sci. 544 (2017) 35–46. https://doi.org/10.1016/j.memsci.2017.08.068.

[176] A. Wolińska-Grabczyk, P. Kubica, A. Jankowski, M. Wójtowicz, Gas and water vapor transport properties of mixed matrix membranes containing 13X zeolite, 526 (2017) 334–347. https://doi.org/10.1016/j.memsci.2016.11.031.

[177] K. Zarshenas, A. Raisi, A. Aroujalian, Mixed matrix membrane of nano-zeolite NaX / poly (ether-block-amide) for gas separation applications, J. Memb. Sci. 510 (2016) 270–283. https://doi.org/10.1016/j.memsci.2016.02.059.

[178] A. Mundstock, N. Wang, S. Friebe, J. Caro, Microporous and Mesoporous Materials Propane / propene permeation through Na-X membranes : The interplay of separation performance and pre-synthetic support functionalization, Microporous Mesoporous Mater. 215 (2015) 20–28. https://doi.org/10.1016/j.micromeso.2015.05.019.

[179] J. Hedlund, M. Noack, P. Kölsch, D. Creaser, J. Caro, J. Sterte, ZSM-5 membranes synthesized without organic templates using a seeding technique, 159 (1999) 263–273.

[180] C.C. Pavel, W. Schmidt, Generation of hierarchical pore systems in the titanosilicate ETS-10 by hydrogen peroxide treatment under microwave irradiation, 5 (2006) 882–884. https://doi.org/10.1039/b515720j.

[181] R. Mahajan, W.J. Koros, Mixed matrix membrane materials with glassy polymers. Part 1, Polym. Eng. Sci. 42 (2002) 1420–1431. https://doi.org/10.1002/pen.11041.

[182] Z. Kang, Y. Peng, Y. Qian, D. Yuan, M.A. Addicoat, T. Heine, Z. Hu, L. Tee, Z. Guo, D. Zhao, Mixed Matrix Membranes (MMMs) Comprising Exfoliated 2D Covalent Organic Frameworks (COFs) for E ffi cient CO 2 Separation, (2016). https://doi.org/10.1021/acs.chemmater.5b02902.

[183] X. Feng, X. Ding, D. Jiang, Covalent organic frameworks, Chem Soc Rev. 41 (2012) 6010–6022. https://doi.org/10.1039/c2cs35157a.

[184] H. Jiang, Y. Chen, S. Song, Z. Guo, Z. Zhang, C. Zheng, G. He, H. Wang, H. Wu, T. Huang, Y. Ren, X. Liu, J. Zhang, Y. Yin, Z. Jiang, M.D. Guiver, Confined facilitated transport within covalent organic frameworks for propylene / propane membrane separation, Chem. Eng. J. 439 (2022) 135657. https://doi.org/10.1016/j.cej.2022.135657.

[185] Y. Liu, H. Wu, R. Li, J. Wang, Y. Kong, Z. Guo, H. Jiang, Y. Ren, Y. Pu, X. Liang, F. Pan, Y. Cao, S. Song, G. He, Z. Jiang, MOF – COF " Alloy " Membranes for Efficient Propylene / Propane Separation, Adv. Mater. 2201423 (2022) 1–8. https://doi.org/10.1002/adma.202201423.

[186] N. Azizi, T. Mohammadi, R. Mosayebi Behbahani, Comparison of permeability performance of PEBAX-1074/TiO2, PEBAX-1074/SiO2 and PEBAX-1074/Al2O3 nanocomposite membranes for CO2/CH4 separation, Chem. Eng. Res. Des. 117 (2017) 177–189. https://doi.org/10.1016/j.cherd.2016.10.018.

[187] M. Bhattacharya, M.K. Mandal, Synthesis of rice straw extracted nano-silica-composite membrane for CO2 separation, J. Clean. Prod. 186 (2018) 241–252. https://doi.org/10.1016/j.jclepro.2018.03.099.

[188] Z. Aghaei, L. Naji, V. Hadadi, G. Khanbabaei, F. Dezhagah, The influence of fumed silica content and particle size in poly (amide 6-b- ethylene oxide) mixed matrix membranes for gas separation, Sep. Purif. Technol. 199 (2018) 47–56. https://doi.org/10.1016/j.seppur.2018.01.035.

[189] J. Ahn, W.-J. Chung, I. Pinnau, J. Song, N. Du, G.P. Robertson, M.D. Guiver, Gas transport behavior of mixed-matrix membranes composed of silica nanoparticles in a polymer of intrinsic microporosity (PIM-1), J. Memb. Sci. 346 (2010) 280–287.

[190] S. Zhou, X. Niu, X. Zhang, Y. Zhao, The effect of silica and copper nanoparticles in polyimide on the friction and wear of polyethersulfone / polyimide mixture, 30 (2022) 1–13. https://doi.org/10.1177/09673911221133438.

[191] T. Suzuki, Y. Yamada, Effect of thermal treatment on gas transport properties of hyperbranched polyimide – silica hybrid membranes, J. Memb. Sci. 417–418 (2012) 193–200. https://doi.org/10.1016/j.memsci.2012.06.035.

[192] R. Xing, W.S.W. Ho, Crosslinked polyvinylalcohol-polysiloxane/fumed silica mixed matrix membranes containing amines for CO2/H2 separation, J. Memb. Sci. 367 (2011) 91–102. https://doi.org/10.1016/j.memsci.2010.10.039.

[193] A. Galve, D. Sieffert, C. Staudt, M. Ferrando, C. Güell, C. Téllez, J. Coronas, Combination of ordered mesoporous silica MCM-41 and layered titanosilicate JDF-L1 fillers for 6FDA-based copolyimide mixed matrix membranes, J. Memb. Sci. 431 (2013) 163–170. https://doi.org/10.1016/j.memsci.2012.12.046.

[194] B. Zornoza, C. Téllez, J. Coronas, Mixed matrix membranes comprising glassy polymers and dispersed mesoporous silica spheres for gas separation, J. Memb. Sci. 368 (2011) 100–109. https://doi.org/10.1016/j.memsci.2010.11.027.

[195] Y. Kinoshita, K. Wakimoto, A.H. Gibbons, A.P. Isfahani, H. Kusuda, E. Sivaniah, B. Ghalei, Enhanced PIM-1 membrane gas separation selectivity through efficient dispersion of functionalized POSS fillers, J. Memb. Sci. 539 (2017) 178–186. https://doi.org/10.1016/j.memsci.2017.05.072.

[196] M. Lanč, P. Sysel, M. Šoltys, F. Štěpánek, K. Fónod, M. Klepić, O. Vopička, M. Lhotka, P. Ulbrich, K. Friess, Synthesis, preparation and characterization of novel hyperbranched 6FDA-TTM based polyimide membranes for effective CO2 separation: Effect of embedded mesoporous silica particles and siloxane linkages, Polymer (Guildf). 144 (2018) 33–42. https://doi.org/10.1016/j.polymer.2018.04.033.

[197] W.K. Setiawan, K.Y. Chiang, Silica applied as mixed matrix membrane inorganic filler for gas separation: A review, Sustain. Environ. Res. 1 (2019) 1–21. https://doi.org/10.1186/s42834-019-0028-1.

[198] C. Li, A. Qi, Y. Ling, Y. Tao, Y. Zhang, T. Li, Establishing gas transport highways in MOF-based mixed matrix membranes, 5087 (2023). https://doi.org/10.1126/sciadv.adf5087.

[199] H. Furukawa, K.E. Cordova, M. O'Keeffe, O.M. Yaghi, The chemistry and applications of metal-organic frameworks, Science (80-.). 341 (2013). https://doi.org/10.1126/science.1230444.

[200] B. Seoane, J. Coronas, J. Gascon, M. Etxeberria-Benavides, O. Karvan, J. Caro, F. Kapteijn, J. Gascon, Metal – organic framework based mixed matrix membranes : a solution for highly efficient CO2 capture ? †, Chem Soc Rev. 44 (2015) 2421–2454. https://doi.org/10.1039/c4cs00437j.

[201] R. Lin, B.V. Hernandez, L. Ge, Z. Zhu, Metal organic framework based mixed matrix membranes: An overview on filler/polymer interface, J. Mater. Chem. A. 6 (2018) 293–312. https://doi.org/10.1039/C7TA07294E.

[202] J.C. Moreton, M.S. Denny, S.M. Cohen, High MOF loading in mixed-matrix membranes utilizing styrene/butadiene copolymers† Jessica, Chem. Commun. 52 (2016) 14376–14379. https://doi.org/10.1039/c6cc07329h.

[203] A. Knebel, A. Bavykina, L. Sundermann, S.J. Datta, L. Garzon-tovar, Solution processable metal organic frameworks for gas separations : from porous liquids to mixed-matrix membranes, (n.d.) 1–29.

[204] L. Xiang, L. Sheng, C. Wang, L. Zhang, Y. Pan, Y. Li, Amino-Functionalized ZIF-7 Nanocrystals: Improved Intrinsic Separation Ability and Interfacial Compatibility in Mixed-Matrix Membranes for CO2/CH4 Separation, Adv. Mater. 29 (2017) 1–8. https://doi.org/10.1002/adma.201606999.

[205] H. Wang, S. He, X. Qin, C. Li, T. Li, Interfacial Engineering in Metal-Organic Framework-Based Mixed Matrix Membranes Using Covalently Grafted Polyimide Brushes, J. Am. Chem. Soc. 140 (2018) 17203–17210. https://doi.org/10.1021/jacs.8b10138.

[206] Z. Wong, H. Ren, S. Zhang, F. Zhang, J. Jin, Polymer of Intrinsic Microporosity/Metal Organic Framework Hybrid Membrane with Improved Interfacial Interaction for High- performance CO2 Separation, J. Mater. Chem. A. (2017). https://doi.org/10.1039/C7TA01773A.

[207] R. Lin, L. Ge, H. Diao, V. Rudolph, Z. Zhu, Ionic Liquids as the MOFs/Polymer Interfacial Binder for Efficient Membrane Separation, ACS Appl. Mater. Interfaces. 8 (2016) 32041−32049. https://doi.org/10.1021/acsami.6b11074.

[208] T.H. Lee, J.G. Jung, Y.J. Kim, J.S. Roh, H.W. Yoon, B.S. Ghanem, H.W. Kim, Y.H. Cho, I. Pinnau, H.B. Park, Defect Engineering in Metal – Organic Frameworks Towards Advanced Mixed Matrix Membranes for Efficient Propylene Propane Separation, Angew. Chemie - Int. Ed. 133 (2021) 13191–13198. https://doi.org/10.1002/ange.202100841.

[209] M. Vu, R. Lin, H. Diao, Z. Zhu, S. Bhatia, S. Smart, Effect of ionic liquids (ILs) on MOFs/polymer interfacial enhancement in mixed matrix membranes, J. Memb. Sci. 587 (2019) 117157. https://doi.org/10.1016/j.memsci.2019.05.081.

[210] Y. Sun, L. Tian, Z. Qiao, C. Geng, X. Guo, C. Zhong, Surface modification of bilayer structure on metal-organic frameworks towards mixed matrix membranes for efficient propylene / propane separation, J. Memb. Sci. 648 (2022) 120350. https://doi.org/10.1016/j.memsci.2022.120350.

[211] C. Zhang, Y. Dai, J.R. Johnson, O. Karvan, W.J. Koros, High performance ZIF-8/6FDA-DAM mixed matrix membrane for propylene/propane separations, J. Memb. Sci. 389 (2012) 34–42. https://doi.org/10.1016/j.memsci.2011.10.003.

[212] S.J.D. Smith, B.P. Ladewig, A.J. Hill, C.H. Lau, M.R. Hill, Post-synthetic Ti Exchanged UiO-66 Metal-Organic Frameworks that Deliver Exceptional Gas Permeability in Mixed Matrix Membranes, (2015) 15–18. https://doi.org/10.1038/srep07823.

[213] M.Z. Ahmad, M. Navarro, M. Lhotka, B. Zornoza, C. Téllez, W.M. de Vos, N.E. Benes, N.M. Konnertz, T. Visser, R. Semino, G. Maurin, V. Fila, J. Coronas, Enhanced gas separation performance of 6FDA-DAM based mixed matrix membranes by incorporating MOF UiO-66 and its derivatives, J. Memb. Sci. 558 (2018) 64–77. https://doi.org/10.1016/j.memsci.2018.04.040.

[214] O. de la Iglesia, S. Sorribas, E. Almendro, B. Zornoza, Metal-organic framework MIL-101 (Cr) based mixed matrix membranes for esteri fi cation of ethanol and acetic acid in a membrane reactor, Renew. Energy. 88 (2016) 12–19. https://doi.org/10.1016/j.renene.2015.11.025.

[215] T. Rodenas, M. Van Dalen, P. Serra-crespo, F. Kapteijn, J. Gascon, Mixed matrix membranes based on NH2 -functionalized MIL-type MOFs: Influence of structural and operational parameters on the CO2/CH4 separation performance, Microporous Mesoporous Mater. 192 (2014) 35–42. https://doi.org/10.1016/j.micromeso.2013.08.049.

[216] Z. Yang, Z. Wu, S. Bo, Y. Ying, H. Yang, D. Zhao, Mixed-Matrix Membranes Containing Porous Materials for Gas Separation : From Metal – Organic Frameworks to Discrete Molecular Cages, Engineering. 23 (2023) 40–55. https://doi.org/10.1016/j.eng.2022.07.022.

[217] Y. Bai, Y. Dou, L. Xie, W. Rutledge, J. Li, H. Zhou, Zr-based metal–organic frameworks: design, synthesis, structure, and applications, Chem. Soc. Rev. 45 (2016) 45, 2327–2367. https://doi.org/10.1039/C5CS00837A.

[218] N. Prasetya, B.C. Donose, B.P. Ladewig, A new and highly robust light-responsive Azo-UiO-66 for highly selective and low energy post-combustion CO2 capture and its application in a mixed matrix membrane for CO2/N2 separation, J. Mater. Chem. A. 6 (2018) 16390–16402. https://doi.org/10.1039/C8TA03553A.

[219] L. Feng, H.-B. Hou, H. Zhou, UiO-66 derivatives and their composite membranes for effective proton conduction, Dalt. Trans. 49 (2020) 17130–17139. https://doi.org/10.1039/D0DT03051A.

[220] A. Marti, S. Venna, E.A. Roth, J.T. Culp, D.P. Hopkinson, A Simple Fabrication Method for Mixed Matrix Membranes with In- situ MOF Growth for Gas Separation, ACS Appl. Mater. Interfaces. 10 (2018) 24784–24790. https://doi.org/10.1021/acsami.8b06592.

[221] Z. Tahir, M. Aslam, M.A. Gilani, M.R. Bilad, M.W. Anjum, L. Zhu, A.L. Khan, -SO3H functionalized UiO-66 nanocrystals in Polysulfone based mixed matrix membranes: Synthesis and application for efficient CO2 capture, Sep. Purif. Technol. 224 (2019) 524–533. https://doi.org/10.1016/j.seppur.2019.05.060.

[222] Y. Katayama, K.C. Bentz, S.M. Cohen, Defect-Free MOF-Based Mixed Matrix Membranes Obtained by Corona Crosslinking Defect-Free MOF-Based Mixed Matrix Membranes Obtained by Corona Crosslinking, ACS Appl. Mater. Interfaces. 11 (2019) 13029–13037. https://doi.org/10.1021/acsami.9b02539.

[223] H. Wang, Y. Ni, Z. Dong, Q. Zhao, A mechanically enhanced metal-organic framework/PDMS membrane for CO2/N2 separation, React. Funct. Polym. 160 (2021) 104825. https://doi.org/10.1016/j.reactfunctpolym.2021.104825.

[224] R. Thür, N. Van Velthoven, S. Slootmaekers, J. Didden, R. Verbeke, S. Smolders, M. Dickmann, W. Egger, D. De Vos, I.F.J. Vankelecom, Bipyridine-based UiO-67 as novel fi ller in mixed-matrix membranes for CO2-selective gas separation, J. Memb. Sci. 576 (2019) 78–87. https://doi.org/10.1016/j.memsci.2019.01.016.

[225] S.B. Peh, A. Karmakar, D. Zhao, Multiscale Design of Flexible Metal – Organic Frameworks, Trends Chem. 2 (2020) 199–213. https://doi.org/10.1016/j.trechm.2019.10.007.

[226] Y. Fan, C. Li, X. Zhang, X. Yang, X. Su, H. Ye, N. Li, Tröger's base mixed matrix membranes for gas separation incorporating NH2-MIL-53(Al) nanocrystals, J. Memb. Sci. 573 (2019) 359–369. https://doi.org/10.1016/j.memsci.2018.12.004.

[227] M. Loloei, S. Kaliaguine, D. Rodrigue, Mixed matrix membranes based on NH2-MIL-53 (Al) and 6FDA-ODA polyimide for CO2 separation: Effect of the processing route on improving MOF-polymer interfacial interaction, Sep. Purif. Technol. 270 (2021) 118786. https://doi.org/10.1016/j.seppur.2021.118786.

[228] W.W. Lestari, M.A. Khafidhin, R. Wijiyanti, N. Widiastuti, D. Suci, Novel mixed matrix membranes based on polyethersulfone and MIL-96 (Al) for - CO2 gas separation, Chem. Pap. 96 (2021). https://doi.org/10.1007/s11696-021-01562-6.

[229] A. Nuhnen, M. Klopotowski, H.B.T. Jeazet, S. Sorribas, B. Zornoza, C. Téllez, J. Coronas, C. Janiak, High performance MIL-101(Cr)@6FDA-mPD and MOF-199@6FDA-mPD mixed-matrix membranes for CO2/CH4 separation†, Dalt. Trans. 49 (2020) 1822. https://doi.org/10.1039/C9DT03222C.

[230] H.N. Suhaimi, F.Y. Yeong, N. Jusoh, T.L. Chew, M.A. Bustam, S. Suleman, Separation of CO2 from CH4 using mixed matrix membranes incorporated with amine functionalized MIL-125 (Ti) nanofiller, Chem. Eng. Res. Des. 159 (2020) 236–247. https://doi.org/10.1016/j.cherd.2020.04.020.

[231] Y. Fan, H. Yu, S. Xu, Q. Shen, H. Ye, N. Li, Zn(II)-modified imidazole containing polyimide/ZIF-8 mixed matrix membranes for gas separations, J. Memb. Sci. (2020) 117775. https://doi.org/10.1016/j.memsci.2019.117775.

[232] C. Zhang, Y. Dai, J.R. Johnson, O. Karvan, W.J. Koros, High performance ZIF-8/6FDA-DAM mixed matrix membrane for propylene/propane separations, J. Memb. Sci. 389 (2012) 34–42. https://doi.org/10.1016/j.memsci.2011.10.003.

[233] P. Tang, P.B. So, W. Li, Z. Hui, C. Hu, C. Lin, Carbon Dioxide Enrichment PEBAX/MOF Composite Membrane for CO2 Separation, Membranes (Basel). 11 (2021) 404.

[234] D.A. Kang, K. Kim, J. Yup, J. Tae, J. Hak, Mixed matrix membranes consisting of ZIF-8 in rubbery amphiphilic copolymer : Simultaneous improvement in permeability and selectivity, Chem. Eng. Res. Des. 153 (2019) 175–186. https://doi.org/10.1016/j.cherd.2019.10.009.

[235] X. Zhang, T. Zhang, Y. Wang, J. Li, C. Liu, N. Li, J. Liao, Mixed-matrix membranes based on Zn Ni-ZIF-8-PEBA for high performance CO2 separation, J. Memb. Sci. 560 (2018) 38–46. https://doi.org/10.1016/j.memsci.2018.05.004.

[236] Z. Gu, Z. Yang, X. Guo, Z. Qiao, C. Zhong, Vacuum resistance treated ZIF-8 mixed matrix membrane for effective CH4/N2 separation, Sep. Purif. Technol. 272 (2021) 118845. https://doi.org/10.1016/j.seppur.2021.118845.

[237] Y. Liu, J. Zhang, X. Tan, High Performance of PIM-1/ZIF-8 Composite Membranes for O2/N2 Separation, ACS Omega. 4 (2019) 16572. https://doi.org/10.1021/acsomega.9b02363.

[238] J. Gao, H. Mao, H. Jin, C. Chen, A. Feldhoff, Y. Li, Functionalized ZIF-7/Pebax ® 2533 mixed matrix membranes for CO2/N2 separation, Microporous Mesoporous Mater. 297 (2020) 110030. https://doi.org/10.1016/j.micromeso.2020.110030.

[239] M. Safak Boroglu, A.B. Yumru, Gas separation performance of 6FDA-DAM-ZIF-11 mixed-matrix membranes for H2/CH4 and CO2/CH4 separation, Sep. Purif. Technol. 173 (2017) 269–279. https://doi.org/10.1016/j.seppur.2016.09.037.

[240] M. Mubashir, L.F. Dum, J. Lukose, W.S. Chai, P. Loke, Cellulose acetate-based membranes by interfacial engineering and integration of ZIF-62 glass nanoparticles for CO2 separation, J. Hazard. Mater. 415 (2021) 125639. https://doi.org/10.1016/j.jhazmat.2021.125639.

[241] C. Ye, X. Wu, H. Wu, L. Yang, Y. Ren, Y. Wu, Y. Liu, Z. Guo, R. Zhao, Z. Jiang, Incorporating nano-sized ZIF-67 to enhance selectivity of polymers of intrinsic

microporosity membranes for biogas upgrading, Chem. Eng. Sci. 216 (2020) 115497. https://doi.org/10.1016/j.ces.2020.115497.

[242] S. Feng, M. Bu, J. Pang, W. Fan, L. Fan, H. Zhao, G. Yang, H. Guo, G. Kong, H. Sun, Z. Kang, D. Sun, Hydrothermal stable ZIF-67 nanosheets via morphology regulation strategy to construct mixed-matrix membrane for gas separation, J. Memb. Sci. 593 (2020) 117404. https://doi.org/10.1016/j.memsci.2019.117404.

[243] M. van Essen, L. van den Akker, R. Thür, M. Houben, I.F.J. Vankelecom, Z. Borneman, K. Nijmeijer, Investigation of ZIF-78 Morphology and Feed Composition on the Mixed Gas CO2/N2 Separation Performance in Mixed Matrix Membranes, Adv. Mater. Interfaces. 8 (2021). https://doi.org/10.1002/admi.202001478.

[244] I. Ilicak, M.S. Boroglu, A. Durmus, I. Boz, Journal of Natural Gas Science and Engineering Influence of ZIF-95 on structure and gas separation properties of polyimide-based mixed matrix membranes, J. Nat. Gas Sci. Eng. 91 (2021) 103941. https://doi.org/10.1016/j.jngse.2021.103941.

[245] J. Yuan, H. Zhu, J. Sun, Y. Mao, G. Liu, W. Jin, Novel ZIF-300 Mixed-Matrix Membranes for Efficient CO Capture, (2017). https://doi.org/10.1021/acsami.7b12507.

[246] A.S. Ghanem, M. Ba-shammakh, M. Usman, M.F. Khan, H. Dafallah, M.A.M. Habib, B.A. Al-maythalony, High gas permselectivity in ZIF-302 polyimide self-consistent mixed- matrix membrane, J. Appl. Polym. Sci. 48513 (2019) 1–11. https://doi.org/10.1002/app.48513.

[247] S. Japip, H. Wang, Y. Xiao, T.S. Chung, Highly permeable zeolitic imidazolate framework (ZIF)-71 nano-particles enhanced polyimide membranes for gas separation, J. Memb. Sci. 467 (2014) 162–174. https://doi.org/10.1016/j.memsci.2014.05.025.

[248] Y. Liu, G. Liu, C. Zhang, W. Qiu, S. Yi, V. Chernikova, Z. Chen, Y. Belmabkhout, O. Shekhah, M. Eddaoudi, W. Koros, Enhanced CO2/CH4 Separation Performance of a Mixed Matrix Membrane Based on Tailored MOF-Polymer Formulations, Adv. Sci. 5 (2018) 2–6. https://doi.org/10.1002/advs.201800982.

[249] N. Tien-Binh, H. Vinh-Thang, X.Y. Chen, D. Rodrigue, S. Kaliaguine, Crosslinked MOF-polymer to enhance gas separation of mixed matrix membranes, J. Memb. Sci. 520 (2016) 941–950. https://doi.org/10.1016/j.memsci.2016.08.045.

[250] K. Chen, K. Xu, L. Xiang, X. Dong, Y. Han, C. Wang, L.B. Sun, Y. Pan, Enhanced CO2/CH4 separation performance of mixed-matrix membranes through dispersion of sorption-selective MOF nanocrystals, J. Memb. Sci. 563 (2018) 360–370. https://doi.org/10.1016/j.memsci.2018.06.007.

[251] G. Liu, V. Chernikova, Y. Liu, K. Zhang, Y. Belmabkhout, O. Shekhah, C. Zhang, S. Yi, M. Eddaoudi, W.J. Koros, Mixed matrix formulations with MOF molecular sieving for key energy-intensive separations, Nat. Mater. 17 (2018) 283–289. https://doi.org/10.1038/s41563-017-0013-1.

[252] G. Liu, A. Cadiau, Y. Liu, K. Adil, V. Chernikova, I.D. Carja, Y. Belmabkhout, M. Karunakaran, O. Shekhah, C. Zhang, A.K. Itta, S. Yi, M. Eddaoudi, W.J. Koros, Enabling Fluorinated MOF-Based Membranes for Simultaneous Removal of H2S and CO2 from Natural Gas, Angew. Chemie - Int. Ed. 57 (2018) 14811–14816. https://doi.org/10.1002/anie.201808991.

[253] N. Prasetya, A.A. Teck, B.P. Ladewig, Matrimid-JUC-62 and Matrimid-PCN-250 mixed matrix membranes displaying light-responsive gas separation and beneficial ageing characteristics for CO2/N2 separation, Sci. Rep. 8 (2018) 1–14. https://doi.org/10.1038/s41598-018-21263-7.

[254] S. Shahid, K. Nijmeijer, Performance and plasticization behavior of polymer-MOF membranes for gas separation at elevated pressures, J. Memb. Sci. 470 (2014) 166–177. https://doi.org/10.1016/j.memsci.2014.07.034.

[255] H.B. Tanh Jeazet, C. Staudt, C. Janiak, Metal-organic frameworks in mixed-matrix membranes for gas separation, Dalt. Trans. 41 (2012) 14003–14027. https://doi.org/10.1039/c2dt31550e.

[256] M. Valero, B. Zornoza, C. Téllez, J. Coronas, Mixed matrix membranes for gas separation by combination of silica MCM-41 and MOF NH2-MIL-53(Al) in glassy

polymers, Microporous Mesoporous Mater. 192 (2014) 23–28. https://doi.org/10.1016/j.micromeso.2013.09.018.

[257] P. Burmann, B. Zornoza, C. Téllez, J. Coronas, Mixed matrix membranes comprising MOFs and porous silicate fillers prepared via spin coating for gas separation, Chem. Eng. Sci. 107 (2014) 66–75. https://doi.org/10.1016/j.ces.2013.12.001.

[258] Y. Cheng, S.J. Datta, S. Zhou, J. Jia, O. Shekhah, M. Eddaoudi, Advances in metal–organic framework-based membranes, Chem Soc Rev Adv. 51 (2022) 8300–8350. https://doi.org/10.1039/d2cs00031h.

[259] Y.L. Liu, K.T. Takata, Y.M. Mukai, H.K. Kita, K.T. Tanaka, Nano-porous Zeolite and MOF Filled Mixed Matrix Membranes for Gas Separation, MATEC Web Conf. 33 (2021) 04008.

[260] M. Askari, T.S. Chung, Natural gas purification and olefin/paraffin separation using thermal cross-linkable co-polyimide/ZIF-8 mixed matrix membranes, J. Memb. Sci. 444 (2013) 173–183. https://doi.org/10.1016/j.memsci.2013.05.016.

[261] H.T. Kwon, H. Jeong, A.S. Lee, H.S. An, J.S. Lee, H.T. Kwon, H. Jeong, A.S. Lee, H.S. An, J.S. Lee, Heteroepitaxially-grown Zeolitic Imidazolate Framework Membranes with Unprecedented Propylene / Propane Separation Performances, J. Am. Chem. Soc. (2015). https://doi.org/10.1021/jacs.5b06730.

[262] P. Krokidas, M. Castier, S. Moncho, D.N. Sredojevic, N. Edward, H.T. Kwon, H. Jeong, J.S. Lee, I.G. Economou, ZIF-67 Framework : A Promising New Candidate for Propylene / Propane Separations - Experimental Data and Molecular Simulations ZIF-67 Framework : a Promising New Candidate for Propylene / Propane Separation Experimental Data and Molecular Simulations, (2016). https://doi.org/10.1021/acs.jpcc.6b00305.

[263] H. An, S. Park, H.T. Kwon, H.K. Jeong, J.S. Lee, A new superior competitor for exceptional propylene/propane separations: ZIF-67 containing mixed matrix membranes, Poster Sess. 2017 - Core Program. Area 2017 AIChE Annu. Meet. 3 (2017) 1362–1371. https://doi.org/10.1016/j.memsci.2016.12.053.

[264] Y. Liu, Z. Chen, G. Liu, Y. Belmabkhout, K. Adil, M. Eddaoudi, W. Koros, Conformation-Controlled Molecular Sieving Effects for Membrane-Based Propylene/Propane Separation, Adv. Mater. 31 (2019) 1–7. https://doi.org/10.1002/adma.201807513.

[265] G. Chen, X. Chen, Y. Pan, Y. Ji, G. Liu, W. Jin, M-gallate MOF/6FDA-polyimide mixed-matrix membranes for C2H4/C2H6 separation, J. Memb. Sci. 620 (2021) 118852. https://doi.org/10.1016/j.memsci.2020.118852.

[266] J.E. Bachman, Z.P. Smith, T. Li, T. Xu, J.R. Long, Enhanced ethylene separation and plasticization resistance in polymer membranes incorporating metal – organic framework nanocrystals, Nature. (2016) 1–7. https://doi.org/10.1038/NMAT4621.

[267] Y. Feng, L. Yu, K. Zhang, W. Fan, L. Fan, Z. Kang, D. Sun, Fabrication of mixed matrix membranes with regulated MOF fillers via incorporating guest molecules for optimizing light hydrocarbon separation performance†, CrystEngComm. 24 (2022) 7658–7668. https://doi.org/DOI https://doi.org/10.1039/D2CE01073A.

[268] F. Moghadam, T.H. Lee, I. Park, H.B. Park, Thermally annealed polyimide-based mixed matrix membrane containing ZIF-67 decorated porous graphene oxide nanosheets with enhanced propylene/propane selectivity, J. Memb. Sci. 603 (2020) 118019. https://doi.org/10.1016/j.memsci.2020.118019.

[269] Z. Sumer, S. Keskin, Computational Screening of MOF-Based Mixed Matrix Membranes for CO2/N2 Separations, J. Nanomater. 2016 (2016). https://doi.org/10.1155/2016/6482628.

[270] S. Keskin, S.A. Altinkaya, A Review on Computational Modeling Tools for MOF-Based Mixed Matrix Membranes, Computation. 7 (2019).

[271] S. Keskin, D.S. Sholl, Selecting metal organic frameworks as enabling materials in mixed matrix membranes for high efficiency natural gas purification, Energy Environ. Sci. 3 (2010) 343–351. https://doi.org/10.1039/c003390c.

[272] H. Demir, H. Daglar, H.C. Gulbalkan, G.O. Aksu, S. Keskin, Recent advances in computational modeling of MOFs: From molecular simulations to machine learning, Coord. Chem. Rev. 484 (2023) 215112. https://doi.org/10.1016/j.ccr.2023.215112.

[273] H. Daglar, S. Aydin, S. Keskin, MOF-based MMMs breaking the upper bounds of polymers for a large variety of gas separations, Sep. Purif. Technol. 281 (2022) 119811. https://doi.org/10.1016/j.seppur.2021.119811.

[274] S. Budhathoki, O. Ajayi, A. Steckel, C.E. Wilmer, Environmental Science High-throughput computational prediction of the membranes †, (2018). https://doi.org/10.1039/c8ee02582g.

[275] H. Demir, S. Keskin, A New Era of Modeling MOF-Based Membranes: Cooperation of Theory and Data Science, Macromol. Mater. Eng. 2300225 (2023) 1–15. https://doi.org/10.1002/mame.202300225.

[276] T. Yuan, L. Sarkisov, Lattice Model of Fluid Transport in Mixed Matrix Membranes, Adv. Theory Simulations. 2200159 (2022) 1–11. https://doi.org/10.1002/adts.202200159.

[277] L. Zhang, Z. Hu, J. Jiang, Metal-organic framework/polymer mixed-matrix membranes for H 2/CO 2 separation: A fully atomistic simulation study, J. Phys. Chem. C. 116 (2012) 19268–19277. https://doi.org/10.1021/jp3067124.

[278] R. Semino, N.A. Ramsahye, A. Ghou, G. Maurin, Microscopic Model of the Metal − Organic Framework / Polymer Interface : A First Step toward Understanding the Compatibility in Mixed Matrix Membranes, ACS Appl. Mater. Interfaces. 8 (2016) 809–819. https://doi.org/10.1021/acsami.5b10150.

[279] R. Semino, N.A. Ramsahye, A. Ghoufi, G. Maurin, Role of MOF surface defects on the microscopic structure of MOF/polymer interfaces: A computational study of the ZIF-8/PIMs systems, Microporous Mesoporous Mater. 254 (2017) 184–191. https://doi.org/10.1016/j.micromeso.2017.02.031.

[280] A. Ozcan, R. Semino, G. Maurin, A.O. Yazaydin, Modeling of Gas Transport through Polymer/MOF Interfaces: A Microsecond-Scale Concentration Gradient-Driven Molecular

Dynamics Study, Chem. Mater. 32 (2020) 1288–1296. https://doi.org/10.1021/acs.chemmater.9b04907.

[281] D. Fan, A. Ozcan, N.A. Ramsahye, D. Zhao, G. Maurin, R. Semino, Is Porosity at the MOF/Polymer Interface Necessarily an Obstacle to Optimal Gas-Separation Performances in Mixed Matrix Membranes?, ACS Mater. Lett. 3 (2021) 344–350. https://doi.org/10.1021/acsmaterialslett.0c00560.

[282] M. Balçık, S.B. Tantekin-Ersolmaz, M.G. Ahunbay, Interfacial analysis of mixed-matrix membranes under exposure to high-pressure CO2, J. Memb. Sci. 607 (2020). https://doi.org/10.1016/j.memsci.2020.118147.

[283] R.C. Dutta, S.K. Bhatia, Interfacial Engineering of MOF-Based Mixed Matrix Membrane through Atomistic Simulations, J. Phys. Chem. C. 124 (2020) 594–604. https://doi.org/10.1021/acs.jpcc.9b09384.

[284] P. Ortiz-albo, H. Takaba, I. Kumakiri, J.G. Crespo, L.A. Neves, An overview of Molecular Simulations Studies in Mixed Matrix Membranes for Gas Separation Processes, J. Membr. Sci. Res. 8 (2022) 549436. https://doi.org/10.22079/JMSR.2022.549436.1536.

[285] H. Daglar, I. Erucar, S. Keskin, Recent advances in simulating gas permeation through MOF membranes, Mater. Adv. 2 (2021) 5300–5317. https://doi.org/10.1039/d1ma00026h.

CHAPTER 2

MOLECULAR SIMULATION

2.1 Introduction

Molecular simulation methods are powerful tools that aim to simulate the behavior and interactions of molecules at the atomistic levels. It involves the application of numerical methods and theoretical models to investigate diverse aspects of molecular systems, including their structure, dynamics, thermodynamics, and properties. Molecular simulation, facilitated by computer algorithms, enables scientists to explore phenomena that that can only be accessible by considering sophisticated experiments. Many researches widely used molecular simulation methods in various fields, including computational chemistry, biochemistry, material science, drug discovery, and nanotechnology. The rapid developments of mathematical methods and computational software and hardware offer a unique platform to assist the experimentalist from the birth of new materials to the characterization of their performances for a wide range of applications. Molecular modelling embodies force field and quantum-chemical methods that model a system at the atomistic/electronic levels respectively. They enable to construct reliable microscopic representations of the systems of interest that are further used to simulate the adsorption/diffusion properties for a wide variety of gas(vapor)/systems to gain microscopic insight into guest adsorption/diffusion mechanisms, rationalize the experimental/simulated data and further guide the experimentalist towards the discovery of refined systems with even better performances. This chapter offers a brief overview of the theoretical methods employed for modelling MOFs such as ZIF-67 and UTSA-280, along with polymers and their composites as well as their adsorption/diffusion properties for a given guest molecules.

Hence, the chapter provides a concise overview of statistical ensembles, force fields, and molecular simulation methods, using a minimal number of mathematical equations to explain the computational approach behind the PhD study. For more details, the readers are referred to specialized books and review articles provided in each section to get more technical details.

2.2 Statistical Ensembles

The concept of statistical ensemble is fundamental in the field of statistical mechanics, providing a powerful tool to bridging the microstates of a system and the macroscopic properties of large systems. A statistical ensemble comprises a collection of various states of the system, each satisfying a specific set of constraints, such as an imposed temperature or a fixed number of molecules. In molecular simulation, researchers generate multiple configurations of the system and calculate the average of these configurations to perform the desired measurements. Depending on the desired application, various statistical ensembles can be employed, each defined by specific constrained variables and its associated probability density. These ensembles enable the analysis of different aspects of the system and provide valuable information about the likelihood of different states occurring within the ensemble [1,2]. There are several different types of statistical ensembles, depending on the type of system and the conditions, which are listed on Table 2.1.

Table 2.1 : Statistical ensembles [1].

Statistical ensemble	**Imposed variables**	**Probability density**
Microcanonical	*N, V, E*	$\exp(-\beta\varepsilon_i)$
Canonical	*N, V, T*	$\exp(-\beta\varepsilon_i)$
Grand Canonical	μ_i, V, T	$\exp\left(-\beta\varepsilon_i - \beta\sum_j \mu_j N_{ji}\right)$
Isothermal-Isobaric	*N, P, T*	$\exp(-\beta\varepsilon_i - \beta PV_i)$
Gibbs at imposed global volume (m phases)	$N = N_1 + \ldots N_m$, $V = V + \ldots V_m$, T	$\exp(-\beta\varepsilon_i)$
Gibbs at imposed global pressure (m phases)	$N = N_1 + \ldots N_m$, *P, T*	$\exp(-\beta\varepsilon_i - \beta PV_i)$

In the formulations of statistical ensembles presented in Table 2.1, N is number of molecules, V is system volume, T is temperature, P is pressure and μ_i is chemical potential of molecular type i. The probability density is given in phase space of all positions and momenta, where ε is total energy (kinetic+potential).

For a given problem, selecting the ensemble type is typically guided by aligning the constraints with variables controlled in the experimental setup. Unconstrained variables are able to fluctuate, and their statistical averages yield predictions that can be compared with experimental outcomes [1].

In order to compare MD results with experimental data, it is often desirable to work at conditions where temperature and/or pressure are held constant.

The microcanonical ensemble (NVE), the most fundamental one, describes an ideally isolated system with a constant volume that cannot exchange particles or energy with its surroundings (constant energy). Its probability density is

$$P_i \propto \exp(-\beta\varepsilon_i) \tag{2.1}$$

where P_i is the probability of a microstate i, $\varepsilon_i$represents the energy of the system state. β, Boltzman factor serving as a weighting factor to all the energies, is determined using Equation 2.2 where k is the Boltzman constant and equals to 1.381 10^{-23} $J.K^{-1}$.

$$\beta = \frac{1}{kT} \tag{2.2}$$

For example, entropy (S) can be obtained directly from the microcanonical partition function.

$$S = k \ln (Z_{NVE}) \tag{2.3}$$

where Z represents the total number of states found in each ensemble.

The canonical ensemble (NVT), which maintains fixed temperature, volume and number of molecules, is commonly used for monophasic fluids with known densities. This ensemble was developed for original Monte Carlo (MC) simulations by Metropolis et al.[3] in 1953. In classical thermodynamics, energy is typically imposed to the system. However, in the

canonical ensemble, the energy fluctuates such that the collection includes system states at different energy levels. We can calculate the average energy, denoted ⟨E⟩:

$$\langle E \rangle = \frac{1}{m} \sum_{i=1}^{m} E_i \tag{2.4}$$

where m is the number of system states in the ensemble. The energy of a particular state of the system may not provide meaningful insights, but the average energy, can be compared with experimental results.

$$\varepsilon = \frac{N_A}{N} \langle E \rangle \tag{2.5}$$

where ε is molar energy, N_A= 6.02 10^{23} is Avogadro's number and N is the total number of molecules of the system. The Helmholtz function (A) is associated with the canonical ensemble, as demonstrated in Equation 2.6.

$$A = -k\,T \ln (\mathrm{Z_{NVT}}) \tag{2.6}$$

Another statistical ensemble is the isothermal-isobaric ensemble (NPT), wherein pressure is controlled instead of volume, and it utilizes the average volume of the system to predict fluid density. The NPT ensemble is particularly useful for determining the density of a gas mixture under known pressure and temperature conditions. It is probability density is defined as follows:

$$\mathrm{P_i} \propto \exp(-\beta\varepsilon_\mathrm{i} - \beta \mathrm{P V_i}) \tag{2.7}$$

where $\mathrm{V_i}$ is the volume of system state i. Due to the fluctuations of volume, the volume of an individual state does not follow an equation of state, but the average volume does. The Gibbs ensemble is the most commonly used ensemble for phase equilibrium calculations. It introduces two phases without an explicit interface. It can be achieved by imposing the global volume or the pressure of the two phases. For pure compounds, it is applied at constant volume to respect the phase rule and provides equilibrium properties like saturated vapor pressure, vaporization enthalpy, and coexisting densities of the liquid and vapor. For

mixtures, the Gibbs ensemble can be applied at either an imposed volume or an imposed pressure. Gibbs free energy (G) is thus expressed as follows:

$$G = -k\,T \ln\left(\mathrm{Z_{NPT}}\right) \tag{2. 8}$$

Alternatively, we can express G,

$$G = U - TS + PV = F + PV \tag{2.9}$$

where U is the total energy, T is the temperature of the thermostat, S is the entropy and V is the volume of the system. For a single component is directly related to the chemical potential μ

$$G = \mu N \tag{2.10}$$

The Grand Canonical ensemble (μVT) is particularly suitable for studying adsorption in microporous solids. In this ensemble, the imposed variables include the temperature, volume, and chemical potential of each species. Its probability density is given by the following equation:

$$\mathrm{P_i} \propto \exp\left(-\beta\varepsilon_\mathrm{i} - \beta\sum_j \mu_j N_{ji}\right) \tag{2.11}$$

where the chemical potential μ_j of each species j are the imposed variables and N_{ji} is the number of molecules of type j in system state i. In the context of adsorption on porous solids, the chemical potentials can be determined from the partial pressure each guest molecules while the energy computation must consider the interaction energy between each molecule and the porous materials. The pressure (P) is the appropriate thermodynamic function for the grand canonical ensemble.

$$PV = -k\,T \ln\left(\mathrm{Z_{\mu VT}}\right) \tag{2.12}$$

There are primarily two methods to simulate statistical ensembles (Figure 2.1): molecular dynamics, which is a powerful technique for calculating both the equilibrium and dynamical

properties where the equations of motion are solved, and Monte Carlo simulation, which employs time independent stochastic method that depends on probabilities via random configurations. Average properties can be derived from time averages in MD and ensemble averages in MC. These two types of averages are equivalent, thanks to the ergodicity theorem.

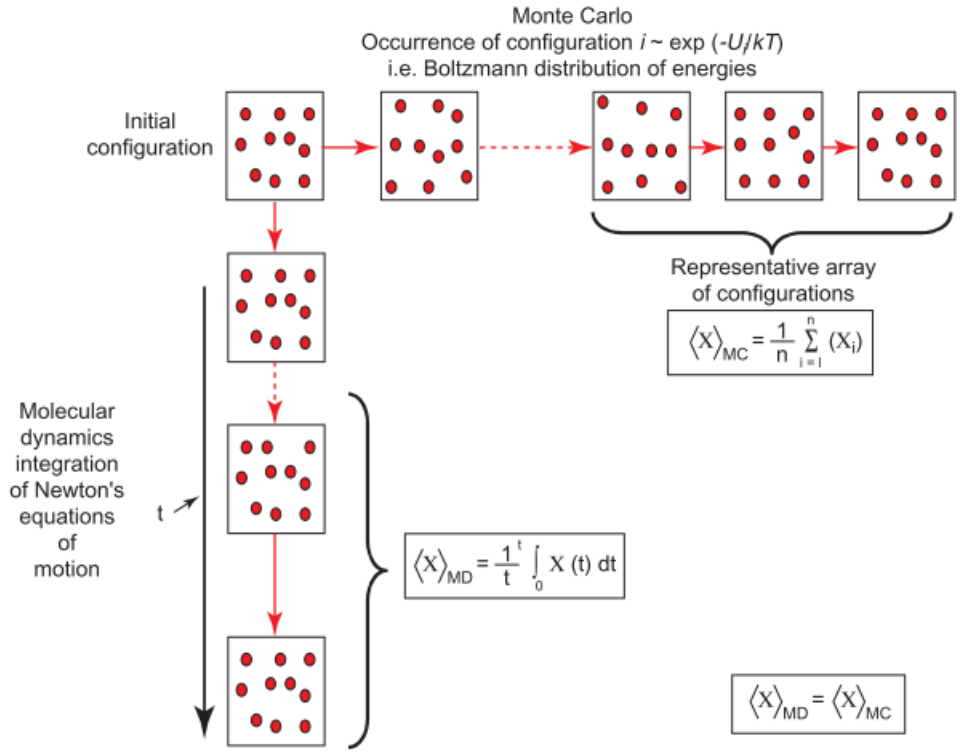

Figure 2.1 : Illustration of the use of MC and MD simulations to build a reliable statistical ensemble and extract the desired properties [2].

2.3 Microscopic models for MOFs, polymers and MOF/polymer composites

The first pre-requirement to explore the sorption properties of polymers, MOFs, and MOF/polymer composites consists of building a realistic atomistic description of them. For sake of clarity, I have deliberately made the choice to describe the procedures in details in the Chapter 3 dealing with the construction of atomistic models for the polymers that are validated in light their computed densities that match well the experimental values as well as the MOF/polymer models.

Basically for the ZIF-67/polymer models, the methodology involves obtaining spherical shaped-atomistic ZIF-67 surface models with its outer surface is terminated by based on the chosen solvent, which is then coupled with various polymers to create composites using Materials Studio 7 ® [4] software. Subsequently, Force-field MD simulations are employed to refine and optimize these models and calculate the necessary properties for a comprehensive analysis. The number of polymer chains was controlled in order to build atomistic models corresponding to different filler loadings of ZIF-67 in the resulting composites.

Further, sorption simulations of guest molecules in the polymers, ZIF-67 NP models and their composites were carried out using a hybrid approach combining Grand Canonical Monte Carlo (GCMC) and MD simulations via LAMMPS [5] code to enable for the capture of possible guest-induced relaxation of the overall systems.

2.4 Force fields

Accurate descriptions of relatively small systems containing hundreds of atoms can be achieved at the electronic level through quantum mechanics (QM) calculations. However, with limited computational power, QM calculations cannot be applied to large systems as it the case for the adsorption of olefin/paraffin in Mixed Matrix Membranes, my topic of interest. Hence, to simulate the system sizes ranging from a few thousands to a few millions of atoms, several approximations are introduced. These approximations are implemented through the use appropriate forms and parameters of a mathematical function selected to reproduce as fairly as possible the potential energy of the overall system. This so-called force field function and parameter sets are issued from the literature derived using ab initio calculations or semi-empirical approaches [6]. To avoid any ambiguity, the readers should bear in mind that the terms ‘force field’ and ‘interatomic potentials’ currently manipulated by the modelers in the literature and employed along the manuscript refer to an energy term.

Therefore, the potential energy of a system can be analytically expressed as a sum of bonded (U_{bonded}) and non-bonded ($U_{non-bonded}$) energy terms:

$$U = U_{bonded} + U_{non-bonded} \tag{2.13}$$

The bonded interactions also called intramolecular interactions are expressed by bond stretching, angle bending, torsional/dihedral (implying four consecutive atoms) and inversion (associated with one atom having three bonds with three other atoms) as presented in Equation 2.14.

$$U_{bonded} = U_{bonding} + U_{bending} + U_{torsion/dihedral} + U_{inversion} \quad (2.14)$$

The non-bond terms also called intermolecular interactions are usually expressed by the sum of two terms, i.e. the repulsion-dispersion and the electrostatic interactions (see equation 2.15). The repulsion-dispersion term is the electron dispersion effect, generally modeled by van der Waals interactions. In molecular simulations, the van der Waals intermolecular interactions are typically considered between all pairs of atoms from different molecules and between atoms within the same molecule that are separated by at least three bonds. Hence, the intermolecular interaction energy is defined as follows:

$$U_{non-bonded} = U_{repulsion-dispersion} + U_{electrostatic} \quad (2.15)$$

For liquids and polymers, non-bonded interactions are commonly modeled using a Lennard-Jones (LJ) 12-6 potential for van der Waals interactions, along with a Coulombic potential for electrostatic interactions. The most common van der Waals interactions of Lennard-Jones (LJ) 12-6 potential, given as Equation 2.16.

$$U_{vdw} = \sum_{\substack{i,j \\ i<j}} 4\epsilon_{ij}\left[\left(\frac{\sigma_{ij}}{r_{ij}}\right)^{12} - \left(\frac{\sigma_{ij}}{r_{ij}}\right)^{6}\right] \quad (2.16)$$

where, i and j represents the atoms i and j, r_{ij} defines the separating distance between atoms, ϵ_{ij} represents the well depth of energy and measures the strength of interactions between the two atoms and σ_{ij} corresponds to the van der Waals diameter of i and j atoms that defines how close two non-bonding atoms can get. The term r^{-6} corresponds to the attractive force at long distance, while the term r^{-12} represents the repulsive force at short distance as illustrated in Figure 2.2. The Lennard-Jones potential has its minimum at a distance of $r = r_{min} = 2^{\frac{1}{6}}\sigma$

Other analytical potentials to describe the van der Waals interactions include Morse and Buckingham potentials.

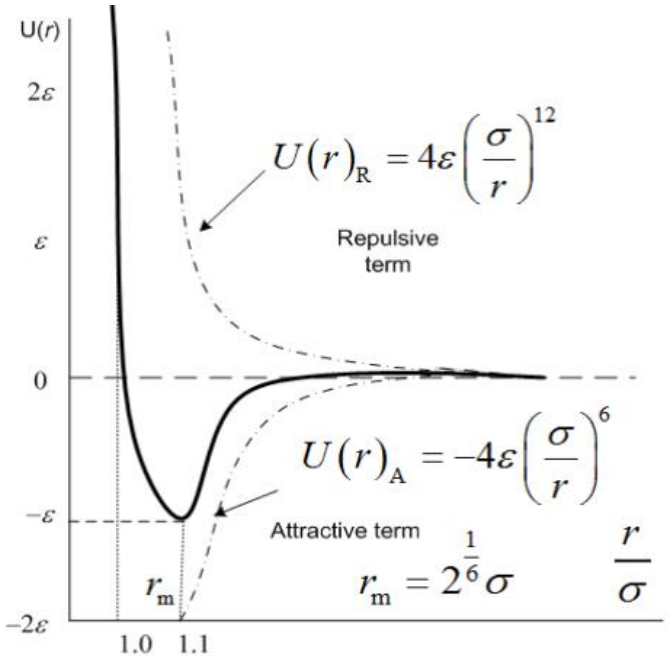

Figure 2.2 : Representation of the Lennard-Jones potential to describe the interactions between two atom pairs. [7].

The electrostatic term is widely modeled by the interactions between the partial charges carried out by the two atoms i and j, i.e. q_i and q_j with the following equation:

$$U_{electrostatic} = \frac{1}{4\pi\epsilon_0}\sum_{i,j}\frac{q_i q_j}{|r_{ij}|} \tag{2.17}$$

where r_{ij} is the separating distance between the two atoms and ϵ_0 corresponds to the vacuum permittivity.

The sensitivity of electrostatic interactions to long-range order is higher compared to van der Waals interactions. Therefore, calculations for every periodic image are necessary, as the truncation approximation is applied with the use of a cut-off distance. It should be noted that utilization of periodic boundary conditions is another important aspect for force field based simulations. Indeed, to prevent any interactions between particles and their own mirror images, it is crucial to ensure that the shortest cell dimensions are at least twice the selected cutoff distance. Most of the time, the cut off distance of 12 Å is a default value usually

applied to explore solid state. The Ewald summation [8] is the most used method to assess the electrostatic interactions.

In Ewald summation, the electrostatic potential is separated into short-range and long-range interactions, each of which is handled in real and Fourier space, respectively. The utilization of Fourier space enables the incorporation of periodic boundary conditions (PBC). In this procedure, point charges can be screened by an opposite charge distribution, typically represented by a Gaussian function with a width of $\sqrt{2/\alpha}$, as defined by Equation 2.18. The parameter α represents an empirical value, typically chosen as $\alpha = 3.2/(l_{min}/2)$, where l_{min} corresponds to the smallest side length of the simulation box. This charge distribution is then neutralized by applying another Gaussian distribution in the Fourier space, which can be applied periodically.

$$\rho^{\text{Gaussian}}(r) = -q_i \left(\frac{\alpha}{\pi}\right)^{\frac{3}{2}} \exp(-\alpha^2 r^2) \tag{2.18}$$

The Coulombic potential in a periodic system, as given by Equation 2.19 can be expressed using three-term functions, as given in Equation 2.20.

$$U_{elec} = \frac{1}{2}\frac{1}{4\pi\epsilon_0}\sum_n \sum_i \sum_j \frac{q_i q_j}{|r_{ij} + nL|} \tag{2.19}$$

$$U_{elec} = \frac{1}{4\pi\epsilon_0}\frac{1}{2}\sum_n \sum_i \sum_j \frac{q_i q_j}{|r_i - r_j + nL|} erfc\left(\frac{|r_i - r_j + nL|}{\sqrt{2}\sigma}\right) + \frac{1}{2\epsilon_0}\sum_{k\neq 0} \frac{e^{\frac{-\sigma^2 k^2}{2}}}{k^2}|S(k)|^2 - \frac{1}{4\pi\epsilon_0}\frac{1}{\sqrt{2\pi}\sigma}\sum_{i=1}^{N} q_i^2 \tag{2.20}$$

where k is a vector of the reciprocal space defined as $k = (2\pi/L)a$, with a corresponding to the lattice vectors in the Fourier space. The term $\text{erfc}\left(\frac{|r_i - r_j + nL|}{\sqrt{2}\sigma}\right)$ represents a complementary error function, which gradually approaches 0 as r increases. In summary, the Ewald summation method involves the substitution of point charges with a combination of screened charges and Gaussian distributions. The interactions associated with screened charges are

computed in real space, while those related to the Gaussian distributions are summed in Fourier space.

Numerous different force fields have been formulated for diverse systems, and their respective parameters, as well as their validation, have been documented extensively in the literature. Typically, parameterization involves adjusting each type of interaction with the overarching objective of reproducing specific experimental properties. There are many generic force fields available in the literature, such as Universal Force Field (UFF) [9] to describe inorganic systems while organic and biological molecules are generally described by the Transferable Potentials for Phase Equilibria (TraPPE) [10], Dreiding Force Field [11], Chemistry at HARvard Macromolecular Mechanics (CHARMM) Force Field [12], Optimized Potentials for Liquid Simulations (OPLS) [13], AMBER Force Field [14] or Generalized Amber Force Field (GAFF) [15] among others. On the other hand, there are other force fields that were developed specifically for polymers. Typically, they include Polymer Consistent Force Field (PCFF) [16] and the Condensed-phase Optimized Molecular Potentials for Atomistic Simulation Studies (COMPASS) [17], although they are much less employed. In particular, the parameters of COMPASS are directly implemented in commercial software and they are not accessible in a readable format.

In this work, the GAFF force field was employed to describe the polymers 6FDA-DAM, 6FDA-DABA and PIM-1. For ZIF-8 and ZIF-67, force field parameters were taken from the previous work reported by Krokidas et al. [18], who used a flexible force field through modification in AMBER force field to describe the bonded interactions as well as the non-bonded LJ 12-6 interaction. For UTSA-280, the UFF [9] force field was employed.

The total energy of the corresponding MOF/polymer composite was calculated as a sum of intramolecular energy terms for both MOF and polymer (bond stretching, and angle-bending, cosine-based potential term for the torsional potential) while the non-bonded interaction term is described as sum of LJ 12-6 potential and Coulombic interactions. This overall energy term is described as follows:

$$\mathrm{U_{Total}} = \mathrm{U_{bonding}} + \mathrm{U_{bending}} + \mathrm{U_{torsion}} + \mathrm{U_{non-bonded}}$$

$$U_{tot} = \sum \frac{k_l}{2}\left(l_i - l_{i,0}\right)^2 + \sum \frac{k_\theta}{2}\left(\theta_i - \theta_{i,0}\right)^2 + \sum \frac{V_n}{2}\left(1 + \cos(n\phi - \gamma)\right) + \sum_{\substack{i,j \\ i<j}} 4\epsilon_{ij}\left[\left(\frac{\sigma_{ij}}{r_{ij}}\right)^{12} - \left(\frac{\sigma_{ij}}{r_{ij}}\right)^{6}\right] + \frac{1}{4\pi\epsilon_0}\sum_{i,j}\frac{q_i q_j}{|r_{ij}|} \quad (2.21)$$

Here k_l, k_θ and V_n are force constants, n is multiplicity and γ is the phase angle for the torsional angle parameters. The non-bonded terms explained above. Regarding the adsorbates, they were described by the well-known transferable potentials for phase equilibria (TRAPPE-UA) [10] force field whose parameters were fitted to reproduce the liquid-phase equilibrium properties of the corresponding guest molecules. In this force field, the united atom (UA) approach is adopted, so that hydrogen atoms are lumped into the carbon atoms where the $-CH_x$ as x=1, 2, 3 groups are considered as a single LJ uncharged interacting site. The Lorentz−Berthelot mixing rules were used for the for the cross-LJ terms corresponding to the MOF/guest, MOF/polymer and polymer/guest interactions. For atoms i and j, their associated LJ parameters are obtained using:

$$\sigma_{ij} = \frac{\sigma_i + \sigma_j}{2} \text{ and } \epsilon_{ij} = \sqrt{\epsilon_i \epsilon_j} \quad (2.22)$$

Typically, simulations involve a system of N atoms within a vacuum environment. However, in most cases where we must simulate the bulk properties, specific boundary conditions become necessary. Numerous solids exhibit atomistic-level symmetries, allowing for the consideration of the unit cell of the material under periodic boundary conditions, as illustrated in Figure 2.3. This typically reduces the number of atoms in the simulations for the systems such as supercells of MOFs.

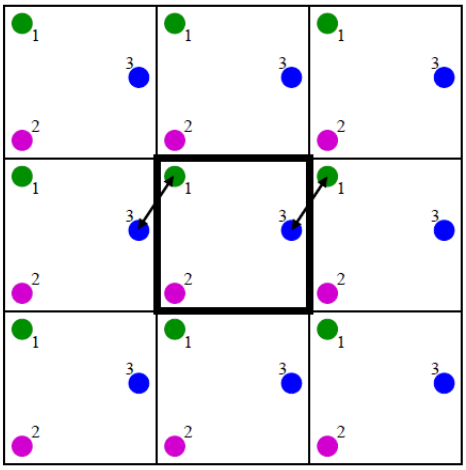

Figure 2.3 : Schematic representation of the periodic boundary conditions [19].

In this system, when a particle comes close to the boundary and eventually leaves the central box from one side, it enters the box on the other side resulting in a pseudo-infinite system. In Figure 2.3, particle 1 in the central box could theoretically interact with multiple copies of particle 3 located in different instances of the central box. Nonetheless, for convenience, it is more practical to account for a single interaction between particle 1 and 3. I therefore consider the interactions between the particles with the shortest interatomic and this principle is referred to as the nearest image convention [19]. By employing this approach, the density of the box remains maintained. When the central box is replicated n times, the position of a particle i can be expressed as $r_i + nL$, where L denotes the length of the box. The potential energy of a system with n atoms within a box can be expressed as follows:

$$(\mathrm{r_1}, \mathrm{r_2}, \ldots, \mathrm{r_n}) = \sum_{\mathrm{i<j}} \mathrm{U}(\mathrm{r_{ij}}) + \sum_{\mathrm{n}} \sum_{\mathrm{i<j}} \mathrm{U}(|\mathrm{r_i} - \mathrm{r_j} + \mathrm{nL}|) \qquad (2.23)$$

As the interactions between each particle and all images is computationally impractical due to the system's pseudo-infinite nature, a cut-off distance must be introduced for calculating van der Waals interactions, typically limited to a maximum of half the dimension of the simulation box as already mentioned above.

2.5 Molecular Dynamics Simulations

Molecular dynamics (MD) is a powerful technique for calculating both the equilibrium and dynamical properties of classical many-body systems. At the heart of this technique is the solution of the classical equations of motion, which are integrated numerically to give information for the positions and velocities of atoms in the system. With this technique, Newton's equation of motion is numerically integrated to provide insights into the positions and velocities of atoms within the system. In a system with N interacting molecules described by a potential energy function U with q_k being the generalized coordinates describing the molecular configuration and their time derivatives, the classical equations of motion can be formulated in multiple ways. The Lagrangian formulation,

$$q(t) = q_1(t), q_2(t), \dots, q_k(t), \dots \tag{2.24}$$

satisfies the following set of differential equations:

$$\frac{\partial L}{\partial q_k} = \frac{d}{dt}\left(\frac{\partial L}{\partial \dot{q}_k}\right) \tag{2.25}$$

where L is the Lagrangian of the system. This is expressed using the kinetic, K, and potential energy, U, as

$$L = L(q, \dot{q}, t) \equiv K - U \tag{2.26}$$

The generalized momenta p_k conjugate to the generalized coordinates q_k are expressed as follows:

$$p_k = \frac{\partial L}{\partial q_k} \tag{2.27}$$

Alternatively, with Hamilton's equations in terms of the generalized coordinates and momenta,

$$\dot{q}_k = \frac{\partial H}{\partial p_k}, \qquad \dot{p}_k = -\frac{\partial H}{\partial q_k} \tag{2.28}$$

where H is the Hamiltonian of the system, which can be defined by the following equation:

$$H(\mathbf{p}, \mathbf{q}) \equiv \sum_k \dot{q}_k \, p_k - L \tag{2.29}$$

If the potential U is independent of velocities and time, then H becomes equal to the total energy of the system:

$$H(\mathbf{p}, \mathbf{q}) = K(\mathbf{p}) + U(\mathbf{q}) \tag{2.30}$$

In Cartesian coordinates, Hamilton's equations of motion described as follows:

$$\dot{\mathbf{r}}_i \equiv U_i = \frac{\mathbf{p}_i}{m_i}, \dot{\mathbf{p}}_i = -\nabla_{r_i} U \equiv -\frac{\partial U}{\partial r_i} = \mathbf{F}_i \tag{2.31}$$

Then the Equation 2.31 becomes the following,

$$m_i \ddot{\mathbf{r}}_i \equiv m_i \, \dot{\mathbf{q}}_i = \mathbf{F}_i \tag{2.32}$$

where $\mathbf{F}_i$ is the force acting on atom i.

Molecular Dynamics is a deterministic and time-dependent technique utilized for obtaining dynamic properties such as guest diffusivity and viscoelastic properties of the materials. MD generates configurations by numerically solving Newton's equations of motion using an integration scheme such as the velocity-Verlet [20,21], Leap Frog [22], predictor-corrector and Beeman [23] algorithm. Calculations for the new position and velocity of each particle in the system is discretized into a small time step, which are typically around 1−2 fs in atomistic simulations. While the computing time associated with MD can be notably higher that that associated with MC due to the necessity of following a specific trajectory with a small-time step, its implementation is considerably simpler, especially for complex or large molecules.

In this work, the Verlet algorithm was selected owing to its time-reversibility, computationally efficiency implying integration of force calculations only once per time step, setting it apart from other algorithms [24]. The initial version of the Verlet equations is derived by applying a Taylor expansion at times *t-dt* and *t+dt* as follows:

$$\mathrm{r}(t+dt) = \boldsymbol{r}(t) - dt\mathbf{v}(t) + \frac{dt^2}{2}\ddot{\mathbf{r}}(t) + \frac{dt^3}{2}\dddot{\mathbf{r}}(t) + \mathcal{O}(dt^4) \tag{2.33}$$

$$\mathbf{r}(t-dt) = \mathbf{r}(t) - dt\mathbf{v}(t) + \frac{dt^2}{2}\ddot{\mathbf{r}}(t) - \frac{dt^3}{2}\dddot{\mathbf{r}}(t) + \mathcal{O}(dt^4) \tag{2.34}$$

The sum of the two Equations 2.33 and 2.34 leads to the following equation:

$$\mathbf{r}(t+dt) = 2\mathbf{r}(\mathrm{t}) - \mathbf{r}(t-dt) + dt^2\ddot{\mathbf{r}}(\mathrm{t}) + \mathcal{O}(\mathrm{dt}^4) \tag{2.35}$$

It should be also noted that the new position of a particle is accurate to order Δt^4 with $\ddot{\mathbf{r}}(\mathrm{t})$ calculated from the forces at the current positions.

The Verlet algorithm does not directly employ velocity to compute new positions; however, the velocity can be obtained from the trajectory, which has an accuracy of dt^2, through the following equation:

$$\boldsymbol{v}(\mathrm{t}) = \frac{\mathbf{r}(t+\Delta t) - \mathbf{r}(t-\Delta t)}{2dt} + \mathcal{O}(dt^2) \tag{2.36}$$

For velocity calculations, the estimated error is to order dt^2.

In the leap-frog modification of the Verlet algorithm, positions and velocities are not simultaneously computed; velocities are instead evaluated at half-integer time steps and we cannot compute the total energy directly. The coordinates and velocities are defined as follows:

$$\mathbf{r}(t+dt) = \mathbf{r}(t) + dt\mathbf{v}\left(t + \frac{dt}{2}\right) \tag{2.37}$$

$$\mathbf{v}\left(t+\frac{dt}{2}\right)=\mathbf{v}\left(\mathrm{t}-\frac{dt}{2}\right)+dt\ddot{\mathbf{r}}(\mathrm{t}) \tag{2.38}$$

The challenge of defining positions and velocities at the same time can be resolved by reformulating the Verlet algorithm in an alternative modification of velocity-Verlet algorithm. In the velocity Verlet algorithm, positions and velocities obtained through the usual Taylor expansion as follows:

$$\mathbf{r}(t+dt)=\mathbf{r}(t)+dt\mathbf{v}\,(t)+\frac{dt^2}{2}\ddot{\mathbf{r}}(\mathrm{t}) \tag{2.39}$$

$$\mathbf{v}(t+dt)=\mathbf{v}(t)+\frac{dt}{2}[\ddot{\mathbf{r}}(t)+\ddot{\mathbf{r}}(t+dt)] \tag{2.40}$$

The previously mentioned methods described the solution of Newton's equations of motion in the microcanonical (NVE) ensemble. In practice, MD simulations are often conducted under specific temperature and/or pressure conditions. Hence, in the literature, a variety of methodologies exist for conducting MD simulations under isochoric or isothermal conditions [24]. Most of these methods involve a reformulation of the Lagrangian equations of motion to incorporate the constraints of constant temperature and/or pressure. The two primary methods commonly employed for MD simulations under constant temperature and/or pressure conditions are the Nosé-Hoover [25,26] and Berendsen [27] methods. In this work, the MD simulations were carried out using Nosé-Hoover thermostat. In order to constrain temperature, Nosé introduced an extra degree of freedoms, "s" within the Lagrangian framework. The parameter "s" serves as a heat bath, with the purpose of damp out temperature deviations from the desired level. This requires incorporating an additional potential term of the following form into the total energy:

$$U_s=\mathrm{g}k_BT\ln \mathrm{s} \tag{2.41}$$

as well as an additional term for the kinetics energy (K_s)

$$K_s=\frac{\mathrm{Q}}{2}\left(\frac{\dot{s}}{s}\right)^2=\frac{p_s^2}{2Q} \tag{2.42}$$

where g is the total number of degrees of freedom, Q is the effective mass and p_s is the momentum.

The equations of motion according to Hoover's analysis are written as follows:

$$\dot{\mathbf{r}}_i = \frac{\mathbf{p}_i}{m_i} \tag{2.43}$$

$$\dot{\mathbf{p}}_i = -\frac{\partial V}{\partial r_i} - \frac{\dot{s}}{s}\mathbf{p}_i \tag{2.44}$$

$$\dot{p}_s = \frac{\left(\sum_{i=1}^{N} \frac{\mathbf{p}_i^2}{m_i} - \mathrm{g}k_B T\right)}{Q}, \qquad \mathbf{p}_s = Q\frac{\dot{s}}{s} \tag{2.45}$$

It should be noted that, an important outcome of Hoover's analysis is the uniqueness of the set of equations of motion, meaning that no other equations of the same form can lead to a canonical distribution.

The total Hamiltonian of the system, which should be conserved during the MD simulation, is expressed as follows:

$$H_{Nose-Hoover} = \sum_{i=1}^{N} \frac{\mathbf{p}_i^2}{m_i} + U(\mathbf{r}^N) + \mathrm{g}k_B T \ln s + \frac{p_s^2}{2Q} \tag{2.46}$$

Anderson [28] proposed a similar reformulation of the Lagrangian approach under constant P for MD simulations. Anderson's constant-pressure method allows isotropic alterations in the volume of the simulation box. Later, Hoover [26] combined this technique with the previously described isothermal MD approach to create a set of equations suitable for MD simulations within the NPT ensemble. Later, Parrinello and Rahman [29] further extended Andersen's approach to accommodate alterations not only in the size but also in the shape of the simulation box, which is important in the simulation of solids, such as crystalline

polymers as it permits the representation of phase transitions involving adjustments in both unit cell dimensions and angles [30].

In this work, the MD simulations were carried out using the LAMMPS [5] code for the potential of mean force (PMF) simulations to achieve accurate calculation of the free energy profile along one or more specific variables, known as the reaction coordinate(s) (RC). Free energy is a crucial quantity that plays a significant role in characterizing both chemical and biological processes. The modification in free energy determines the directionality and extent of binding and unbinding kinetics. Various methods for calculating free energy have been developed over the past decades, including perturbation theory [31], thermodynamic integration [32], umbrella sampling (US) [33,34], partition function from density of states [35], and the MM/PBSA-type [36] approach.

US stands as one of the most widely used methods, effectively and dependably computing the potential of mean force (PMF) through rigorous probability calculations along a specified reaction coordinate. Intensive conformational sampling is accomplished by imposing external restraints on conformations along the RC within a series of successful overlapping windows. Ultimately, PMF can be generated by eliminating the external restraints [37].

US is a free energy technique that is restrained with a biasing potential which is the harmonic potential of the form

$$\mathrm{W}\left(f_1(r_1,\dots,r_N),s\right)=\frac{1}{2}\kappa\left(\left(f_1(r_1,\dots,r_N)-s\right)^2\right. \tag{2.47}$$

which is also known as an umbrella potential.

The total potential is $\mathrm{U(r)}+\mathrm{W}\left(f_1(r_1,\dots,r_N),s\right)$, that could be used in MD or MC calculation. Each MD or MC simulation consequently generates a biased probability distribution $\tilde{P}(s,s^{(k)})$ where k ranges from 1 to n with $s^{(1)}=\ s^{(i)}$ and $s^{(n)}=\ s^{(f)}$ about each point $s^{(k)}$. From this set of distribution functions, it is necessary to reconstruct the true free energy profile across the entire range of the reaction coordinate.

$$\tilde{P}\left(q,s^{(k)}\right)=e^{\beta A_k}\int \mathrm{d^N}\,\boldsymbol{r}\ e^{-\beta\,U(\boldsymbol{r})}\,e^{-\beta W\left(f_1(\boldsymbol{r}),s^{(k)}\right.}\,\delta\left(f_1(\boldsymbol{r})-q\right) \tag{2.48}$$

where the unbiased configurational partition function can be expressed as follows:

$$e^{-\beta\,(A_0)} = \int \mathrm{d}^{\mathrm{N}}\,\boldsymbol{r}\;\; e^{-\beta\,U(\mathbf{r})} \tag{2.49}$$

We can then define unbiased probability distribution function $P_k\,(q)$ corresponding to the distribution $\tilde{P}\left(q, s^{(k)}\right)$ as follows:

$$P_k\,(q) = e^{-\beta\,(A_k - A_0)}\; e^{\beta W\,(\,q,\, s^{(k)})}\tilde{P}\left(q, s^{(k)}\right) \tag{2.50}$$

2.6 Monte Carlo Simulations

The Monte Carlo method is a time independent stochastic method that depends on probabilities via random configurations. In a more specific context, the approach adopted by Metropolis et al. [3] in 1953 involves the selection of a reasonable number of representative points, ensuring an optimal exploration of the system and thereby enabling a precise evaluation of the statistical averages. In this technique, the configurations generated through the Metropolis technique are characterized by a Maxwell-Boltzmann distribution.

Starting with an initially randomized configuration, MC simulations involve millions of random moves, allowing an effective sampling of the chosen ensemble. Due to the randomness, the system can explore microstates. Throughout the simulations, various Monte Carlo "moves", such as translational and rotational displacements of the molecules, are considered while attempts to insert and to remove molecules ensure a variation in their number. The corresponding random moves are accepted or rejected with appropriate criteria, based on the Metropolis algorithm [24]. In contrast to MD methods MC simulations do not require momentum contributions, resulting in an inability to determine time-dependent quantities through the use of these stochastic algorithms. Ensemble configurations are generated through the construction of a Markov chain [38]. A Markov chain is a sequence of trials in which each trial's outcome depends solely on the outcomes of the immediately preceding trials. In a Markov chain, a new state is accepted only if it is more 'favorable' than the current state. In an ensemble-based simulation context, this usually signifies that the new trial state possesses lower energy.

Given the initial configuration labeled by *o* (o for old) of the system $\boldsymbol{r}^N$ with a Boltzmann density probability of *η(o)*, the probability to swap from configuration *o* to the *n* (n for new) is determined by *π(o → n)*. To maintain equilibrium without disruption, the average number of accepted transitions from "o" to "n" must be equivalent to the reverse process. This principle is so-called balance equation.

$$\eta(o) \times \pi(o \to n) = \eta(n) \times \pi(n \to o) \tag{2.51}$$

The probability $\pi(o \to n)$ can be expressed as the probability of selecting the new configuration *n*, i.e. $[\alpha(o \to n)]$, multiplied by the probability of accepting this trial move, $[\mathrm{acc}(o \to n)]$

$$\pi(o \to n) = \alpha(o \to n) \times acc(o \to n) \tag{2.52}$$

Considering a symmetric probability of selection from *o* to *n* and vice-versa, Equation 2.43 is defined as Equation 2.48:

$$\frac{acc(o \to n)}{acc(n \to o)} = \frac{\eta(n)}{\eta(o)} = exp\{-\beta[U(n) - U(o)]\} \tag{2.53}$$

where the energies $U(n)$ is the calculated initial potential energy and $U(o)$ is the calculated new potential energy with β=1/kT.

Hence, following the Metropolis algorithm, the trial move $(o \to n)$ is accepted with a probability:

$$\mathrm{acc}(o \to n) = \min\left(1, \frac{\eta(n)}{\eta(o)}\right) = \min(1, exp[-\beta\Delta U]) \tag{2.54}$$

The attempt is considered successful when the energy of the new configuration is lower than that of the old configuration. If this is not the case, the Boltzmann factor $(\exp(-\beta\Delta U))$ is computed and compared with a random number (*Ranf*), generated within the range [0,1]. If *Ranf* is greater than $e^{-\beta\Delta U}$, the new configuration is accepted, otherwise it is rejected and another trial move is attempted. This process is repeated for a specified number of steps, typically in the range of several millions, to generate an ensemble of configurations that obey

to the Boltzmann statistical rule. To achieve efficient equilibrium approximation, it is common practice to set the acceptance rate to around 40-50%. For accurate statistical outcomes, it is advisable to first equilibrate the system, followed by calculating the desired averages over several million configurations.

For gas adsorption/separation applications, Monte Carlo simulations can be employed to derive various relevant properties, including simulated adsorption isotherms and adsorption enthalpies. Two commonly chosen ensembles are the grand canonical (μVT) and the constant pressure Gibbs (NPT-Gibbs) ensemble, often denoted as Grand Canonical Monte Carlo (GCMC) and Gibbs ensemble Monte Carlo (GEMC), respectively. GCMC is the most widely used approach, requiring the specification of chemical potential, volume, and temperature. During adsorption, there is an equilibrium where gas molecules enter and leave the polymer at equal rates.

In my thesis, the sorption calculations were carried out within the GCMC ensemble at fixed temperature, volume and chemical potential using the Metropolis Algorithm. With this grand-canonical (μ, V, T) ensemble, the average number of adsorbed molecules N in the porous materials can be calculated for a given value of the chemical potential (μ), while V and T are kept constant.

In this ensemble, the partition function is formulated as follows:

$$\mathrm{Q}(\mu, V, T) = \sum_{N=0}^{\infty} \frac{V^N e^{\beta\mu N}}{\Lambda^{3N}\, N!} \int e^{-\beta\mu s^N} ds^N \tag{2.55}$$

Where Λ denotes the Broglie thermal wavelength, determined by $\mathrm{h}/\sqrt{2\pi\mathrm{m}/\beta}$, where H is the Planck constant and m is the molecular mass of the particle, respectively, while s^N corresponds to the scaled coordinates.

The probability of a given configuration within a system of N particles at coordinates s^N, confined within a fixed *V*, is expressed by:

$$\mathrm{P}(s^N, V) \propto \frac{V^N e^{\beta\mu N}}{\Lambda^{3N}\, N!} e^{-\beta\mu s^N} \tag{2.56}$$

The probability of acceptance of a trial move in which a particle is transferred from the ideal reservoir to our system is given by the ratio of the probability densities is given by:

$$\frac{\mathrm{acc}(o \to n)}{\mathrm{acc}(n \to o)} = \frac{(V^N e^{\beta\mu N})/(\Lambda^{3N}\, N!)e^{-\beta U_n(s^N)}}{(V^N e^{\beta\mu N})/(\Lambda^{3N}\, N!)e^{-\beta U_o(s^N)}} = e^{-\beta[U_n(s^N)-U_o(s^N)]} \tag{2.57}$$

So,

$$\mathrm{P_{acc}}(o \to n) = \min\left(1, e^{-\beta[U_n(s^N)-U_o(s^N)]}\right) \tag{2.58}$$

The insertion of a particle can be determined by the following criteria:

$$\mathrm{P_{acc}}(o \to n) = \min\left(1, \frac{\frac{V^{(N+1)} e^{\beta\mu(N+1)}}{\Lambda^{3(N+1)}\,(N+1)!} e^{-\beta U_n(s^{N+1})}}{\frac{V^N e^{\beta\mu N}}{\Lambda^{3N}\, N!} e^{-\beta U_0(s^N)}}\right) \tag{2.59}$$

$$= \min\left(1, \frac{V e^{\beta\mu}}{\Lambda^3\,(N+1)} e^{-\beta[U_n(s^{N+1})-U_o(s^N)]}\right)$$

The deletion of a particle can be determined by the following criteria:

$$\mathrm{P_{acc}}(o \to n) = \min\left(1, \frac{\frac{V^{(N-1)} e^{\beta\mu(N-1)}}{\Lambda^{3(N-1)}\,(N-1)!} e^{-\beta U_n(s^{N-1})}}{\frac{V^N e^{\beta\mu N}}{\Lambda^{3N}\, N!} e^{-\beta U_0(s^N)}}\right) \tag{2.60}$$

$$= \min\left(1, \frac{\Lambda^3\, N}{V e^{\beta\mu}} e^{-\beta[U_n(s^{N-1})-U_o(s^N)]}\right)$$

Typically, the fugacity (f) is employed instead of the chemical potential (μ). The concept of fugacity is closely linked to pressure and shares the same units as p. In the case of an ideal gas component, the fugacity of the system can be defined as the system pressure at the same μ. Under the ideal gas condition and using the ideal gas law, it expressed by:

$$f = \frac{e^{\beta\mu}}{\beta\,\Lambda^3} \tag{2.61}$$

where $\mu = k_B T \ln \rho\,\Lambda^3$.

The relation between fugacity and pressure can be shown by:

$$\ln\frac{f}{P} = \int_0^P dP' \frac{Z(P') - 1}{P'} \tag{2.62}$$

where Z represents the compressibility factor ($Z = PV/Nk_BT$).

The fugacity's for each adsorbed species used in the work (C_3H_6, C_3H_8, C_2H_4, C_2H_6) under the investigated thermodynamic conditions were computed using the Peng-Robinson equation of state [39], as shown in equation 2.63:

$$\mathbf{P} = \frac{RT}{V_m - b} - \frac{a\alpha}{V_m^2 + 2bV_m - b^2} \tag{2.63}$$

Here the constants *a*, *b* and α can be determined using the critical temperature and pressure, *Tc* and p_c, and the reduced temperature *Tr (=T/Tc)*, as follows:

$$\alpha = 0.45724\,\frac{R^2 T_C^2}{p_C}, \qquad b = 0.07780\,\frac{R\,T_C}{p_C} \tag{2.64}$$

$$\alpha = \left[1 + (0.37464 + 1.54226\omega - 0.26992\omega^2)\,(1 - \sqrt{T_r}\right]^2$$

where ω is the acentric factor, obtained from reference [40] for each gas.

The open access LAMMPS software [5] was used in all Monte Carlo (MC) simulations.

2.7 Quantum Calculations

The purpose of quantum calculations is to provide a comprehensive description of the behavior of all electrons within the system. One of the fundamental principles of quantum mechanics assumes that all the details of the electronic structure for a given system are incorporated within its wave function (Ψ). This requires to solve a Schrödinger equation [41] that can be computationally demanding. The time-independent wave equation of Schrödinger

equation, is employed to derive the microscopic properties of systems formed by interacting particles like atoms, molecules, and solids. Schrödinger equation is expressed as follows:

$$\widehat{H}\left|\psi\left(\boldsymbol{R}_{\mu},\boldsymbol{r}_{i}\right)\right\rangle = E\left|\psi\left(\boldsymbol{R}_{\mu},\boldsymbol{r}_{i}\right)\right\rangle \tag{2.65}$$

where, $\widehat{H}$ is the Hamiltonian operator, E is the system energy eigenvalue for the state function of the system $\left|\psi\left(\boldsymbol{R}_{\mu},\boldsymbol{r}_{i}\right)\right\rangle$. The variables $(\mathrm{r}_{\mu},\mathrm{r}_{i})$ represent the coordinate vectors of the electrons and nuclei, respectively.

The Hamiltonian for this system can be expressed as follows:

$$\hat{H} = \hat{T}_{n} + \hat{T}_{e} + \hat{V}_{n-n} + \hat{V}_{n-e} + \hat{V}_{e-e} \tag{2.66}$$

This equation can be further developed and reformulated as follows:

$$\hat{H} = -\sum_{\mu=1}^{M}\frac{\hbar^{2}}{2\mathrm{M}_{\mu}}\nabla_{\boldsymbol{R}_{\mu}}^{2} - \sum_{i=1}^{N}\frac{\hbar^{2}}{2\mathrm{m}_{i}}\nabla_{\boldsymbol{r}_{i}}^{2} + \frac{1}{4\pi\epsilon_{0}}\sum_{\mu=1}^{M}\sum_{J=\mu+1}^{M}\frac{e^{2}Z_{\mu}Z_{J}}{\left|\boldsymbol{R}_{\mu}-\boldsymbol{R}_{J}\right|} \tag{2.67}$$

$$-\frac{1}{4\pi\epsilon_{0}}\sum_{\mu=1}^{M}\sum_{i=1}^{N}\frac{e^{2}Z_{\mu}}{\left|\boldsymbol{R}_{\mu}-\boldsymbol{R}_{i}\right|} + \frac{1}{4\pi\epsilon_{0}}\sum_{i=1}^{N}\sum_{j=i+1}^{N}\frac{e^{2}}{\left|\boldsymbol{R}_{i}-\boldsymbol{R}_{j}\right|}$$

where, ħ is the reduced Plank constant h divided by 2π, m_{i} and e represent the electron's masses and charges, M_{μ} and Z are the mass and the atomic number of the nuclei.

The Schrödinger equation for systems with multiple electrons cannot be solved exactly due to the coupling between the motion of electrons and nuclei, and the repulsive interactions among electrons. Therefore, the Born-Oppenheimer approximation [42] is employed to simplify the many-body Schrödinger equation. Due to the significantly larger mass and lower mobility of nuclei compared to electrons, the nuclei are considered to be stationary while the electrons exhibit mobility. This approximation eliminates the kinetic energy term for nuclei and simplifies the potential energy arising from nucleus-nucleus repulsion to a constant, which can be directly added to the electronic energy determined by the Schrödinger equation.

Hence, the terms of $\hat{H}$ that are essential for accurately describing the electronic structure becomes the following:

$$\hat{H} = \hat{T}_e + \hat{V}_{n-n} + \hat{V}_{n-e} + \hat{V}_{e-e} \tag{2.68}$$

where $\hat{T}_n$ is zero and $\hat{V}_{n-n}$ is a constant. The term in the Hamiltonian that defines electron-electron interactions is the most crucial one when it comes to solving the Schrödinger equation. This interaction implies that it is not possible to determine the wave function of an individual electron without considering the wave functions of all other electrons. In other words, in an N-electron system with N wave functions, the electron density can be expressed in one vectorial variable($\boldsymbol{r}$):

$$\rho(\boldsymbol{r}) = N \int d^3\boldsymbol{r}_2 \int d^3\boldsymbol{r}_3 \dots \int d^3\boldsymbol{r}_N \, |\psi(\boldsymbol{r}, \boldsymbol{r}_2, \dots, \boldsymbol{r}_N)|^2 \tag{2.69}$$

where $\rho(\boldsymbol{r})$ defines the probability of locating any of the N electrons within the volume element $d^3\boldsymbol{r}_1$, accounting for arbitrary spins, while the remaining N-1 electrons have diverse positions and spins within the state characterized by ψ.

Addressing the Schrödinger equation for a many-body system is highly complex and time-consuming processes, even with the utilization of various dedicated techniques. An approximation to solve the Schrödinger equation is the Density Functional Theory (DFT) formalism, which offers a systematic approach to mapping the complex many-body problem onto a simpler single-body problem. In this work, the DFT method was used for calculating the atomic partial charges and geometry optimization of the functionalized ZIF-67s and UTSA-280 using representative clusters that mimic the local environment of the periodic structures. DFT is developed based on two theorems proposed by Hohenberg and Kohn [43].

The first theorem states that the electronic density ρ(r), derived from the Schrödinger equation and representing the ground-state energy, serves as a fundamental function from which various other observables of a system can be derived. This fundamental principal uniquely determines all properties, including the ground state energy and wave function. For each system, the external potential v(r), and hence the total energy, is a determined by the

electron density ρ(r). A consequence is that the energy functional can be expressed in relation to the external potential and the universal functional of *ρ(r)* and *F*[*ρ(r)*], as described by the following equation:

$$E[\rho(r)] = \int \rho(r)v(r)dr + F[\rho(r)] \tag{2.70}$$

E[ρ(r)] represents an observable of the Hamiltonian associated with a wave function. This theorem simplifies the problem from needing multiple wave functions, each based on the motion of individual electrons, to a single wave function derived from the electron density.

The second theorem states that the true electron density can only be obtained if the overall functional energy can be minimized by the electron density. Hence, in order for the energy to be minimized, it must satisfy the following variational equation:

$$\frac{\partial E(\rho(\boldsymbol{r}))}{\partial \rho(\mathbf{r})} = 0 \tag{2.71}$$

The energy as a functional of the density can be expressed as follows:

$$E[\rho(\boldsymbol{r})] = T_e[\rho(\boldsymbol{r})] + V_{e-e}[\rho(\boldsymbol{r})] + \int \rho(\boldsymbol{r})V_{ext}(\boldsymbol{r})d^3\boldsymbol{r} \tag{2.72}$$

This equation can be further expanded by expressing the energy term as the sum of the total electronic kinetic (T), internal (U) and external (V) potential energies, all of which are functional of the density:

$$E[\rho(\boldsymbol{r})] = T[\rho(\boldsymbol{r})] + U[\rho(\boldsymbol{r})] + V[\rho(\boldsymbol{r})] = T[\rho(\boldsymbol{r})] + U[\rho(\boldsymbol{r})] + \int \rho(\boldsymbol{r})v(\boldsymbol{r})d^3\boldsymbol{r} \tag{2.73}$$

The implementation of DFT can take various approaches. Kohn and Sham [44] introduced the concept of a non-interacting reference system utilizing a set of orbitals to accurately compute a significant portion of the kinetic energy. Through this method, a maximal amount of information is computed precisely, thereby relegating a minor portion of the total energy to be determined by an approximate functional.

In the Kohn-Sham approach, the kinetic term $T[\rho(\boldsymbol{r})]$ is divided into non-interacting $T_s[\rho(\boldsymbol{r})]$ and correlation $T_c[\rho(\boldsymbol{r})]$ terms. Additionally, the internal electrostatic potential

$V_{e-e}[\rho(\boldsymbol{r})]$ can be separated into three parts: a Hartree interaction term $V_H[\rho(\boldsymbol{r})]$, an exchange term $V_x[\rho(\boldsymbol{r})]$ and a correlation term $V_c[\rho(\boldsymbol{r})]$. Hence, the functional of the density can be rewritten as:

$$E[\rho(\boldsymbol{r})] = T_s[\rho(\boldsymbol{r})] + T_c[\rho(\boldsymbol{r})] \; + \; V_H[\rho(\boldsymbol{r})] + V_x[\rho(\boldsymbol{r})] + V_c[\rho(\boldsymbol{r})] + \int \rho(\boldsymbol{r}) V_{ext}(\boldsymbol{r}) d^3\boldsymbol{r} \quad (2.74)$$

The terms $T_c[\rho(\boldsymbol{r})], V_x[\rho(\boldsymbol{r})]$ and $V_c[\rho(\boldsymbol{r})]$, encompassing all the quantum mechanical effects, can be grouped into a unified term referred as the exchange-correlation potential $E_{xc}[\rho(\boldsymbol{r})]$.

$$E[\rho(\boldsymbol{r})] = T_s[\rho(\boldsymbol{r})] + V_H[\rho(\boldsymbol{r})] + V_{xc}[\rho(\boldsymbol{r})] + \int \rho(\boldsymbol{r}) V_{ext}(\boldsymbol{r}) d^3\boldsymbol{r} \quad (2.75)$$

2.7.1 Geometry optimization

DFT calculations are widely employed to perform geometry optimization of the crystal structure of materials. This involves systematically assessing the electronic energy while varying geometric parameters, such as bond distances, angles, and torsions among all atoms, to achieve optimized structures. To determine the global minimum, various algorithms have been employed, with the Newton-Raphson algorithm and its derivative quasi-Newton methods being particularly common choices. While the Newton-Raphson method is well-suited for molecular geometry optimization due to its rapid convergence, it becomes computationally expensive due to the calculation of the Hessian matrix at each step. In order to overcome this computational cost, the Hessian matrix approximation can be derived from the gradient history. The Broyden-Fletcher-Goldfarb-Shanno (BFGS) [45] and limited memory BFGS [46] methods are both efficient. The energy minimization can be a fast process can vary based on some factors such as the initial configuration and the number of atoms in the system. In addition to minimizing the total energy, other criteria are employed to achieve better convergence, such as minimizing the average atom displacement and individual forces on each atom. In this study, representative clusters of the functionalized ZIF-67 and UTSA-280 were geometry optimized using Gaussian 09 package [47].

2.7.2 Charge calculations

Quantum calculations are frequently used to determine the atomic partial charges. Usually these charges provide a useful simplification of the electron distribution polarization between all bonded atoms. Based on DFT calculations, atomic partial charges can be determined through population analysis of wave functions, such as natural population analysis [48], Mulliken population analysis [49], partitioning of electron density distribution such as DDEC [50], Bader [51], CM5 [52] and Hirshfield [53] charges. The most widely used schemes involve fitting charges to replicate the electrostatic potential (ESP) [54] around the molecule, such as CHelpG [55] or Merz-Kollman [56].

In this work, the atomic partial charges for functionalized ZIFs such as ZIF-67-IDip and ZIF-67-IPD, ZIF-67 surfaces terminated by different functions were calculated using cluster-based DFT calculations with the combination of PBE functional and the 6-31G basis set as implemented in Gaussian package 09 [47]. A crystal cluster was extracted from the periodic structures and further saturated to eliminate the presence of any dangling bonds. The charges were obtained based on the orientation of the molecular coordinate system and the selection of fitting points on the grid. On the other hand, the atomic partial charges of UTSA-280 were obtained using the DDEC6 approach implemented within the CHARGEMOL module [57]. The DDEC approach optimizes the net atomic charges to ensure chemical validity and to accurately replicate the electrostatic potential energy surface beyond the electron distribution. Simultaneously, the distribution of atomic electron density is optimized to closely resemble a symmetric sphere and mimic the reference state of the atoms within the framework.

Further, the partial charges for PIM-1 were adopted from Larsen et al.'s study, where they employed the HF/6-31G* level of theory, followed by a restrained electrostatic potential (RESP) charge model [14]. On the other hand, for 6FDA-DAM and 6FDA-DABA, the electrostatic potential (ESP) derived partial charges were computed through DFT calculations utilizing the $Dmol^3$ [58] module of Materials Studio 7 employing the B3LYP (Becke 3-parameter LeeYang Parr) [59] functional.

REFERENCES

[1] P. Ungerer, C. Nieto-Draghi, B. Rousseau, G. Ahunbay, V. Lachet, Molecular simulation of the thermophysical properties of fluids: From understanding toward quantitative predictions, J. Mol. Liq. 134 (2007) 71–89. https://doi.org/10.1016/j.molliq.2006.12.019.

[2] P. Ungerer, V. Lachet, B. Tavitian, Applications of molecular simulation in oil and gas production and processing, Oil Gas Sci. Technol. 61 (2006) 387–403. https://doi.org/10.2516/ogst:2006040a.

[3] N. Metropolis, A.W. Rosenbluth, M.N. Rosenbluth, A.H. Teller, E. Teller, Equation of state calculations by fast computing machines, J. Chem. Phys. 21 (1953) 1087–1092. https://doi.org/10.1063/1.1699114.

[4] BIOVIA, Dassault Systèmes, Materials Studio, 7.0, (2017).

[5] S. Plimpton, Fast Parallel Algorithms for Short-Range Molecular Dynamics, J. Comput. Phys. 117 (1995) 1–19. https://doi.org/10.1039/c7sm02429k.

[6] G. Kupgan, L.J. Abbott, K.E. Hart, C.M. Colina, Modeling Amorphous Microporous Polymers for CO2 Capture and Separations, Chem. Rev. 118 (2018) 5488–5538. https://doi.org/10.1021/acs.chemrev.7b00691.

[7] C.. Maghfiroh, A. Arkundato, Misto, W. Maulina, Parameters (σ , ε) of Lennard-Jones for Fe , Ni , Pb for Potential and Cr based on Melting Point Values Using the Molecular Dynamics Method of the Lammps Program, J. Phys. Conf. Ser. 1491 (2020) 0–7. https://doi.org/10.1088/1742-6596/1491/1/012022.

[8] P.P. Ewald, Die Berechnung optischer und elektrostatischer Gitterpotentiale., Ann. Phys. 369 (1918) 253–287.

[9] A.K. Rappe, C.J. Casewit, K.S. Colwell, W.A. III Goddard, W.M. Skiff, UFF, a Full Periodic Table Force Field for Molecular Mechanics and Molecular Dynamics Simulations, J. Am. Chem. Soc. 114 (1992) 10024−10035. https://doi.org/10.1007/978-3-642-04431-1_17.

[10] M.G. Martin, J.I. Siepmann, Transferable potentials for phase equilibria. 1. United-atom description of n-alkanes, J. Phys. Chem. B. 102 (1998) 2569–2577. https://doi.org/10.1021/jp972543+.

[11] S.L. Mayo, B.D. Olafson, W.A. Goddard, DREIDING: A generic force field for molecular simulations, J. Phys. Chem. 94 (1990) 8897–8909. https://doi.org/10.1021/j100389a010.

[12] A.D. MacKerell, D. Bashford, M. Bellott, R.L. Dunbrack, J.D. Evanseck, M.J. Field, S. Fischer, J. Gao, H. Guo, S. Ha, D. Joseph-McCarthy, L. Kuchnir, K. Kuczera, F.T.K. Lau, C. Mattos, S. Michnick, T. Ngo, D.T. Nguyen, B. Prodhom, W.E. Reiher, B. Roux, M. Schlenkrich, J.C. Smith, R. Stote, J. Straub, M. Watanabe, J. Wiórkiewicz-Kuczera, D. Yin, M. Karplus, All-atom empirical potential for molecular modeling and dynamics studies of proteins, J. Phys. Chem. B. 102 (1998) 3586–3616. https://doi.org/10.1021/jp973084f.

[13] W.L. Jorgensen, D.S. Maxwell, J. Tirado-Rives, Development and testing of the OPLS all-atom force field on conformational energetics and properties of organic liquids, J. Am. Chem. Soc. 118 (1996) 11225–11236. https://doi.org/10.1021/ja9621760.

[14] W.D. Cornell, P. Cieplak, C.I. Bayly, I.R. Gould, K.M. Merz, D.M. Ferguson, D.C. Spellmeyer, T. Fox, J.W. Caldwell, P.A. Kollman, A Second Generation Force Field for the Simulation of Proteins, Nucleic Acids, and Organic Molecules, J. Am. Chem. Soc. 117 (1995) 5179–5197. https://doi.org/10.1021/ja00124a002.

[15] J. Wang, R.M. Wolf, J.W. Caldwell, P.A. Kollman, D.A. Case, Development and Testing of a General Amber Force Field, J. Comput. Chem. 56531 (2004) 1157–1174.

[16] H. Sun, Force field for computation of conformational energies, structures, and vibrational frequencies of aromatic polyesters, J. Comput. Chem. 15 (1994) 752–768. https://doi.org/10.1002/jcc.540150708.

[17] H. Sun, Compass: An ab initio force-field optimized for condensed-phase applications - Overview with details on alkane and benzene compounds, J. Phys. Chem. B. 102 (1998) 7338–7364. https://doi.org/10.1021/jp980939v.

[18] P. Krokidas, M. Castier, S. Moncho, D.N. Sredojevic, N. Edward, H.T. Kwon, H. Jeong, J.S. Lee, I.G. Economou, ZIF-67 Framework : A Promising New Candidate for

Propylene / Propane Separations - Experimental Data and Molecular Simulations ZIF-67 Framework : a Promising New Candidate for Propylene / Propane Separation Experimental Data and Molecular Simulations, (2016). https://doi.org/10.1021/acs.jpcc.6b00305.

[19] T.J.H. Vlugt, J.P.J.M. van der Eerden, M. Dijkstra, B. Smit, D. Frenkel, Introduction to Molecular Simulation and Statistical Thermodynamics, Delft, The Netherlands, 2008.

[20] L. Verlet, Computer "Experiments" on Classical Fluids. I. Thermodynamical Properties of Lennard-Jones Molecules, Phys. Rev. 159 (1967).

[21] D. Levesque, L. Verlet, Molecular Dynamics and Time Reversibility, J. Stat. Phys. 72 (1993) 519–537.

[22] R.W. Hockney, J.W. Eastwood, Computer Simulation Using Particles, CRC Press. (1988).

[23] D. Beeman, Some multistep methods for use in molecular dynamics calculations, J. Comput. Phys. 20 (1976) 130–139. https://doi.org/10.1016/0021-9991(76)90059-0.

[24] B.S. Frenkel, Daan, Understanding molecular simulation: from algorithms to applications, 2nd ed., Academic Press, 2001.

[25] S. Nosé, A unified formulation of the constant temperature molecular dynamics methods, J. Chem. Phys. 81 (1984) 511–519. https://doi.org/10.1063/1.447334.

[26] W.G. Hoover, Canonical dynamics: equilibrium phase-space distributions, 31 (1985) 1695–1697.

[27] H.J.C. Berendsen, J.P.M. Postma, W.F. Van Gunsteren, A. Dinola, J.R. Haak, H.J.C. Berendsen, J.P.M. Postma, W.F. Van Gunsteren, A. Dinola, J.R. Haak, Molecular dynamics with coupling to an external bath, J. Chem. Phys. 81 (1984) 3684. https://doi.org/10.1063/1.448118.

[28] H.C. Andersen, Molecular dynamics simulations at constant pressure and/or temperature, J. Chem. Phys. 72 (1980) 2384–2393. https://doi.org/10.1063/1.439486.

[29] M. Parrinello, A. Rahman, Crystal Structure and Pair Potentials: A Molecular-Dynamics Study, Phys. Rev. Lett. 45 (1980) 1196–1199.

[30] M. Kotelyanskii, D.N. Theodorou, eds., Simulation Methods for Polymers, 1st ed., CRC Press, Boca Raton, 2004. https://doi.org/https://doi.org/10.1201/9780203021255.

[31] R.W. Zwanzig, HighTemperature Equation of State by a Perturbation Method. I. Nonpolar Gases, 1420 (1954). https://doi.org/10.1063/1.1740409.

[32] I. V Khavrutskii, A. Wallqvist, Improved Binding Free Energy Predictions from Single-Reference Thermodynamic Integration Augmented with Hamiltonian Replica Exchange, (2011) 3001–3011.

[33] G.M. Torrie, J.P. Valleau, Nonphysical Sampling Distributions in Monte Carlo Free-Energy Estimation: Umbrella Sampling, J. Comput. Phys. 23 (1977) 187–199.

[34] J. Kästner, Umbrella Sampling, Wiley Interdisciplinary Reviews-Computational Molecular Science, 2011.

[35] H. Do, J.D. Hirst, R.J. Wheatley, Calculation of Partition Functions and Free Energies of a Binary Mixture Using the Energy Partitioning Method : Application to Carbon Dioxide and Methane, J. Phys. Chem. B. 16 (2012) 4535–4542.

[36] C. Wang, D.A. Greene, L. Xiao, R. Qi, R. Luo, R. Luo, Recent Developments and Applications of the MMPBSA Method, Front. Mol. Biosc. 4 (2018) 1–18. https://doi.org/10.3389/fmolb.2017.00087.

[37] W. You, Z. Tang, C.E.A. Chang, Potential Mean Force from Umbrella Sampling Simulations: What Can We Learn and What Is Missed?, J. Chem. Theory Comput. 15 (2019) 2433–2443. https://doi.org/10.1021/acs.jctc.8b01142.

[38] N.G. van Kampen, Stochastic Processes in Physics and Chemistry, 3rd ed., North-Holland Publishing Company Amsterdam, New York, Oxford., 1981.

[39] K.A.M. Gasem, W. Gao, Z. Pan, R.L. Robinson, A modified temperature dependence for the Peng-Robinson equation of state, Fluid Phase Equilib. 181 (2001) 113–125. https://doi.org/10.1016/S0378-3812(01)00488-5.

[40] B.E. Poling, J.M. Prausnitz, J.P. O'Connell, The Properties of Gases and Liquids, 5th ed., 2011.

[41] D. SHOLL, J. STECKEL, Density functional theory - A Pratical Introduction, John Wiley Sons, Hoboken, New Jersey, 2011.

[42] M. Born, R. Oppenheimer, Zur Quantentheorie der Molekeln, Ann. Phys. 389 (1927) 457–484. https://doi.org/10.1002/andp.19273892002.

[43] P. Hohenberg, W. Kohn, Inhomogeneous Electron Gas, in: Phys. Rev., 1964: p. B864. https://doi.org/10.1007/BF01198136.

[44] D. Vanderbilt, Soft self-consistent pseudopotentials in a generalized eigenvalue formalism, Phys. Rev. B. 41 (1990) 7892–7895.

[45] J.D. Head, M.C. Zerner, A Broyden—Fletcher—Goldfarb—Shanno optimization procedure for molecular geometries, Chem. Phys. Lett. 122 (1995).

[46] D.R.S. Saputro, P. Widyaningsih, Limited Memory Broyden-Fletcher-Goldfarb-Shanno (L-BFGS) Method for The Parameter Estimation on Geographically Weighted Ordinal Logistic Regression Model (GWOLR), in: AIP Conf. Proc., 2017. https://doi.org/10.1063/1.4995124.

[47] M.J. Frisch, G.W. Trucks, H.B. Schlegel, G.E. Scuseria, M.A. Robb, J.R. Cheeseman, G. Scalmani, V. Barone, G.A. Petersson, H. Nakatsuji, X. Li, M. Caricato, A. V. Marenich, J. Bloino, B.G. Janesko, R. Gomperts, B. Mennucci, H.P. Hratchian, J. V. Ortiz, D. Izmaylov, A. F. Sonnenberg, J. L. Williams-Young, F. Ding, F. Lipparini, F. Egidi, J. Goings, B. Peng, A. Petrone, V.G. Henderson, T. Ranasinghe, D. Zakrzewski, J. Gao, N. Rega, G. Zheng, W. Liang, M. Hada, M. Ehara, K. Toyota, R. Fukuda, J. Hasegawa, M. Ishida, T. Nakajima, Y. Honda, O. Kitao, H. Nakai, T. Vreven, J.E. Throssell, K. Montgomery, J. A., Jr. Peralta, F. Ogliaro, M.J. Bearpark, J.J. Heyd, E.N. Brothers, K.N. Kudin, V.N. Staroverov, T.A. Keith, R. Kobayashi, A.P. Normand, J. Raghavachari, K.; Rendell, J.C. Burant, S.S. Iyengar, J. Tomasi, M. Cossi, J.M. Millam, M. Klene, C. Adamo, R. Cammi, J.W. Ochterski, R.L. Martin, K. Morokuma, O. Farkas, J.B. Foresman, D.J. Fox, Gaussian 09, Revision E.01, (2009).

[48] A.E. Reed, R.B. Weinstock, F. Weinhold, Natural population analysis, J. Chem. Phys. 83 (1985) 735–746. https://doi.org/10.1063/1.449486.

[49] R.S. Mulliken, Electronic Population Analysis on LCAOMO Molecular Wave Functions. I, J. Chem. Phys. 23 (1955) 1833–1840. https://doi.org/10.1063/1.1740588.

[50] T.A. Manz, D.S. Sholl, Improved Atoms-in-Molecule Charge Partitioning Functional for Simultaneously Reproducing the Electrostatic Potential and Chemical States in Periodic and Nonperiodic Materials, J. Chem. Theory Comput. 8 (2012) 2844–2867.

[51] R.F.W. Bader, Atoms in Molecules - A Quantum Theory, 1990.

[52] A. V Marenich, S. V Jerome, C.J. Cramer, D.G. Truhlar, Charge Model 5 : An Extension of Hirshfeld Population Analysis for the Accurate Description of Molecular Interactions in Gaseous and Condensed Phases, J. Chem. Theory Comput. 8 (2012) 527–541.

[53] F.L. Hirshfeld, Bonded-Atom Fragments for Bonded-Atom Fragments for Describing Molecular Charge Densities, Theor. Chim. Acta. 44 (1977) 129–138.

[54] J.J. Gutierrez-sevillano, S. Calero, C.O. Ania, J.B. Parra, F. Kapteijn, J. Gascon, S. Hamad, Towards a Transferable Set of Charges to Model Zeolitic Imidazolate Frameworks : A Combined Experimental-Theoretical Research, J. Phys. Chem. C. 117 (2012) 466–471. https://doi.org/10.1021/jp3107167.

[55] C.M. Breneman, K.B. Wiberg, Determining Atom-Centered Monopoles from Molecular Electrostatic Potentials . The Need for High Sampling Density in Formamide Conformational Analysis, J. Comput. Chem. 11 (1990) 361–373.

[56] U.C. Singh, P.A. Kollman, An approach to computing electrostatic charges for molecules, J. Comput. Chem. 5 (1984) 129–145. https://doi.org/10.1002/jcc.540050204.

[57] T.A. Manz, D.S. Sholl, Chemically meaningful atomic charges that reproduce the electrostatic potential in periodic and nonperiodic materials, J. Chem. Theory Comput. 6 (2010) 2455–2468. https://doi.org/10.1021/ct100125x.

[58] B. Delley, An all-electron numerical method for solving the local density functional for polyatomic molecules, J. Chem. Phys. 92 (1990) 508–517. https://doi.org/10.1063/1.458452.

[59] A.D. Becke, Density-functional thermochemistry. III. The role of exact exchange, J. Chem. Phys. 98 (1993) 5648–5652. https://doi.org/10.1063/1.464913.

CHAPTER 3

CONSTRUCTION OF ATOMISTIC MODELS OF MOFS, POLYMERS AND THEIR COMPOSITES AND EXPLORATION OF THEIR SORPTION PROPERTIES

3.1 Introduction

Chapter 3 presents advanced atomistic computational tools with the objective to (i) reveal the microscopic origin of the improved adhesion of ZIF-67 and 6FDA-DAM in the resulting composites by functionalizing the MOF by the N-heterocyclic carbene (NHC) 1,3-bis(2,4,6-diisopropylphenyl)imidazole-2-ylidene (IDip) function, (ii) understand how the MOF surface functionalization affects the propane and propylene adsorption performance of the resulting composites and, (iii) systematically assess the impact of the nature of the polymers on the ZIF-67/polymer adhesion in the corresponding composites and its adsorption properties with a selection of three polymers of distinct physical properties, i.e. 6FDA-DAM with its rigid backbone and inhibited polymer chain packing[1], 6FDA-DABA with its plasticizing controlling capability by crosslinking owing to the presence of polar –COOH groups[2] and Polymer-of-Intrinsic Microporosity-1 (PIM-1) with its rigid contorted chains and relatively high porosity[3].

3.2 ZIF-67 Surface Models

A representative model of ZIF-67 NP was extracted from a supercell consisting of (2×2×2) unit cells of the previously reported crystal structure[54] as illustrated in Figure 3.1.

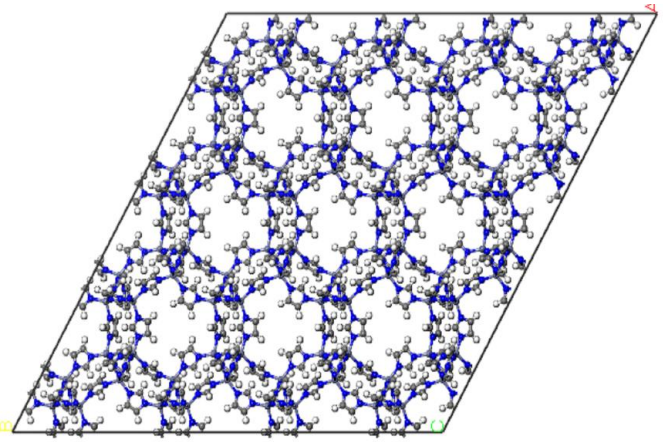

Figure 3.1 : Representative ZIF-67 super-cell. Color code: C (gray), N (blue), Co (steel blue), and H (white).

The resulting atomistic model, which has a spherical shape, contains 16 cages (size of ~11.5 Å), and its outer surface was terminated by −OH groups and −H considering the dissociative adsorption of water. This is in line with the standard hydrothermal synthesis of ZIF-67, which takes place in an aqueous solution [5,6]. The resulting outer surface can be schematically described as a "zig-zag" model, where the outermost atoms correspond to the NH groups of the imidazole linkers, while the innermost atoms are the OH groups directly bonded to the Co atoms. As seen in Figure 3.2, OH^- of water attaches itself to the under coordinated surface Co atoms, while the remaining H^+ ions compensate for the imidazolate ligand on the surface.

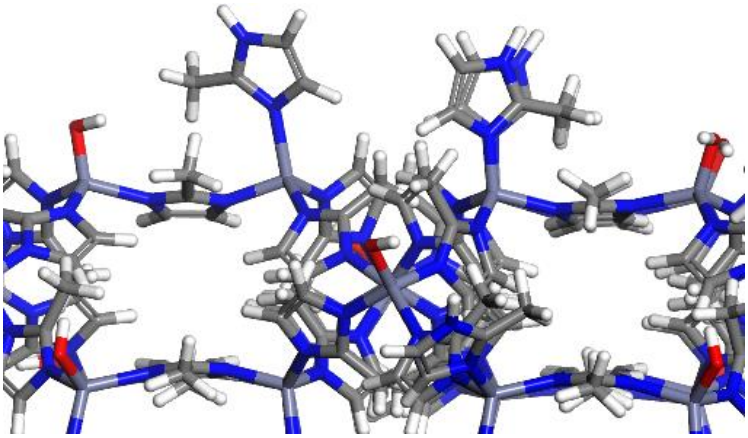

Figure 3.2 : Schematic representation of the ZIF-67 external surface. Color code: C (gray), O (red), N (blue), Co (steel blue), and H (white).

The atomic partial charges for this representative model of ZIF-67 (Table 3.1) and the force field parameters were taken from the work of Krokidas et al.[7] who used flexible force field through modification in AMBER[8] force field to describe the bonded interactions as well as the non-bonded LJ interaction parameters for the ZIF-67 bulk atoms. The intramolecular non-bonded framework interactions were carried out using the scaled 1-4 approach: interactions between atoms separated by three bonds were subject to 0.5 scaling of the Coulombic term and 0.83 of the van der Waals terms, as successfully implemented by Krokidas et al.[7,9]. To ensure the charge neutrality of the ZIF-67 NP model, the charges of the surface terminal groups, including −OH groups and −H atoms, were appropriately adjusted.

Table 3.1 : The atomic partial charges for ZIF-67.

Atom type	ZIF-67 Partial charges (e)
C1	0.7846
C2	-0.0581
C3	-0.3094
H1	0.0584
H2	0.0910
N	-0.6956
Co	1.3497
OH	-0.1320
H	0.1330

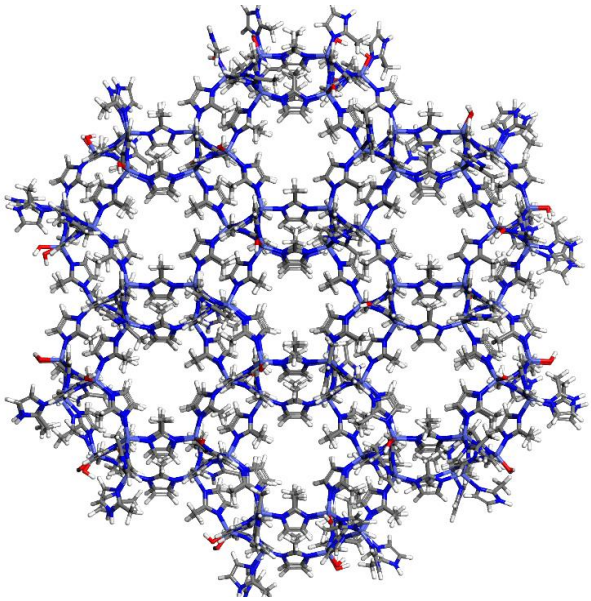

Figure 3.3 : ZIF-67 crystal, terminated by OH and ligand groups.

The windows size distribution of the ZIF-67 NP cage was first calculated throughout NPT-MD simulations performed at 308 K at 1 bar. Analysis of the MD trajectories revealed a flipping motion of the linkers that controls the flexibility of the gate opening resulting into a Gaussian-type distribution of the windows size as shown in Figure 3.4. The resulting distribution leads to an averaged value of 3.33 Å in excellent agreement with previously reported experimental [10] (3.33 Å) and simulated [4] (3.30 Å) data. This validates the force field to describe the flexibility of the MOF.

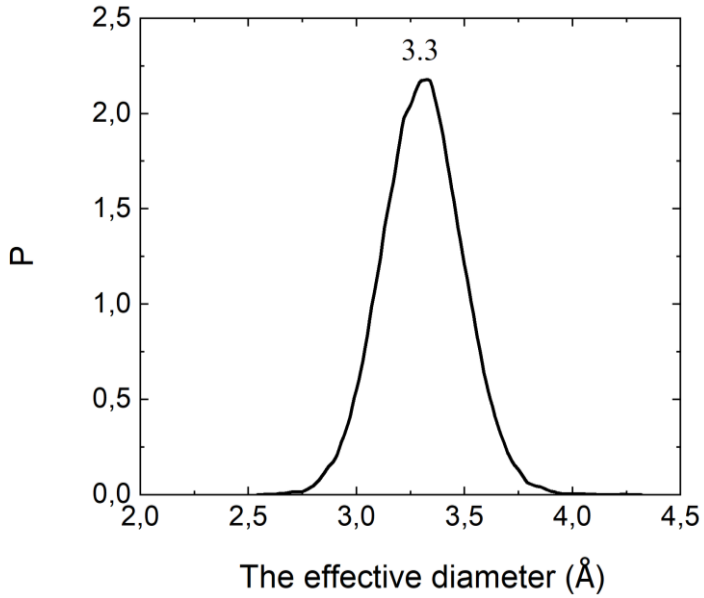

Figure 3.4 : MD-simulated aperture size distribution of ZIF-67 NP at 308 K.

The ZIF-67/guests force field parameters were further validated by achieving a good agreement between the simulated propane and propylene sorption isotherms at 308 K and the experimental data collected for ZIF-67, as reported in Figure 3.5, up to 1 bar.

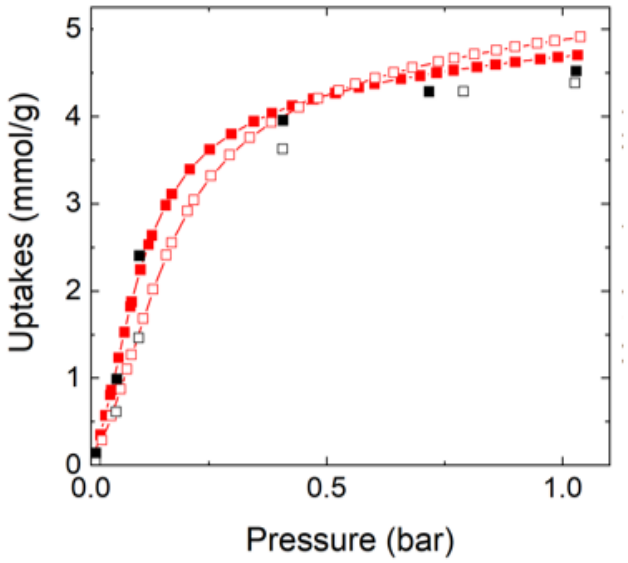

Figure 3.5 : ZIF-67 model validation using propane (solid) and propylene (open) adsorption isotherms obtained with experimental [43] (red line) and computational data (black) at 308 K up to 1 bar.

3.3 Polymer Models

The atomistic models of all polymers were built using the same strategy previously applied to model PIM-1 [12,13], whereas polymers were constructed using the *Polymer* module of Materials Studio 7 software[14]. The flexible force field used to describe the three polymers includes bonded (stretching, bond angle bending and torsional angle distortion) and non-bonded (LJ and electrostatic) terms. The LJ parameters were taken from the TRAPPE-UA [15] force field, while bonded intra-molecular interactions were represented by the GAFF force field[8]. The GAFF is a flexible force field model where the -CF_3 and –CH_x as x=1, 2, 3 groups are considered as a single site (the united atom approach). The bonds and angles were treated with harmonic potentials, whereas cosine-based potential terms were used for the dihedrals. The partial charges for PIM-1 were taken from the work of Larsen et al. where they used HF/6-31G* level of theory followed by a RESP charge model[16]. On the other hand, for 6FDA-DAM and 6FDA-DABA, the electrostatic potential (ESP) derived partial charges were computed by DFT calculations using *Dmol*^{3} module[17] of Materials Studio 7 with the B3LYP [18] functional. The atomic partial charges for polymer repeat units are reported in Figure 3.6.

6FDA-DAM

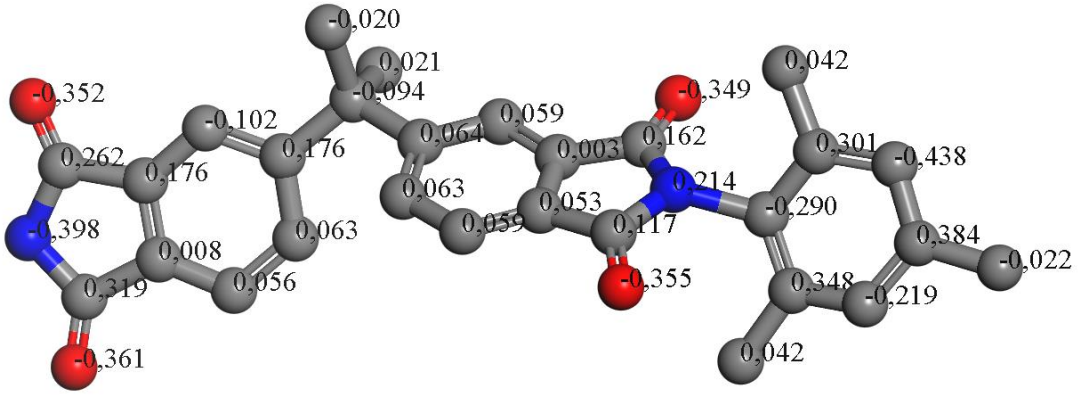

6FDA-DABA

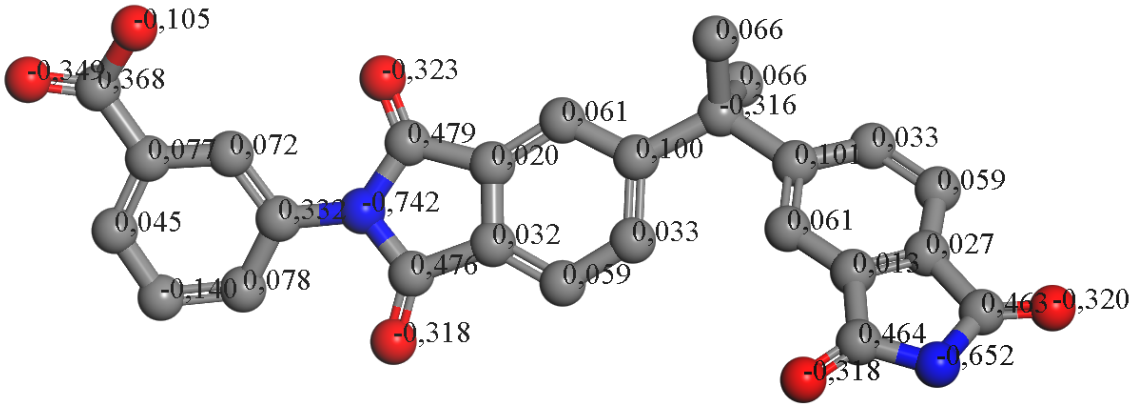

PIM-1

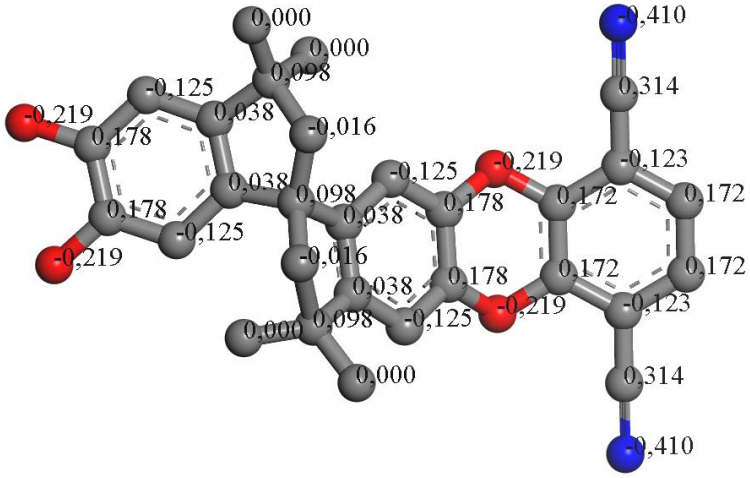

Figure 3.6 : Schematic representation of the 6FDA-DAM, 6FDA-DABA and PIM-1 repeat units with their charges. Color code: C (gray), O (red) and N (blue).

In this thesis, four polyimide chains of 6FDA-DAM and 6FDA-DABA, while two PIM-1 chains were constructed using 40 repeat units each, followed by geometry optimization to create the final structures. The "chain lengths" and "numbers" were determined through numerous trial-and-error iterations, guided by model validations that will be clarified in following section. A cubic simulation cell with a side length of about 40 Å was created for each matrix model. The cut-off distance was set to half the length of the simulation cell, and the simulation cells were constructed using the *Amorphous Cell* module of the Materials Studio software package. To prevent issues such as ring catenation and spearing, the initial density of the simulation cells was chosen to be as low as 0.1 g/cm^3. The simulation cells were converted into LAMMPS format using a tool provided by the LAMMPS package, known as msi2lmp.

It is essential for atomistic models of amorphous polymeric materials to closely resemble the physical molecular arrangement to obtain meaningful data. Hence, the equilibration of the polymer simulation cells were achieved by a 21-step MD decompression-compression method [12] with P_{max} equal to 10 kbar using LAMMPS [19]. The compression/decompression scheme methodology involves a sequence of alternating NVT and NPT MD cycles at progressively increasing temperatures and pressures, coupled with short cycles of controlled decompression, followed by a comparatively "lengthy" NPT simulation conducted at the desired temperature and pressure [20] The 21-step method is summarized in Table 3.2.

Table 3.2 : Description of the 21-steps equilibration method [12].

step	ensemble	T (K)	P (kbar)	duration (ps)
1	NVT	600		50
2	NVT	300		50
3	NPT	300	0.2 ($0.02P_{max}$)	50
4	NVT	600		50
5	NVT	300		100
6	NPT	300	6 ($0.6P_{max}$)	50
7	NVT	600		50
8	NVT	300		100
9	NPT	300	10 (P_{max})	50
10	NVT	600		50
11	NVT	300		100
12	NPT	300	5 ($0.5P_{max}$)	5
13	NVT	600		5
14	NVT	300		10
15	NPT	300	1 ($0.1P_{max}$)	5
16	NVT	600		5
17	NVT	300		10
18	NPT	300	0.1 ($0.01P_{max}$)	5
19	NVT	600		5
20	NVT	300		10
21	NPT	300	0.001	800

The MD simulations were carried out for 1 ns with a time step of 1 fs using Nosé-Hoover thermostat and barostat with relaxation times of 0.1 ps and 1 ps, respectively [21,22]. A 14-Å cut-off was applied for the LJ interactions while tail corrections and Ewald summations were used to assess the Coulombic contributions.

The validation of the three polymer models was conducted by comparing their density and FFV with experimental data from the literature, as presented in Table 3.3. The fractional free volume (FFV) values of all constructed polymers were calculated using the Poreblazer 4.0 software [23]. FFV was determined with inserting Helium atoms as probe into the system, so that the entire free volume of the structure would be occupied by these probes. Remarkably the densities for the simulated 6FDA-DAM and 6FDA-DABA models show a deviation from the experimental data by only 1% and 2% respectively. Meanwhile, the density of the simulated PIM-1 model aligns well with the range of values reported in the literature. Further, the obtained FFV values for all polymers exhibit good agreement with the data previously reported, either using the Bondi's group-contribution method [24] or/and molecular simulations [13,25]. This observation highlights the reliability of the computational methods and the accuracy of the force field parameters employed in developing robust atomistic models for the three polymers.

Table 3.3 : Comparison between the simulated properties for the three polymer models and the corresponding data available in the literature.

		Density (g/cm^3)	Fractional free volume
6FDA-DAM	literature	1.350[72]	0.189 [a,][73], 0.163[b,][71]
	this work	1.336±0.002	0.161
6FDA-DABA	literature	1.511[74]	0.175 [a,][74]
	this work	1.482±0.002	0.120
PIM-1	literature	0.94-1.4[75]	0.260 [a,][76] , 0.241[b,][59]
	this work	0.991±0.002	0.281

[a] Bondi's method [b] molecular simulations

Further validation was achieved by a good agreement between the grand canonical Monte Carlo (GCMC) simulated isotherms and the experimental ones obtained for propane and propylene for 6FDA-DAM in the low domain of pressure up to 1 bar as shown in Figure 3.7. This suggests that the gas-polymer interactions are represented accurately by the selected

force fields and the GCMC-MD coupled approach to account for the structural guest-induced relaxation of the polymers is reliable.

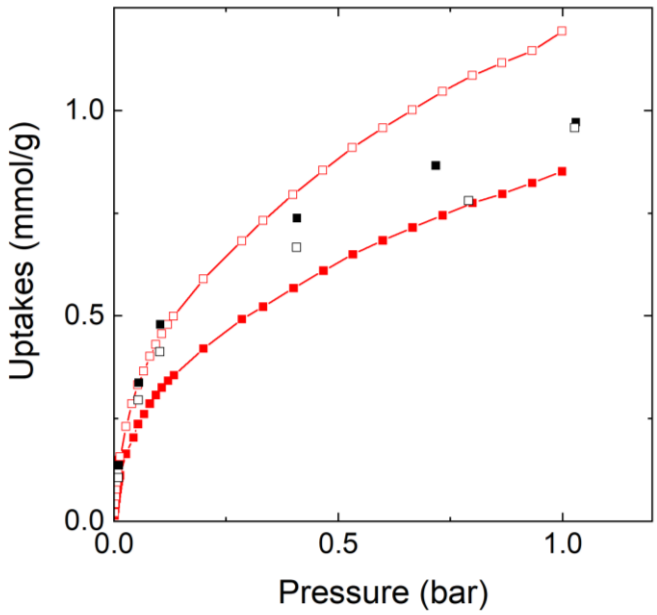

Figure 3.7 : 6FDA-DAM model validation comparing experimental [43] propane (red line with solid markers) and propylene (red line with open markers) adsorption isotherms to the simulated data (black) at 308 K up to 1 bar.

3.4 MOF/polymer MMM Models

The interface models of MOF/polymer were constructed using all three polymer models i.e., 6FDA-DAM, 6FDA-DABA and PIM-1 with ZIF-67 surface model combining them together in a simulation box. Hence, the MOF/polymer models were further constructed by embedding the ZIF-67 NPs in the three different polymer matrices with the *Packing* tool of the *Amorphous Cell* module of Material Studio 7 followed by a full geometry optimization using the flexible force fields mentioned above for both MOF NPs and polymers. The number of polymer chains was controlled in order to build atomistic models corresponding to 18 wt.% and 34.5 wt.% of ZIF-67 in the resulting models.

Typically, in order to construct the ZIF-67/6FDA-DAM composite containing 34.5 wt.% ZIF-67, four chains of polymers were packed around the ZIF-67 NP, whereas nine chains were used to achieve composite with 18 wt.% ZIF-67 content. On the other hand, four chains

of PIM-1 consisting of 40 repeat units packed around the ZIF-67 NP were considered to build the ZIF-67/ PIM-1 composite containing 34.5 wt. % ZIF-67 NP, while 11 polymer chains were used for the construction of the composite with 18 wt. % ZIF-67 NP. Moreover, four chains of 6FDA-DABA consisting of 40 repeat units, were arranged around the ZIF-67 NP to create the ZIF-67/6FDA-DABA composite containing 34.5 wt. % ZIF-67 NP, while nine polymer chains were employed for the construction of the composite with 18 wt. % ZIF-67 NP. MOF-based MMMs achieved with a side of ~59 Å for ZIF-67/6FDA-DAM MMM containing 34.5 wt. % ZIF-67 matrices, while ~70 Å cubic simulation cell of composite with 18 wt. % ZIF-67 was obtained as an outcome. PIM-1 consisting cubic simulation cell of composites with a side of ~61 Å and ~78 Å achieved with 34.5 wt. and 18 wt % ZIF-67 fillers, respectively. On the other hand, a cubic simulation cells of the 6FDA-DABA composite were constructed with a side length of approximately 57 Å and 68 Å, corresponding to the compositions with 34.5 wt. % and 18 wt. % ZIF-67 fillers, respectively. The simulation models have enough vacuum space, allowing the initial polymer configurations to adjust effectively on their respective surfaces. The ZIF-67 NP was kept at the center of the box, while the polymer repeat units were strategically distributed around ZIF-67 within the simulation box. The equilibration of the so-obtained MOF/polymer composites were achieved by a 21-step MD decompression-compression method[12] with Pmax equal to 10 kbar using LAMMPS [19]. The MD simulations were carried out for 1 ns with a time step of 1 fs using Nosé-Hoover thermostat and barostat with relaxation times of 0.1 ps and 1 ps, respectively [21,22]. A 14-Å cut-off was applied for the LJ interactions, while the Coulombic contributions were evaluated using tail corrections and Ewald summations. As a typical example, representative atomistic models of the ZIF-67/6FDA-DAM composite and its interface are shown in Figure 3.8a-b.

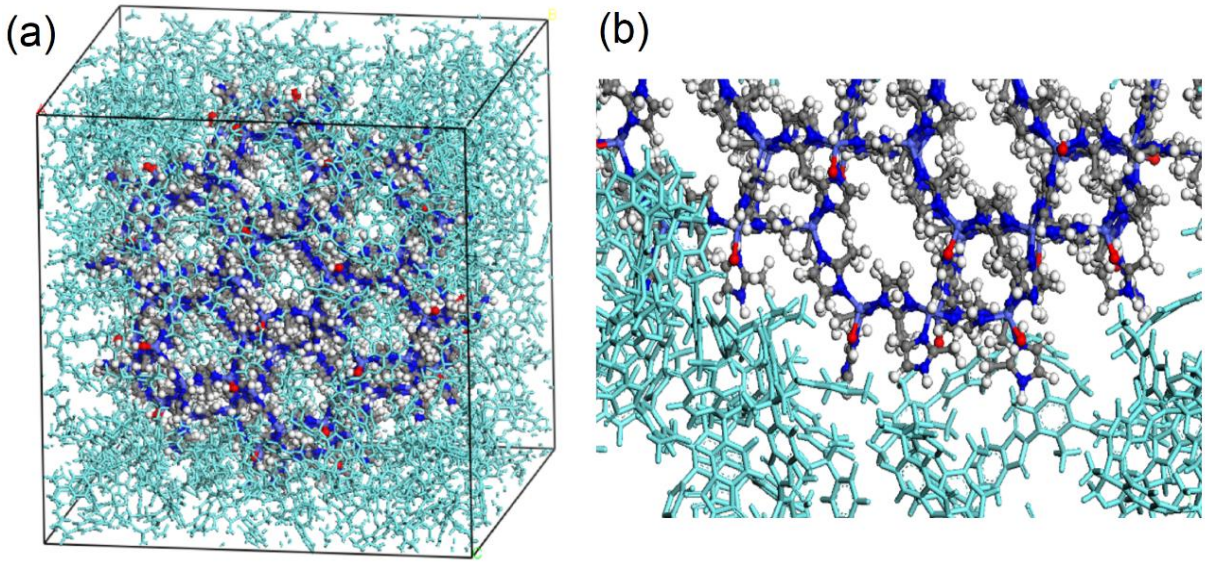

Figure 3.8 : Representative atomistic model for the (a) ZIF-67/6FDA-DAM composite containing 34.5 wt.% ZIF-67 and (b) its resulting MOF/polymer interface. ZIF-67 atoms are represented as ball and stick atoms and polymer chains in light blue lines. Color code: O (red), C (grey), H (white), N (blue) and Co (steel blue).

3.5 Analysis of the ZIF-67/6FDA-DAM MMM Interface

Figure 3.9 reports the radial atomic density for the 6FDA-DAM/ZIF-67 composite calculated over spherical shells using a 0.1 Å bin size, with the center of the outer MOF cage exposed to the polymer considered as origin (r = 0). In Figure 3.9a, the dark blue colored line at r = 11.3 Å delimits the upper limit of the ZIF-67 surface. One can observe that the black curve, associated with the polymer starts to increase at r = 10.5 Å, highlighting that there is a tiny overlap ~ 0.8 Å (hatched area) with the upper limit of the MOF region and indeed no compelling polymer penetration towards the MOF gate as illustrated in Figure 3.9b. This polymer radial atomic density further gradually increases and fluctuates around a mean value from r = 16.3 Å, thus defining an interfacial MOF/polymer light blue-shaded region with a length of about 6 Å consistent with the result of the previously simulation study of 9 Å for the ZIF-8/6FDA-DAM composite [31], followed by a first-neighbor polymer domain (grey shaded area) which is not a polymer-bulk region since it is within the interaction range with the MOF surface, a behavior already modelled for a series of MOF/polymer systems [32–35].

Figure 3.9b evidences the presence of voids at the MOF/polymer interface associated with micropores up to 6 Å size. It seems that, our modelling for ZIF-67 and 6FDA-DAM predict poor interactions between the polymer and the ZIF-67 as the appearance of microvoids at the MOF/polymer interface as well as short overlap region less than 1 Å.

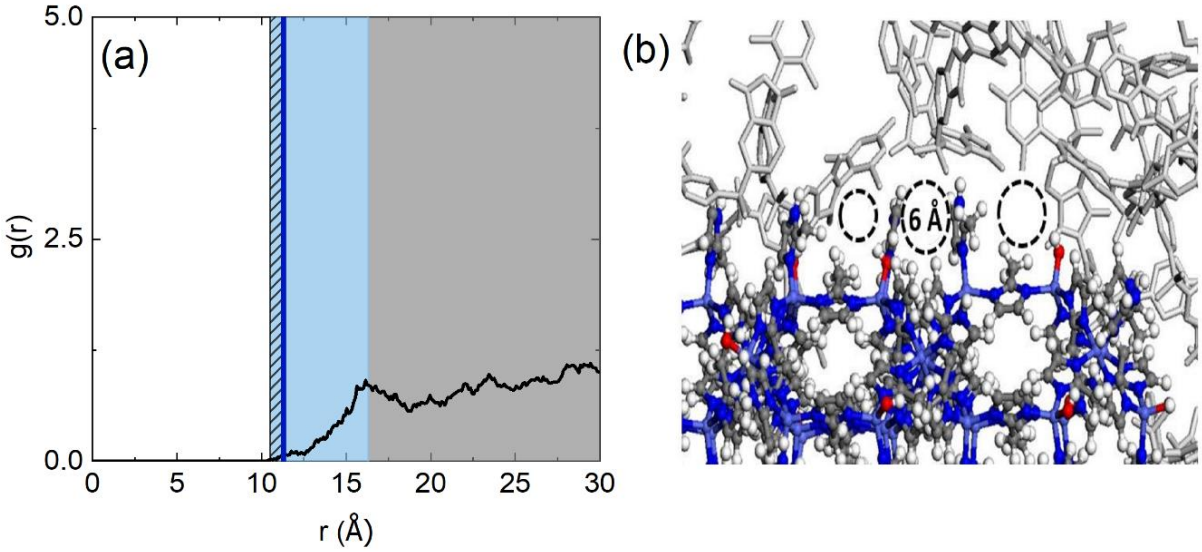

Figure 3.9 : Calculated radial atomic density distribution **of** (a) 6FDA-DAM (black) in the unfunctionalized ZIF-67/6FDA-DAM composite with respect to the center of the nanoparticle (r = 0), (b) Representative snapshot of the unfunctionalized ZIF-67/6FDA-DAM interface showing the presence of microvoids. Color scheme: 6FDA-DAM, grey wireframe; ZIF-67, ball and stick; O, red; C, gray; H, white; Co, blue.

The next step consisted of understanding the preferential interactions between the ZIF-67 and 6FDA-DAM at the interfacial region. Figure 3.10 displays the radial distribution function (RDF) plots between the hydrogen atom of the -OH functional groups present at the ZIF-67 surface and the oxygen atoms of the 6FDA-DAM. The shortest interacting distance is found to be about ~2.45 Å, corresponding to the O(6FDA-DAM)-H(OH) distance.

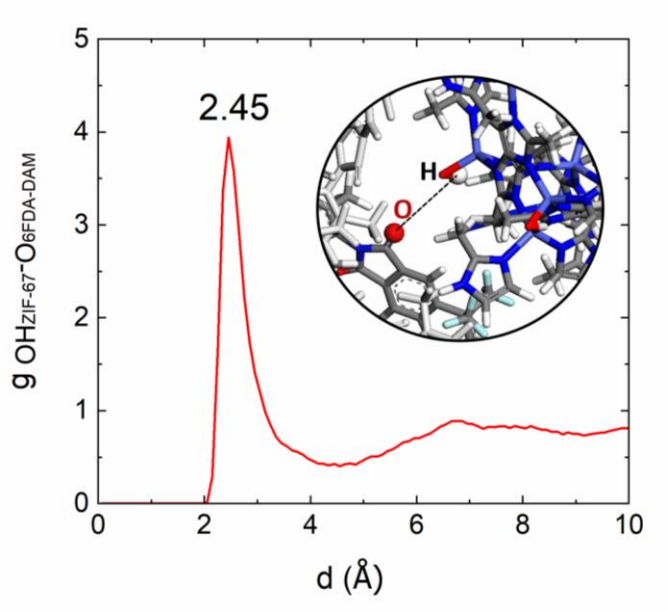

Figure 3.10 : Calculated radial distribution functions between oxygen atoms of 6FDA-DAM and – H(OH) of the ZIF-67 along with illustration of the preferential site-to-site interactions for the ZIF-67/6FDA-DAM composite.

In order to quantify the deformations of 6FDA-DAM in the vicinity of the ZIF-67 surface, the torsion angle distribution was calculated between the chain dynamics of the interfacial polymer vs bulk polymer, along with the neat polymer. The torsional angle distribution of the diamine–dianhydride linkage ($\varphi_{C-N-C-C}$) (Figure 3.11) was averaged over the MD trajectories for ZIF-67/6FDA-DAM composite. Such these calculations were performed of a 1-ns NPT-MD run over 100 snapshots.

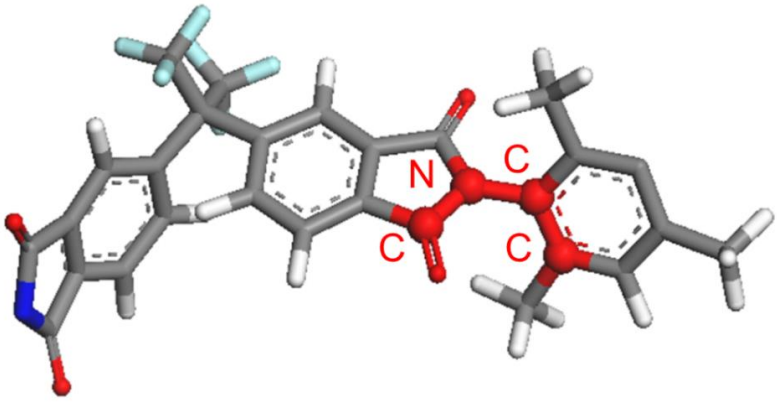

Figure 3.11 : Diamine–dianhydride linkage of torsional angle $\varphi_{C-N-C-C}$ in 6FDA-DAM.

One note that the torsional angle distribution is slightly different at the interfacial region with respect to the bulk polymer, as illustrated in Figure 3.12. A minor conformational change is observed, characterized by a slightly narrower distribution of torsional angles in the polymer at the interfacial region. This phenomenon can be attributed to a reduction in the polymer's mobility, resulting in a more rigid conformation. On the other hand, the profiles for the bulk polymer composite and the neat polymer are almost identical.

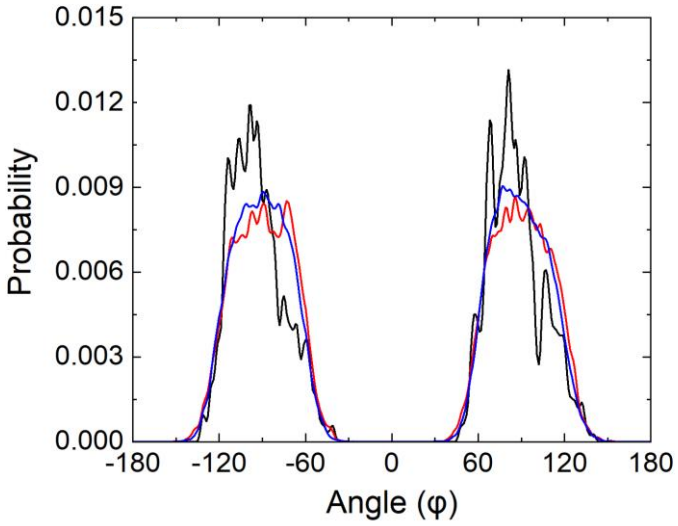

Figure 3.12 : Torsional angle Distributions ($\varphi_{C-N-C-C}$) in the 6FDA-DAM for the ZIF-67/6FDA-DAM at the interface (black) and at the bulk phase (red) and neat 6FDA-DAM (blue).

3.6 Effect of IDip-functionalized MOF Surface on ZIF-67/6FDA-DAM MMM Interface

To utilize the full potential of the MOF/polymer composites, enhancing the MOF/polymer interfacial interactions through ZIF-67 surface modification can significantly improve the adhesion between the two components. This approach is expected to promote a better dispersion of the MOF filler into the polymer matrix. For this purpose, NHC-based surface functionalized group of IDip (see Figure 3.13) was chosen due to its potential high affinity to unsaturated metal sites, along with its similar chemistry to the imidazole linker found in ZIF-67. Knebel et al. [11] reported that MMM with a ZIF-67-IDip filler loading in 6FDA-DAM as high as 47.5 wt.%, exhibited improved dispersion of the MOF filler in the polymer matrix,

educed plasticization of the polymer along with no agglomeration, in comparison to unfunctionalized ZIF-67/6FDA-DAM MMMs. Furthermore, their findings demonstrate that, in contrast to polymer-coating methods described in existing literature [36], where MOF pores were partially blocked by coating polymers, carbene functionalization approach allows for the preservation of the overall porosity of MOF fillers. This is achieved as carbene moieties exclusively bind to unsaturated metal sites on the outer surface of the MOF, avoiding entry into the MOF channels due to their bulkiness. For this purpose, the surface arrangement of composites containing IDip-functionalized ZIF-67 was investigated in this work.

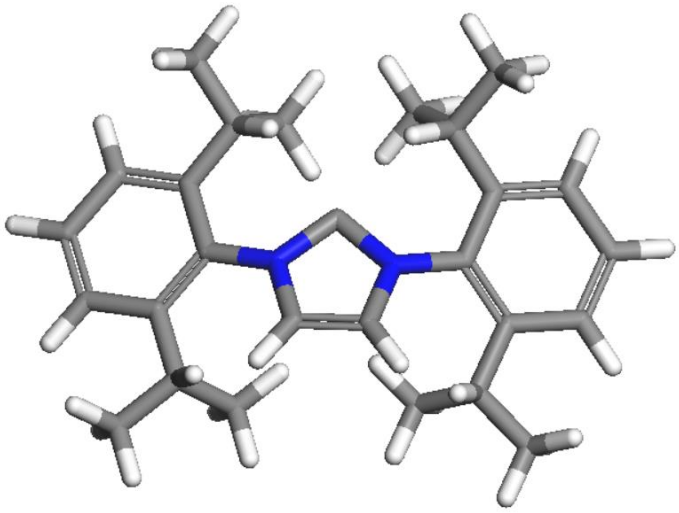

Figure 3.13 : Schematic representation of the IDip molecule. Color code: C (gray), N (blue), and H (white).

3.6.1 ZIF67-IDip surface models

The model of the IDip surface-modified ZIF-67 NP (ZIF-67-IDip) was obtained using the same method applied to the pristine ZIF-67 NP, by cleaving it from a supercell with (2×2×2) unit cells. The resulting atomistic model, with a spherical shape, contains 16 cages and its outer surface IDip functions bonded to Co atoms, while the innermost atoms were coordinated to −OH groups and −H atoms. The resulting outer surface of the ZIF-67-IDip crystal shows a “zig-zag” shape, as represented in Figure 3.14.

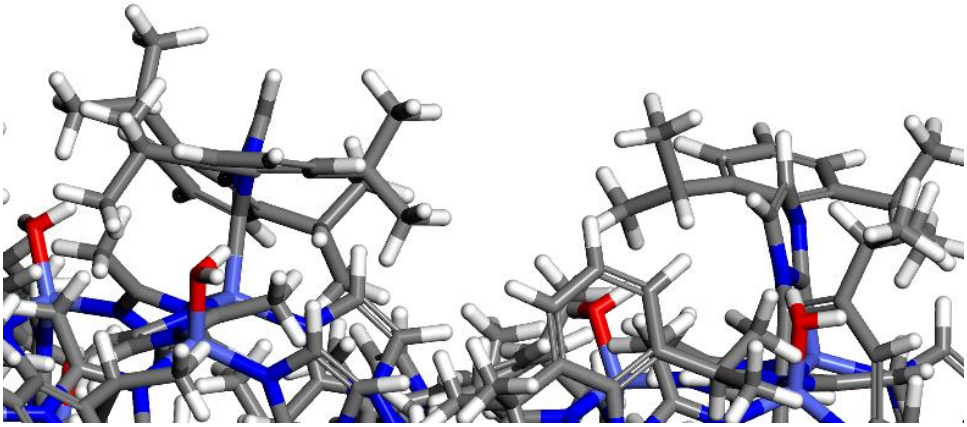

Figure 3.14 : Schematic representation of the ZIF-67-IDip surface. Color code: C (gray), O (red), N (blue), Co (steel blue), and H (white)

The atomic partial charges for ZIF-67-IDip (Table 3.4 and Figure 3.16) were obtained through cluster-based DFT calculations (see Figure 3.15) with the combination of PBE functional and the 6-31G basis set, as implemented in Gaussian 09 [37]. In the earlier model, to calculate the charges of the surface terminal groups, the −OH groups and −H atoms were initially established to maintain the charge neutrality of the ZIF-67 NP model. Meanwhile, for the ZIF-67-IDip model, the charges of the terminal groups were derived from the first cluster model in conjunction with the charges of the imidazole linkers. Additionally, the charges of the IDip groups were obtained using the second cluster, as illustrated in Figure 3.15. The force field parameters for the IDip function were taken from GAFF[8]. Illustrations of the ZIF-67-IDip NP (size of ~64 Å) are represented in Figure 3.17. The intramolecular non-bonded framework interactions were carried out using the scaled 1-4 approach: involving a 0.5 scaling of the Coulombic term and 0.83 of the van der Waals terms.

.

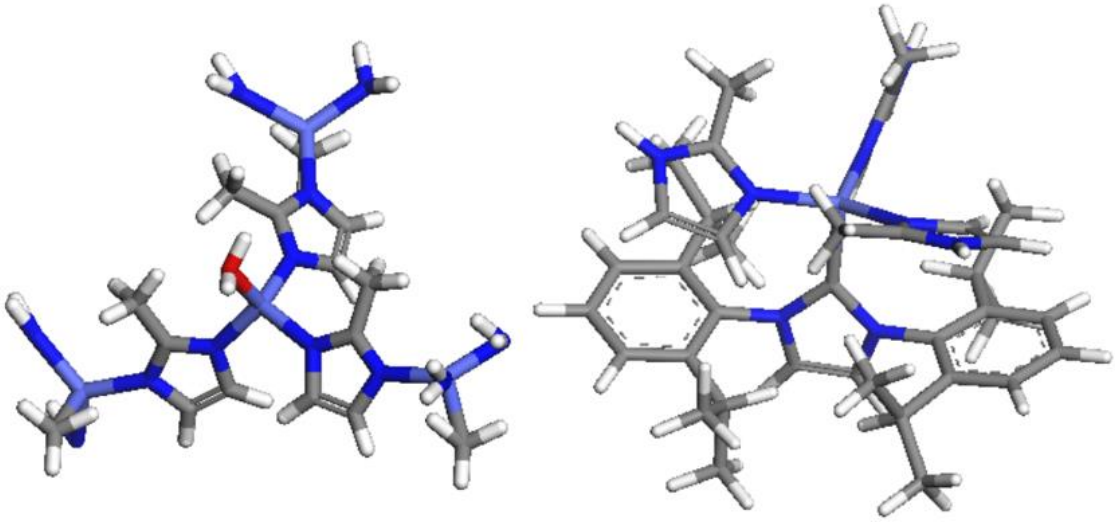

Figure 3.15 : Schematic representation of the clusters used to calculate charges for the ZIF-67 imidazolate linkers and IDip at the DFT-level.

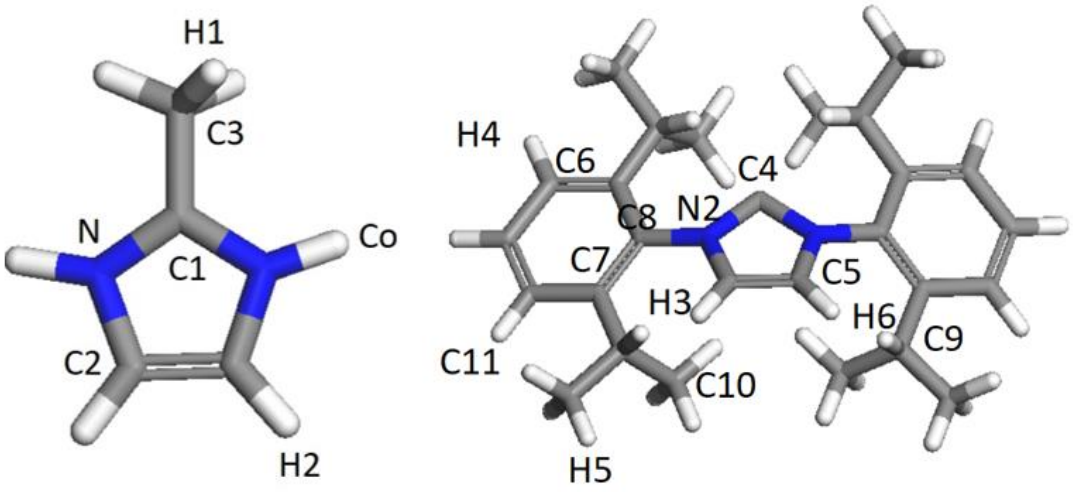

Figure 3.16 : Schematic representation of the atom types for the charges.

Table 3.4 : Atom types and charges for ZIF-67-IDip.

Atom type	Partial charges (e)
Carbon (C1)	0.442
Carbon (C2)	0.027
Carbon (C3)	-0.518
Carbon (C4)	0.246
Carbon (C5)	0.044
Carbon (C6)	-0.133
Carbon (C7)	0.164
Carbon (C8)	0.128
Carbon (C9)	-0.220
Carbon (C10)	-0.445
Carbon (C11)	-0.201
Cobalt (Co)	0.599
Hydrogen (H1)	0.206
Hydrogen (H2)	0.203
Hydrogen (H3)	0.165
Hydrogen (H4)	0.125
Hydrogen (H5)	0.146
Hydrogen (H6)	0.196
Nitrogen (N)	-0.628
Nitrogen (N2)	-0.723
OH	-0.704
H	0.450

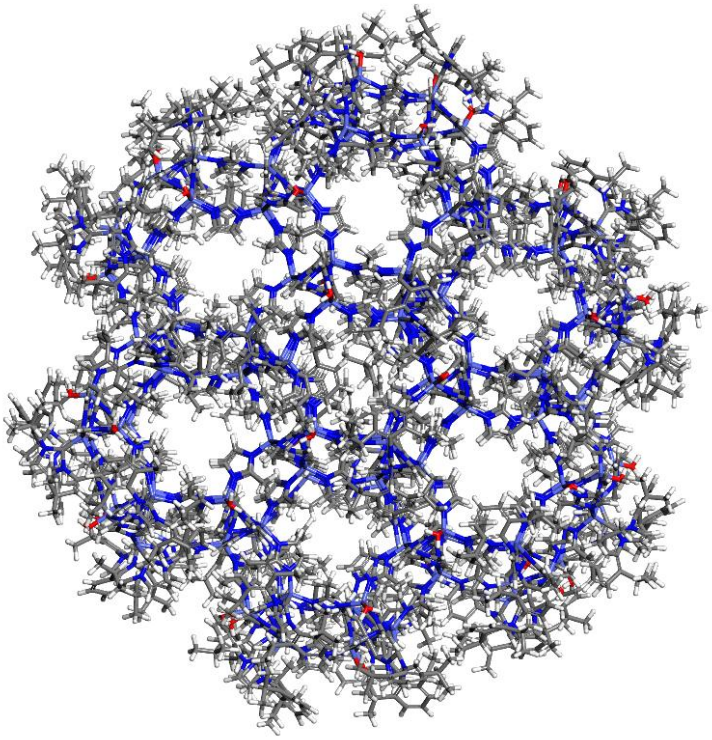

Figure 3.17 : ZIF-67-IDip crystal, terminated by OH and ligand groups. Color code: C (gray), O (red), N (blue), Co (steel blue), and H (white).

The interface models of surface-functionalized MOF/polymers were constructed using the same method as applied to the MOF/polymers interface models, combining all three polymer models with the ZIF-67-IDip surface in a simulation box. The number of polymer chains was controlled to build atomistic models corresponding to 18 wt.% and 34.5 wt.% of ZIF-67-IDip in the resulting models, following the procedure applied to ZIF-67/polymer composites.

In the construction of the ZIF-67-IDip/6FDA-DAM composite containing 34.5 wt.% ZIF-67-IDip, a typical arrangement involved packing five polymer chains around the ZIF-67-IDip NP, while 12 chains were used to achieve composite with 18 wt.% ZIF-67- IDip content. In the case for the construction of the ZIF-67-IDip/PIM-1 composite with 34.5 wt.% ZIF-67-IDip NP, six polymer chains packed around the ZIF-67-IDip NP, while 14 polymer chains were employed for the construction of the composite with 18 wt.% ZIF-67-IDip NP. Furthermore, five chains of 6FDA-DABA, were arranged around the ZIF-67-IDip NP to create the ZIF-67-IDip/6FDA-DABA composite containing 34.5 wt. % ZIF-67-IDip NP, for the composite containing 18 wt.% ZIF-67-IDip NP, 12 polymer chains were employed for its construction. The MOF-based composites were obtained with a cubic simulation cell size of

approximately 63 Å for the ZIF-67-IDip/6FDA-DAM composite containing 34.5 wt. % ZIF-67-IDip, whereas a ~59 Å cubic simulation cell size was achieved for the 34.5 wt. % ZIF-67 NP composite as previously described. PIM-1 consisting cubic simulation cell of composites with a side of ~68 Å and ~82 Å achieved with 34.5 wt. and 18 wt % ZIF-67-IDip fillers, respectively. Cubic simulation cells for the 6FDA-DABA composite were constructed with side lengths of approximately 62 Å and 75 Å, corresponding to compositions with 34.5 wt. % and 18 wt. % ZIF-67-IDip fillers, respectively.

3.6.2 Analysis of the ZIF-67-IDip/6FDA-DAM MMM interface

Figure 3.18 showcases the radial atomic density for the ZIF-67-IDip/6FDA-DAM composite calculated over spherical shells using a 0.1 Å bin size, with the center of the outer MOF cage exposed to the polymer considered as origin (r = 0). In Figure 3.18a, the upper limit of the functionalized MOF surface is indicated by the dark blue colored line at r=13 Å, which is shifted to a higher r value compared to ZIF-67 (r=11.3 Å) due to the presence of the functional IDip groups. The radial atomic density of the polymer gradually increases from 13.0 Å to 18.5 Å resulting into an interfacial MOF/polymer region length (6 Å) similar to what was simulated for the pristine ZIF-67/6FDA-DAM composite. Notably, it becomes apparent that the 6FDA-DAM approaches closer to the functionalized MOF surface when compared to the pristine ZIF-67 scenario, even resulting in a small overlapping region between the MOF surface and the polymer at the interface. The overlap length between the MOF and polymer (indicated by the hatched area) is notably larger in the case of the IDip-functionalized MOF surface, measuring 2.3 Å, as opposed to the MOF/polymer composite, which shows only 0.8 Å of overlap length. The IDip functionalization therefore contributes to improve the compatibility between the MOF NP and the polymer. This indicates that the IDip functionalization enables a more effective packing of the 6FDA-DAM in the vicinity of the MOF surface as illustrated in Figure 3.18b, with the polymer conforming to the pocket created on the MOF surface by the IDip functions. This is expected to improve the adhesion between the two components, in alignment with a more homogeneous dispersion of ZIF-67-IDip within the polymeric matrix, and aligns with experimental observations [11] that demonstrate the absence of ZIF-67-IDip agglomeration.

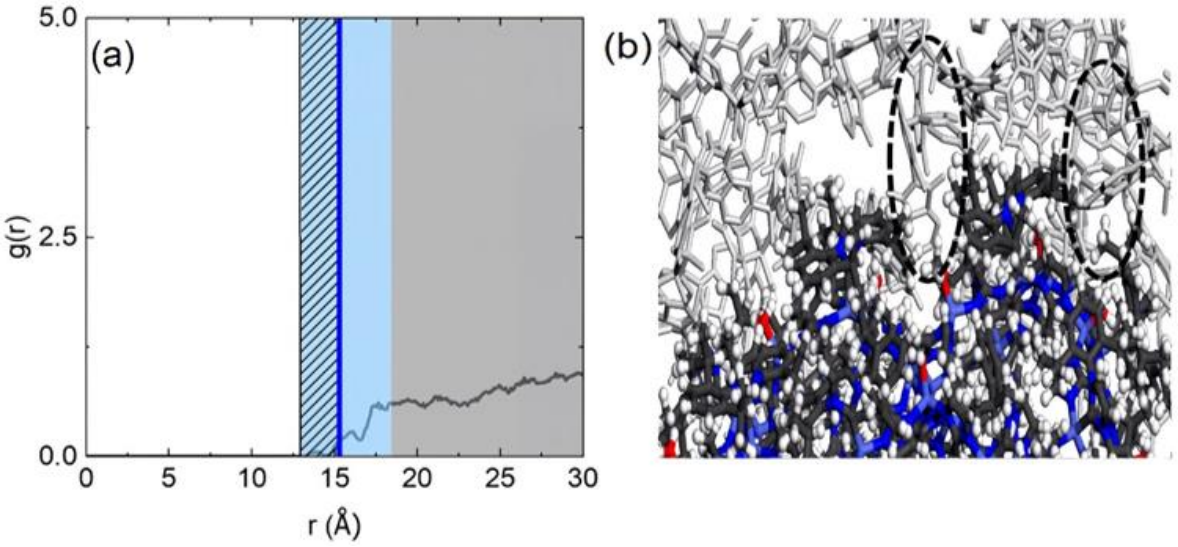

Figure 3.18 : Calculated radial atomic density distribution of (a) 6FDA-DAM (black) in the functionalized ZIF-67-IDip/6FDA-DAM composite with respect to the center of the nanoparticle (r = 0), (b) Representative snapshot of the functionalized ZIF-67-IDip/6FDA-DAM interface where MOF/polymer overlap is marked by a dashed circle. The interfacial MOF/polymer overlap regions are marked by the dashed area. Color scheme: 6FDA-DAM, grey wireframe; ZIF-67-IDip, ball and stick; O, red; C, gray; H, white; Co, blue.

Figure 3.19a illustrates the radial distribution functions (RDF) calculated between the oxygen atoms of 6FDA-DAM and the hydrogen atoms of the terminal –OH groups of both the functionalized and unfunctionalized MOF surfaces in their respective composites. It is noticeable that the interfacial interactions between MOF and polymer are rather strong in both composites, characterized by an associated O(6FDA-DAM)-H(OH) distance of 2.45 Å. Interestingly, the intensity of the corresponding peak is even greater in the composite based on the unfunctionalized MOF surface. Remarkably, the improved polymer packing within the ZIF-67-IDip/6FDA-DAM composite leads to additional interactions between the oxygen atoms and $–CF_3$ groups of 6FDA-DAM and the carbon atoms of the IDip functional groups of the MOF. These interactions are observed at separating distances of approximately 3 Å, as shown in Figure 3.19b.

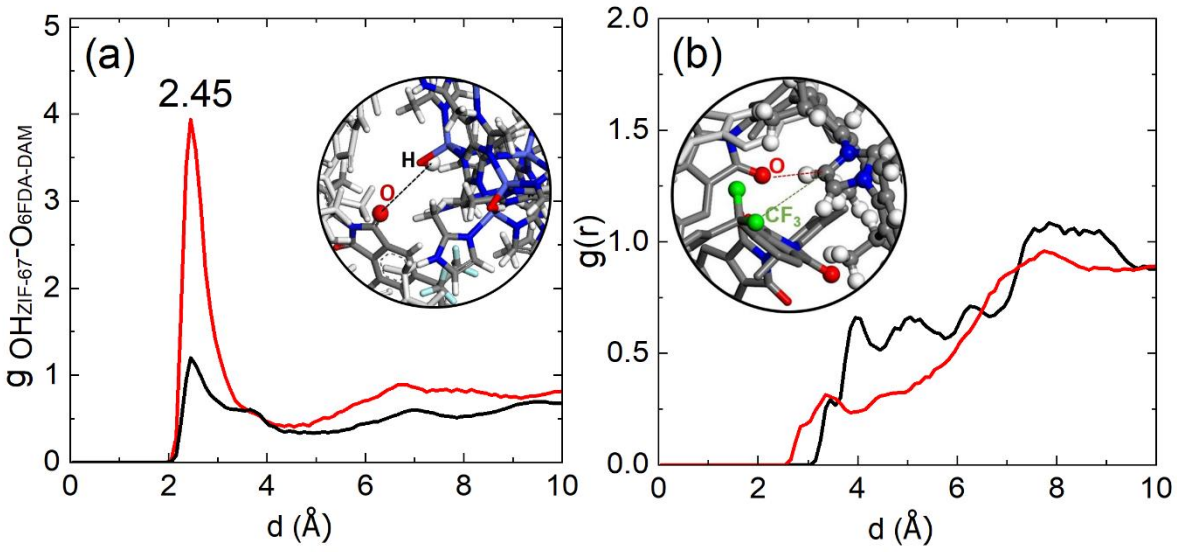

Figure 3.19 : Calculated radial distribution functions in the composites (a) between oxygen atoms of 6FDA-DAM and –H(OH) of the ZIF-67 functionalized (black) and unfunctionalized (red) surface in the corresponding composites along with illustration of the preferential site-to-site interactions for the ZIF-67/6FDA-DAM composite and (b) between oxygen atoms (red curve) and $–CF_3$ groups (black curve) of 6FDA-DAM and carbon atoms of the IDip functional groups attached at the ZIF-67 surface along with illustration of the preferential site-to-site interactions of the ZIF-67-IDip/6FDA-DAM composite.

A more in-depth analysis of the interfacial study was performed via the consideration of torsion angle distribution to better understand the chain dynamics of the polymer at the interface compared to the bulk polymer, taking into consideration the impact of MOF surface functionalization. The torsional angle distribution of the diamine–dianhydride linkage ($\varphi_{C–N–C-C}$) (Figure 3.11) was averaged over the MD trajectories for ZIF-67-IDip/6FDA-DAM composites. It seems that, the torsional angle distribution shows slight differences between the interfacial region and the bulk polymer, as illustrated in Figure 3.20. A minor conformational change with a slightly narrower torsional angle distribution for the polymer at the interfacial region might be related to a less marked mobility of the polymer and hence its rigidification.

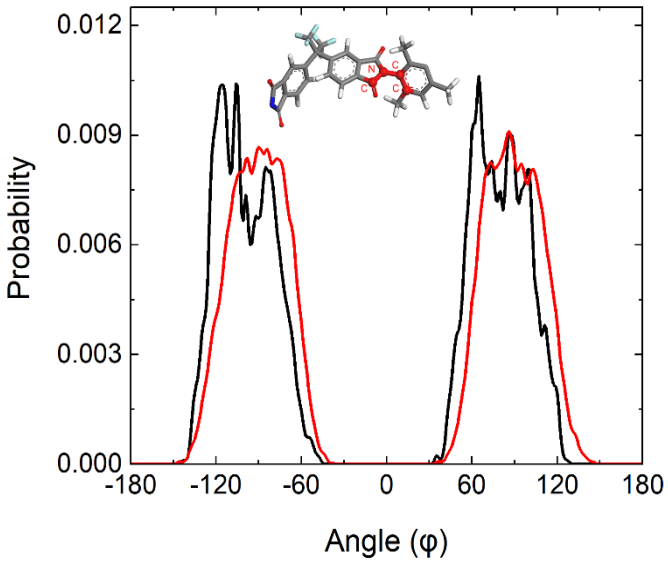

Figure 3.20 : Torsional angle Distributions ($\varphi_{C-N-C-C}$) in the 6FDA-DAM for the ZIF-67-IDip/6FDA-DAM at the interface (black) and at the bulk phase (red).

The comparison between the torsional angle distributions for ZIF-67/6FDA-DAM and ZIF-67-IDip/6FDA-DAM in the interfacial region in Figure 3.21 shows only a slight difference between the two composites.

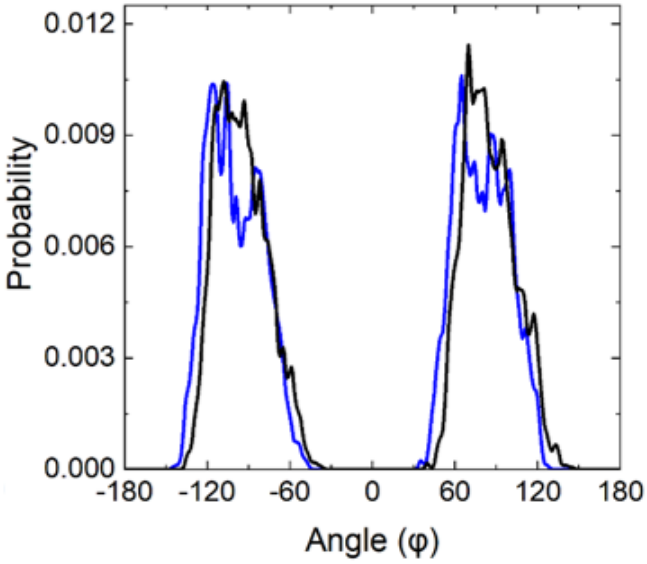

Figure 3.21 : Torsional angle ($\varphi_{C-N-C-C}$) distributions in the 6FDA-DAM for the ZIF-67/6FDA-DAM (black) and ZIF-67-IDip/6FDA-DAM (blue) composites at the interface.

3.7 Impact of Polymers on ZIF-67-based MMM Interfaces

One of the important challenges in the fabrication of MOF-based MMMs is preventing particle aggregation within the polymer matrix and enhancing the interaction between the particles and the polymer matrix. Glassy polymers possess rigid chain structures, which endow them with excellent separation performance. However, this very rigidity can weaken the interaction between the polymers and particles. MOFs feature organic functionality within their bridging ligands, facilitating potential interactions with the organic functionality present in polymers [38]. It has been found that using MOFs with these organic linkers structurally resembling the polymer's monomers can be considered as a viable strategy for enhancing the interfacial properties of MMMs. Their findings indicate that the microstructure of MMMs depends on various factors, including the molecular structure and rigidity of the polymer, as well as interactions between the MOF and polymer [39]. Given that ZIF-8 and ZIF-67 are among the most commonly employed MOF fillers in MMM applications, this PhD research has also focused on investigating the compatibility of ZIF-67 with different types of polymers exhibiting various degrees of rigidity. For this purpose, the next step involves an examination of the microscopic structure of the ZIF-67/PIM-1 composites.

3.7.1 ZIF-67/PIM-1 vs ZIF-67/6FDA-DAM MMM interfaces

Previous studies showed that rigidity of the polymer usually impacts the MOF/polymer interfacial structuring and their compatibility [39]. This encouraged us to examine the microscopic structuring of the ZIF-67/PIM-1 composites starting by exploring its radial atomic density profile. Figure 3.22a and Figure 3.22b show the radial atomic density profile of 6FDA-DAM in ZIF-67 composite and a representative snapshot, while Figure 3.22c and Figure 3.22d report the same set of data for the PIM-1 in ZIF-67 composite. In Figure 3.22a and Figure 3.22c, the dark blue colored line represents the upper limit of the ZIF-67 surface, measuring at r=11.3 Å and 11.2 Å for composites with 6FDA-DAM and PIM-1, respectively. The radial atomic density of the polymer exhibits a gradual increases from 9.4 Å to 14.3 Å, leading to an interfacial MOF/polymer region length (~5 Å) that is similar to what was simulated for the pristine ZIF-67/6FDA-DAM composite. In contrast to ZIF-67/6FDA-DAM, the ZIF-67/PIM-1 composite exhibits a slightly larger MOF/polymer overlap length (1.8 Å

vs. 0.8 Å), despite the fact that this polymer is inherently more rigid. Polymers with more flexibility, such as 6FDA-DAM, are anticipated to have an easier way adapting their shape when the MOF surfaces are flat. However, ZIF-67 shows a "zig-zag" shape surface which hampers its effective coverage by 6FDA-DAM. On the other hand, PIM-1 features an L-shape vertex, which is ready to plug into the troughs formed by the "zig-zag" MOF surface [5], thereby expanding the MOF/polymer overlap length. Moreover, Figure 3.22b and Figure 3.22d clearly illustrate the existence of voids at the MOF/polymer interface, which are connected to micropores of up to 6 Å in size in the case of the ZIF-67/6FDA-DAM composite. However, these micropores are slightly larger, exceeding 6 Å for ZIF-67/PIM-1 composite. Similar to the modeling of ZIF-67/ 6FDA-DAM composite, there are poor interactions between PIM-1 and ZIF-67, evident from the presence of microvoids at the MOF/polymer interface.

To quantify the deformations of PIM-1 in the vicinity of the ZIF-67 surface, the torsion angle distribution was computed to compare the chain dynamics of the interfacial polymer vs. bulk polymer. The two representative torsional angles $\varphi_{C-C-O-C}$ and $\varphi_{C-C-C-C}$ (Figure 3.23) was averaged over the MD trajectories for ZIF-67/PIM-1 composite. Such these calculations were performed of a 1-ns NPT-MD run over 100 snapshots. $\varphi_{C-C-O-C}$ angle gives information about the flexibility degree of planar PIM-1, while $\varphi_{C-C-C-C}$ angle represents the flexibility of the "L" vertex of the polymer involving spiro carbon atoms [5].

Almost identical torsional profiles are obtained for $\varphi_{C-C-O-C}$ (Figure 3.24a) in the ZIF-67/PIM-1 composite in line with a similar polymer planar conformation. On the other hand, spiro Carbon atoms play a more active role, as evidenced by the slightly different torsional angle distribution between the polymers at the interfacial region with respect to the bulk polymer. This suggests a minor reduction in the polymer's dynamics at the interfacial region within the ZIF-67/PIM-1 composite (Figure 3.24b). This information is in line with how the functionalization of MOF enhances the embedding of polymer to MOF surface despite reducing the flexibility of polymer [40].

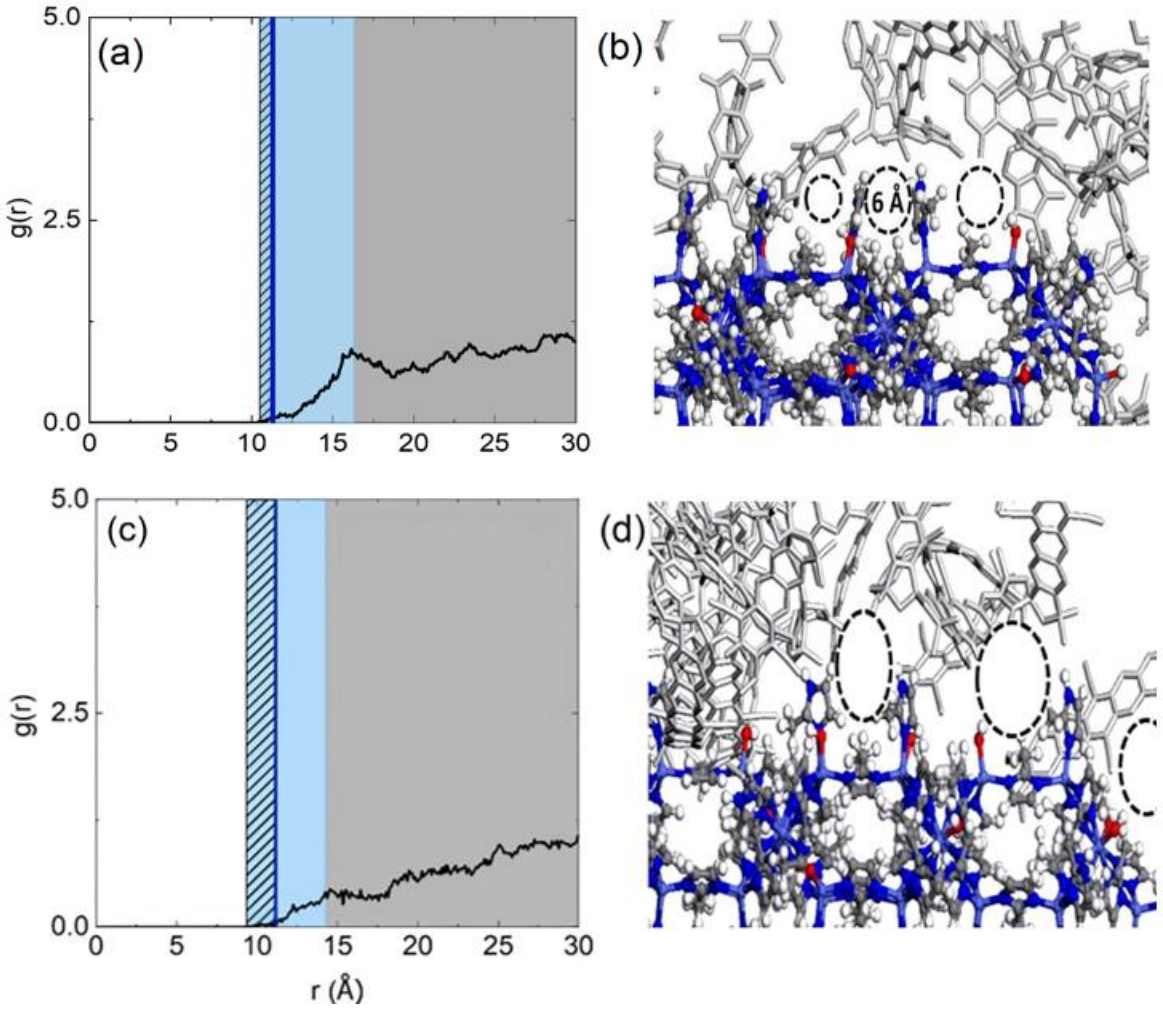

Figure 3.22 : Calculated radial atomic density distribution of (a) 6FDA-DAM (black) in the ZIF-67/6FDA-DAM composite with respect to the center of the nanoparticle (r = 0), (b) Representative snapshot of the ZIF-67/6FDA-DAM interface showing the presence of microvoids, (c) PIM-1 (black) in the ZIF-67/PIM-1 composite with respect to the center of the nanoparticle (r = 0), (d) Representative snapshot of the interface of ZIF-67/PIM-1 showing the presence of microvoids. The interfacial MOF/polymer overlap regions are marked by black dashed shaded areas. Color scheme: 6FDA-DAM and PIM-1, grey wireframe; ZIF-67, ball and stick; O, red; C, gray; H, white; Co, blue.

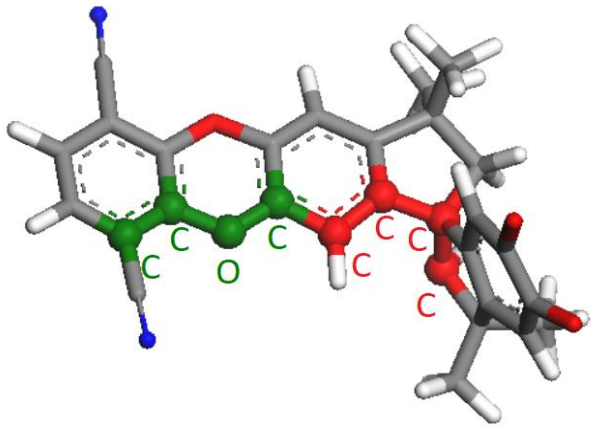

Figure 3.23 : Torsional angle of $\varphi_{C-C-O-C}$ (green colored) and $\varphi_{C-N-C-C}$ (red colored) for PIM-1.

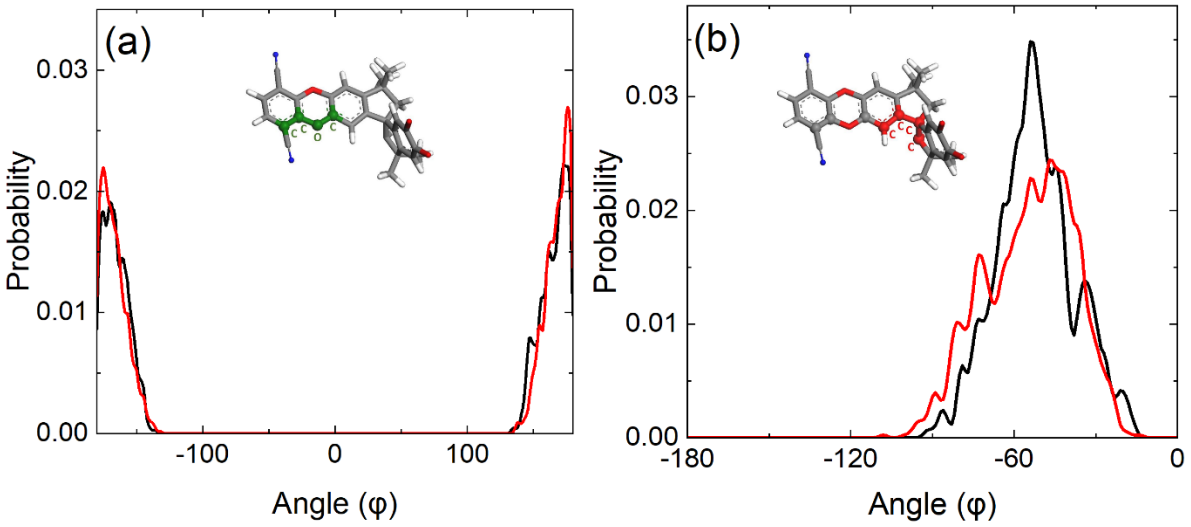

Figure 3.24 : Torsional angle distributions in the PIM-1 for the ZIF-67/PIM-1 composite (a) $\varphi_{C-C-O-C}$ angle at the interface (black) and at the bulk phase (red) (b) $\varphi_{C-C-C-C}$ angle at the interface (black) and at the bulk phase (red).

3.7.2 ZIF-67-IDip/PIM-1 vs ZIF-67-IDip/6FDA-DAM MMM interfaces

To enhance the polymer affinity of MOF fillers within the membrane, ZIF-67 nanoparticles were functionalized with IDip. As detailed in Chapter 3.6, Surface-modified ZIF-67-IDip was coupled with the more rigid PIM-1, resulting in ZIF-67-IDip/PIM-1. In this research, the objective was to understand how functionalization enhances the adhesion between the MOF and the polymer, while investigating the impact of polymer rigidity. Hence, the influence of

polymer rigidity were explored by comparing the outcomes of the studies conducted on ZIF-67-IDip/PIM-1 and ZIF-67-IDip/6FDA-DAM composites.

Figure 3.25a and Figure 3.25b show the radial atomic density profile of 6FDA-DAM in ZIF-67-IDip composite and a representative snapshot, while Figure 3.25c and Figure 3.25d report the corresponding data for PIM-1 within the ZIF-67-IDip composite. In Figure 3.25a and Figure 3.25c, the dark blue colored line represents the upper limit of the ZIF-67-IDip surface, measuring at r=13.0 Å and 10.2 Å for composites with 6FDA-DAM and PIM-1, respectively. The radial atomic density of the polymer undergoes a gradual increase, extending from 10.2 Å to 16.7 Å. Consequently, this results in an interfacial MOF/polymer region length of 6.5 Å, surpassing the simulated length observed in the ZIF-67-IDip/6FDA-DAM composite (5.5 Å). In contrast to the ZIF-67-IDip/6FDA-DAM composite discussed earlier in Chapter 3.6.2, there is a slightly larger MOF/polymer overlap length in the case of ZIF-67-IDip/PIM-1 (2.6 Å vs. 2.3 Å), even though this polymer is more rigid. As mentioned earlier, the L-shape vertex of PIM-1, easily can plug into the troughs created by the "zig-zag" MOF surface, ultimately leading to an expansion of the MOF/polymer overlap length.

In the case of ZIF-67-IDip/PIM-1, both the interfacial region (blue colored area) and the MOF/polymer overlap region (black shaded area) are much larger (6.5 Å vs. 4.9 Å and 2.6 Å vs. 1.8 Å respectively) compared to ZIF-67/PIM-1 surface. This comparison follows the same sequence as detailed previously for 6FDA-DAM. Therefore, IDip functionalization facilitates a more effective packing of the PIM-1 in the vicinity of the MOF surface, as portrayed in Figure 3.25d, where the polymer conforms to the pocket generated on the MOF surface by the IDip functional groups.

On the other hand, both composites exhibit similar interfacial micropores up to 5-6 Å of diameters which further confirms that, IDip functionalization improves the compatibility between the MOF and the polymer without modifying the interfacial pore dimensions.

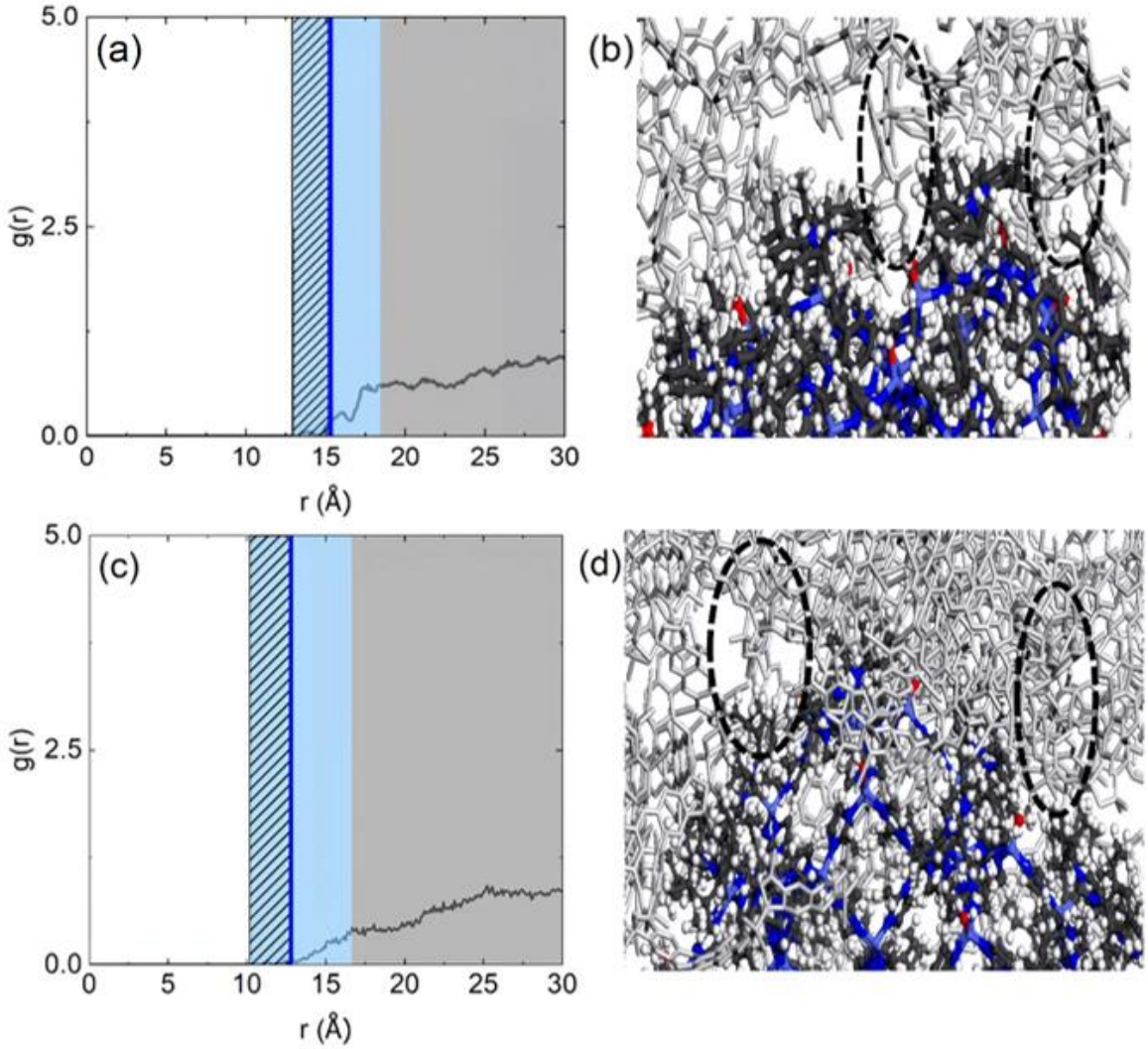

Figure 3.25 : Calculated radial atomic density distribution of (a) 6FDA-DAM (black) in the functionalized ZIF-67-IDip/6FDA-DAM composite with respect to the center of the nanoparticle (r = 0), (b) Representative snapshot of the functionalized ZIF-67-IDip/6FDA-DAM interface showing the presence of microvoids, (c) PIM-1 (black) in the functionalized ZIF-67-IDip/PIM-1 composite with respect to the center of the nanoparticle (r = 0), (d) Representative snapshot of the interface of functionalized ZIF-67-IDip/PIM-1 showing the presence of microvoids. The interfacial MOF/polymer overlap regions are marked by black dashed shaded areas. Color scheme: 6FDA-DAM and PIM-1, grey wireframe; ZIF-67-IDip, ball and stick; O, red; C, gray; H, white; Co, blue.

Here, a comprehensive analysis of the interfacial study was performed through the examination of the torsion angle distribution. This analysis aimed to provide deeper insights into the chain dynamics of the polymer at the interface compared to the bulk polymer, with a specific focus on considering the influence of MOF surface functionalization. The two representative torsional angles $\varphi_{C-C-O-C}$ and $\varphi_{C-C-C-C}$ were averaged over the MD trajectories for ZIF-67-IDip/PIM-1 composite. Nearly identical torsional profiles are observed for $\varphi_{C-C-O-C}$ in the ZIF-67 IDip/PIM-1 composite, consistent with a similar polymer planar conformation (Figure 3.26a). On the other hand, for the case of torsional angle $\varphi_{C-C-C-C}$, slightly different torsional angle distribution observed in the polymer at the interfacial region with respect to the bulk polymer in the ZIF-67-IDip/PIM-1 composite (Figure 3.26b). This observation aligns with the idea that MOF functionalization enhances the integration of the polymer with the MOF surface, even though reducing the flexibility of polymer.

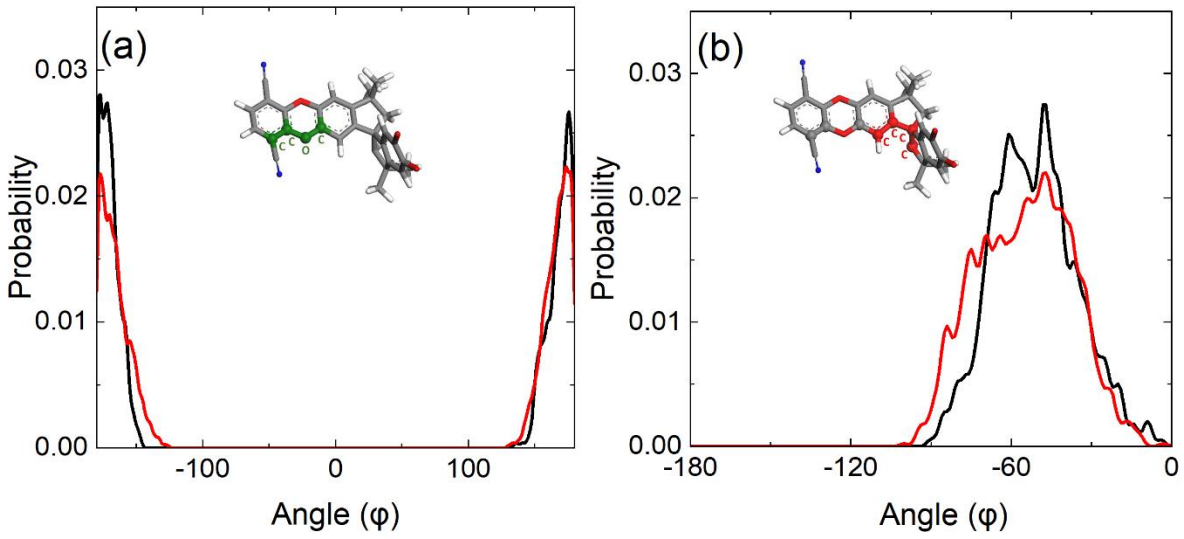

Figure 3.26 : Torsional angle distributions in the PIM-1 for the functionalized ZIF-67-IDip/PIM-1 composite (a) $\varphi_{C-C-O-C}$ angle at the interface (black) and at the bulk phase (red) (b) $\varphi_{C-C-C-C}$ angle at the interface (black) and at the bulk phase (red).

3.8 Adsorption Studies on ZIF-67-based MMMs

The adsorption isotherms of single components propane and propylene were performed by a hybrid approach combining GCMC and MD simulations on the so-obtained polymers, ZIF-67, ZIF-67-IDip NP models at 308 K using LAMMPS [19] to enable to capture the possible guest-induced relaxation of the overall systems. Sorption-relaxation cycles (SRCs), were integrated into GCMC and MD runs, ensuring that NPT-MD and NVT-MD steps were applied following each GCMC step to account for the guest-induced flexibility of the systems [13,41]. For one SRC cycle, 500 000 exchange moves with guest insertion and deletion, 2000 and 5000 rotational and translational moves respectively were considered followed by 20 ps MD-NVT and 20 ps MD-NPT runs at 308 K up to 8 bar. This cycle was repeated at each pressure for 100 times, the last 30 SRCs being used for production runs. The number of SRCs and the duration of the MD runs within these SRCs were optimized to ensure the achievement of equilibrium while using the most efficient and least resource-intensive approach. Nosé-Hoover thermostat and barostat were used during for the MD runs with relaxation times of 0.2 ps and 2 ps, respectively [21,22]. Both guest molecules were modeled with the TraPPE united atom force field model[15] while the atoms of both MOFs and polymers were treated using the force field parameters described above. Gas fugacities were computed for all pressure range using the Peng-Robinson equation of state [42].

3.8.1 Impact of polymers on the adsorption properties of ZIF-67-based MMMs

For the sorption simulations of propane and propylene, the single component studies on pristine polymers were conducted including 6FDA-DAM, 6FDA-DABA, and PIM-1, at 308 K up to 8 bar (Figure 3.27). Highest propane and propylene uptakes were obtained for PIM-1 as expected, since PIM-1 has a higher FFV compared to the less porous 6FDA-based polyimides as presented in Table 3.3 in Chapter 3.3 [43]. The slightly lower simulated propane and propylene uptake for 6FDA-DABA compared to 6FDA-DAM is also consistent with its lower FFV value (0.120 vs. 0.161).

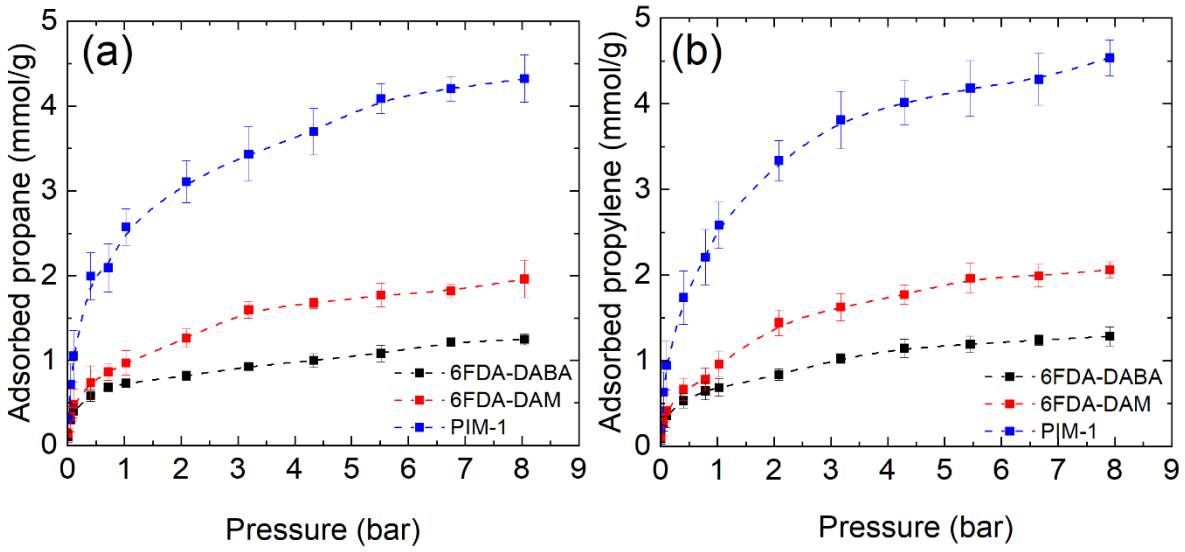

Figure 3.27 : Gas adsorption of (a) Propane uptakes (b) Propylene uptakes in PIM-1 (blue), 6FDA-DAM (red) and 6FDA-DABA (black) at 308 K up to 8 bar. (Dashed lines are to guide the eye).

It is further evaluated how the different degrees of polymer rigidity impact the single component sorption isotherms for propane and propylene within composites containing 34.5 wt. % ZIF-67 fillers as shown in Figure 3.28. In comparison to the gas uptakes observed in pristine polymers, the composites consistently improved the sorption properties in all instances, owing to the higher adsorption capacity of ZIF-67. As shown in Figure 3.28, the 34.5 wt. % ZIF-67/PIM-1 composite exhibits the highest propane and propylene uptakes. Additionally, slightly greater uptakes of propane and propylene are achieved in the 34.5 wt. % ZIF-67/6FDA-DAM composite when compared to the 34.5 wt. % ZIF-67/6FDA-DABA composite.

In order to understand the influence of polymer/MOF interfacial region on gas adsorption, it is also compared the simulated gas uptake to the "ideal" gas uptake, which was calculated based on the volume additive adsorption capacities of the individual components. The "excess" gas uptake can be related to the interfacial interactions that disrupt the packing of polymer chains, leading to an increased inter-chain spacing among the polymer chains. Hence, the microporous structures of MMMs with fillers were altered [33]. As shown in Figure 3.28c and Figure 3.28d, the volume additive propane and propylene uptakes are

slightly lower than the gas uptakes observed in the 34.5 wt. % ZIF-67/ 6FDA-DAM composites. This may be due to the generation of some additional free volume elements by ZIF-67 that alters the packing of the polymer and allows guest molecules to pass through its cages [44].

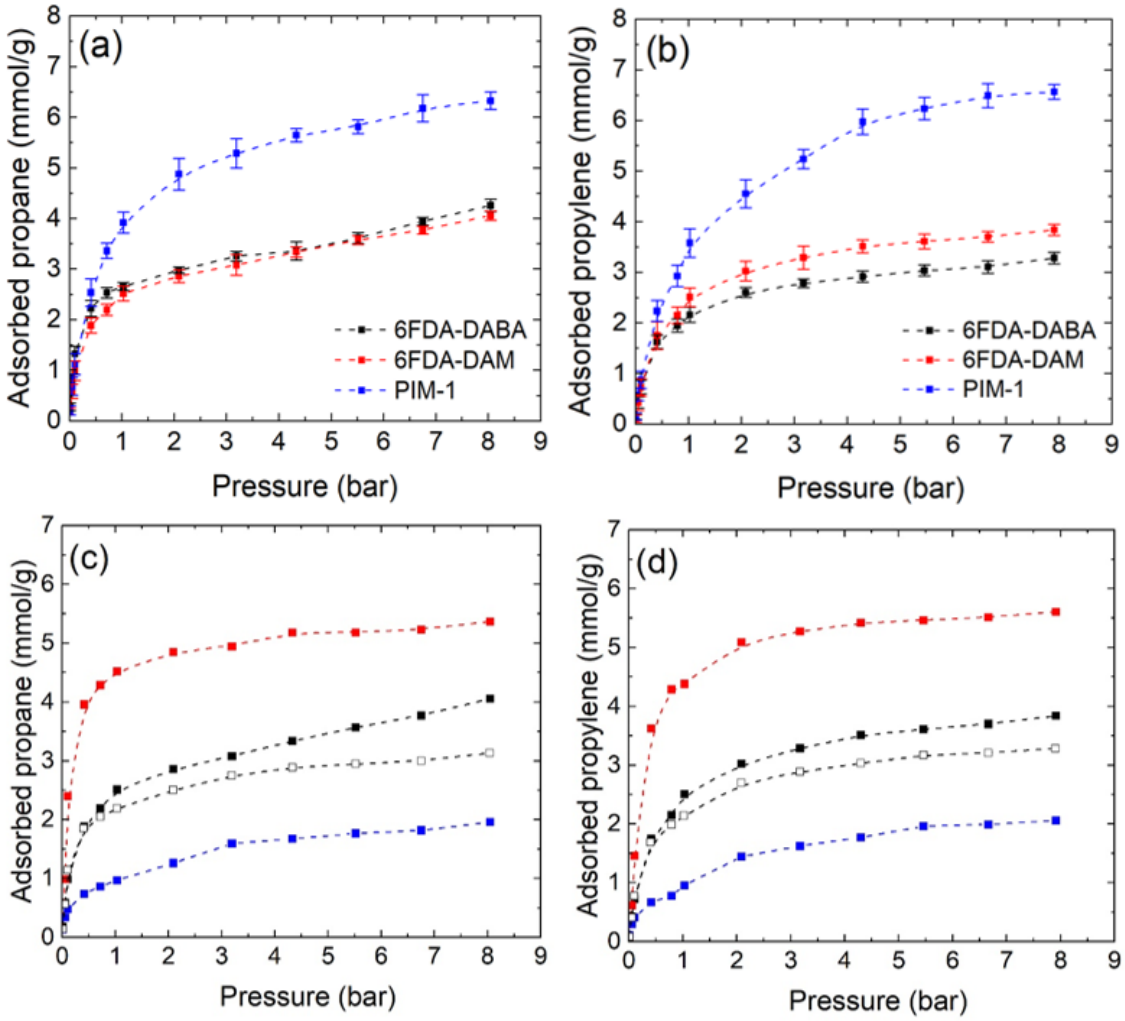

Figure 3.28 : Gas adsorption of (a) Propane uptakes in 34.5 wt % ZIF-67/PIM-1 (blue), ZIF-67/6FDA-DAM (red) and ZIF-67/6FDA-DABA (black) (b) Propylene uptakes in 34.5 wt % ZIF-67/PIM-1 (blue), ZIF-67/6FDA-DAM (red) and ZIF-67/6FDA-DABA (black) (c) Propane uptakes in ZIF-67(red), 6FDA-DAM (blue), 34.5 wt % ZIF-67/6FDA-DAM (black solid) and volume additive 34.5 wt % ZIF-67/6FDA-DAM (black empty) (d) Propylene uptakes in ZIF-67(red), 6FDA-DAM (blue), 34,5 wt % ZIF-67/6FDA-DAM (black solid) and volume additive 34.5 wt % ZIF-67/6FDA-DAM (black empty) at 308 K up to 8 bar. (Dashed lines are to guide the eye).

Further, a more detailed analysis of the intermolecular interactions in ZIF-67 with different polymer matrices were obtained using site-to-site RDFs. These RDFs were calculated for various MOF/polymer pairs to identify the most significant interactions, which primarily involve the $(O)_{6FDA\text{-}DAM}$ and $(O)_{6FDA\text{-}DABA}$ with H atoms of the –OH functions terminating the Co atoms on the MOF surface (Figure 3.29). For both 6FDA-DAM and 6FDA-DABA, the main RDF peak is observed at a distance of 2.5 Å, indicating similar interactions with the ZIF-67 surface groups. However, O atoms in PIM-1 have fewer interactions with the MOF surface due to its increased rigidity compared to the other polymers. Hence, PIM-1 is unable to adapt its conformation effectively to interact with the MOF surface [33]. Consequently, the dominant interaction for PIM-1 occurs between the N in CN groups of PIM-1 and ZIF-67 surface groups.

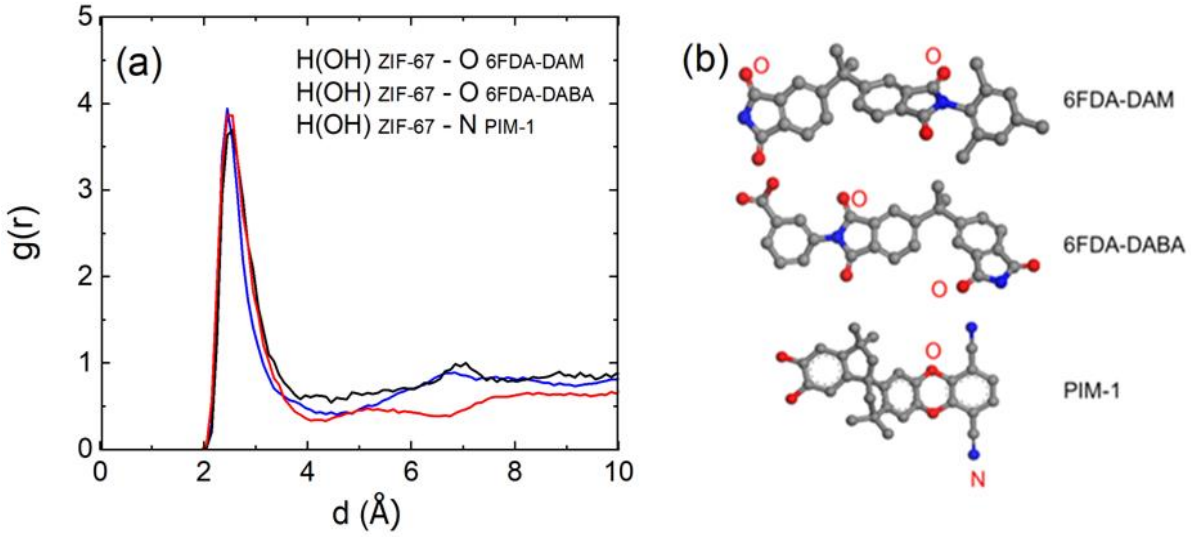

Figure 3.29 : Radial distribution functions (a) Favored MOF/polymer interactions between the – O (blue and black) of and – H(OH) of ZIF-67 surface for 6FDA-DAM and 6FDA-DABA and – N (red) of PIM-1 and – H(OH) of ZIF-67 surface. (b) Selected sorption sites are in red colors for the 6FDA-DAM, 6FDA-DABA and PIM-1 repeat units.

3.8.2 Impact of IDip-functionalized MOF surface on the adsorption properties of ZIF-67-based MMMs

In this work, it is evaluated how the MOF functionalization impacts the single component sorption isotherms for propane and propylene in 34.5 wt. % ZIF-67/6FDA-DAM and 34.5 wt. % ZIF-67-IDip/6FDA-DAM. The corresponding sorption isotherms reported in Figure 3.30 were calculated at 308 K up to 8 bar. The comparison of the isotherms reveals two key observations: (i) the functionalization does not play a detrimental role on the adsorptive ability of the composite, despite a slightly lower sorption capacity of ZIF-67-IDip/6FDA-DAM is obtained, and (ii) the similar adsorption behavior exhibited by propane and propylene in the ZIF-67/6FDA-DAM composite remains true for ZIF-67-IDip/6FDA-DAM. This later observation suggests that the MOF surface functionalization does not boost the thermodynamic propylene/propane separation of the composite in line with the previously reported experimental data [11].

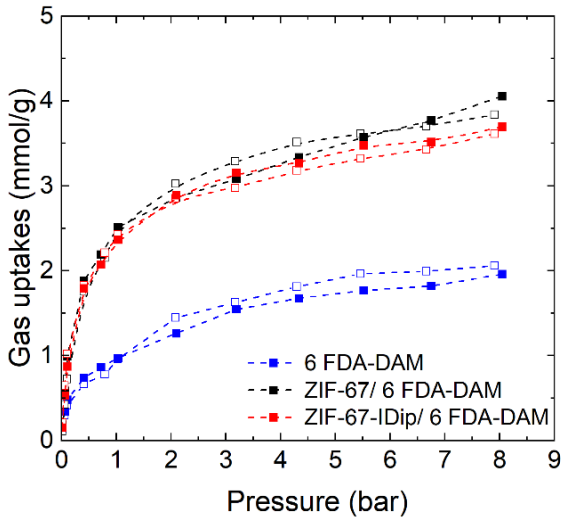

Figure 3.30 : Simulated propane (solid symbols) and propylene (open symbols) sorption isotherms for the composites. 34.5 wt. % ZIF-67/6FDA-DAM (black) and ZIF-67-IDip/6FDA-DAM (red) at 308 K up to 8 bar and comparison with pure 6FDA-DAM (blue) (dashed lines are to guide the eyes).

It is further explored whether guest adsorption can induce a significant alteration in the MOF/polymer interfacial structure. In Figure 3.31a-b, the radial atomic density profile of the functionalized ZIF-67/6FDA-DAM composite obtained at 8 bar of propane/propylene and 308 K shows that the blue colored interfacial region ranges from 13.5 Å to 16.6 Å in both scenarios, whether propylene or propane are present. Therefore, it becomes evident that the interfacial MOF/polymer length is reduced in the presence of both propane and propylene molecules (3.2 Å vs 5.5 Å in absence of guest molecules) while a similar MOF/polymer overlap length is obtained (2.2 Å and 2.5 Å for propylene and propane respectively vs. 2.3 Å). This observation highlights that the guest molecules do not affect the adhesion of the two components, which is maintained through interactions between the IDip functional groups and 6FDA-DAM, despite a reduction in the length of the interfacial region.

The situation differs significantly for the ZIF-67/6FDA-DAM composite, with the interfacial MOF/polymer length increasing (6.3 Å and 5.9 Å for propylene and propane, respectively, compared to 6 Å in the absence of guest molecules) upon guest adsorption (Figure 3.31c-d). Additionally, the MOF/polymer overlap length expands significantly upon propylene adsorption (from 0.8 Å to 2.5 Å), while remaining relatively unchanged upon propane adsorption (0.9 Å). This suggests that propylene induces significant re-structuring of the polymer, whereas propane does not seem to affect the affinity between the MOF and the polymer.

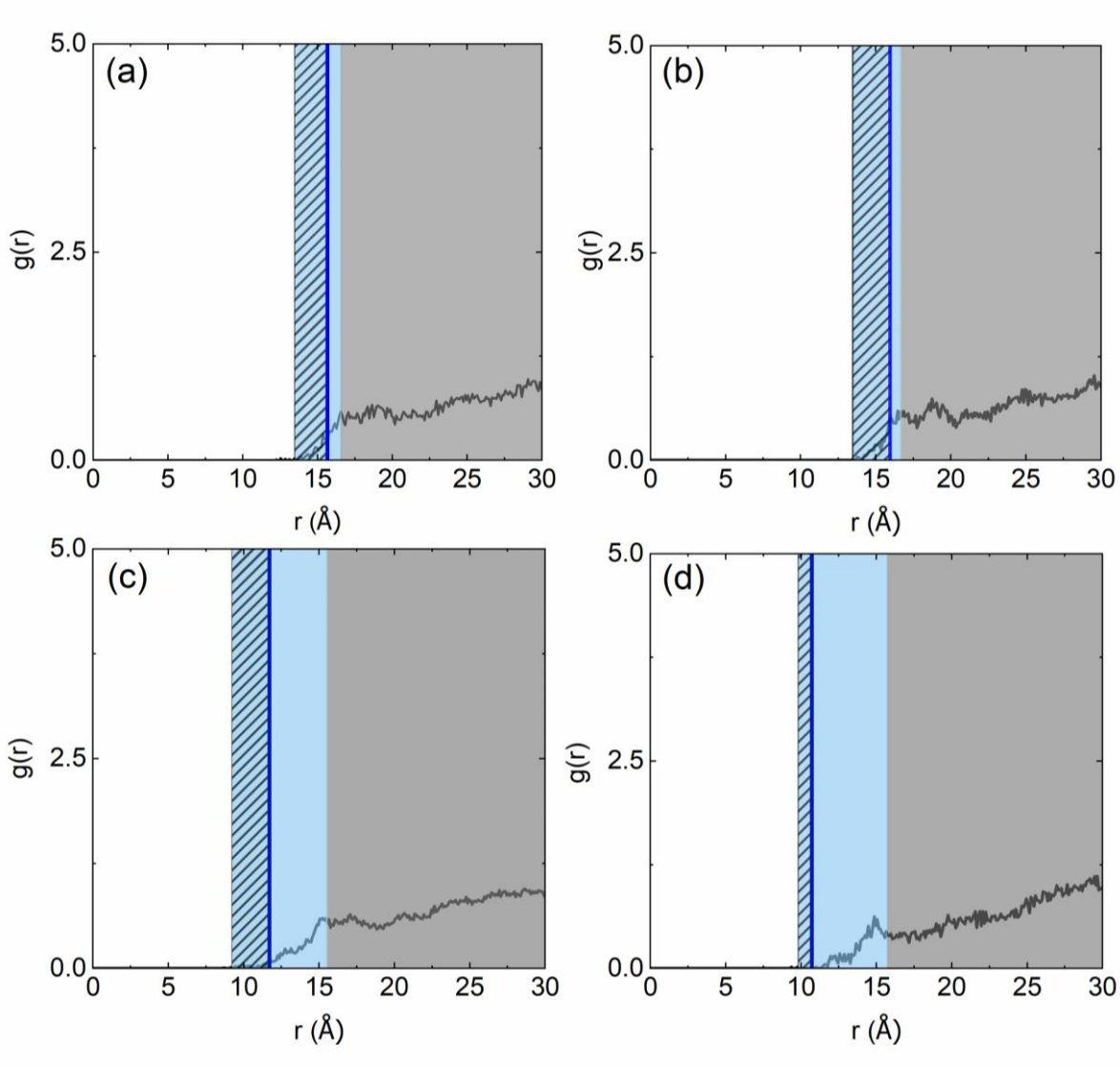

Figure 3.31 : Calculated radial atomic density distribution of functionalized ZIF-67-IDip/6FDA-DAM composite of 6FDA-DAM (black) when exposed to (a) propylene and (b) propane molecules, unfunctionalized ZIF-67/6FDA-DAM composite of 6FDA-DAM (black) when exposed to (c) propylene and (d) propane molecules with respect to the center of the nanoparticle (r = 0).

It is further examined how MOF functionalization influences the single-component sorption isotherms for propane and propylene while also considering the impact of polymer rigidity. Hence, it is observed that both the overlap and interfacial region lengths for PIM-1/ZIF-67-IDip expand upon adsorption of both propane and propylene (Figure 3.32). Specifically, the overlap length increases to 3.8 Å for propane and 2.8 Å for propylene, compared to 2.6 Å in

the guest-free composite. Additionally, the interfacial length extends to 7.9 Å for propane and 9 Å for propylene, in contrast to 6.5 Å in the guest-free composite.

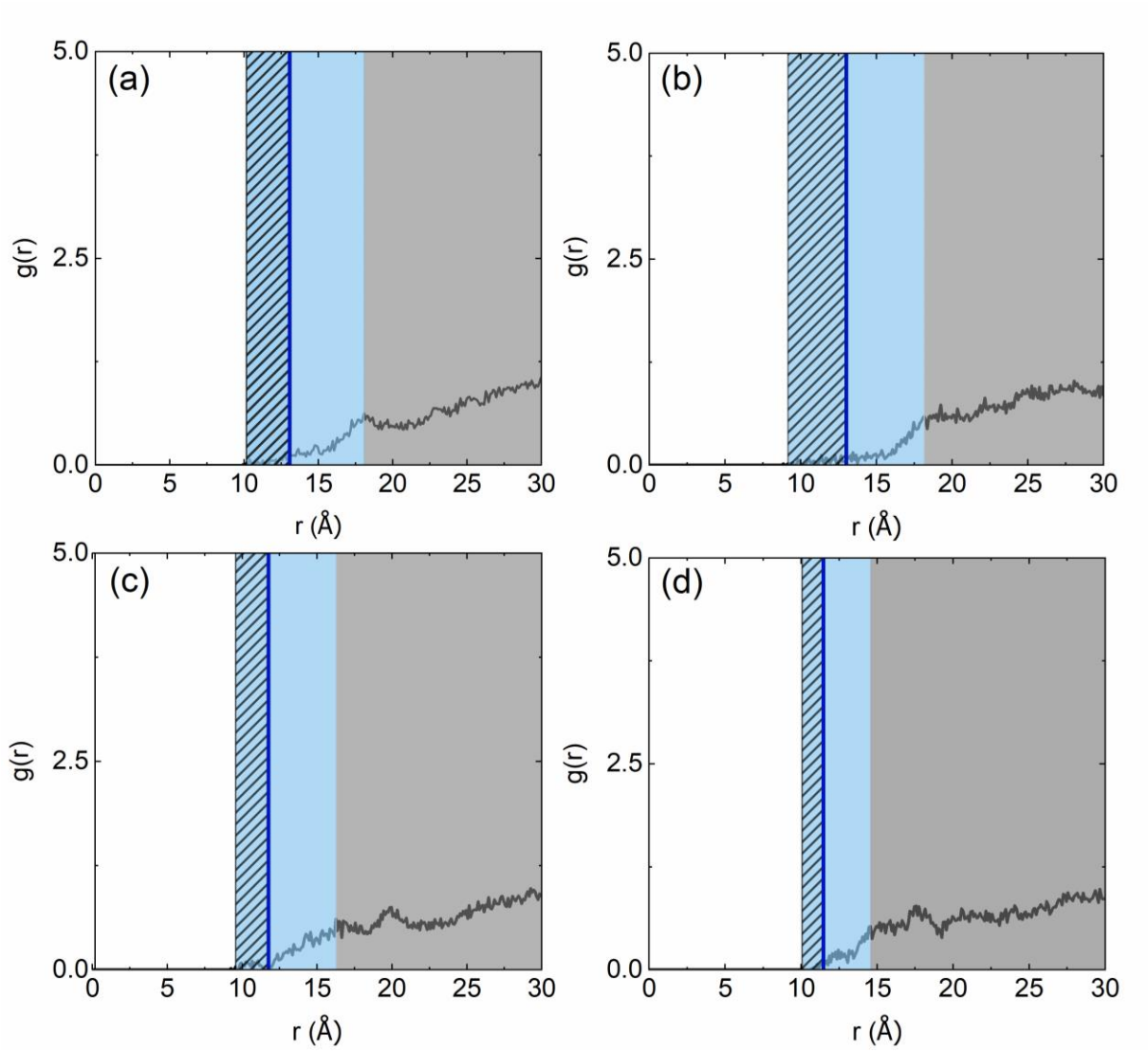

Figure 3.32 : Calculated radial atomic density distribution of functionalized ZIF-67-IDip/PIM-1 composite of PIM-1 (black) when exposed to (a) propylene and (b) propane molecules, unfunctionalized ZIF-67/ PIM-1 composite of PIM-1 (black) when exposed to (c) propylene and (d) propane molecules with respect to the center of the nanoparticle (r = 0).

The analysis of the FFV (Table 3.5) for both unfunctionalized and functionalized MOF-based composites revealed that the global FFV increases for the guest-free composites compared to pure 6FDA-DAM. Notably, in the case of the single component adsorption of propane and

propylene at 308 K and 8 bar, the FFV for the functionalized ZIF-67-IDip/6FDA-DAM composite is increased similarly in the presence of propane and propylene (23 % vs 23.4 % for propylene and propane respectively) in line with a similar MOF/polymer overlap region discussed earlier. However, the situation differs for the unfunctionalized MOF/6FDA-DAM composite, with a propylene-induced FFV increase (14.5 %) lower than that obtained for propane (23.8%). This observation suggests that propylene induces a higher degree of plasticization of the corresponding unfunctionalized MOF surface-based composite compared to propane [45–47].

Table 3.5 : FFV increase in 6FDA-DAM and MOF/6FDA-DAM composites at T=35°C and P=8 bar, induced by the single component adsorption of C_3H_6 and C_3H_8.

Species	6FDA-DAM		ZIF-67/6FDA-DAM		ZIF-67-IDip/6FDA-DAM	
	FFV	% Increase	FFV	% Increase	FFV	% Increase
Pure	0.161		0.282		0.235	
C_3H_6	0.195	21.1	0.323	14.5	0.289	23.0
C_3H_8	0.179	11.2	0.349	23.8	0.290	23.4

Figure 3.33 further compares the propane and propylene sorption isotherms for the ZIF-67-IDip-based composites with 6FDA-DAM, 6FDA-DABA and PIM-1 at 308 K up to 8 bar for the 34.5 wt. % MOF filler loading. Despite, the highest propane and propylene uptakes were obtained for ZIF-67-IDip/PIM-1 followed by ZIF-67/6FDA-DAM and ZIF-67/6FDA-DABA composites, in line with the discussion above, the thermodynamic sorption selectivity is not expected to be improved neither for ZIF-67-IDip/PIM-1 vs ZIF-67/PIM-1.

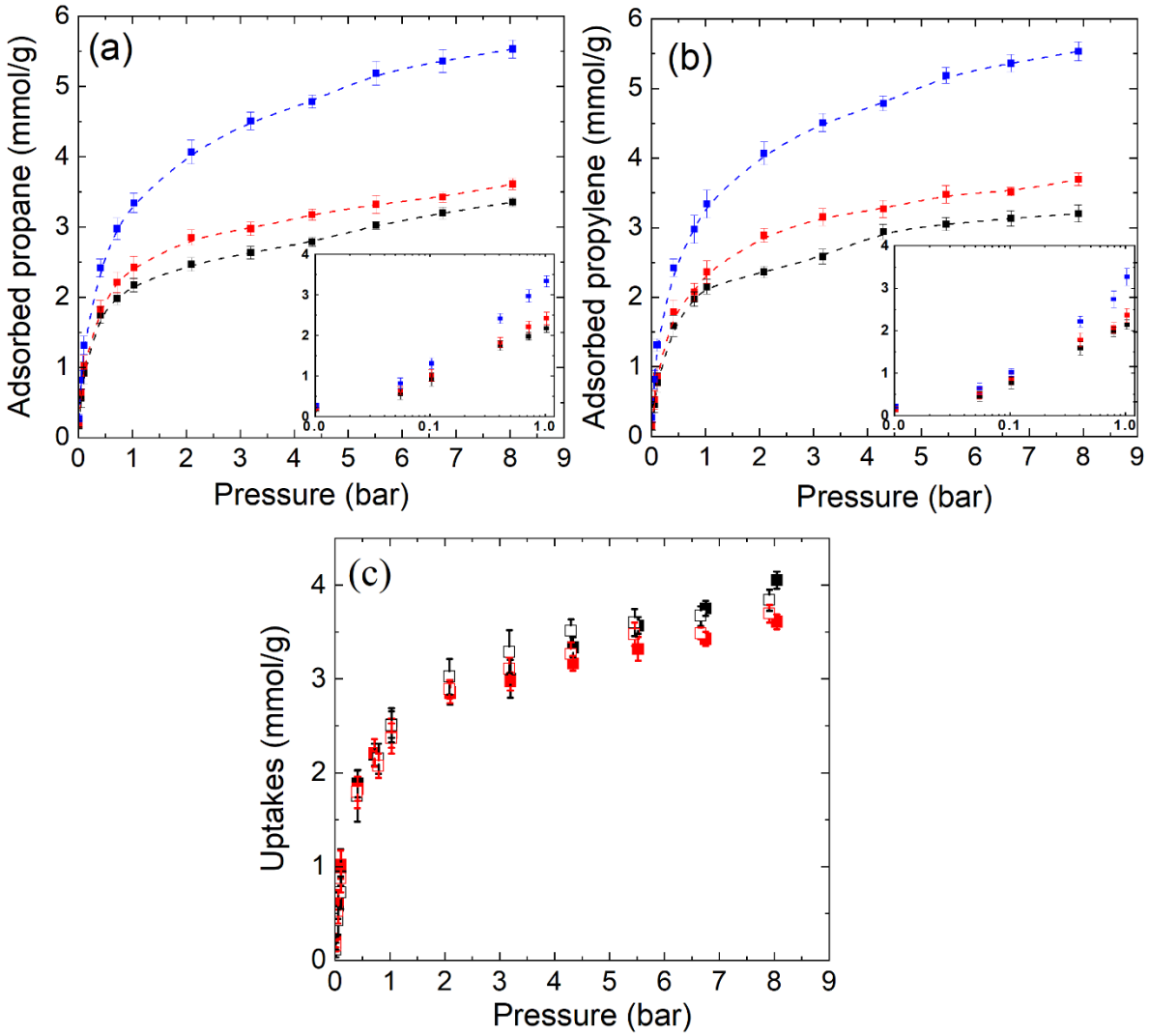

Figure 3.33 : Simulated propane and propylene sorption isotherms for 34.5 wt. % ZIF-67-IDip/PIM-1 (blue), ZIF-67-IDip/6FDA-DAM (red) and ZIF-67-IDip/6FDA-DABA (black) at 308 K up to 8 bar, with an inset up to 1 bar at logarithmic scale (dashed lines are to guide the eye): (a) Propane and (b) Propylene (c) Comparison of propane (solid) and propylene (blank) uptakes in 34.5 wt. % ZIF-67-IDip/6FDA-DAM (black) and ZIF-67/6FDA-DAM (red).

The further analysis of the torsion angle distribution are analyzed to gain insights into the chain dynamics of the interfacial polymer vs bulk polymer while investigating the impact of guest molecules. The effect of guest molecules on the distribution of diamine–dianhydride linkage at 8 bar are compared in Figure 3.34, both for the unfunctionalized ZIF-67/6FDA-DAM and functionalized ZIF-67-IDip/6FDA-DAM composites. In the presence of guest molecules, the angle distributions do not change significantly between the interfacial polymer

and bulk polymer in both functionalized and unfunctionalized composites**.** It seems that the polymer at the interface tends to behave like the bulk polymer due to the reduced rigidity of torsion.

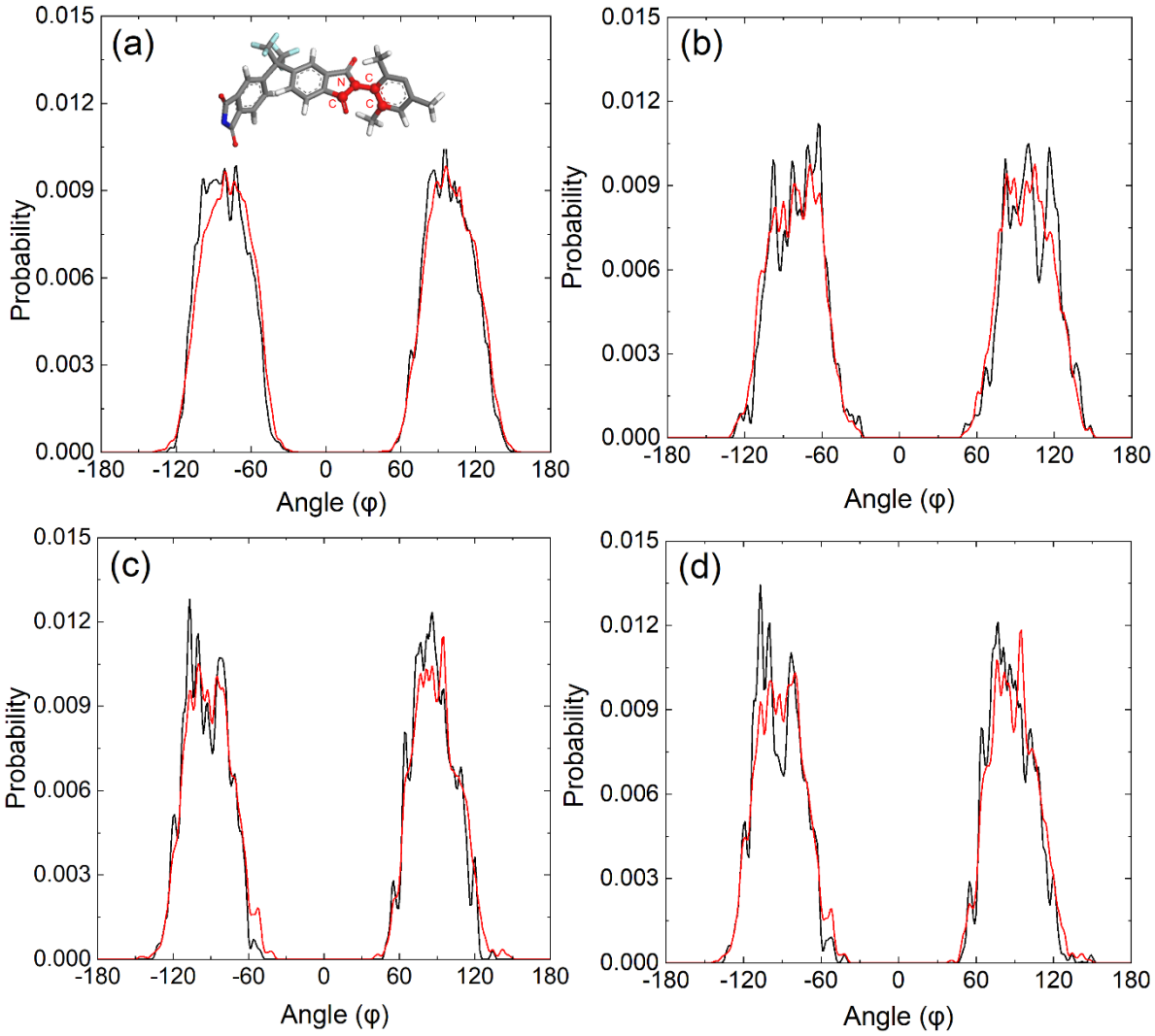

Figure 3.34 : Torsional angle ($\varphi_{C-N-C-C}$) distributions in the 6FDA-DAM for the unfunctionalized ZIF-67/6FDA-DAM at the interface (black) and at the bulk phase (red) when exposed to (a) propylene and (b) propane molecules, functionalized ZIF-67-IDip/6FDA-DAM at the interface (black) and at the bulk phase (red) when exposed to (c) propylene and (d) propane molecules.

On the other hand, the effect of guest molecules on the distribution of $\varphi_{C-C-O-C}$ and $\varphi_{C-C-C-C}$ angles at 8 bar are compared in Figure 3.35 and Figure 3.36, both for the unfunctionalized

ZIF-67/PIM-1 and functionalized ZIF-67-IDip/PIM-1 composites. Just as observed in the cases of unfunctionalized and functionalized ZIF-67 with 6FDA-DAM composites, the behavior of the polymer at the interface in both the ZIF-67/PIM-1 and ZIF-67-IDip/PIM-1 composites tends to resemble that of the bulk polymer due to the reduced rigidity of torsion. Hence, solvate induced conformational changes in the torsional angles correlate with the de-rigidification effect previously reported by Balçık[48] and van Essen[49,50].

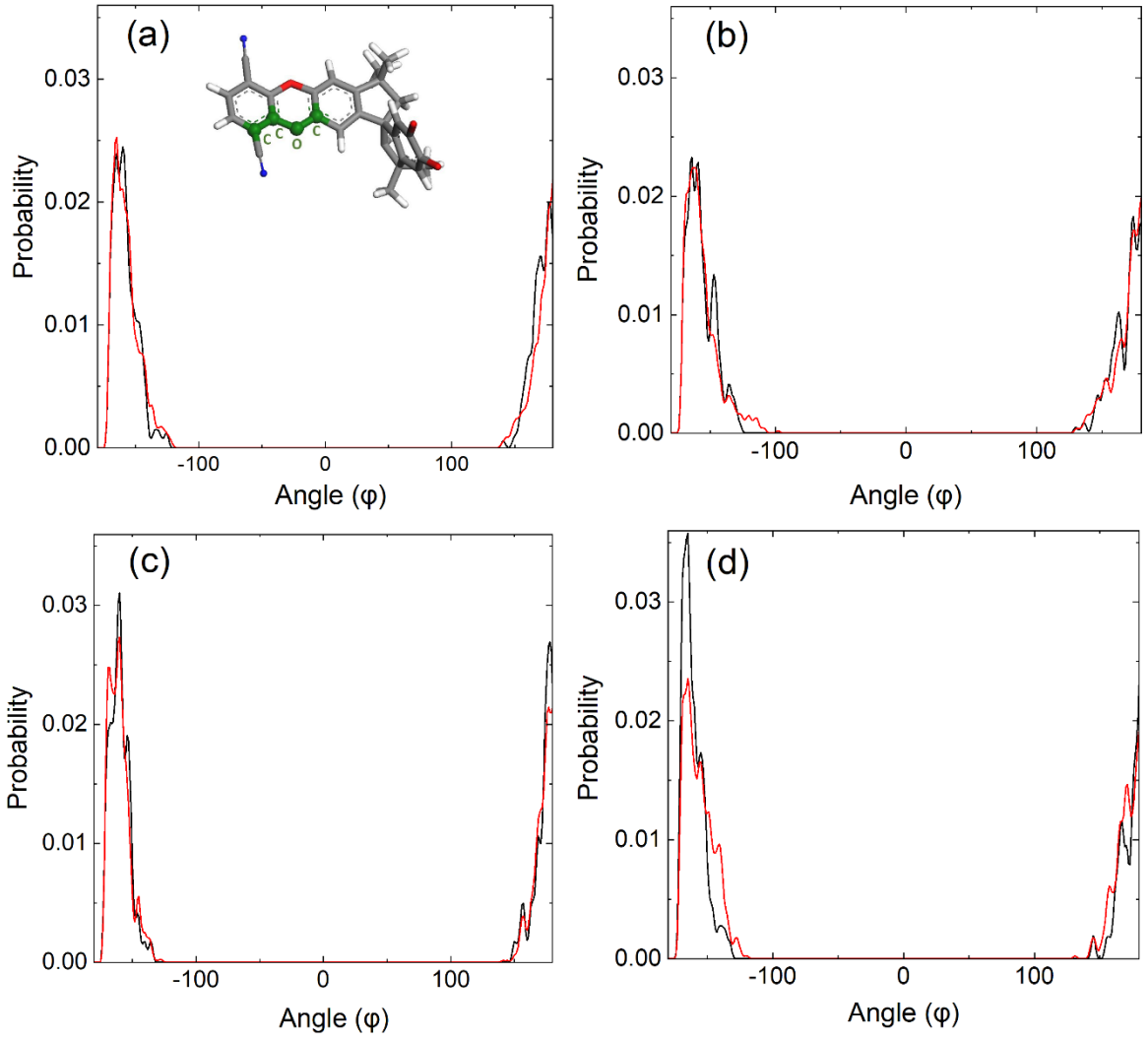

Figure 3.35 : Torsional angle ($\varphi_{C-N-C-C}$) distributions in the PIM-1 for the unfunctionalized ZIF-67/PIM-1 at the interface (black) and at the bulk phase (red), when exposed to (a) propylene and (b) propane molecules, functionalized ZIF-67-IDip/PIM-1 at the interface (black) and at the bulk phase (red) when exposed to (c) propylene and (d) propane molecules.

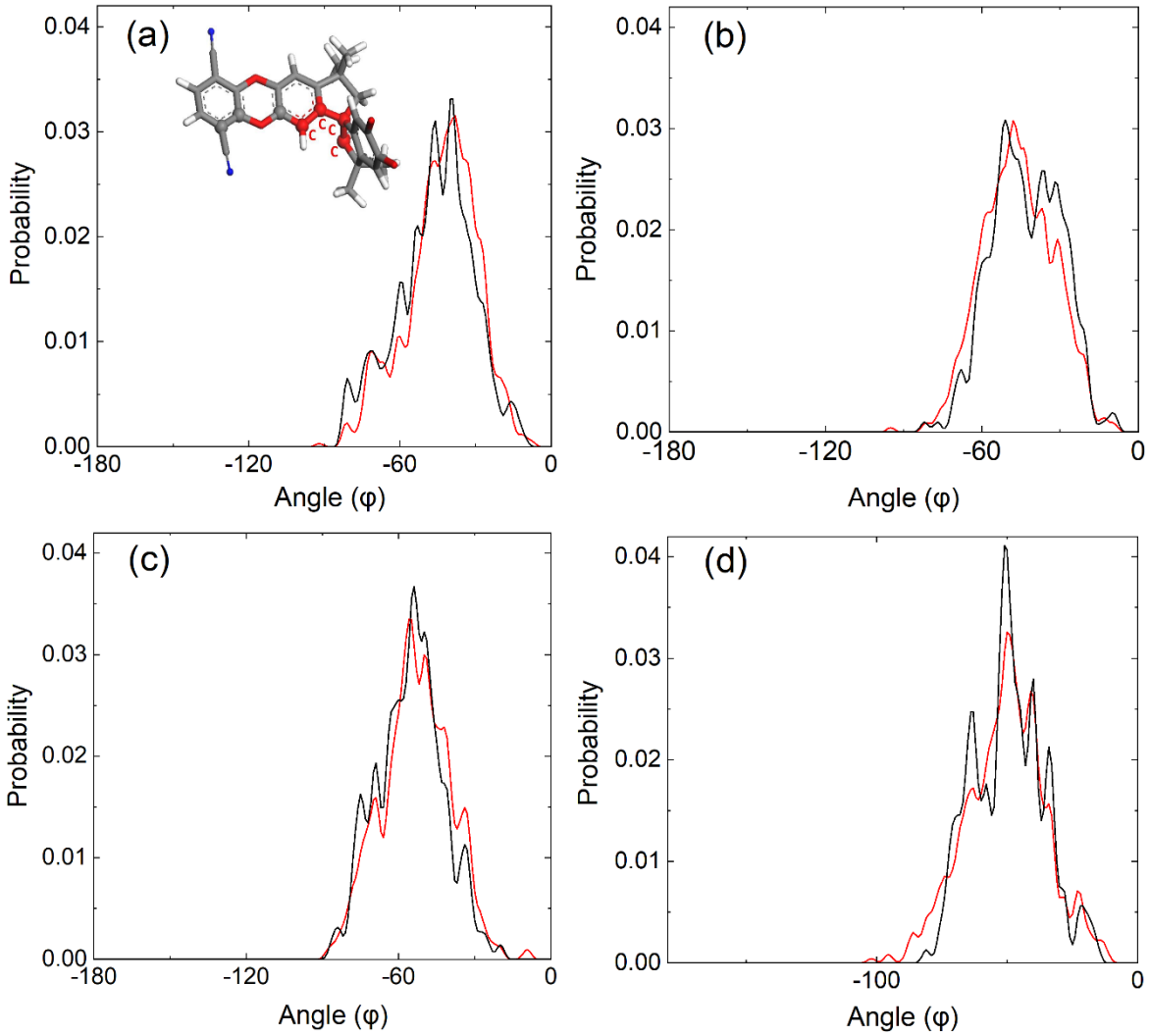

Figure 3.36 : Torsional angle ($\varphi_{C-N-C-C}$) distributions in the PIM-1 for the ZIF-67/PIM-1 at the interface (black) and at the bulk phase (red), when exposed to (a) propylene and (b) propane molecules, functionalized ZIF-67-IDip/PIM-1 at the interface (black) and at the bulk phase (red) when exposed to (c) propylene and (d) propane molecules.

3.8.3 Impact of MOF loading on the adsorption properties of ZIF-67-based MMMs

The sorption isotherms of composites are shown in Figure 3.37 for both 34.5 and 18 wt. % ZIF-67 content. As anticipated, reducing the MOF content resulted in decreased propane and propylene uptakes. However, it is noteworthy that the ZIF content did not alter the thermodynamic separation selectivity of the composites. In Figure 3.37c, it can be observed

how the sorption properties were affected by increasing the ZIF-67 filler content in the 6FDA-DAM matrices, using a volume additive approach. It appears that reducing the MOF content does not have a detrimental impact on the adsorptive capacity of the composite, despite obtaining a slightly lower sorption capacity with 18 wt. % ZIF-67/6FDA-DAM. This behavior may be attributed to the formation of interfacial defects, such as non-selective voids or polymer rigidification [33,51].

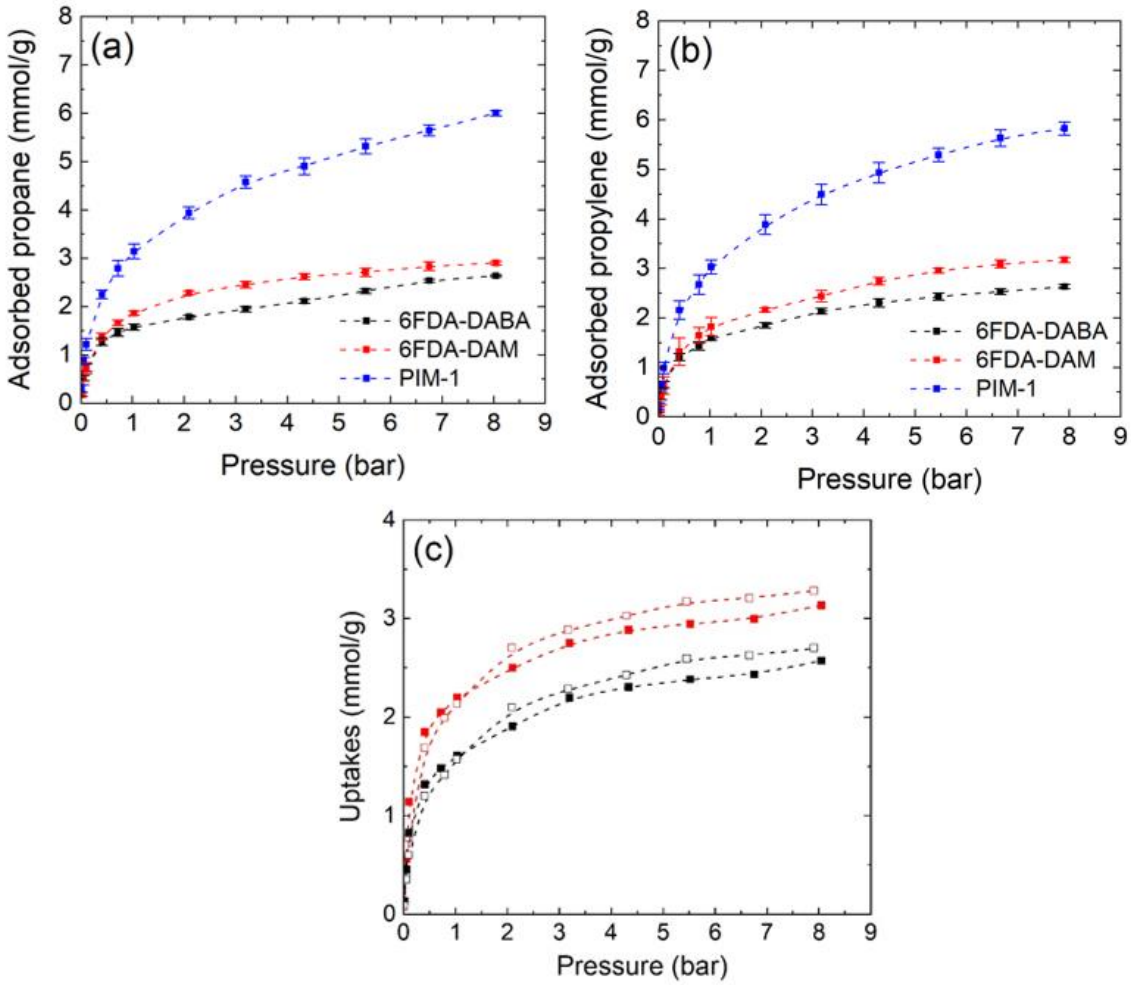

Figure 3.37 : Gas adsorption of (a) Propane uptakes in 18 wt % ZIF-67/PIM-1 (blue), ZIF-67/6FDA-DAM (red) and ZIF-67/6FDA-DABA (black) (b) Propylene uptakes in 18 wt % ZIF-67/PIM-1 (blue), ZIF-67/6FDA-DAM (red) and ZIF-67/6FDA-DABA (black) at 308 K up to 8 bar. (c) Volume additive approach in propane (solid) and propylene (open) uptakes in 34.5 wt % ZIF-67/6FDA-DAM (red) and 18 wt % ZIF-67/6FDA-DAM (black) (dashed lines are guide to the eye).

3.9 Conclusion

In this work, various atomistic models of ZIF-67/polymer composites were constructed and evaluated in terms of MOF/polymer compatibility and separation properties for propane/propylene mixtures. Simulated sorption data showed that these composites do not demonstrate significant potential for thermodynamic separation. Hence, the favorable separation performance of ZIF-67 MMMs reported in the literature is most likely kinetic-driven. The interfacial interactions between MOF and polymer were further explored. It was revealed that the IDip functionalization of the ZIF-67 surface enables a more efficient packing of the polymers at the MOF surface since much larger MOF/polymer overlap length was computed. This is expected to improve the adhesion between polymer and MOF surface, while preventing agglomeration, consistent with the experimental findings. It was also explored the affinity between the MOF and polymers upon guest adsorption, revealing that propane does not significantly impact MOF/polymer interactions, while propylene leads to a slight alteration in the MOF/polymer overlap length. Furthermore, the analysis of the torsion distributions in the interfacial MOF/polymer region and bulk polymer region were suggested a less marked mobility of the polymer at the interfacial region. In terms of chain rigidity, the ZIF-67/PIM-1 composite demonstrated enhanced compatibility with the slightly higher MOF/polymer overlap region, as the L-shape vertex of PIM-1 can more easily adapt to the MOF surface.

Regarding these key aspects, the interplay between (i) MOF/polymer overlap region, (ii) the rigidity of the polymer, and (iii) the balance between the interfacial rigidification in MOF/polymer composites and sorption behavior were confirmed to be key parameters for the fabrication of homogeneous MOF/polymer composites. This preliminary study of the ZIF-67/polymer system has inspired further systematic exploration, including the functionalization of the ZIF-67 surface with various surface modifiers, such as isophthalic dihydrazide (IPD), as well as modifying the solvent-driven terminations by employing methanol as a surface terminating agent, as discussed in Chapter 4. Additionally, the next following step will focus on an in-depth analysis of the kinetics propylene/propane separation

processes in these composites with the study of free energy profiles as presented in Chapter 5.

REFERENCES

[1] J. Sánchez-Laínez, A. Pardillos-Ruiz, M. Carta, R. Malpass-Evans, N.B. McKeown, C. Téllez, J. Coronas, Polymer engineering by blending PIM-1 and 6FDA-DAM for ZIF-8 containing mixed matrix membranes applied to CO2 separations, Sep. Purif. Technol. 224 (2019) 456–462. https://doi.org/10.1016/j.seppur.2019.05.035.

[2] Z. Liu, Y. Liu, W. Qiu, W.J. Koros, Molecularly Engineered 6FDA-Based Polyimide Membranes for Sour Natural Gas Separation, Angew. Chemie - Int. Ed. 59 (2020) 14877–14883. https://doi.org/10.1002/anie.202003910.

[3] N.B. Mc Keown, P.M. Budd, Polymers of intrinsic microporosity (PIMs): Organic materials for membrane separations, heterogeneous catalysis and hydrogen storage, Chem. Soc. Rev. 35 (2006) 675–683. https://doi.org/10.1039/b600349d.

[4] P. Krokidas, S. Moncho, E.N. Brothers, M. Castier, I.G. Economou, Tailoring the gas separation efficiency of metal organic framework ZIF-8 through metal substitution: A computational study, Phys. Chem. Chem. Phys. 20 (2018) 4879–4892. https://doi.org/10.1039/c7cp08456k.

[5] R. Semino, N.A. Ramsahye, A. Ghou, G. Maurin, Microscopic Model of the Metal − Organic Framework / Polymer Interface : A First Step toward Understanding the Compatibility in Mixed Matrix Membranes, ACS Appl. Mater. Interfaces. 8 (2016) 809–819. https://doi.org/10.1021/acsami.5b10150.

[6] F. Tian, A.M. Cerro, A.M. Mosier, H.K. Wayment-Steele, R.S. Shine, A. Park, E.R. Webster, L.E. Johnson, M.S. Johal, L. Benz, Surface and stability characterization of a nanoporous ZIF-8 thin film, J. Phys. Chem. C. 118 (2014) 14449–14456. https://doi.org/10.1021/jp5041053.

[7] P. Krokidas, M. Castier, S. Moncho, D.N. Sredojevic, E.N. Brothers, H.T. Kwon, H.K. Jeong, J.S. Lee, I.G. Economou, ZIF-67 Framework: A Promising New Candidate for Propylene/Propane Separation. Experimental Data and Molecular Simulations, J. Phys. Chem. C. 120 (2016) 8116–8124. https://doi.org/10.1021/acs.jpcc.6b00305.

[8] J. Wang, R.M. Wolf, J.W. Caldwell, P.A. Kollman, D.A. Case, Development and Testing of a General Amber Force Field, J. Comput. Chem. 56531 (2004) 1157–1174.

[9] P. Krokidas, M. Castier, I.G. Economou, Computational Study of ZIF-8 and ZIF-67 Performance for Separation of Gas Mixtures, J. Phys. Chem. C. 121 (2017) 17999–18011. https://doi.org/10.1021/acs.jpcc.7b05700.

[10] S. Fu, G.B. Wenz, E.S. Sanders, S.S. Kulkarni, W. Qiu, C. Ma, W.J. Koros, Effects of

pyrolysis conditions on gas separation properties of 6FDA/DETDA:DABA(3:2) derived carbon molecular sieve membranes, J. Memb. Sci. 520 (2016) 699–711. https://doi.org/10.1016/j.memsci.2016.08.013.

[11] A. Knebel, A. Bavykina, S.J. Datta, L. Sundermann, L. Garzon-Tovar, Y. Lebedev, S. Durini, R. Ahmad, S.M. Kozlov, G. Shterk, M. Karunakaran, I.D. Carja, D. Simic, I. Weilert, M. Klüppel, U. Giese, L. Cavallo, M. Rueping, M. Eddaoudi, J. Caro, J. Gascon, Solution processable metal–organic frameworks for mixed matrix membranes using porous liquids, Nat. Mater. 19 (2020) 1346–1353. https://doi.org/10.1038/s41563-020-0764-y.

[12] G.S. Larsen, P. Lin, K.E. Hart, C.M. Colina, Molecular simulations of pim-1-like polymers of intrinsic microporosity, Macromolecules. 44 (2011) 6944–6951. https://doi.org/10.1021/ma200345v.

[13] M. Balçık, S.B. Tantekin-Ersolmaz, I. Pinnau, M.G. Ahunbay, CO2/CH4 mixed-gas separation in PIM-1 at high pressures: Bridging atomistic simulations with process modeling, J. Memb. Sci. 640 (2021) 119838. https://doi.org/10.1016/j.memsci.2021.119838.

[14] BIOVIA, Dassault Systèmes, Materials Studio, 7.0, (2017).

[15] M.G. Martin, J.I. Siepmann, Transferable potentials for phase equilibria. 1. United-atom description of n-alkanes, J. Phys. Chem. B. 102 (1998) 2569–2577. https://doi.org/10.1021/jp972543+.

[16] W.D. Cornell, P. Cieplak, C.I. Bayly, I.R. Gould, K.M. Merz, D.M. Ferguson, D.C. Spellmeyer, T. Fox, J.W. Caldwell, P.A. Kollman, A Second Generation Force Field for the Simulation of Proteins, Nucleic Acids, and Organic Molecules, J. Am. Chem. Soc. 117 (1995) 5179–5197. https://doi.org/10.1021/ja00124a002.

[17] B. Delley, An all-electron numerical method for solving the local density functional for polyatomic molecules, J. Chem. Phys. 92 (1990) 508–517. https://doi.org/10.1063/1.458452.

[18] A.D. Becke, Density-functional thermochemistry. III. The role of exact exchange, J. Chem. Phys. 98 (1993) 5648–5652. https://doi.org/10.1063/1.464913.

[19] S. Plimpton, Fast Parallel Algorithms for Short-Range Molecular Dynamics, J. Comput. Phys. 117 (1995) 1–19. https://doi.org/10.1039/c7sm02429k.

[20] G. Kupgan, L.J. Abbott, K.E. Hart, C.M. Colina, Modeling Amorphous Microporous Polymers for CO2 Capture and Separations, Chem. Rev. 118 (2018) 5488–5538. https://doi.org/10.1021/acs.chemrev.7b00691.

[21] S. Nosé, A unified formulation of the constant temperature molecular dynamics methods, J. Chem. Phys. 81 (1984) 511–519. https://doi.org/10.1063/1.447334.

[22] W.G. Hoover, Canonical dynamics: equilibrium phase-space distributions, 31 (1985) 1695–1697.

[23] L. Sarkisov, J. Kim, Computational structure characterization tools for the era of

material informatics, Chem. Eng. Sci. 121 (2015) 322–330. https://doi.org/10.1016/j.ces.2014.07.022.

[24] A. Bondi, Physical Properties of Molecular Crystals Liquids and Gases, John Wiley, New York, 1968.

[25] M. Balçık, M.G. Ahunbay, Prediction of CO2-induced plasticization pressure in polyimides via atomistic simulations, J. Memb. Sci. 547 (2018) 146–155. https://doi.org/10.1016/j.memsci.2017.10.038.

[26] B. Zornoza, C. Tellez, J. Coronas, J. Gascon, F. Kapteijn, Metal organic framework based mixed matrix membranes: An increasingly important field of research with a large application potential, Microporous Mesoporous Mater. 166 (2013) 67–78. https://doi.org/10.1016/j.micromeso.2012.03.012.

[27] A. Shimazu, T. Miyazaki, M. Maeda, K. Ikeda, Relationships between the Chemical Structures and the Solubility , Diffusivity , and Permselectivity of Propylene and Propane in 6FDA-Based Polyimides, (2000) 2525–2536.

[28] S.H. Park, K.J. Kim, W.W. So, S.J. Moon, S.B. Lee, Gas separation properties of 6FDA-based polyimide membranes with a polar group, Macromol. Res. 11 (2003) 157–162. https://doi.org/10.1007/BF03218346.

[29] A. Gonciaruk, K. Althumayri, W.J. Harrison, P.M. Budd, F.R. Siperstein, PIM-1/graphene composite: A combined experimental and molecular simulation study, Microporous Mesoporous Mater. 209 (2015) 126–134. https://doi.org/10.1016/j.micromeso.2014.07.007.

[30] M.L. Connolly, Analytical molecular surface calculation, J. Appl. Crystallogr. 16 (1983) 548–558. https://doi.org/10.1107/s0021889883010985.

[31] S. Hwang, R. Semino, B. Seoane, M. Zahan, C. Chmelik, R. Valiullin, M. Bertmer, J. Haase, F. Kapteijn, J. Gascon, G. Maurin, J. Kärger, Revealing the Transient Concentration of CO2 in a Mixed-Matrix Membrane by IR Microimaging and Molecular Modeling, Angew. Chemie - Int. Ed. 57 (2018) 5156–5160. https://doi.org/10.1002/anie.201713160.

[32] R. Semino, J.P. Durholt, R. Schmid, G. Marin, Multiscale modeling of the HKUST-1/polyvinyl alcohol) interface: From an atomistic to a coarse graining approach, J. Phys. Chem. C. 121 (2017) 21491–21496. https://doi.org/10.1021/acs.jpcc.7b07090.

[33] M. Benzaqui, R. Semino, N. Menguy, F. Carn, T. Kundu, J.M. Guigner, N.B. McKeown, K.J. Msayib, M. Carta, R. Malpass-Evans, C. Le Guillouzer, G. Clet, N.A. Ramsahye, C. Serre, G. Maurin, N. Steunou, Toward an Understanding of the Microstructure and Interfacial Properties of PIMs/ZIF-8 Mixed Matrix Membranes, ACS Appl. Mater. Interfaces. 8 (2016) 27311–27321. https://doi.org/10.1021/acsami.6b08954.

[34] R. Semino, N.A. Ramsahye, A. Ghoufi, G. Maurin, Role of MOF surface defects on the microscopic structure of MOF/polymer interfaces: A computational study of the ZIF-8/PIMs systems, Microporous Mesoporous Mater. 254 (2017) 184–191.

https://doi.org/10.1016/j.micromeso.2017.02.031.

[35] M.Z. Ahmad, M. Navarro, M. Lhotka, B. Zornoza, C. Téllez, W.M. de Vos, N.E. Benes, N.M. Konnertz, T. Visser, R. Semino, G. Maurin, V. Fila, J. Coronas, Enhanced gas separation performance of 6FDA-DAM based mixed matrix membranes by incorporating MOF UiO-66 and its derivatives, J. Memb. Sci. 558 (2018) 64–77. https://doi.org/10.1016/j.memsci.2018.04.040.

[36] K. Xie, Q. Fu, J. Kim, H. Lu, Y. He, Q. Zhao, J. Scofield, P.A. Webley, G.G. Qiao, Increasing both selectivity and permeability of mixed-matrix membranes: Sealing the external surface of porous MOF nanoparticles, J. Memb. Sci. 535 (2017) 350–356. https://doi.org/10.1016/j.memsci.2017.04.022.

[37] M.J. Frisch, G.W. Trucks, H.B. Schlegel, G.E. Scuseria, M.A. Robb, J.R. Cheeseman, G. Scalmani, V. Barone, G.A. Petersson, H. Nakatsuji, X. Li, M. Caricato, A. V. Marenich, J. Bloino, B.G. Janesko, R. Gomperts, B. Mennucci, H.P. Hratchian, J. V. Ortiz, D. Izmaylov, A. F. Sonnenberg, J. L. Williams-Young, F. Ding, F. Lipparini, F. Egidi, J. Goings, B. Peng, A. Petrone, V.G. Henderson, T. Ranasinghe, D. Zakrzewski, J. Gao, N. Rega, G. Zheng, W. Liang, M. Hada, M. Ehara, K. Toyota, R. Fukuda, J. Hasegawa, M. Ishida, T. Nakajima, Y. Honda, O. Kitao, H. Nakai, T. Vreven, J.E. Throssell, K. Montgomery, J. A., Jr. Peralta, F. Ogliaro, M.J. Bearpark, J.J. Heyd, E.N. Brothers, K.N. Kudin, V.N. Staroverov, T.A. Keith, R. Kobayashi, A.P. Normand, J. Raghavachari, K.; Rendell, J.C. Burant, S.S. Iyengar, J. Tomasi, M. Cossi, J.M. Millam, M. Klene, C. Adamo, R. Cammi, J.W. Ochterski, R.L. Martin, K. Morokuma, O. Farkas, J.B. Foresman, D.J. Fox, Gaussian 09, Revision E.01, (2009).

[38] S. Keskin, S.A. Altinkaya, A Review on Computational Modeling Tools for MOF-Based Mixed Matrix Membranes, Computation. 7 (2019).

[39] R. Semino, J.C. Moreton, N.A. Ramsahye, S.M. Cohen, G. Maurin, Understanding the origins of metal-organic framework/polymer compatibility, Chem. Sci. 9 (2018) 315–324. https://doi.org/10.1039/c7sc04152g.

[40] W. Fang, L. Zhang, J. Jiang, Polymers of intrinsic microporosity for gas permeation: A molecular simulation study, Mol. Simul. 36 (2010) 992–1003. https://doi.org/10.1080/08927022.2010.498828.

[41] S. Velioğlu, M.G. Ahunbay, Ş.B. Tantekin-Ersolmaz, Investigation of CO2-induced plasticization in fluorinated polyimide membranes via molecular simulation, J. Memb. Sci. 418 (2012) 217–227. https://doi.org/10.1016/j.memsci.2012.06.043.

[42] D. Peng, D.B. Robinson, A New Two-Constant Equation of State, 15 (1976) 59–64.

[43] C. Muzzi, A. Fuoco, M. Monteleone, E. Esposito, J.C. Jansen, E. Tocci, Optical Analysis of the Internal Void Structure in Polymer Membranes for Gas Separation, (2020).

[44] Q. Shen, S. Cong, R. He, Z. Wang, Y. Jin, H. Li, X. Cao, J. Wang, B. Van Der Bruggen, Y. Zhang, SIFSIX-3-Zn / PIM-1 mixed matrix membranes with enhanced permeability for propylene / propane separation, J. Memb. Sci. 588 (2019) 117201. https://doi.org/10.1016/j.memsci.2019.117201.

[45] M. Das, W.J. Koros, Performance of 6FDA-6FpDA polyimide for propylene/propane separations, J. Memb. Sci. 365 (2010) 399–408. https://doi.org/10.1016/j.memsci.2010.09.029.

[46] S. Park, H.K. Jeong, Transforming polymer hollow fiber membrane modules to mixed-matrix hollow fiber membrane modules for propylene/propane separation, J. Memb. Sci. 612 (2020). https://doi.org/10.1016/j.memsci.2020.118429.

[47] S. Velioğlu, M.G. Ahunbay, S.B. Tantekin-Ersolmaz, Propylene/propane plasticization in polyimide membranes, J. Memb. Sci. 501 (2016) 179–190. https://doi.org/10.1016/j.memsci.2015.11.034.

[48] M. Balçık, S.B. Tantekin-Ersolmaz, M.G. Ahunbay, Interfacial analysis of mixed-matrix membranes under exposure to high-pressure CO2, J. Memb. Sci. 607 (2020). https://doi.org/10.1016/j.memsci.2020.118147.

[49] M. van Essen, R. Thür, L. van den Akker, M. Houben, I.F.J. Vankelecom, K. Nijmeijer, Z. Borneman, Tailoring the separation performance of ZIF-based mixed matrix membranes by MOF-matrix interfacial compatibilization, J. Memb. Sci. 637 (2021) 119642. https://doi.org/10.1016/j.memsci.2021.119642.

[50] M. van Essen, L. van den Akker, R. Thür, M. Houben, I.F.J. Vankelecom, Z. Borneman, K. Nijmeijer, Investigation of ZIF-78 Morphology and Feed Composition on the Mixed Gas CO2/N2 Separation Performance in Mixed Matrix Membranes, Adv. Mater. Interfaces. 8 (2021). https://doi.org/10.1002/admi.202001478.

[51] A. Jain, M.Z. Ahmad, A. Linkès, V. Martin-gil, R. Castro-muñoz, P. Izak, Z. Sofer, W. Hintz, V. Fila, 6FDA-DAM:DABA Co-Polyimide Mixed Matrix Membranes with GO and ZIF-8 mixtures for effective CO2/CH4 separation, Nanomaterials. 11 (2021) 1–16. https://doi.org/10.3390/nano11030668.

ARTICLE

THE JOURNAL OF PHYSICAL CHEMISTRY C
A JOURNAL OF THE AMERICAN CHEMICAL SOCIETY

pubs.acs.org/JPCC Article

Atomistic Insight into the Interfacial Structuring of ZIF-67 MOF/Polymer Composites and Their Propylene–Propane Adsorption Properties

Elif Begüm Doğan, Guillaume Maurin, and M. Göktuğ Ahunbay*

Cite This: *J. Phys. Chem. C* 2023, 127, 20491–20502 Read Online

ACCESS | Metrics & More | Article Recommendations | Supporting Information

ABSTRACT: Herein, we present a systematic computational study on a series of ZIF-67/polymer composites to reveal how the surface functionalization of the ZIF-67 with carbene groups and the nature of the polymers affect the structuring of the MOF/polymer interface and the resulting interfacial interactions as well as their thermodynamic propane and propylene adsorption properties. Hence, the surface-functionalized ZIF-67 nanoparticles with 1,3-bis(2,4,6-diisopropylphenyl)imidazole-2-ylidene (IDip) were predicted to improve the compatibility of the ZIF-67/6FDA-DAM composite enabling a better packing of the polymer at the MOF surface. The sorption simulations confirmed that the propylene/propane separation by these composites is not thermodynamically driven. Composites made of ZIF-67 and 6FDA-DABA as well as PIM-1 were then typically considered to gain an in-depth understanding of the role of the polymer on the MOF/polymer compatibility. We found that the ZIF-67/PIM-1 composite shows a better compatibility vs the ZIF-67/6FDA-DAM composite because the conformation of PIM-1 provides a better way to conform the polymer chains at the MOF surface.

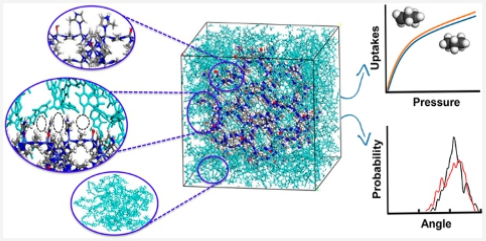

1. INTRODUCTION

Propylene with its annual worldwide production of 100 million tons is the second largest feedstock in the petrochemical industry after ethylene, and its production is expected to grow 4.0% per year by 2025.[1−4] Propylene is mainly used for polypropylene production, while it is also essential for acrylonitrile, cumene, and propylene oxide production.[4,5] However, this alkene molecule is produced in a mixture with propane, and their separation is highly challenging. Current separation techniques, mostly dominated by cryogenic distillation, are energy-intensive processes due to the similarities of these two molecules in terms of molecular size and boiling point.[6,7] Membrane-based separation has become an appealing alternative technology due to its cheaper operating costs, continuous operation, and energy efficiency[2,7,8] with a use of 90% less energy compared to distillation.[9]

For commercial large-scale gas separation processes, polymeric membranes are generally preferred over inorganic membranes due to their easy processability, scalability, and mechanical strength. However, these polymeric membranes suffer from a permeability−selectivity trade-off, forming the so-called Robeson upper bound that prohibits the achievement of very high permeability (productivity) combined with excellent selectivity (efficiency).[7,10−12] Moreover, condensable gases, such as propylene and propane, have the potential to cause polymer chains to swell under relatively high gas pressure working conditions. This can result in severe plasticization and/or dilation effects in many polymeric membranes, although there are exceptions, particularly in the case of fluoropolymers.[13] Mixed-matrix membranes (MMMs) consisting of a continuous polymer phase and dispersed inorganic or inorganic/organic fillers offer an effective alternative solution to overcome the disadvantages of polymer-based membranes.[14] Embedding fillers, e.g., zeolites and metal−organic frameworks (MOFs), among others, into polymers enables to combine the high gas permeability and selectivity of fillers and the good processability and mechanical robustness of polymeric membranes.[15−23] Such an approach often results in an enhancement of either permeability, selectivity, or even both.[24] However, achieving a good interfacial adhesion between these two components is a key parameter for fabricating continuous and mechanically stable membranes, ensuring high MOF loading and achieving homogeneous dispersion of MOF filler nanoparticles within the polymer matrices.[25−27] Indeed, a poor adhesion between the two components can be at the origin of filler particle aggregation

Received: June 29, 2023
Revised: August 29, 2023
Published: October 4, 2023

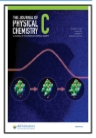

ACS Publications © 2023 American Chemical Society

https://doi.org/10.1021/acs.jpcc.3c04377
J. Phys. Chem. C 2023, 127, 20491−20502

and nonselective interfacial voids that most of the time lead to membranes with weak mechanical stability and/or poor separation performance.[14,28,29] Typically, interfacial adhesion is influenced by van der Waals and electrostatic interactions between the two components as well as the polymer flexibility/rigidity.[30,31]

Among the MMM fillers, the zeolitic imidazolate frameworks (ZIFs), a subfamily of MOFs, are of particular interest due to their highly stable and selective architectures encompassing cages accessible to certain guest molecules by ultramicropore windows.[32,33] ZIFs composed of metal nodes, e.g., Zn^{2+}, Co^{2+}, Cd^{2+}, and Fe^{2+} bridged by imidazole linkers, are topologically similar to zeolites.[34−36] In particular, ZIF-8 has been intensively explored as a sorbent and membrane for propylene/propane separation owing to its narrow and flexible gate of about 4.0 Å, which favors a kinetically driven discrimination between the two guests,[37−42] the alkane molecule of larger size (∼4.3 Å) diffusing slower as compared to propylene (∼4 Å).[43] ZIF-67 ($Co(Hmim)_2$, Hmim = 2-methylimidazole)), isostructural to ZIF-8, was also demonstrated to be effective for propylene/propane separation by both experimental and computational studies.[44−47] These findings encouraged the incorporation of ZIF-67 as filler in a range of polymeric matrixes for the fabrication of propylene/propane selective MMMs.[48−50] As an example, An et al. reported a defect-free ZIF-67/6 FDA-DAM MMM with a selectivity twice higher than its ZIF-8-MMM analogue while showing a better physical aging resistance.[48] Moghadam et al. evidenced that thermally annealed 6 FDA-DAM-based ZIF-67-decorated porous graphene oxide nanofiller membrane achieves an effective propylene/propane separation combined with a great resistance to plasticization via favorable polymer−filler interfacial interactions.[49] More recently, Knebel et al.[50] reported a novel series of MMMs for propylene/propane separation made of ZIF-67 nanoparticles (NPs) with their outer surfaces modified by the N-heterocyclic carbene (NHC) 1,3-bis(2,4,6-diisopropylphenyl)imidazole-2-ylidene (IDip) and 6 FDA-DAM and derivative polymers. This NHC-based surface functionalized group was selected owing to its potentially high affinity to unsaturated metal sites as well as their similar chemistry to the imidazole linker present in ZIF-67. These authors successfully fabricated MMM with a ZIF-67-IDip filler loading in 6 FDA-DAM as high as 47.5 wt %, with no agglomeration of ZIF-67-IDip NPs observed. This MMM was demonstrated to exhibit a much better dispersion of the MOF filler in the polymer matrix and a lower plasticization of the polymer as compared to the unfunctionalized ZIF-67/6 FDA-DAM. Both features suggested an improvement of the MOF/polymer adhesion by functionalizing the MOF similarly to the scenario reported for a range of functionalized MOF/polymer MMMs,[51−54] although no direct evidence was delivered. Molecular modeling combining quantum and force field simulation techniques has been proven over the past few years to enable the construction of reliable interfacial atomistic models for a series of MOF/polymer pairs. This enabled to gain invaluable microscopic insight into the compatibility between the two components that dominates the feasibility and hence the stability of the corresponding MMMs as well as into the microscopic mechanism that drives their adsorption/separation performances.[29,31,55−59] Herein, we deployed advanced atomistic computational tools with the objective to (i) reveal the microscopic origin of the improved adhesion of ZIF-67 and 6 FDA-DAM in the resulting composites by functionalizing the MOF by carbene groups, (ii) understand how the MOF functionalization affects the propane and propylene adsorption properties of the composites, and (iii) systematically assess the impact of the nature of the polymers on the ZIF-67/polymer compatibility in the corresponding composites and its adsorption properties with a selection of three polymers of distinct physical properties, i.e., 6FDA-DAM with its rigid backbone and inhibited polymer chain packing,[60] 6FDA-DABA with its plasticizing controlling capability by cross-linking owing to the presence of polar −COOH groups,[61] and polymer of intrinsic microporosity-1 (PIM-1) with its rigid contorted chains and relatively high porosity.[62]

2. METHODS

2.1. Construction of the Atomistic Models for MOFs, Polymers, and MOF/Polymer Composites. A representative model of ZIF-67 NP was cleaved from the supercell made of 2 × 2 × 2 unit cells of the previously reported crystal structure[63] (Figure S1). The resulting spherical-shaped atomistic model contains 16 cages (cage size of ∼11.5 Å), and its outer surface was terminated by −OH groups and −H considering the dissociative adsorption of water since the standard hydrothermal synthesis of ZIF-67 proceeds in aqueous solution.[55,64] The size of our modeled ZIF-67 NP is 53 Å, falling within the range of NP sizes recently obtained for certain MOFs (50−100 Å)[65] using various synthetic routes, thus bridging the gap between experimental and theoretical length scales. The resulting outer surface can be schematically described as a "zigzag" model where the outermost atoms are the NH groups of the imidazole linkers and the innermost atoms are the OH groups directly bonded to the Co atoms. The atomic partial charges for this representative model of ZIF-67 (Table S1) and the force field parameters were taken from the work previously reported by Krokidas et al.,[44] who used flexible force field through modification in AMBER[66] force field to describe the bonded interactions as well as the nonbonded Lennard-Jones (LJ) interaction parameters for the ZIF-67 bulk atoms. The charges of the surface terminal groups, −OH groups, and −H atoms were set to maintain the charge neutrality of the ZIF-67 NP model. The IDip surface-modified ZIF-67 NP (ZIF-67-IDip) model was obtained using the same approach as that applied to the pristine ZIF-67 NP with the IDip functions bonded to Co atoms, while the innermost atoms were coordinated to −OH groups and −H atoms. The atomic partial charges for ZIF-67-IDip (Table S2) were obtained using cluster-based density functional theory (DFT) calculations (see Figure S7) with the combination of PBE functional and the 6-31G basis set as implemented in Gaussian 09.[67] The extra force field parameters for the IDip function were taken from Generalized Amber Force Field (GAFF).[66] Illustrations of the ZIF-67 NP (size of ∼53 Å) and its external surface are reported in Figures S2 and S3 while the corresponding models for ZIF-67-IDip NP (size of ∼64 Å) are represented in Figures S4 and S5.

The atomistic models of all polymers were built using the same strategy previously applied to model PIM-1,[68,69] whereas polymers were constructed using the Polymer module of Materials Studio 7[70] software. The flexible force field used to describe the three polymers includes bonded (stretching, bond angle bending, and torsional angle distortion) and nonbonded (Lennard-Jones (LJ) and electrostatic) terms. The LJ parameters were taken from the transferable potentials for phase equilibria−united atom (TRAPPE-UA)[71] force field,

https://doi.org/10.1021/acs.jpcc.3c04377
J. Phys. Chem. C 2023, 127, 20491−20502

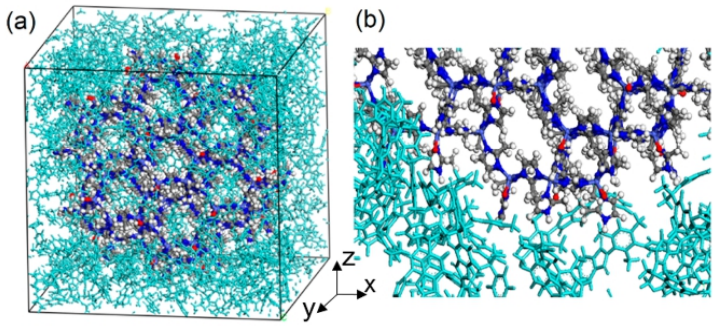

Figure 1. Representative atomistic model for the (a) ZIF-67/6 FDA-DAM composite containing 34.5 wt % ZIF-67 and (b) its resulting MOF/polymer interface. ZIF-67 atoms are represented as ball and stick atoms and polymer chains in light blue lines. Color code: O (red), C (gray), H (white), N (blue), and Co (steel blue).

while bonded intramolecular interactions were represented by the GAFF force field.[66] The GAFF is a flexible force field model where the $-CF_3$ and $-CH_x$ (x = 1, 2, 3) groups are considered as a single site (the united atom approach). The bonds and angles were treated with harmonic potentials, whereas cosine-based potential terms were used for the dihedrals. The partial charges for PIM-1 were taken from Larsen et al.'s work where they used the HF/6-31G* level of theory followed by the application of a restrained electrostatic potential (RESP) charge model.[72] On the other hand, for 6 FDA-DAM and 6 FDA-DABA, the electrostatic potential (ESP) derived partial charges were computed by DFT calculations using the Dmol3[73] module of Materials Studio 7 with the B3LYP (Becke 3-parameter Lee−Yang−Parr)[74] functional. The atomic partial charges for polymer repeat units are reported in Figure S8.

The composite models were further constructed by embedding the ZIF-67 and ZIF-67-IDip NPs in the three different polymer matrices with the Packing tool of the Amorphous Cell module of Material Studio 7 followed by full geometry optimization using the flexible force fields mentioned above for both MOF NPs and polymers. The number of polymer chains was controlled in order to build atomistic models corresponding to 34.5 wt % of ZIF-67 in the resulting composites, to be in line with the MOF loading explored experimentally in the work reported by Knebel et al.[50] Typically, in order to construct the ZIF-67/6 FDA-DAM composite containing 34.5 wt % ZIF-67, four chains of polymers were packed around the ZIF-67 NP, whereas five chains of 6 FDA-DAM were used to achieve the ZIF-67-IDip/6 FDA-DAM composite associated with a 34.5 wt % ZIF-67-IDip content. On the other hand, four chains of PIM-1 consisting of 40 repeat units packed around the ZIF-67 NP were considered to build the ZIF-67/PIM-1 composite containing 34.5 wt % ZIF-67 NP while six polymer chains were used for the construction of the composite with 34.5 wt % ZIF-67-IDip. MOF-based composites were achieved with a size of ∼59 Å for the ZIF-67/6 FDA-DAM composite containing 34.5 wt % ZIF-67 matrices, while ∼63 Å cubic simulation cell of composite was obtained as an outcome with 34.5 wt % ZIF-67-IDip. PIM-1 consisting of a cubic simulation cell of composites with a side of ∼61 and ∼68 Å was achieved with 34.5 wt % ZIF-67 and ZIF-67-IDip fillers, respectively. The equilibration of the so-obtained MOF/polymer composites was achieved by a 21-step molecular dynamics (MD) decompression−compression method[68] with P_{max} equal to 10 kbar using LAMMPS.[75] The MD simulations were performed for 1 ns with a time step of 1 fs using a Nosé−Hoover thermostat and barostat with relaxation times of 0.1 and 1 ps, respectively.[76,77] A 14 Å cutoff was applied for the LJ interactions while tail corrections and Ewald summations were used to assess the Coulombic contributions. As a typical example, representative atomistic models of the ZIF-67/6 FDA-DAM composite and its interface are shown in Figure 1a,b.

The fractional free volume (FFV) values of all constructed polymers were calculated using the Poreblazer 4.0 software.[78] FFV was determined by inserting helium atoms as a probe into the system, so that the entire free volume of the structure would be occupied by these probes. The atomic density (ρN) distribution was evaluated for the polymers in both ZIF-67 and ZIF-67-IDip based composites. This distribution was calculated over spherical shells using a 0.1 Å bin size, with the center of the outer MOF cage exposed to the polymer considered as origin (r = 0). In order to characterize the interactions between different MOF/polymer atom pairs, we further computed radial distribution functions (RDFs) between the MOF atoms and the preferential sorption sites of the polymers. All fractional free volume calculations and the atomic density distribution calculations were performed using a 1 ns NPT-MD run in order to obtain reliable averaged values.

2.2. Sorption Simulations. Sorption simulations of propane and propylene in the polymers, ZIF-67, ZIF-67-IDip NP models, and their composites were performed using a hybrid approach combining grand canonical Monte Carlo (GCMC) and MD simulations at 308 K using LAMMPS[75] to enable to capture the possible guest-induced relaxation of the overall systems. Sorption−relaxation cycles (SRCs), were integrated into GCMC and MD runs, such as that NPT-MD and NVT-MD steps were applied after each GCMC step to account for the guest-induced flexibility of the systems.[69,79] For one SRC cycle, 500000 exchange moves with guest insertion and deletion and 2000 and 5000 rotational and translational moves, respectively, were considered followed by 20 ps MD-NVT and 20 ps MD-NPT runs at 308 K up to 8 bar. This cycle was repeated at each pressure 100 times, the last 30 SRCs being used for production runs. The number of SRCs and the duration of the MD runs within these SRCs were optimized to ensure the achievement of equilibrium while using the most efficient and least resource-intensive approach. A Nosé−

https://doi.org/10.1021/acs.jpcc.3c04377
J. Phys. Chem. C 2023, 127, 20491−20502

Hoover thermostat and barostat were used during for the MD runs with relaxation times of 0.2 and 2 ps, respectively.[76,77] Both guest molecules were modeled with the TraPPE united atom force field model[71] while the atoms of both MOFs and polymers were treated using the force field parameters described above. Gas fugacities were computed for all pressure range using the Peng−Robinson equation of state.[80]

3. RESULTS AND DISCUSSION

3.1. Validation of the Atomistic Polymer Models. The three polymer models were validated by comparing their density and FFV with the experimental data reported in the literature, as shown in Table 1. Remarkably the densities for the simulated 6FDA-DAM and 6FDA-DABA models differ from the experimental data by only 1% and 2%, respectively, while the density for the simulated PIM-1 model matches well with the range of values reported in the literature. Further, the FFV values obtained for all polymers are in good agreement with the data reported previously using the Bondi's group-contribution method[81] or/and molecular simulations.[69,82] This observation highlights the robustness of the computational methods and the force field parameters for the construction of reliable atomistic models for the three polymers.

Table 1. Comparison between the Simulated Properties for the Three Polymer Models and the Corresponding Data Available in the Literature

		density (g/cm^3)	fractional free volume
6 FDA-DAM	literature	1.350[83]	0.189,[a,84] 0.163[b,82]
	this work	1.336 ± 0.002	0.161
6 FDA-DABA	literature	1.511[85]	0.175[a,85]
	this work	1.482 ± 0.002	0.120
PIM-1	literature	0.94−1.4[86]	0.260,[a,87] 0.241[b,69]
	this work	0.991 ± 0.002	0.281

[a]Bondi's method. [b]Molecular simulations.

Further validation was achieved by a good agreement between the GCMC simulated and experimental propane and propylene sorption isotherms for 6 FDA-DAM in the low domain of pressure up to 1 bar (Figure S9). This suggests that the gas−polymer interactions are represented accurately by the selected force fields, and the GCMC-MD coupled approach to account for the structural guest-induced relaxation of the polymers is reliable. Next, sorption simulations were extended to calculate the propane and propylene sorption isotherms for the two other polymers at 308 K up to 8 bar (Figure 2). Highest propane and propylene uptakes were obtained for PIM-1 as expected because PIM-1 has a higher FFV compared to the less porous 6FDA-based polyimides.[88] The slightly lower simulated propane and propylene uptake for 6 FDA-DABA compared to that for 6FDA-DAM is also in line with its lower FFV value.

3.2. Validation of the Atomistic ZIF-67 NP Model. The window size distribution of the ZIF-67 NP cage was first calculated throughout NPT-MD simulations performed at 308 K at 1 bar. Analysis of the MD trajectories revealed a flipping motion of the linkers that controls the flexibility of the gate opening, resulting in a Gaussian-type distribution of the windows size as shown in Figure S10. The resulting distribution leads to an averaged value of 3.33 Å, in excellent agreement with previously reported experimental[89] (3.33 Å) and simulated[63] (3.30 Å) data. This validates the force field to describe the flexibility of the MOF. The ZIF-67/guests force field parameters were further validated by a good agreement between the simulated propane and propylene sorption isotherms at 308 K and the experimental data collected for ZIF-67 as reported in Figure S11a up to 1 bar. At a higher pressure up to 8 bar, Figure S11b shows that the propylene adsorption uptake for ZIF-67 is substantially higher than the corresponding value for propane.

3.3. Exploration of MOF/Polymer Composites. Figure 3 reports the radial atomic density of 6 FDA-DAM in both ZIF-67 and ZIF-67-IDip composites calculated over spherical shells using a 0.1 Å bin size, with the center of the outer MOF cage exposed to the polymer considered as the origin (r = 0). In Figure 3a, the dark blue colored line at r = 11.3 Å delimits the upper limit of the ZIF-67 surface. One can observe that the black curve associated with the polymer starts to increase at r = 10.5 Å, highlighting that there is a tiny overlap ∼0.8 Å (hatched area) with the upper limit of the MOF region and indeed no compelling polymer penetration toward the MOF gate as illustrated in Figure 3b. This polymer radial atomic density further gradually increases and fluctuates around a mean value from r = 16.3 Å, thus defining an interfacial MOF/polymer light-blue-shaded region with a length of about 6 Å consistent with the data previously simulated for the ZIF-8/6 FDA-DAM composite[90] (9 Å), followed by a first-neighbor polymer domain (gray shaded area) which is not a polymer-bulk region because it still feels the impact of the MOF surface,

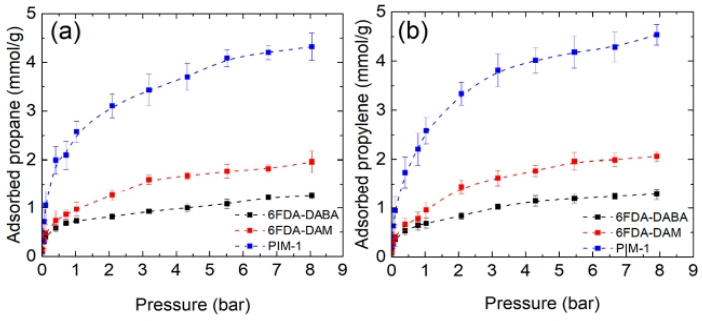

Figure 2. Simulated propane and propylene sorption isotherms for the polymers at 308 K up to 8 bar: (a) propane sorption isotherms and (b) propylene sorption isotherms for PIM-1 (blue), 6FDA-DAM (red), and 6FDA-DABA (black). The dashed lines are to guide the eyes.

https://doi.org/10.1021/acs.jpcc.3c04377
J. Phys. Chem. C 2023, 127, 20491−20502

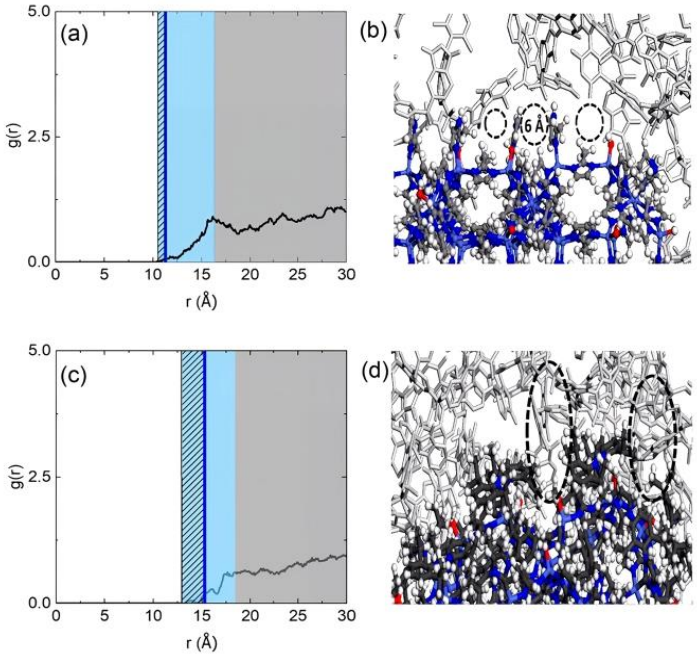

Figure 3. Calculated radial atomic density distribution of (a) 6 FDA-DAM (black) in the unfunctionalized ZIF-67/6 FDA-DAM composite with respect to the center of the nanoparticle (r = 0), (b) representative snapshot of the unfunctionalized ZIF-67/6 FDA-DAM interface showing the presence of microvoids, (c) radial atomic density distribution of 6 FDA-DAM (black) in the functionalized ZIF-67-IDip/6 FDA-DAM composite with respect to the center of the MOF nanoparticle (r = 0), and (d) representative snapshot of the functionalized ZIF-67-IDip/6 FDA-DAM interface where MOF/polymer overlap is marked by a dashed circle. The interfacial MOF/polymer overlap regions are marked by black dashed shaded areas. Color scheme: 6 FDA-DAM, gray wireframe; ZIF-67 and ZIF-67-IDip, ball and stick; O, red; C, gray; H, white; Co, blue.

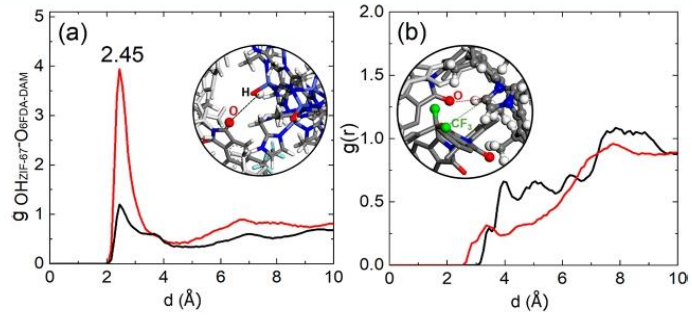

Figure 4. Calculated radial distribution functions in the composites (a) between oxygen atoms of 6 FDA-DAM and −H(OH) of the ZIF-67 functionalized (black) and unfunctionalized (red) surface in the corresponding composites along with illustration of the preferential site-to-site interactions for the ZIF-67/6 FDA-DAM composite and (b) between oxygen atoms (red curve) and $-CF_3$ groups (black curve) of 6 FDA-DAM and carbon atoms of the IDip functional groups attached at the ZIF-67 surface along with illustration of the preferential site-to-site interactions of the ZIF-67-IDip/6 FDA-DAM composite.

a behavior already modeled for a series of MOF/polymer systems.[59,91−93] Figure 3b evidence the presence of voids at the MOF/polymer interface associated with micropores up to 6 Å size.

With regard to the ZIF-67-IDip/6 FDA-DAM composite, Figure 3c shows that the upper limit of the MOF surface (dark blue line) is shifted at a higher r value (r = 13 Å) owing to the presence of the functional IDip groups. The radial atomic density of the polymer gradually increases from 13.0 to 18.5 Å, resulting in an interfacial MOF/polymer region length (6 Å) similar to that simulated for the pristine ZIF-67/6 FDA-DAM composite. Interestingly, one can observe that the 6 FDA-DAM approaches closer to the functionalized MOF surface compared to the pristine ZIF-67 scenario with even a tiny overlap region between the MOF surface and the polymer at the interface. The MOF/polymer overlap length (hatched area) is significantly larger in the case of the IDip-functionalized MOF surface compared to the MOF/polymer

https://doi.org/10.1021/acs.jpcc.3c04377
J. Phys. Chem. C 2023, 127, 20491−20502

composite (2.3 Å vs 0.8 Å, respectively). The IDip functionalization therefore contributes to improve the compatibility between the MOF NP and the polymer. This suggests that the IDip functionalization enables a more effective packing of the 6 FDA-DAM in the vicinity of the MOF surface, as illustrated in Figure 3d with the polymer conforming to the pocket generated at the MOF surface by the IDip functions. This is expected to improve the adhesion of the two components in line with a more homogeneous dispersion of ZIF-67-IDip in the polymeric matrix and the absence of ZIF-67 IDip agglomeration as observed experimentally.[50]

Figure 4a shows the radial distribution functions (RDF) calculated between the oxygen atoms of 6 FDA-DAM and the hydrogen atoms of the terminal −OH groups of both the functionalized and unfunctionalized MOF surfaces in their respective composites. One observes that these interfacial MOF/polymer interactions are rather strong in both composites with an associated O(6 FDA-DAM)-H(OH) distance of 2.45 Å, the intensity of the corresponding peak being even higher for the unfunctionalized MOF surface-based composite. Interestingly, the more effective packing of the polymer in the ZIF-67-IDip/6 FDA-DAM composite induces additional interactions between the oxygen atoms and $-CF_3$ groups of 6 FDA-DAM with the carbon atoms of the IDip function of the MOF with separating distances about 3 Å as shown in Figure 4b.

We further explored if guest adsorption can induce a substantial change of the MOF/polymer interfacial structuring. In Figure S12a,b, the RDF profile of the functionalized ZIF-67/6 FDA-DAM composite obtained at 8 bar of propane/propylene and 308 K shows that the blue colored interfacial region ranges from 13.5 to 16.6 Å in both scenarios where either propylene or propane is present. It therefore appears that the interfacial MOF/polymer length is reduced in the presence of both propane and propylene molecules (3.2 Å vs 5.5 Å in the absence of guest molecules), while a similar MOF/polymer overlap length is obtained (2.2 and 2.5 Å for propylene and propane, respectively, vs 2.3 Å). This observation highlights that the guest molecules do not affect the adhesion of the two components ensured by the interactions between the IDip functions and 6 FDA-DAM although they reduce the interfacial region length. For the ZIF-67/6 FDA-DAM composite, the interfacial MOF/polymer length remains similar (6.3 and 5.9 Å for propylene and propane vs 6 Å in the absence of guest molecules) upon guest adsorption (Figure S12c,d) and the MOF/polymer overlap length expands upon propylene adsorption (from 0.8 to 2.5 Å) while remaining similar upon propane adsorption (0.9 Å). This suggests that propylene induces a substantial restructuring of the polymer while propane does not impact the MOF/polymer affinity.

Analysis of the fractional free volume-FFV (Table 2) for the unfunctionalized and functionalized MOF-based composites revealed that the global FFV increases for the guest-free composites compared to pure 6 FDA-DAM. Notably in the case of the single component adsorption of propane and propylene at 308 K and 8 bar, the FFV for the functionalized ZIF-67-IDip/6 FDA-DAM composite is increased similarly in the presence of propane and propylene (23% vs 23.4% for propylene and propane, respectively) in line with a similar MOF/polymer overlap region discussed above. The scenario differs for the unfunctionalized MOF/6 FDA-DAM composite, with a propylene-induced FFV increase (14.5%) lower than that obtained for propane (23.8%). This observation suggests that propylene induces a higher degree of plasticization of the corresponding unfunctionalized MOF surface-based composite compared to propane.[94−96]

Table 2. FFV Increase in 6 FDA-DAM and MOF/6 FDA-DAM Composites at T = 35 °C and P = 8 bar, Induced by the Single-Component Adsorption of C_3H_6 and C_3H_8

	6 FDA-DAM		ZIF-67/6 FDA-DAM		ZIF-67-IDip/6 FDA-DAM	
species	FFV	% increase	FFV	% increase	FFV	% increase
pure	0.161		0.282		0.235	
C_3H_6	0.195	21.1	0.323	14.5	0.289	23.0
C_3H_8	0.179	11.2	0.349	23.8	0.290	23.4

We further evaluated how the MOF functionalization affects the single-component sorption isotherms for propane and propylene in 34.5 wt % ZIF-67/6 FDA-DAM and 34.5 wt % ZIF-67-IDip/6 FDA-DAM. The corresponding sorption isotherms reported in Figure 5 were calculated at 308 K up to 8 bar. The comparison of the isotherms reveals that (i) the functionalization does not play a detrimental role on the adsorptive ability of the composite, despite a slightly lower sorption capacity of ZIF-67-IDip/6 FDA-DAM is obtained, and (ii) the similar adsorption behavior exhibited by propane and propylene in the ZIF-67/6 FDA-DAM composite remains true for ZIF-67-IDip/6 FDA-DAM. This later observation suggests that the MOF surface functionalization does not boost the thermodynamic propylene/propane separation of the composite in line with the previously reported experimental data.[50]

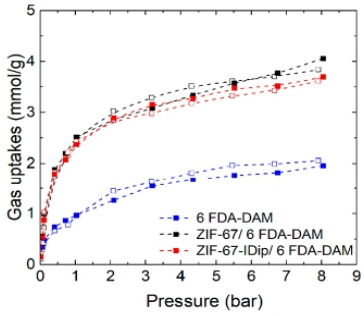

Figure 5. Simulated propane (solid symbols) and propylene (open symbols) sorption isotherms for the composites. 34.5 wt % ZIF-67/6 FDA-DAM (black) and ZIF-67-IDip/6 FDA-DAM (red) at 308 K up to 8 bar and comparison with pure 6 FDA-DAM (blue) (dashed lines are to guide the eyes).

Previous studies showed that rigidity of the polymer usually impacts the MOF/polymer interfacial structuring and their compatibility.[31] This encouraged us to examine the microscopic structuring of the ZIF-67/PIM-1 composites starting by exploring their RDF profile. Figures 6a and 6b show the radial atomic density profile of PIM-1 in ZIF-67 composite and representative snapshots, while Figures 6c and 6d report the same set of data for the functionalized MOF/PIM-1 composites. Compared to ZIF-67/6 FDA-DAM presented above, a slightly larger MOF/polymer overlap length is obtained for ZIF-67/PIM-1 (1.8 Å vs 0.8 Å) while this

https://doi.org/10.1021/acs.jpcc.3c04377
J. Phys. Chem. C 2023, 127, 20491−20502

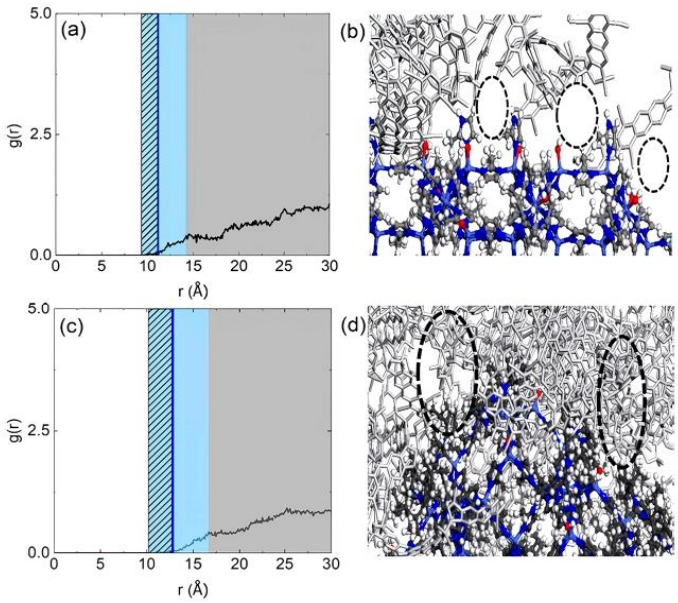

Figure 6. Calculated radial atomic density distribution of (a) PIM-1 (black) in the unfunctionalized ZIF-67/PIM-1 composite with respect to the center of the nanoparticle (r = 0), (b) representative snapshot of the interface of unfunctionalized ZIF-67/PIM-1 showing the presence of microvoids, (c) radial atomic density distribution of PIM-1 (black) in the functionalized ZIF-67-IDip/PIM-1 composite with respect to the center of the nanoparticle (r = 0), and (d) representative snapshot of the interface of functionalized ZIF-67-IDip/PIM-1 where MOF/polymer overlap is marked by a dashed circle. The interfacial MOF/polymer overlap regions are marked by black dashed shaded areas. Color scheme: PIM-1, gray wireframe; ZIF-67 and ZIF-67-IDip, ball and stick; O, red; C, gray; H, white; Co, blue.

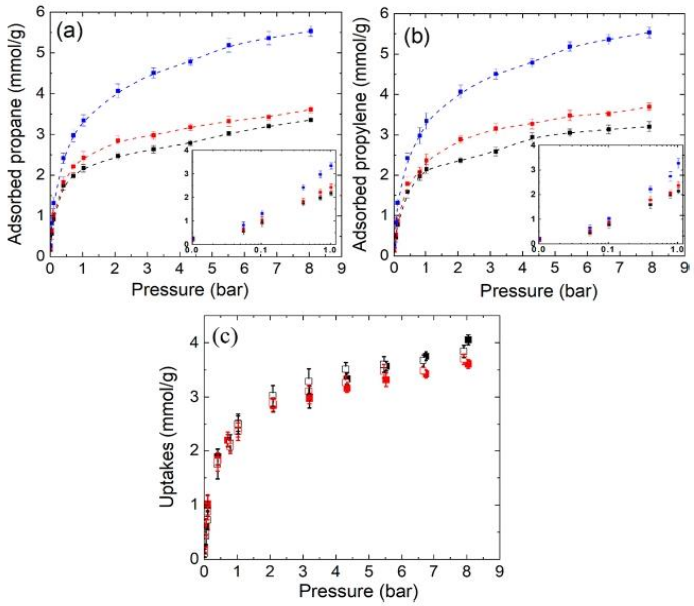

Figure 7. Simulated propane and propylene sorption isotherms for 34.5 wt % ZIF-67-IDip/PIM-1 (blue), ZIF-67-IDip/6 FDA-DAM (red), and ZIF-67-IDip/6 FDA-DABA (black) at 308 K up to 8 bar, with an inset up to 1 bar at logarithmic scale (dashed lines are to guide the eye): (a) propane and (b) propylene. (c) Comparison of propane (solid) and propylene (blank) uptakes in 34.5 wt % ZIF-67-IDip/6 FDA-DAM (black) and ZIF-67/6 FDA-DAM (red).

https://doi.org/10.1021/acs.jpcc.3c04377
J. Phys. Chem. C 2023, 127, 20491−20502

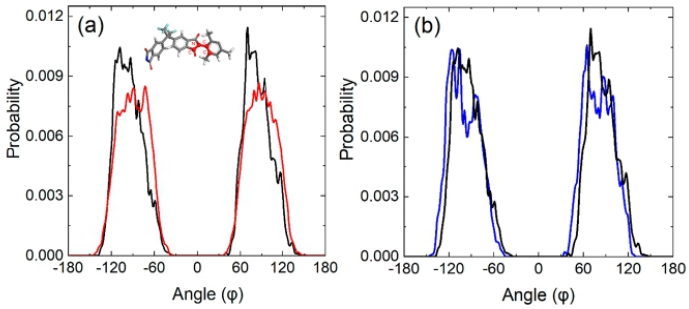

Figure 8. Torsional angle ($\phi_{C-N-C-C}$) distributions in the 6 FDA-DAM for the (a) ZIF-67/6 FDA-DAM at the interface (black) and at the bulk phase (red) and (b) ZIF-67/6 FDA-DAM (black) and ZIF-67-IDip/6 FDA-DAM (blue) composites at the interface.

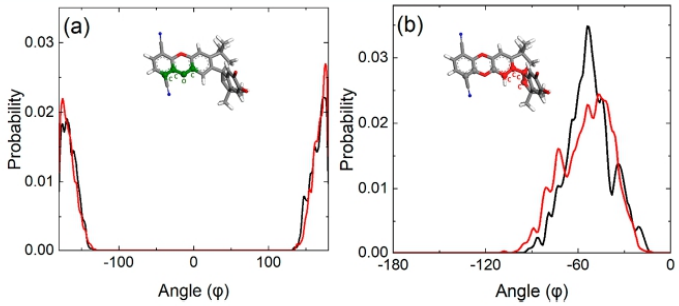

Figure 9. Torsional angle distributions in the PIM-1 for the unfunctionalized ZIF-67/PIM-1 composite (a) $\phi_{C-C-O-C}$ angle at the interface (black) and at the bulk phase (red) (b) $\phi_{C-C-C-C}$ angle at the interface (black) and at the bulk phase (red).

polymer is more rigid. More flexible polymers like 6 FDA-DAM are expected to better adapt its shape once the MOF surfaces are flat. However, ZIF-67 shows a "zigzag" shape surface which hampers its effective coverage by 6 FDA-DAM. On the other hand, PIM-1 exhibits an L-shaped vertex, which is ready to plug into the troughs formed by the "zigzag" MOF surface,[55] expanding the MOF/polymer overlap length. Both interfacial region (blue colored area) and MOF/polymer overlap region (black shaded area) are much larger in the case of ZIF-67-IDip/PIM-1 (6.5 Å vs 4.9 Å and 2.6 Å vs 1.8 Å, respectively) compared to ZIF-67/PIM-1 surface following the same sequence than the one detailed above for 6 FDA-DAM. Both composites exhibit similar interfacial micropores up to 5−6 Å diameters, which further confirms that IDip functionalization improves the compatibility between the MOF and the polymer without modifying the interfacial pore dimensions. We further evidenced that both overlap and interfacial region lengths for PIM-1/ZIF-67-IDip expand upon both propane and propylene adsorption (Figure S13) (3.8 and 2.8 Å, respectively, vs 2.6 Å for the guest-free composite regarding the overlap length and 7.9 and 9 Å, respectively, vs 6.5 Å for the guest-free composite regarding the interfacial length).

Figure 7 further compares the propane and propylene sorption isotherms for the ZIF-67-IDip-based composites with 6 FDA-DAM, 6 FDA-DABA, and PIM-1 at 308 K up to 8 bar for the 35 wt % MOF filler loading. Despite the highest propane and propylene uptakes obtained for ZIF-67-IDip/PIM-1 followed by ZIF-67/6 FDA-DAM and ZIF-67/6 FDA-DABA composites, in line with the discussion above, the thermodynamic sorption selectivity is not expected to be improved neither for ZIF-67-IDip/PIM-1 vs ZIF-67/PIM-1.

We further analyzed the torsion angle distribution to gain insight into the chain dynamics of the interfacial polymer versus bulk polymer. The torsional angle distribution of the diamine−dianhydride linkage ($\phi_{C-N-C-C}$) (Figure S14) was averaged over the MD trajectories for ZIF-67-IDip/6 FDA-DAM and ZIF-67/6 FDA-DAM composites for the guest free and propane/propylene loaded scenarios at 8 bar. The corresponding data are listed in Figure 8. Note that the torsional angle distribution is slightly different at the interfacial region with respect to the bulk polymer in Figure 8a. A minor conformational change with a slightly narrower torsional angle distribution for the polymer in the interfacial region might be related to a less marked mobility of the polymer and hence its rigidification. Further examination of the torsional angle distribution in the interfacial polymer and bulk polymer for the ZIF-67-IDip/6 FDA-DAM composite evidences that the dynamics of the polymer is slightly different at the interface compared to the bulk (Figure S15). The comparison between the torsional angle distributions for ZIF-67/6 FDA-DAM and ZIF-67-IDip/6 FDA-DAM in the interfacial region in Figure 8b shows only a tiny change between the two composites. The two representative torsional angles $\phi_{C-C-O-C}$ and $\phi_{C-C-C-C}$ (Figure S16) of PIM-1 in ZIF-67/PIM-1 and ZIF-67-IDip/PIM-1 composites are reported in Figure 9. The $\phi_{C-C-O-C}$ angle gives information about the flexibility degree of planar PIM-1, while the $\phi_{C-C-C-C}$ angle represents the flexibility of the "L" vertex of the polymer involving spiro carbon atoms.[55] Almost identical torsional profiles are obtained for $\phi_{C-C-O-C}$ (Figure 9a) in the two composites in line with a similar

https://doi.org/10.1021/acs.jpcc.3c04377
J. Phys. Chem. C 2023, 127, 20491−20502

polymer planar conformation in both cases (Figure S17a). On the other hand, spiro carbon atoms have a more active role because of the slightly different torsional angle distribution for the polymer at the interfacial region with respect to the bulk polymer; such a slight reduction of the dynamics of the polymer occurred at the interfacial region for both composites (Figures 9b and S17b). This information is in line with how the functionalization of MOF enhances the embedding of polymer to MOF surface despite reducing the flexibility of the polymer.[97]

The effect of guest molecules on the distribution of diamine−dianhydride linkage at 8 bar is compared in Figure S18, for both the unfunctionalized ZIF-67/6 FDA-DAM and functionalized ZIF-67-IDip/6 FDA-DAM composites. In the presence of guest molecules, the angle distributions do not change significantly between the interfacial polymer and bulk polymer in both functionalized and unfunctionalized composites. It seems that the polymer at the interface tends to behave like the bulk polymer due to the reduced rigidity of torsion (Figures S19 and S20). Hence, solvate-induced conformational changes in the torsional angles correlate with the derigidification effect reported by Balçık[57] and van Essen.[98,99]

4. CONCLUSION

In this work, several atomistic models of ZIF-67/polymer composites were constructed and evaluated in terms of the MOF/polymer compatibility and separation properties for propane/propylene mixtures. Three different polymers with different physical properties were considered in this context: 6 FDA-DAM with its inhibited polymer chain packing, 6 FDA-DABA with its plasticizing controlling capability, and PIM-1 with its rigid contorted molecular backbones. Simulated sorption data showed that these composites do not exhibit any potential for thermodynamic separation. Hence, the favorable separation performance of ZIF-67 MMMs reported in the literature is most likely kinetic driven. The interfacial interactions between the MOF and polymer were further explored. We revealed that the IDip functionalization of the ZIF-67 surface enables a more efficient packing of the polymers at the MOF surface because a much larger MOF/polymer overlap length was computed. This is expected to lead to a better adhesion between polymer and MOF surface without any agglomeration in line with the experimental findings. The affinity between the MOF and polymers was further investigated upon guest adsorption. Our findings suggest that propane does not impact the MOF/polymer affinity, whereas propylene leads to a slight change in the MOF/polymer overlap length. Individual torsion distribution analyses of the interfacial MOF/polymer region and bulk polymer region further suggested a less marked mobility of the polymer in the interfacial region.

In terms of chain rigidity, the ZIF-67/PIM-1 composite was shown to exhibit a better compatibility with the slightly higher MOF/polymer overlap region compared to the ZIF-67/6FDA-DAM composite, as the L-shaped vertex of PIM-1 can more easily adapt to the MOF surface.

With regard to these key aspects, the interplay between (i) the MOF/polymer overlap region, (ii) the rigidity of the polymer, and (iii) the balance between the interfacial rigidification in MOF/polymer composites and sorption behavior was confirmed to be key parameters for the fabrication of homogeneous MOF/polymer composites. The following step will focus on an in-depth analysis of the kinetics of propylene/propane separation processes in these composites.

■ ASSOCIATED CONTENT

Supporting Information

The Supporting Information is available free of charge at https://pubs.acs.org/doi/10.1021/acs.jpcc.3c04377.

Representation of ZIF-67 supercell, ZIF-67 and ZIF-67-IDip crystals, the atomic partial charges, model validation plots and additional radial atomic density distributions, and torsional angle distributions (PDF)

■ AUTHOR INFORMATION

Corresponding Author

M. Göktuğ Ahunbay − *Department of Chemical Engineering, Istanbul Technical University, Istanbul 34469, Turkey;* orcid.org/0000-0003-3595-6419; Email: ahunbaym@itu.edu.tr

Authors

Elif Begüm Doğan − *Department of Chemical Engineering, Istanbul Technical University, Istanbul 34469, Turkey; CNRS, ENSCM, ICGM, Univ. Montpellier, Montpellier 34095, France*

Guillaume Maurin − *CNRS, ENSCM, ICGM, Univ. Montpellier, Montpellier 34095, France;* orcid.org/0000-0002-2096-0450

Complete contact information is available at: https://pubs.acs.org/10.1021/acs.jpcc.3c04377

Notes

The authors declare no competing financial interest.

■ ACKNOWLEDGMENTS

E.B.D. has been supported under 100/2000 Council of Higher Education (YÖK) PhD Scholarship program for her doctoral study. E.B.D. acknowledges the Scientific and Technological Research Council of Turkey (TUBITAK) for the scholarship of international doctoral research fellowship program. The computational work was performed using HPC resources from GENCI-CINES (Grant A0140907613).

■ ABBREVIATIONS

MMM, mixed-matrix membranes; MOF, metal−organic framework; ZIF, zeolitic imidazolate frameworks; ZIF-67, $Co(Hmim)_2$, Hmim = 2-methylimidazole); NPs, nanoparticles; Six FDA, 4,4-(hexafluoroisopropylidene)diphthalic anhydride; DAM, 2,4,6-trimethyl-1,3-diaminobenzene; NHC, *N*-heterocyclic carbene; IDip, 1,3-bis(2,4,6-diisopropylphenyl)imidazole-2-ylidene; DABA, 3,5- diaminobenzoic acid; PIM, polymers of intrinsic microporosity; LJ, Lennard-Jones; DFT, density functional theory; GAFF, Generalized Amber Force Field; TRAPPE, transferable potentials for phase equilibria force field; UA, united atom; ESP, electrostatic potential; B3LYP, Becke 3-parameter Lee−Yang−Parr; MD, molecular dynamics; FFV, fractional free volume; ρN, atomic density; RDF, radial distribution function; GCMC, grand canonical Monte Carlo; SRCs, sorption−relaxation cycles.

https://doi.org/10.1021/acs.jpcc.3c04377
J. Phys. Chem. C 2023, 127, 20491−20502

REFERENCES

(1) Najari, S.; Saeidi, S.; Gallucci, F.; Drioli, E. Mixed Matrix Membranes for Hydrocarbons Separation and Recovery: A Critical Review. *Rev. Chem. Eng.* **2021**, *37*, 363−406.

(2) Guo, M.; Kanezashi, M. Recent Progress in a Membrane-Based Technique for Propylene/Propane Separation. *Membranes (Basel).* **2021**, *11* (5), 310.

(3) Cadiau, A.; Adil, K.; Bhatt, P. M.; Belmabkhout, Y.; Eddaoudi, M. A Metal-Organic Framework-Based Splitter for Separating Propylene from Propane. *Science (80-.).* **2016**, *353* (6295), 137−140.

(4) Ma, X.; Swaidan, R. J.; Wang, Y.; Hsiung, C. en; Han, Y.; Pinnau, I. Highly Compatible Hydroxyl-Functionalized Microporous Polyimide-Zif-8 Mixed Matrix Membranes for Energy Efficient Propylene/Propane Separation. *ACS Appl. Nano Mater.* **2018**, *1* (7), 3541−3547.

(5) Faiz, R.; Li, K. Polymeric Membranes for Light Olefin/Paraffin Separation. *Desalination* **2012**, *287*, 82−97.

(6) Wang, Y.; Peh, S. B.; Zhao, D. Alternatives to Cryogenic Distillation: Advanced Porous Materials in Adsorptive Light Olefin/Paraffin Separations. *Small* **2019**, *15* (25), 1−38.

(7) Lin, R.; Ge, L.; Diao, H.; Rudolph, V.; Zhu, Z. Propylene/Propane Selective Mixed Matrix Membranes with Grape-Branched MOF/CNT Filler. *J. Mater. Chem. A* **2016**, *4* (16), 6084−6090.

(8) Park, C. H.; Lee, J. H.; Jung, J. P.; Kim, J. H. Mixed Matrix Membranes Based on Dual-Functional MgO Nanosheets for Olefin/Paraffin Separation. *J. Membr. Sci.* **2017**, *533*, 48−56.

(9) Sholl, D. S.; Lively, R. P. Seven Chemical Separations. *Nature* **2016**, *532*, 435−437.

(10) Etxeberria-Benavides, M.; David, O.; Johnson, T.; Łozińska, M. M.; Orsi, A.; Wright, P. A.; Mastel, S.; Hillenbrand, R.; Kapteijn, F.; Gascon, J. High Performance Mixed Matrix Membranes (MMMs) Composed of ZIF-94 Filler and 6FDA-DAM Polymer. *J. Membr. Sci.* **2018**, *550*, 198−207.

(11) Ploegmakers, J.; Japip, S.; Nijmeijer, K. Mixed Matrix Membranes Containing MOFs for Ethylene/Ethane Separation Part A: Membrane Preparation and Characterization. *J. Membr. Sci.* **2013**, *428*, 445−453.

(12) Robeson, L. M. The Upper Bound Revisited. *J. Membr. Sci.* **2008**, *320*, 390−400.

(13) Cheng, Y.; Joarder, B.; Datta, S. J.; Alsadun, N.; Poloneeva, D.; Fan, D.; Khairova, R.; Bavykina, A.; Jia, J.; Shekhah, O.; et al. M. Mixed Matrix Membranes with Surface Functionalized Metal-Organic Framework Sieves for Efficient Propylene/Propane Separation. *Adv. Mater.* **2023**, *2300296*, 1−9.

(14) Liu, D.; Xiang, L.; Chang, H.; Chen, K.; Wang, C.; Pan, Y.; Li, Y.; Jiang, Z. Rational Matching between MOFs and Polymers in Mixed Matrix Membranes for Propylene/Propane Separation. *Chem. Eng. Sci.* **2019**, *204*, 151−160.

(15) Zornoza, B.; Téllez, C.; Coronas, J.; Esekhile, O.; Koros, W. J. Mixed Matrix Membranes Based on 6FDA Polyimide with Silica and Zeolite Microsphere Dispersed Phases. *AIChE J.* **2015**, *61*, 4481−4490.

(16) Klaysom, C.; Shahid, S. *Zeolite-Based Mixed Matrix Membranes for Hazardous Gas Removal*; Elsevier Inc.: 2018.

(17) Chung, T. S.; Jiang, L. Y.; Li, Y.; Kulprathipanja, S. Mixed Matrix Membranes (MMMs) Comprising Organic Polymers with Dispersed Inorganic Fillers for Gas Separation. *Prog. Polym. Sci.* **2007**, *32* (4), 483−507.

(18) Surya Murali, R.; Ismail, A. F.; Rahman, M. A.; Sridhar, S. Mixed Matrix Membranes of Pebax-1657 Loaded with 4A Zeolite for Gaseous Separations. *Sep. Purif. Technol.* **2014**, *129*, 1−8.

(19) Zornoza, B.; Seoane, B.; Zamaro, J. M.; Téllez, C.; Coronas, J. Combination of MOFs and Zeolites for Mixed-Matrix Membranes. *ChemPhysChem* **2011**, *12* (15), 2781−2785.

(20) Rodenas, T.; Luz, I.; Prieto, G.; Seoane, B.; Miro, H.; Corma, A.; Kapteijn, F.; Llabrés I Xamena, F. X.; Gascon, J. Metal-Organic Framework Nanosheets in Polymer Composite Materials for Gas Separation. *Nat. Mater.* **2015**, *14* (1), 48−55.

(21) Dechnik, J.; Gascon, J.; Doonan, C. J.; Janiak, C.; Sumby, C. J. Mixed-Matrix Membranes. *Angew. Chemie - Int. Ed.* **2017**, *56* (32), 9292−9310.

(22) Adams, R.; Carson, C.; Ward, J.; Tannenbaum, R.; Koros, W. Metal Organic Framework Mixed Matrix Membranes for Gas Separations. *Microporous Mesoporous Mater.* **2010**, *131* (1−3), 13−20.

(23) Datta, S. J.; Mayoral, A.; Murthy, N.; Bettahalli, S.; Bhatt, P. M.; et al. Rational design of mixed-matrix metal-organic framework membranes for molecular separations. *Science* **2022**, *376*, 1080−1087.

(24) Marti, A.; Venna, S.; Roth, E. A.; Culp, J. T.; Hopkinson, D. P. A Simple Fabrication Method for Mixed Matrix Membranes with In-Situ MOF Growth for Gas Separation. *ACS Appl. Mater. Interfaces* **2018**, *10* (29), 24784−24790.

(25) Fan, D.; Ozcan, A.; Shekhah, O.; Semino, R.; Eddaoudi, M.; Maurin, G. Engineering MOF Surface Defects in Mixed Matrix Membranes: An Effective Strategy to Enhance MOF/Polymer Adhesion and Control Interfacial Gas Transport. *J. Membr. Sci. Lett.* **2022**, *2* (2), 100029.

(26) Lin, R.; Hernandez, B. V.; Ge, L.; Zhu, Z. Metal Organic Framework Based Mixed Matrix Membranes: An Overview on Filler/Polymer Interface. *J. Mater. Chem. A* **2018**, *6*, 293−312.

(27) Qian, Q.; Wu, A. X.; Chi, W. S.; Asinger, P. A.; Lin, S.; Hypsher, A.; Smith, Z. P. Mixed-Matrix Membranes Formed from Imide-Functionalized UiO-66-NH2 for Improved Interfacial Compatibility. *ACS Appl. Mater. Interfaces* **2019**, *11* (34), 31257−31269.

(28) Liu, G.; Chernikova, V.; Liu, Y.; Zhang, K.; Belmabkhout, Y.; Shekhah, O.; Zhang, C.; Yi, S.; Eddaoudi, M.; Koros, W. J. Mixed Matrix Formulations with MOF Molecular Sieving for Key Energy-Intensive Separations. *Nat. Mater.* **2018**, *17* (3), 283−289.

(29) Carja, I. D.; Tavares, S. R.; Shekhah, O.; Ozcan, A.; Semino, R.; Kale, V. S.; Eddaoudi, M.; Maurin, G. Insights into the Enhancement of MOF/Polymer Adhesion in Mixed-Matrix Membranes via Polymer Functionalization. *ACS Appl. Mater. Interfaces* **2021**, *13* (24), 29041−29047.

(30) Lee, C. H.; Khalina, A.; Lee, S. H. Importance of Interfacial Adhesion Condition on Characterization of Plant-Fiber-Reinforced Polymer Composites: A Review. *Polymers (Basel).* **2021**, *13* (3), 438.

(31) Semino, R.; Moreton, J. C.; Ramsahye, N. A.; Cohen, S. M.; Maurin, G. Understanding the Origins of Metal-Organic Framework/Polymer Compatibility. *Chem. Sci.* **2018**, *9* (2), 315−324.

(32) Park, K. S.; Ni, Z.; Cote, A. P.; Choi, J. Y.; Huang, R.; Uribe-Romo, F. J.; Chae, H. K.; O'Keeffe, M.; Yaghi, O. M. Exceptional Chemical and Thermal Stability of Zeolitic Imidazolate Frameworks. *Proc. Natl. Acad. Sci. U. S. A.* **2006**, *103* (27), 10186−10191.

(33) Iacomi, P.; Maurin, G. ResponZIF Structures: Zeolitic Imidazolate Frameworks as Stimuli-Responsive Materials. *ACS Appl. Mater. Interfaces* **2021**, *13* (43), 50602−50642.

(34) Huang, X. C.; Lin, Y. Y.; Zhang, J. P.; Chen, X. M. Ligand-Directed Strategy for Zeolite-Type Metal-Organic Frameworks: Zinc(II) Imidazolates with Unusual Zeolitic Topologies. *Angew. Chemie - Int. Ed.* **2006**, *45* (10), 1557−1559.

(35) Tan, J. C.; Bennett, T. D.; Cheetham, A. K. Chemical Structure, Network Topology, and Porosity Effects on the Mechanical Properties of Zeolitic Imidazolate Frameworks. *Proc. Natl. Acad. Sci. U. S. A.* **2010**, *107* (22), 9938−9943.

(36) Lewis, D. W.; Ruiz-Salvador, A. R.; Gómez, A.; Rodriguez-Albelo, L. M.; Coudert, F. X.; Slater, B.; Cheetham, A. K.; Mellot-Draznieks, C. Zeolitic Imidazole Frameworks: Structural and Energetics Trends Compared with Their Zeolite Analogues. *CrystEngComm* **2009**, *11* (11), 2272−2276.

(37) Böhme, U.; Barth, B.; Paula, C.; Kuhnt, A.; Schwieger, W.; Mundstock, A.; Caro, J.; Hartmann, M. Ethene/Ethane and Propene/Propane Separation via the Olefin and Paraffin Selective Metal-Organic Framework Adsorbents CPO-27 and ZIF-8. *Langmuir* **2013**, *29* (27), 8592−8600.

(38) Zheng, B.; Maurin, G. Mechanical Control of the Kinetic Propylene/Propane Separation by Zeolitic Imidazolate Framework-8. *Angew. Chemie - Int. Ed.* **2019**, *58* (39), 13734−13738.

https://doi.org/10.1021/acs.jpcc.3c04377
J. Phys. Chem. C 2023, 127, 20491−20502

(39) Pan, Y.; Li, T.; Lestari, G.; Lai, Z. Effective Separation of Propylene/Propane Binary Mixtures by ZIF-8 Membranes. *J. Membr. Sci.* **2012**, *390*−*391*, 93−98.
(40) Hara, N.; Yoshimune, M.; Negishi, H.; Haraya, K.; Hara, S.; Yamaguchi, T. Diffusive Separation of Propylene/Propane with ZIF-8 Membranes. *J. Membr. Sci.* **2014**, *450*, 215−223.
(41) Bux, H.; Liang, F.; Li, Y.; Cravillon, J.; Wiebcke, M.; Caro, J. Zeolitic Imidazolate Framework Membrane with Molecular Sieving Properties by Microwave-Assisted Solvothermal Synthesis. *J. Am. Chem. Soc.* **2009**, *131*, 16000−16001.
(42) Kwon, H. T.; Jeong, H. K. In Situ Synthesis of Thin Zeolitic-Imidazolate Framework ZIF-8 Membranes Exhibiting Exceptionally High Propylene/Propane Separation. *J. Am. Chem. Soc.* **2013**, *135* (29), 10763−10768.
(43) Krokidas, P.; Castier, M.; Moncho, S.; Brothers, E.; Economou, I. G. Molecular Simulation Studies of the Diffusion of Methane, Ethane, Propane, and Propylene in ZIF-8. *J. Phys. Chem. C* **2015**, *119* (48), 27028−27037.
(44) Krokidas, P.; Castier, M.; Moncho, S.; Sredojevic, D. N.; Brothers, E. N.; Kwon, H. T.; Jeong, H. K.; Lee, J. S.; Economou, I. G. ZIF-67 Framework: A Promising New Candidate for Propylene/Propane Separation. Experimental Data and Molecular Simulations. *J. Phys. Chem. C* **2016**, *120* (15), 8116−8124.
(45) Kwon, H. T.; Jeong, H. K.; Lee, A. S.; An, H. S.; Lee, J. S. Heteroepitaxially Grown Zeolitic Imidazolate Framework Membranes with Unprecedented Propylene/Propane Separation Performances. *J. Am. Chem. Soc.* **2015**, *137* (38), 12304−12311.
(46) Wang, C.; Yang, F.; Sheng, L.; Yu, J.; Yao, K.; Zhang, L.; Pan, Y. Zinc-Substituted ZIF-67 Nanocrystals and Polycrystalline Membranes for Propylene/Propane Separation. *Chem. Commun.* **2016**, *52* (85), 12578−12581.
(47) Tran, N. T.; Kwon, H. T.; Kim, W. S.; Kim, J. Counter-Diffusion-Based in Situ Synthesis of ZIF-67 Membranes for Propylene/Propane Separation. *Mater. Lett.* **2020**, *271*, 127777.
(48) An, H.; Park, S.; Kwon, H. T.; Jeong, H. K.; Lee, J. S. A New Superior Competitor for Exceptional Propylene/Propane Separations: ZIF-67 Containing Mixed Matrix Membranes. *J. Membr. Sci.* **2017**, *526*, 367−376.
(49) Moghadam, F.; Lee, T. H.; Park, I.; Park, H. B. Thermally Annealed Polyimide-Based Mixed Matrix Membrane Containing ZIF-67 Decorated Porous Graphene Oxide Nanosheets with Enhanced Propylene/Propane Selectivity. *J. Membr. Sci.* **2020**, *603* (March), 118019.
(50) Knebel, A.; Bavykina, A.; Datta, S. J.; Sundermann, L.; Garzon-Tovar, L.; Lebedev, Y.; Durini, S.; Ahmad, R.; Kozlov, S. M.; Shterk, G.; et al. Solution Processable Metal-Organic Frameworks for Mixed Matrix Membranes Using Porous Liquids. *Nat. Mater.* **2020**, *19* (12), 1346−1353.
(51) Venna, S. R.; Lartey, M.; Li, T.; Spore, A.; Kumar, S.; Nulwala, H. B.; Luebke, D. R.; Rosi, N. L.; Albenze, E. Fabrication of MMMs with Improved Gas Separation Properties Using Externally-Functionalized MOF Particles. *J. Mater. Chem. A* **2015**, *3* (9), 5014−5022.
(52) Ghalei, B.; Sakurai, K.; Kinoshita, Y.; Wakimoto, K.; Isfahani, A. P.; Song, Q.; Doitomi, K.; Furukawa, S.; Hirao, H.; et al. Enhanced Selectivity in Mixed Matrix Membranes for CO_2 Capture through Efficient Dispersion of Amine-Functionalized MOF Nanoparticles. *Nat. Energy* **2017**, *2* (7), 17086.
(53) Amedi, H. R.; Aghajani, M. Aminosilane-Functionalized ZIF-8/PEBA Mixed Matrix Membrane for Gas Separation Application. *Microporous Mesoporous Mater.* **2017**, *247*, 124−135.
(54) Rodenas, T.; Van Dalen, M.; García-Pérez, E.; Serra-Crespo, P.; Zornoza, B.; Kapteijn, F.; Gascon, J. Visualizing MOF Mixed Matrix Membranes at the Nanoscale: Towards Structure-Performance Relationships in CO_2/CH4 Separation over NH2-MIL-53(Al)@PI. *Adv. Funct. Mater.* **2014**, *24* (2), 249−256.
(55) Semino, R.; Ramsahye, N. A.; Ghoufi, A.; Maurin, G. Microscopic Model of the Metal - Organic Framework/Polymer Interface : A First Step toward Understanding the Compatibility in Mixed Matrix Membranes. *ACS Appl. Mater. Interfaces* **2016**, *8* (1), 809−819.
(56) Lee, T. H.; Ozcan, A.; Park, I.; Fan, D.; Jang, J. K.; Mileo, P. G. M.; Yoo, S. Y.; Roh, J. S.; Kang, J. H.; Lee, B. K.; et al. Disclosing the Role of Defect-Engineered Metal-Organic Frameworks in Mixed Matrix Membranes for Efficient CO_2 Separation: A Joint Experimental-Computational Exploration. *Adv. Funct. Mater.* **2021**, *31* (38), 1−13.
(57) Balçık, M.; Tantekin-Ersolmaz, S. B.; Ahunbay, M. G. Interfacial Analysis of Mixed-Matrix Membranes under Exposure to High-Pressure CO_2. *J. Membr. Sci.* **2020**, *607*, 118147.
(58) Vornholt, S. M.; Duncan, M. J.; Warrender, S. J.; Semino, R.; Ramsahye, N. A.; Maurin, G.; Smith, M. W.; Tan, J.; Miller, D. N.; Morris, R. E. Multifaceted Study of the Interactions between CPO-27-Ni and Polyurethane and Their Impact on Nitric Oxide Release Performance. *ACS Appl. Mater. Interfaces* **2020**, *12* (52), 58263−58276.
(59) Benzaqui, M.; Semino, R.; Menguy, N.; Carn, F.; Kundu, T.; Guigner, J. M.; McKeown, N. B.; Msayib, K. J.; Carta, M.; Malpass-Evans, R.; Le Guillouzer, C.; Clet, G.; Ramsahye, N. A.; Serre, C.; Maurin, G.; Steunou, N. Toward an Understanding of the Microstructure and Interfacial Properties of PIMs/ZIF-8 Mixed Matrix Membranes. *ACS Appl. Mater. Interfaces* **2016**, *8* (40), 27311−27321.
(60) Sánchez-Laínez, J.; Pardillos-Ruiz, A.; Carta, M.; Malpass-Evans, R.; McKeown, N. B.; Téllez, C.; Coronas, J. Polymer Engineering by Blending PIM-1 and 6FDA-DAM for ZIF-8 Containing Mixed Matrix Membranes Applied to CO_2 Separations. *Sep. Purif. Technol.* **2019**, *224*, 456−462.
(61) Liu, Z.; Liu, Y.; Qiu, W.; Koros, W. J. Molecularly Engineered 6FDA-Based Polyimide Membranes for Sour Natural Gas Separation. *Angew. Chemie - Int. Ed.* **2020**, *59* (35), 14877−14883.
(62) Mc Keown, N. B.; Budd, P. M. Polymers of Intrinsic Microporosity (PIMs): Organic Materials for Membrane Separations, Heterogeneous Catalysis and Hydrogen Storage. *Chem. Soc. Rev.* **2006**, *35* (8), 675−683.
(63) Krokidas, P.; Moncho, S.; Brothers, E. N.; Castier, M.; Economou, I. G. Tailoring the Gas Separation Efficiency of Metal Organic Framework ZIF-8 through Metal Substitution: A Computational Study. *Phys. Chem. Chem. Phys.* **2018**, *20* (7), 4879−4892.
(64) Tian, F.; Cerro, A. M.; Mosier, A. M.; Wayment-Steele, H. K.; Shine, R. S.; Park, A.; Webster, E. R.; Johnson, L. E.; Johal, M. S.; Benz, L. Surface and Stability Characterization of a Nanoporous ZIF-8 Thin Film. *J. Phys. Chem. C* **2014**, *118* (26), 14449−14456.
(65) Fabrizio, K.; Brozek, C. K. Size-Dependent Thermal Shifts to MOF Nanocrystal Optical Gaps Induced by Dynamic Bonding. *Nano Lett.* **2023**, *23* (3), 925−930.
(66) Wang, J.; Wolf, R. M.; Caldwell, J. W.; Kollman, P. A.; Case, D. A. Development and Testing of a General Amber Force Field. *J. Comput. Chem.* **2004**, *25* (9), 1157−1174.
(67) Frisch, M. J.; Trucks, G. W.; Schlegel, H. B.; Scuseria, G. E.; Robb, M. A.; Cheeseman, J. R.; Scalmani, G.; Barone, V.; Petersson, G. A.; et al. *Gaussian 09, Revision E.01*; Gaussian, Inc.: Wallingford, CT, 2009.
(68) Larsen, G. S.; Lin, P.; Hart, K. E.; Colina, C. M. Molecular Simulations of Pim-1-like Polymers of Intrinsic Microporosity. *Macromolecules* **2011**, *44* (17), 6944−6951.
(69) Balçık, M.; Tantekin-Ersolmaz, S. B.; Pinnau, I.; Ahunbay, M. G. CO_2/CH4Mixed-Gas Separation in PIM-1 at High Pressures: Bridging Atomistic Simulations with Process Modeling. *J. Membr. Sci.* **2021**, *640*, 119838.
(70) BIOVIA, Dassault Systèmes, Materials Studio, 7.0. *Dassault Systèmes*; San Diego:2017.
(71) Martin, M. G.; Siepmann, J. I. Transferable Potentials for Phase Equilibria. 1. United-Atom Description of n-Alkanes. *J. Phys. Chem. B* **1998**, *102* (14), 2569−2577.
(72) Cornell, W. D.; Cieplak, P.; Bayly, C. I.; Gould, I. R.; Merz, K. M.; Ferguson, D. M.; Spellmeyer, D. C.; Fox, T.; Caldwell, J. W.; Kollman, P. A. A Second Generation Force Field for the Simulation of

https://doi.org/10.1021/acs.jpcc.3c04377
J. Phys. Chem. C 2023, 127, 20491−20502

Proteins, Nucleic Acids, and Organic Molecules. *J. Am. Chem. Soc.* **1995**, *117* (19), 5179−5197.
(73) Delley, B. An All-Electron Numerical Method for Solving the Local Density Functional for Polyatomic Molecules. *J. Chem. Phys.* **1990**, *92* (1), 508−517.
(74) Becke, A. D. Density-Functional Thermochemistry. III. The Role of Exact Exchange. *J. Chem. Phys.* **1993**, *98* (7), 5648−5652.
(75) Plimpton, S. Fast Parallel Algorithms for Short-Range Molecular Dynamics. *J. Comput. Phys.* **1995**, *117*, 1−19.
(76) Nosé, S. A Unified Formulation of the Constant Temperature Molecular Dynamics Methods. *J. Chem. Phys.* **1984**, *81* (1), 511−519.
(77) Hoover, W. G. *Canonical Dynamics: Equilibrium Phase-Space Distributions.* **1985**, *31* (3), 1695−1697.
(78) Sarkisov, L.; Kim, J. Computational Structure Characterization Tools for the Era of Material Informatics. *Chem. Eng. Sci.* **2015**, *121*, 322−330.
(79) Velioğlu, S.; Ahunbay, M. G.; Tantekin-Ersolmaz, Ş. B. Investigation of CO_2-Induced Plasticization in Fluorinated Polyimide Membranes via Molecular Simulation. *J. Membr. Sci.* **2012**, *418*, 217−227.
(80) Peng, D.; Robinson, D. B. *A New Two-Constant Equation of State.* **1976**, *15* (1), 59−64.
(81) Bondi, A. *Physical Properties of Molecular Crystals Liquids and Gases*; John Wiley: New York, 1968.
(82) Balçık, M.; Ahunbay, M. G. Prediction of CO_2-Induced Plasticization Pressure in Polyimides via Atomistic Simulations. *J. Membr. Sci.* **2018**, *547*, 146−155.
(83) Zornoza, B.; Tellez, C.; Coronas, J.; Gascon, J.; Kapteijn, F. Metal Organic Framework Based Mixed Matrix Membranes: An Increasingly Important Field of Research with a Large Application Potential. *Microporous Mesoporous Mater.* **2013**, *166*, 67−78.
(84) Shimazu, A.; Miyazaki, T.; Maeda, M.; Ikeda, K. Relationships between the Chemical Structures and the Solubility. *Diffusivity, and Permselectivity of Propylene and Propane in 6FDA-Based Polyimides.* **2000**, *38*, 2525−2536.
(85) Park, S. H.; Kim, K. J.; So, W. W.; Moon, S. J.; Lee, S. B. Gas Separation Properties of 6FDA-Based Polyimide Membranes with a Polar Group. *Macromol. Res.* **2003**, *11* (3), 157−162.
(86) Gonciaruk, A.; Althumayri, K.; Harrison, W. J.; Budd, P. M.; Siperstein, F. R. PIM-1/Graphene Composite: A Combined Experimental and Molecular Simulation Study. *Microporous Mesoporous Mater.* **2015**, *209*, 126−134.
(87) Connolly, M. L. Analytical Molecular Surface Calculation. *J. Appl. Crystallogr.* **1983**, *16* (5), 548−558.
(88) Muzzi, C.; Fuoco, A.; Monteleone, M.; Esposito, E.; Jansen, J. C.; Tocci, E. Optical Analysis of the Internal Void Structure in Polymer Membranes for Gas Separation. *Membranes* **2020**, *10*, 328.
(89) Fu, S.; Wenz, G. B.; Sanders, E. S.; Kulkarni, S. S.; Qiu, W.; Ma, C.; Koros, W. J. Effects of Pyrolysis Conditions on Gas Separation Properties of 6FDA/DETDA:DABA(3:2) Derived Carbon Molecular Sieve Membranes. *J. Membr. Sci.* **2016**, *520*, 699−711.
(90) Hwang, S.; Semino, R.; Seoane, B.; Zahan, M.; Chmelik, C.; Valiullin, R.; Bertmer, M.; Haase, J.; Kapteijn, F.; Gascon, J.; et al. Revealing the Transient Concentration of CO_2 in a Mixed-Matrix Membrane by IR Microimaging and Molecular Modeling. *Angew. Chemie - Int. Ed.* **2018**, *57* (18), 5156−5160.
(91) Semino, R.; Durholt, J. P.; Schmid, R.; Maurin, G. Multiscale Modeling of the HKUST-1/Polyvinyl Alcohol) Interface: From an Atomistic to a Coarse Graining Approach. *J. Phys. Chem. C* **2017**, *121* (39), 21491−21496.
(92) Semino, R.; Ramsahye, N. A.; Ghoufi, A.; Maurin, G. Role of MOF Surface Defects on the Microscopic Structure of MOF/Polymer Interfaces: A Computational Study of the ZIF-8/PIMs Systems. *Microporous Mesoporous Mater.* **2017**, *254*, 184−191.
(93) Ahmad, M. Z.; Navarro, M.; Lhotka, M.; Zornoza, B.; Téllez, C.; de Vos, W. M.; Benes, N. E.; Konnertz, N. M.; Visser, T.; Semino, R.; et al. Enhanced Gas Separation Performance of 6FDA-DAM Based Mixed Matrix Membranes by Incorporating MOF UiO-66 and Its Derivatives. *J. Membr. Sci.* **2018**, *558* (April), 64−77.
(94) Das, M.; Koros, W. J. Performance of 6FDA-6FpDA Polyimide for Propylene/Propane Separations. *J. Membr. Sci.* **2010**, *365* (1−2), 399−408.
(95) Park, S.; Jeong, H. K. Transforming Polymer Hollow Fiber Membrane Modules to Mixed-Matrix Hollow Fiber Membrane Modules for Propylene/Propane Separation. *J. Membr. Sci.* **2020**, *612* (June), 118429.
(96) Velioğlu, S.; Ahunbay, M. G.; Tantekin-Ersolmaz, S. B. Propylene/Propane Plasticization in Polyimide Membranes. *J. Membr. Sci.* **2016**, *501*, 179−190.
(97) Fang, W.; Zhang, L.; Jiang, J. Polymers of Intrinsic Microporosity for Gas Permeation: A Molecular Simulation Study. *Mol. Simul.* **2010**, *36* (12), 992−1003.
(98) van Essen, M.; Thür, R.; van den Akker, L.; Houben, M.; Vankelecom, I. F. J.; Nijmeijer, K.; Borneman, Z. Tailoring the Separation Performance of ZIF-Based Mixed Matrix Membranes by MOF-Matrix Interfacial Compatibilization. *J. Membr. Sci.* **2021**, *637* (July), 119642.
(99) van Essen, M.; van den Akker, L.; Thür, R.; Houben, M.; Vankelecom, I. F. J.; Borneman, Z.; Nijmeijer, K. Investigation of ZIF-78 Morphology and Feed Composition on the Mixed Gas CO_2/N2 Separation Performance in Mixed Matrix Membranes. *Adv. Mater. Interfaces* **2021**, DOI: 10.1002/admi.202001478.

https://doi.org/10.1021/acs.jpcc.3c04377
J. Phys. Chem. C 2023, 127, 20491−20502

CHAPTER 4

IMPACT OF MOF SURFACE FUNCTIONALIZATION AND SOLVENT-DRIVEN TERMINATIONS ON THE STRUCTURING & PROPERTIES OF ZIF-67-BASED MMMs

4.1 Introduction

Agglomeration of MOF fillers in the polymeric matrix during the membrane preparation can prevent the formation of homogeneous and defect-free MMMs and alter their separation performance [1–4]. To address this MOF/polymer interface issue, interface modification can be employed to improve the compatibility between MOF and a polymer substrate [3–6]. Hence, to achieve this objective, several strategies have been proposed for tuning MOF particles, including particle size adjustment, chemical grafting, and surface modifications, among others. In the first part of the study in Chapter 4, particular attention is paid to improve the MOF/polymer adhesion by functionalizing the MOF surface. Typically, MOFs can be modified with chemicals such as ionic liquids (ILs) [7], isophthalic dihydrazide (IPD) [8], and polyethylenimine (PEI) [9] among others. Jiao and co-workers incorporated PEI functionalized ZIF-8 (PEI-ZIF-8) into Pebax matrix via in-situ method to create Pebax/PEI-ZIF-8 composite membranes with MOF particle sizes around 15 nm. They demonstrated that MOF surface functionalization with long-chain amine polymers effectively improves interfacial compatibility through hydrogen bonding interactions. Through chemical modification methods, Pebax/PEI-ZIF-8 MMMs exhibits CO_2 permeability of 13 GPU and a CO_2/N_2 ideal selectivity of 49.0, which are respectively 80.6% and 118.8% higher compared to the pristine Pebax membrane [9]. Wang et al. conducted surface modifications on several MOFs sharing the same topology (UiO-66, UiO-67, and BUT-30) using 1,2-dioleoyl-sn-glycero-3-phosphate (DOPA). Their study demonstrated that DOPA functionalization exclusively takes place on the external surface of MOFs, resulting in DOPA-functionalized MOFs that can readily disperse in solvents with low polarity, thanks to their colloidal stability [10]. Knebel et al. obtained a novel series of MMMs for propylene/propane separation made of ZIF-67 NPs in non-polar solvents through its surface modification with IDip and 6FDA-DAM and derivative polymers. These researches successfully fabricated

MMM with a stable dispersion of ZIF-67-IDip fillers with loadings as high as 47.5 wt% in 6FDA-DAM. In their study, they demonstrated that using more viscous solvents could facilitate the preparation of highly loaded porous liquids with improved separation performance, ultimately broadening the spectrum of suitable solvents for industrial processing [11]. It is worth noting that the molecules mentioned earlier, like DOPA and IDip, possess only one polar side for surface modification of the MOF, and they do not offer additional binding forces between MOFs and polymer chains.

Shi and co-workers incorporated ZIF-8 with an isophthalic dihydrazide (IPD) molecular layer, characterized by a polar molecule with two polar sides, through coordination interaction. They reported the successful production of a PI/IPD@ZIF-8 (PI = 6FDA-Durene polyimide), featuring exceptional quality and a high loading of ZIF-8, achieved by ZIF-8 surface modification. The resulting membrane (PI/IPD@ZIF-8), loaded with 45 wt% of IPD@ZIF-8, exhibits H_2 permeability of ~8000 Barrer, along with enhanced selectivities for H_2/CH_4 (selectivity = 15.1) and H_2/N_2 (selectivity = 13) which are 46.6% and 32.7% higher, respectively, compared to (PI/ZIF-8) MMMs[8].

Herein in Chapter 4 the computational strategy validated in Chapter 3 was applied to construct microscopic models of IPD functionalized ZIF-67 with the polymers of 6FDA-DAM and PIM-1. The main objectives of this study are to elucidate the atomistic origins of the enhanced adhesion between ZIF-67 and polymers in the resulting composites, achieved through MOF functionalization by a polar molecule of IPD. Additionally, the aim is to gain insight into how MOF functionalization influences the adsorption performance of propane and propylene in the resulting composites and compare these results with those obtained with the functionalized ZIF-67-IDip presented in Chapter 3.

It is also important to note that ZIFs possess unique properties, including a relatively high surface area, and excellent chemical and thermal stability. For specific applications, optimizing the crystal structure and properties of ZIFs may be necessary to achieve the best performance [12]. It is well-known that the properties of ZIFs are influenced by various conditions, including key parameters such as temperature, pH [13], reaction time, solvent [14], precursor concentration [15], the use of Structure Directing Agents (SDAs) [16], and

the chosen synthesis methods [17]. Among these parameters, the choice of a solvent is a crucial factor in the synthesis process, and its impact on the properties, morphology, and structure of ZIFs is an ongoing area of investigation. As far as we are aware, all known ZIFs have been synthesized exclusively in organic solvents, such as dimethylformamide (DMF), diethylformamide (DEF), or methanol, among other options [18]. Despite the higher cost and environmental pollution associated with organic solvents, efforts to synthesize ZIFs in aqueous solutions have often resulted in the formation of 1D or non-porous materials [19,20].

Bustamante and co-workers synthesized ZIF-8 nanocrystals in several solvents such as water, a series of aliphatic alcohols, DMF and acetone. They demonstrated that alcohols, especially methanol, were the most effective solvents for the formation of ZIF-8, whereas water and DMF failed to produce ZIF-8 [21]. Schejn et al. employed methanol as an organic solvent in their synthesis of ZIF-8, while also studying the impact of zinc salt on the size and morphology of ZIF-8 particles. They demonstrated that the reactivity of the zinc salt in the growth solution influences the size and morphology of ZIF-8 particles [22]. Yang et al. employed a methanol solution in their experimental studies and reused it as a dissolvent to synthesize ZIF-8 many times and investigated how the reused methanol solution affects the properties of the synthesized ZIF-8. They showed that the reused methanol solution does not alter the phase, porous structure, and BET surface area of ZIF-8; however, it led to an increase in particle size when the methanol solution was reused four times [23]. Hence, methanol is the most commonly used organic solvent for the fabrication of ZIFs such as ZIF-8 since it exhibits weak interactions with ZIF-8 and it can be more easily removed compared to other solvents like DMF [24–26].

When obtaining surface models of ZIF-67, it is important to consider that under-coordinated sites on its outer surface may be prone to reactions with solvents present during the synthesis process. In the first section of this chapter, the outer surface of ZIF-67 was terminated by −OH groups and –H, taking into account the dissociative adsorption of water. This approach is supported by the experimental study conducted by Tian et al. [27], as well as computational modeling work by Chizallet et al. [28] and Semino et al [29] to saturate the MOF surface. Therefore, given the critical influence of solvent choice on the properties, morphology, and structure of ZIFs, using an alternative solvent can potentially affect the

interactions between ZIF-67 and the polymer, ultimately enhancing interactions with guest molecules. Hereafter, methanol, the most commonly used organic solvent was used for the outer MOF surface termination by $–CH_3O$ groups and –H considering the dissociative adsorption of methanol. Thus, the second section of this chapter is dedicated to study the influence of solvent on the adhesion between ZIF-67 and the polymers of 6FDA-DAM and PIM-1, as well as how it influences the propane and propylene adsorption performance of these composites.

4.2 ZIF67-IPD/Polymer MMM Models

Improving the interfacial interactions between MOF and polymer via ZIF-67 surface modification can significantly enhance the adhesion between these two components. This strategy enables a more uniform dispersion of the MOF in the polymeric matrix. For this purpose, in Chapter 3, NHC-based surface functionalized group of IDip was selected as it offers high affinity to unsaturated metal sites and shares similar chemistry with the imidazole linker in ZIF-67. However, it has been observed that IDip possesses only one polar side to coordinate the MOF surface, lacking additional binding forces between MOFs and polymer chains.

Shi et al. previously reported that MMMs with a ZIF-8-IPD filler loading as high as 45 wt. % in 6FDA-Durene exhibited improved dispersion of the MOF filler in the polymer matrix, along with the formation of almost defect-free interfaces in the MMMs. They demonstrated that the abundant amino and amide groups in IPD (see Figure 4.1) can effectively coordinate with the exposed uncoordinated Zn(II) atoms on the outer surface of ZIF-8, while also forming hydrogen bonds with the carbonyl groups on FDA-Durene molecules. Hence, IPD modified ZIF-8 NPs demonstrate excellent dispersion in several solvents but also significantly enhance interfacial interactions with the polyimide matrix [8]. For this reason, an atomistic-scale investigation of the surface arrangement of composites containing IPD-functionalized ZIF-67 was conducted to shed microscopic insight into this complex system.

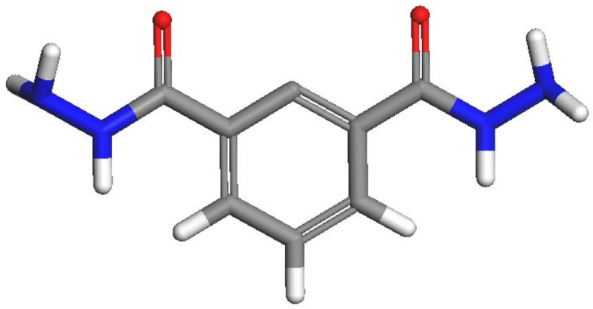

Figure 4.1 : Schematic representation of the IDip molecule. Color code: C (gray), N (blue), and H (white).

4.2.1 ZIF67-IPD surface models

The model of the IPD surface-modified ZIF-67 NP (ZIF-67-IPD) was generated using the same method employed for the pristine ZIF-67 NP and the IDip surface-modified ZIF-67- described in Chapter 3, by cleaving it from a supercell with (2×2×2) unit cells. The resulting atomistic model, possessing a spherical shape, contains 16 cages, with IPD functions on its outer surface bonded to Co atoms, while the innermost atoms are coordinated to −OH groups and −H atoms. The resulting outer surface of the ZIF-67-IPD crystal shows a zig-zag shape as illustrated in Figure 4.2.

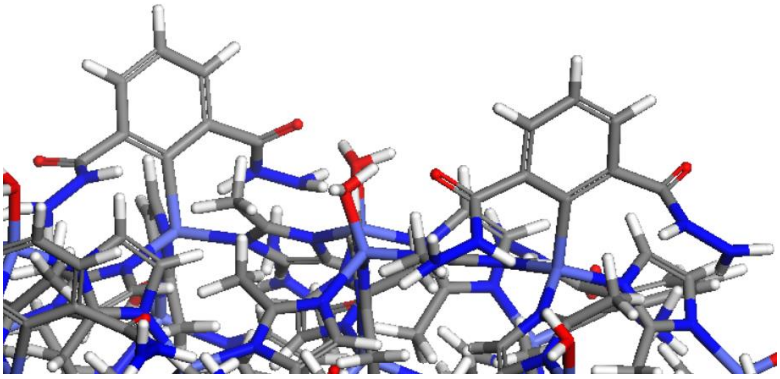

Figure 4.2 : Schematic representation of the ZIF-67-IPD surface. Color codes for the atoms are the same as in Figure 4.1.

The atomic partial charges for ZIF-67-IPD (Table 4.1) were obtained using cluster-based DFT calculations (as shown in Figure 4.3) with the combination of PBE functional and the 6-31G basis set, performed using Gaussian 09 [30]. For the charges of ZIF-67-IPD model, the charges of the terminal groups were derived from the first cluster model in conjunction with

the charges of the imidazole linkers, while the charges of the IPD groups were obtained using the second cluster, as illustrated in Figure 4.3. The atom types in Figure 4.3 shows the derived atoms from the clusters. The force field parameters for the IPD function were taken from GAFF[31]. Illustrations of the ZIF-67-IPD NP (size of ~59 Å) are presented in Figure 4.5. The bonded and the non-bonded LJ interaction parameters for ZIF-67 was obtained from the work by Krokidas et al.[32] who used flexible force field through modification in AMBER[31] force field, as it was employed for ZIF-67 NP and ZIF-67-IDip NP, while for IPD function AMBER force field was used to describe the mentioned interactions. The intramolecular non-bonded framework interactions were calculated using a scaled 1-4 approach, which included a 0.5 scaling of the Coulombic term and 0.83 scaling of the van der Waals terms.

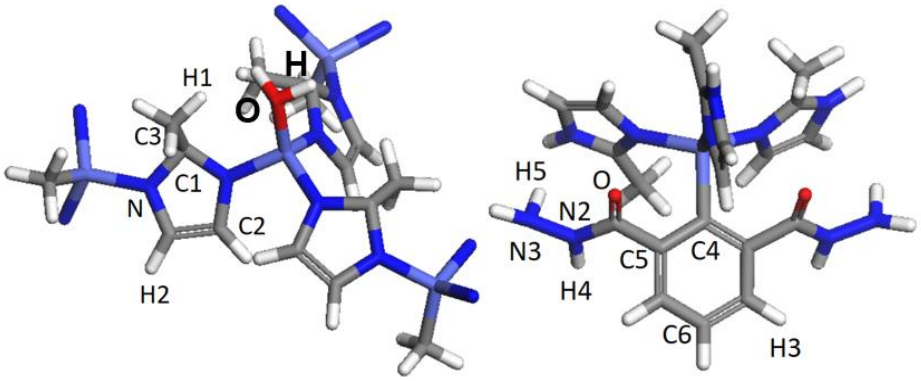

Figure 4.3 : Schematic representation of clusters used to calculate the charges for ZIF-67 and IPD at the DFT-level. Color codes for the atoms are the same as in Figure 4.1.

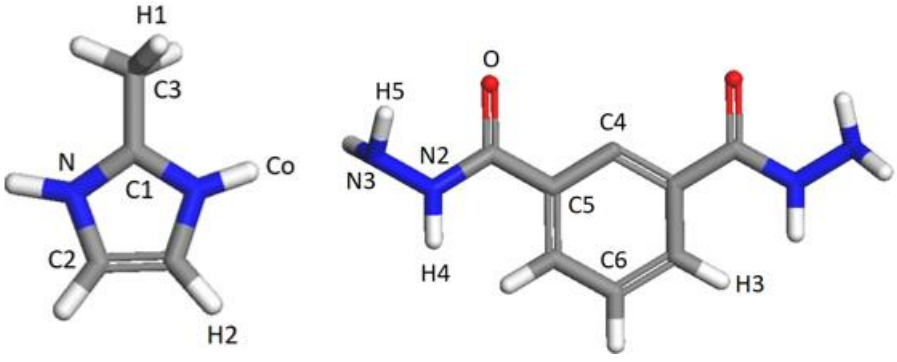

Figure 4.4 : Schematic representation of the atom types for the charges.

Table 4.1 : Atom types and charges for ZIF-67-IPD.

Atom type	Partial charges (e)
Carbon (C1)	0.539
Carbon (C2)	-0.031
Carbon (C3)	-0.634
Carbon (C4)	-0.108
Carbon (C5)	-0.055
Carbon (C6)	-0.155
Carbon (C7)	0.418
Cobalt (Co)	0.599
Hydrogen (H1)	0.239
Hydrogen (H2)	0.226
Hydrogen (H3)	0.120
Hydrogen (H4)	0.328
Hydrogen (H5)	0.302
Nitrogen (N)	-0.657
Nitrogen (N2)	-0.517
Nitrogen (N3)	-0.509
Oxygen (O)	-0.471
-**O**H	-0.580
H	0.302

Based on the data provided for ZIF-67-IDip, the charges of the surface terminal groups of the O atoms of the −**O**H groups and −H atoms were slightly different compared to the ZIF-67-IPD model (-0.704 vs. -0.580) for – O atoms of the −**O**H groups and (0.450 vs.0.302) for –H terminations, respectively.

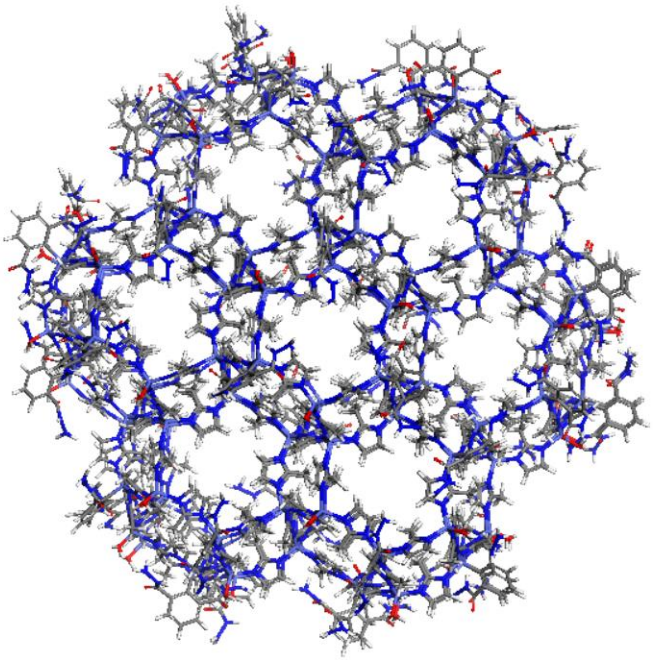

Figure 4.5 : ZIF-67-IPD crystal, terminated by OH and ligand groups. Color code: C (gray), O (red), N (blue), Co (steel blue), and H (white).

4.2.2 ZIF-67-IPD/6FDA-DAM and ZIF-67-IPD/PIM-1 MMM models

The interface models for surface-functionalized MOF/polymers were constructed using the same method applied in Chapter 3. This involved combining the models of 6FDA-DAM and PIM-1 with the surface of ZIF-67-IPD within a simulation box. The number of polymer chains was carefully controlled to create atomistic models representing 34.5 wt.% of ZIF-67-IPD in the resulting models, following also the same procedure described in Chapter 3 for the other MMMs.

In constructing the ZIF-67-IPD/6FDA-DAM composite with 34.5 wt.% ZIF-67-IPD, a typical arrangement involved the packing of four polymer chains around the ZIF-67-IPD NP. Conversely, for the ZIF-67-IPD/PIM-1 composite with 34.5 wt.% ZIF-67-IPD NP, five polymer chains were packed around the ZIF-67-IPD NP. The MOF-based composites were simulated within a cubic simulation cell, with a size of approximately ~59 Å for the ZIF-67-IPD/6FDA-DAM composite containing 34.5 wt. % ZIF-67-IPD and a ~64 Å cubic simulation cell size was employed for the 34.5 wt. % ZIF-67-IPD NP in combination with PIM-1 matrix.

The equilibration of the so-obtained MOF/polymer composites was accomplished using a 21-step MD decompression-compression method [33] with Pmax equal to 10 kbar employing the LAMMPS software [34]. The MD simulations were conducted for 1 ns, employing time step of 1 fs and utilizing the Nosé-Hoover thermostat and barostat with relaxation times of 0.1 ps and 1 ps, respectively [35,36]. A 14-Å cut-off was employed for the LJ interactions, with Coulombic contributions evaluated using tail corrections and Ewald summation method. As an illustrative example, representative MD-equilibrated atomistic model of the ZIF-67-IPD/6FDA-DAM composite is shown in Figure 4.6.

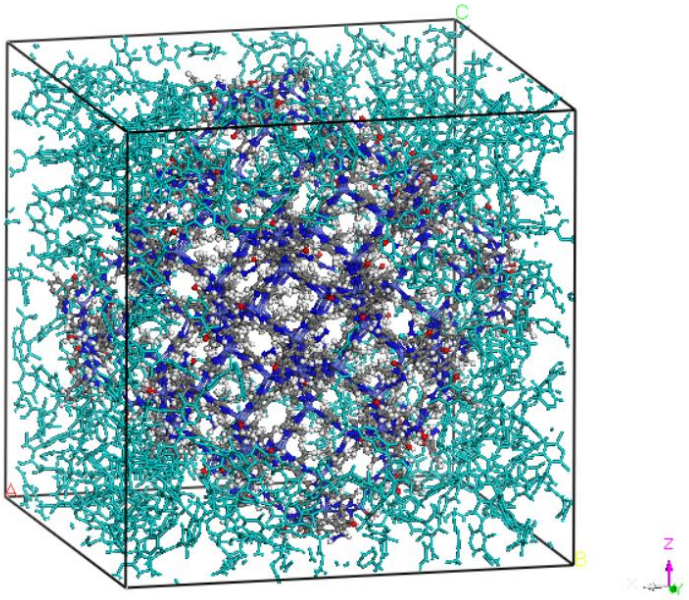

Figure 4.6 : Representative atomistic model for the ZIF-67-IPD/6FDA-DAM composite containing 34.5 wt.% ZIF-67-IPD. ZIF-67 atoms are represented as ball and stick atoms and polymer chains in light blue lines. Color code: O (red), C (grey), H (white), N (blue) and Co (steel blue).

4.2.3 Analysis of the ZIF-67-IPD/6FDA-DAM and ZIF-67-IPD/PIM-1 MMM interfaces

Chapter 3, which explored the interfacial interactions between MOF and polymer, demonstrated that MOF surface functionalization with IDip molecules improved the compatibility of the ZIF-67/6FDA-DAM composite, enabling better polymer packing at the

MOF surface. Here, another surface modification agent, IPD was used to first investigate the interfacial interactions between MOF and 6FDA-DAM. Figure 4.7 presents the radial atomic density of 6FDA-DAM in both ZIF-67 and ZIF-67-IPD-based composites. The calculation was performed over spherical shells using a 0.1 Å bin size, with the center of the outer MOF cage exposed to the polymer considered as the origin (r = 0). Here again, the dark blue colored line delimits the upper limits of the ZIF-67 and ZIF-67-IPD surfaces, while the black curves represent the polymers. Additionally, there is a light blue-shaded region representing interfacial MOF/polymer, along with overlap hatched area. In the case of ZIF-67-IPD/6FDA-DAM composite, Figure 4.5(b) demonstrates that the upper limit of the MOF surface (dark blue line) is shifted to a higher r value (r = 14.5 Å) due to the presence of the functional IPD groups. The radial atomic density of the polymer exhibits a gradual increase from 9.0 Å to 15.5 Å, resulting into an interfacial MOF/polymer region length comparable to that simulated for the pristine ZIF-67/6FDA-DAM composite (6.5 Å and 5.8 Å, respectively). This interfacial MOF/polymer length aligns with the previously simulated data for the ZIF-8/6FDA-DAM composite (9 Å), followed by a first-neighbor polymer domain (grey shaded area) that is not a polymer-bulk region, as it still experiences the influence of the MOF surface. This behavior has been consistently modeled in various MOF/polymer systems [37–40]. Remarkably, 6FDA-DAM exhibits a closer proximity to the functionalized MOF surface compared to the pristine ZIF-67 scenario, leading to a moderate overlap region between the MOF surface and the polymer at the interface. The overlap length between the MOF and polymer (indicated by the hatched area) is considerably longer in the case of the IPD-functionalized MOF surface compared to the MOF/polymer composite (5.5 Å vs. 0.8 Å, respectively). Therefore, the IPD functionalization plays a crucial role in enhancing the compatibility between the ZIF-67 NP and the polymer. This implies that IPD functionalization facilitates a more efficient packing of 6FDA-DAM in the vicinity of the MOF surface, with the polymer conforming to the pocket created at the MOF surface by the IPD functional groups.

In comparison to the previously discussed ZIF-67-IDip/6FDA-DAM composite in Chapter 3.6.2, there is a notably broader overlap region (5.5 Å vs. 2.3 Å), along with a slightly longer MOF/polymer interfacial length (5.8 Å vs. 5.5 Å) in the case of ZIF-67-IPD/6FDA-DAM.

The presence of two polar sites in the IPD molecule, as opposed to the single polar side in the IDip molecule, enhances the compatibility between ZIF-67 and 6FDA-DAM through improved interfacial interactions. This observation also aligns with experimental study by Shin et al. [8]. Based on cross-sectional SEM images of IPD@MOF MMM, they observed that adding an IPD layer on MOF NPs did not only enhance the dispersibility of the MOF particles, but also increased the interfacial adhesion between MOF and fillers.

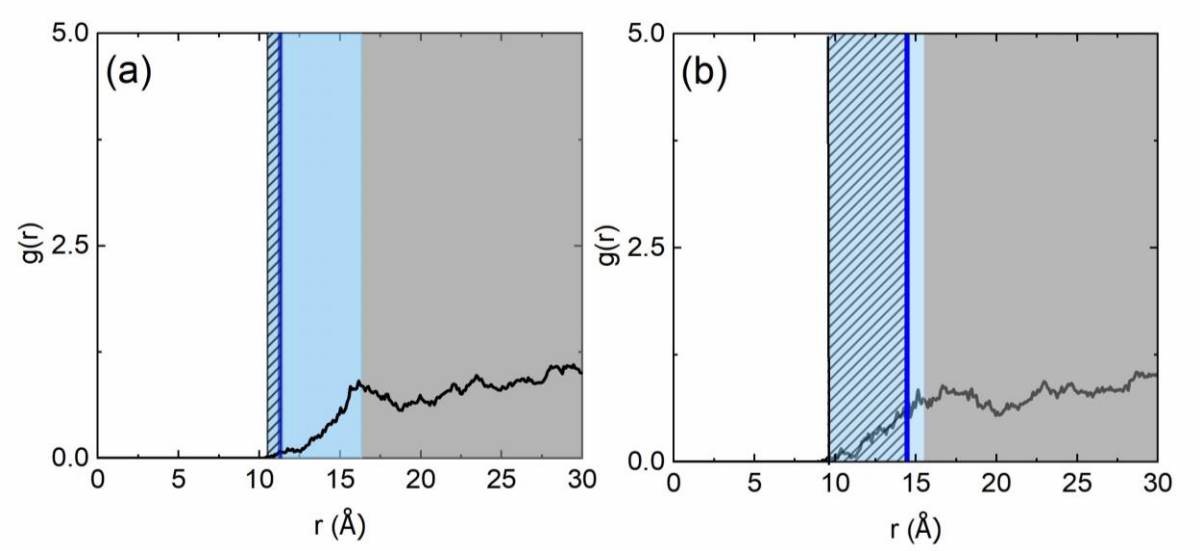

Figure 4.7 : Calculated radial atomic density distribution of (a) 6FDA-DAM (black) in the unfunctionalized ZIF-67/6FDA-DAM composite with respect to the center of the nanoparticle (r = 0), (b) Radial atomic density distribution of 6FDA-DAM (black) in the functionalized ZIF-67-IPD/6FDA-DAM composite with respect to the center of the nanoparticle (r = 0). The interfacial MOF/polymer overlap regions are marked by black dashed shaded areas.

Figure 4.8(a) presents the radial distribution functions (RDF) for the oxygen atoms of 6FDA-DAM and the hydrogen atoms of the terminal -OH groups pairs on both the functionalized and unfunctionalized MOF surfaces in their respective composites. It can be observed that these interfacial MOF/polymer interactions are quite strong in both composites, with an associated O(6FDA-DAM)-H(OH) mean distance of 2.45 Å. Interestingly, the intensity of the corresponding peak is higher for the unfunctionalized MOF surface-based composite compared to IPD and IDip functionalized-based composites. However, it is important to note that with IPD functionalization, the intensity of the peak is higher when compared to IDip

functionalization. Notably, the more efficient polymer packing in the ZIF-67-IPD/6FDA-DAM composite leads to additional interactions between the —CH_3 and –CF_3 groups of 6FDA-DAM with the carbon atoms of the IPD function of the MOF, characterized by separating distances of approximately ~ 3 Å as shown in Figure. 4.8 (b).

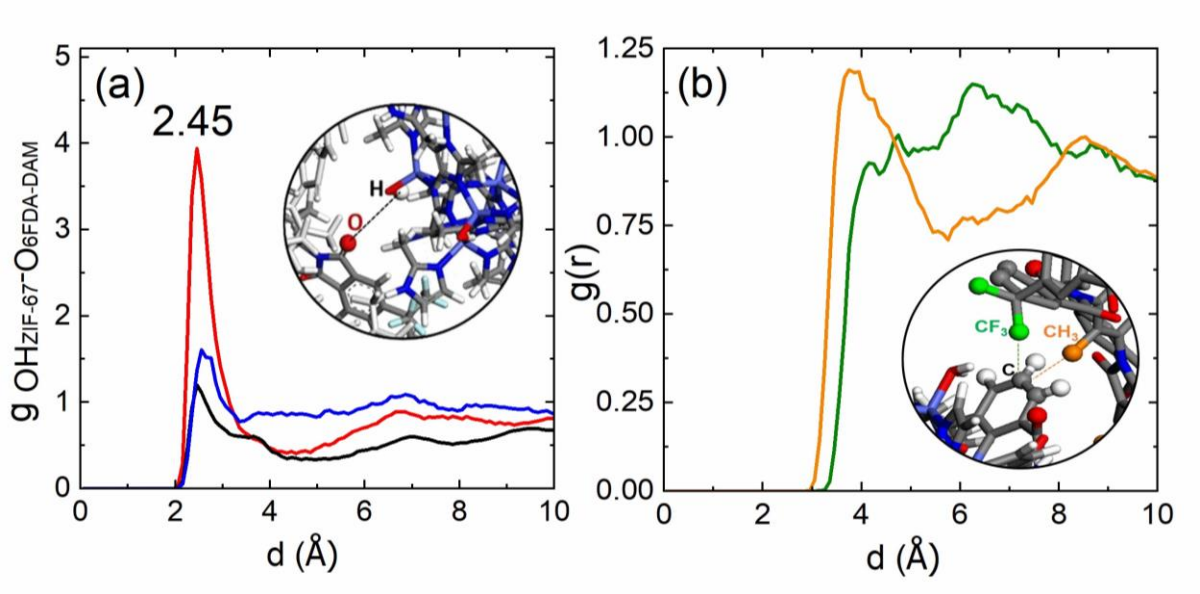

Figure 4.8 : Calculated radial distribution functions in the composites (a) between oxygen atoms of 6FDA-DAM and – H(OH) of the ZIF-67-IPD (blue) and ZIF-67-IDip functionalized (black) and unfunctionalized (red) surface in the corresponding composites along with illustration of the preferential site-to-site interactions for the ZIF-67/6FDA-DAM composite and (b) between –CH_3 groups (orange curve) and –CF_3 groups (green curve) of 6FDA-DAM and Carbon atoms of the IPD functional groups attached at the ZIF-67 surface along with illustration of the preferential site-to-site interactions of the ZIF-67-IPD/6FDA-DAM composite.

Chapter 3 reveals that ZIF-67/PIM-1 composite is characterized by a slightly longer MOF/polymer overlap region compared to the ZIF-67/6FDA-DAM composite, despite the higher rigidity of PIM-1. This is also evident in the case of IDip functionalized MOF with polymers. A slightly longer overlap length between the MOF and the polymer, as well as longer interfacial lengths, was observed in ZIF-67-IDip/PIM-1 composite compared to the ZIF-67-IDip/6FDA-DAM composite. Hence, the objective of this section was to check if this trend remains true for ZIF-67 functionalized with IPD.

Figure 4.9 shows the radial atomic density profile of PIM-1 in ZIF-67-based composite as well as in the functionalized ZIF-67-IPD/PIM-1 composites. The dark blue colored line represents the upper limit of the ZIF-67 surface, measuring at r=11.2 Å and 14.3 Å for PIM-1 with ZIF-67 and ZIF-67-IPD surfaces, respectively. The upper limit of the MOF surface is expanded due to the presence of the functional IPD groups. The radial atomic density of the polymer exhibits a gradual increase from 10.4 Å to 15.9 Å, resulting into an interfacial MOF/polymer region (blue colored area) length slightly higher than that simulated for the pristine ZIF-67/PIM-1 composite (5.5 Å and 4.9 Å, respectively). Compared to ZIF-67/PIM-1, a longer MOF/polymer overlap length (black shaded area) is observed for ZIF-67-IPD/PIM-1 (3.9 Å vs. 1.8 Å). Extended interfacial and overlap lengths follow the same trend as observed for ZIF-67-IPD/6FDA-DAM composite. This indicates that IPD functionalization promotes a more efficient packing of PIM-1 near the MOF surface.

In comparison to the previously discussed ZIF-67-IDip/PIM-1 composite in Chapter 3, the ZIF-67-IPD/PIM-1 composite exhibits a slightly longer overlap region (3.9 Å vs. 2.6 Å), along with a slightly lower MOF/polymer interfacial length (5.5 Å vs. 6.5 Å). This suggests that the increased rigidity of PIM-1, combined with the presence of two polar sites in IPD, may not significantly favor an enhancement of the MOF/polymer interactions and hence leading to a quite similar MOF/polymer compatibility.

Moreover, compared to ZIF-67-IPD/6FDA-DAM, both the interfacial region and the MOF/polymer overlap region are slightly smaller (5.5 Å vs. 6.5 Å and 5.5 Å vs. 3.8 Å respectively) compared to ZIF-67-IPD/PIM-1 surface. Hence, 6FDA-DAM better adapts its shape to ZIF67-IPD surface, while the more rigid PIM-1 cannot accommodate well the ZIF67-IPD surface, in contrast to the case for ZIF-67-IDip/PIM-1, where PIM-1 can plug into the troughs formed by the “zig-zag” MOF surface

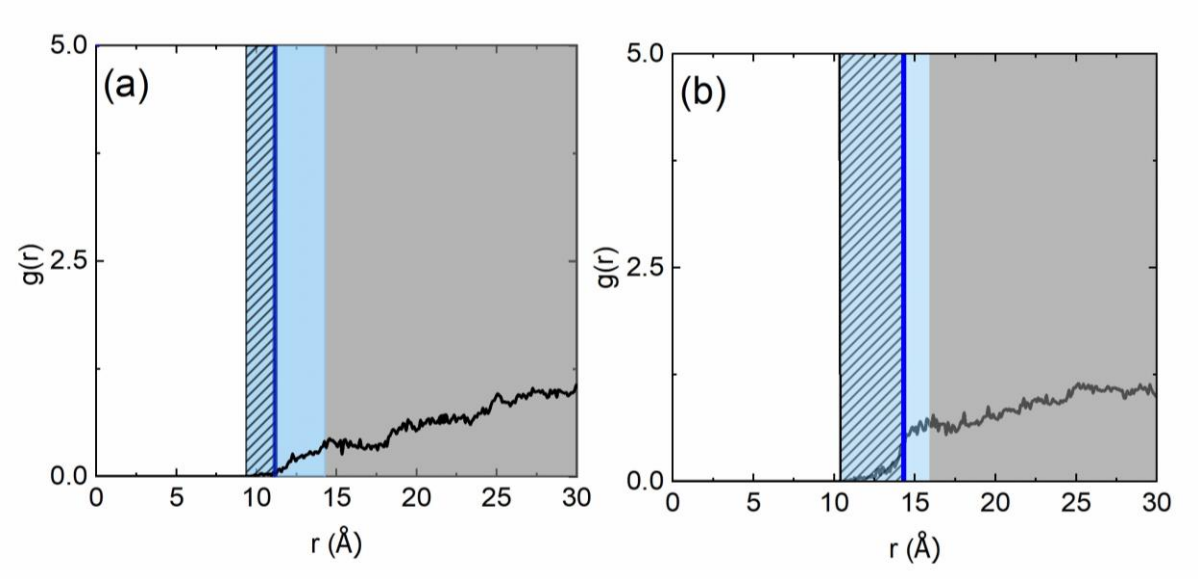

Figure 4.9 : Calculated radial atomic density distribution of (a) PIM-1 (black) in the unfunctionalized ZIF-67/PIM-1 composite with respect to the center of the nanoparticle (r = 0), (b) Radial atomic density distribution of PIM-1 (black) in the functionalized ZIF-67-IPD/PIM-1 composite with respect to the center of the nanoparticle (r = 0), The interfacial MOF/polymer overlap regions are marked by black dashed shaded areas.

To gain further insights into the interfacial behavior, analysis was conducted on the torsion angle distributions. This allowed us to better understand the dynamics of the polymer chains at the interface in comparison to their behavior in the bulk polymer while taking into account the impact of MOF surface functionalization. The torsional angle distribution of the diamine–dianhydride linkage ($\varphi_{C-N-C-C}$) of 6FDA-DAM was averaged over the MD trajectories for ZIF-67-IPD/6FDA-DAM composites. The torsional angle distribution indicates moderate differences between the interfacial region and the bulk polymer, as illustrated in Figure 4.10. A minor conformational change resulting in a moderately narrower torsional angle distribution for the 6FDA-DAM at the interfacial region could be attributed to reduced polymer mobility, leading to increased rigidity.

Furthermore, these findings are supported by the similar torsional angle distribution of 6FDA-DAM with slight differences between the interfacial region and the bulk polymer in the previous composite ZIF-67-IDip/6FDA-DAM models that were discussed in Chapter 3. It suggests that MOF surface functionalization does not significantly enhance the flexibility of the polymer.

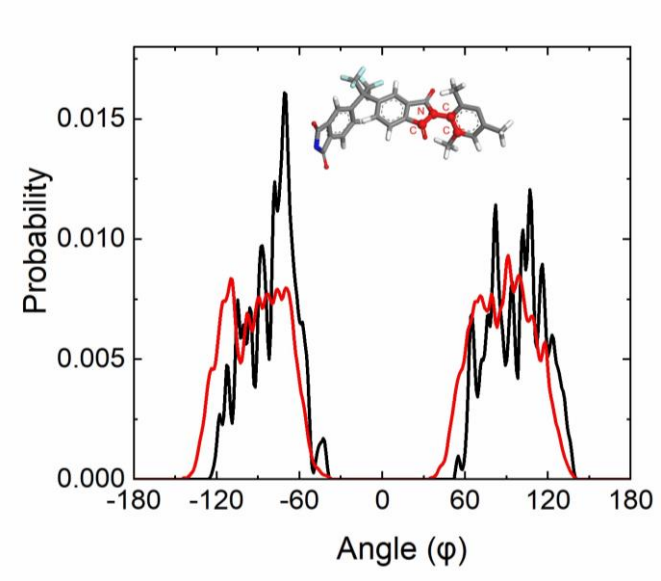

Figure 4.10 : Torsional angle ($\varphi_{C-N-C-C}$) distributions in the 6FDA-DAM for the ZIF-67-IPD/6FDA-DAM at the interface (black) and at the bulk phase (red).

The two representative torsional angles $\varphi_{C-C-O-C}$ and $\varphi_{C-C-C-C}$ of PIM-1 in ZIF-67-IPD/PIM-1 composite are reported in Figure 4.11. The torsional profiles of PIM-1 for $\varphi_{C-C-O-C}$ in the ZIF-67-IPD/PIM-1 composite are nearly identical, indicating a similar polymer planar conformation (Figure 4.11a). On the other hand, the spiro carbon atoms play a more active role, as evidenced by a slightly different torsional angle distribution for the polymer at the interfacial region compared to the bulk polymer. This suggests a slight reduction in the dynamics of the polymer at the interfacial region (Figure 4.11b). This information aligns with the way that MOF functionalization enhances the embedding of polymer to MOF surface, even though it reduces the flexibility of the polymer, as demonstrated in Chapter 3 for both the ZIF-67/PIM-1 and ZIF-67-IDip/PIM-1 composites.

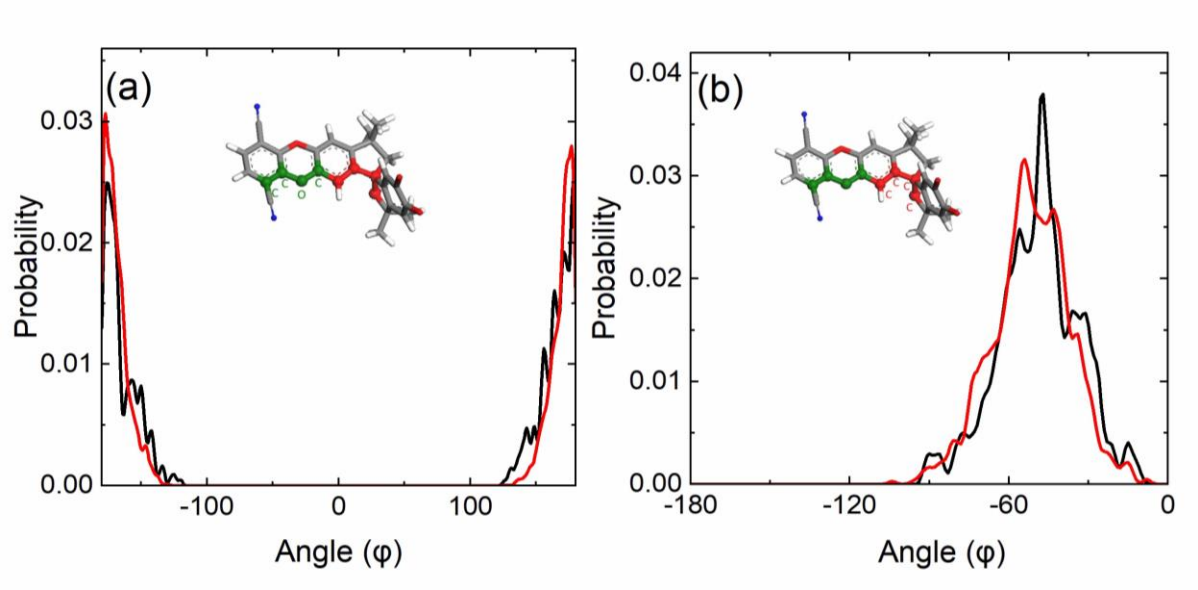

Figure 4.11 : Torsional angle distributions in the PIM-1 for the ZIF-67-IPD/PIM-1 composite (a) $\varphi_{C-C-O-C}$ angle at the interface (black) and at the bulk phase (red) (b) $\varphi_{C-C-C-C}$ angle at the interface (black) and at the bulk phase (red).

4.2.4 Adsorption properties of ZIF-67-IPD/6FDA-DAM and ZIF-67-IPD/PIM-1 MMMs

The single component propane and propylene adsorption isotherms were calculated using a hybrid approach combining GCMC and MD simulations as described in Chapter 3. These simulations were conducted on models for ZIF-67, ZIF-67-IPD NPs, as well as 34.5 wt. % ZIF-67/6FDA-DAM and 34.5 wt. % ZIF-67-IPD/6FDA-DAM composites, employing the LAMMPS software [34]. The corresponding sorption isotherms reported in Figure 4.12, were calculated at 308 K up to 8 bar. These sorption simulations followed the same methodology applied in Chapter 3 for the 34.5 wt. % ZIF-67/6FDA-DAM and 34.5 wt. % ZIF-67-IDip/6FDA-DAM composites.

A comparison of the sorption isotherms reveals that MOF surface functionalization does not significantly influence the adsorptive capacity of the composite, although a slightly lower sorption capacity was observed for ZIF-67-IPD/6FDA-DAM. Furthermore, the similar adsorption behavior of propane and propylene in the previous composite ZIF-67-IDip/6FDA-

DAM models reported in Chapter 3 corroborates these findings, indicating that MOF surface functionalization may not significantly improve the thermodynamic separation of propylene and propane in these composites.

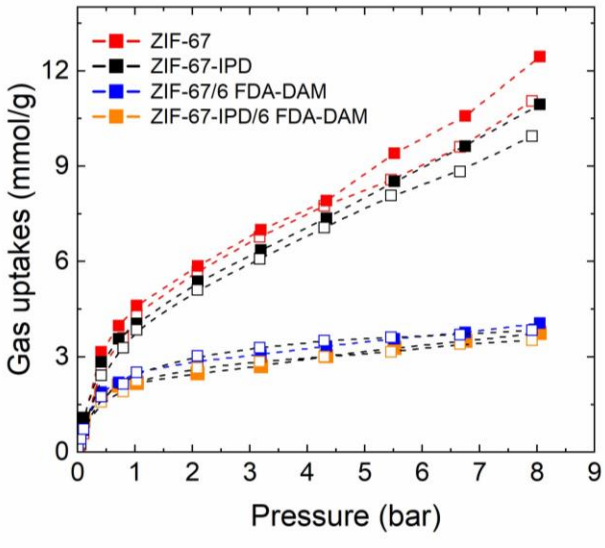

Figure 4.12 : Simulated propane (solid symbols) and propylene (open symbols) sorption isotherms for the composites. 34.5 wt. % ZIF-67/6FDA-DAM (blue) and ZIF-67-IPD/6FDA-DAM (orange) at 308 K up to 8 bar and comparison with ZIF-67 NP (red) and ZIF-67-IPD NP (black).

It was further investigated how the different degree of polymer rigidity affects the single component propane and propylene sorption isotherms for the composites built on ZIF-67-IPD. As shown in Figure 4.13, compared to the 34.5 wt. % ZIF-67/6FDA-DABA composite, 34.5 wt. % ZIF-67-IPD/PIM-1 composite displayed higher propane and propylene uptakes. This can be attributed to the higher rigidity and FFV of PIM-1.

In summary, the surface modification of IDip and IPD, has little influence on the adsorptive behavior of ZIF-67 NPs, along with functionalized ZIF-67 NPs with 6FDA-DAM and PIM-1 fillers in the resulting composites.

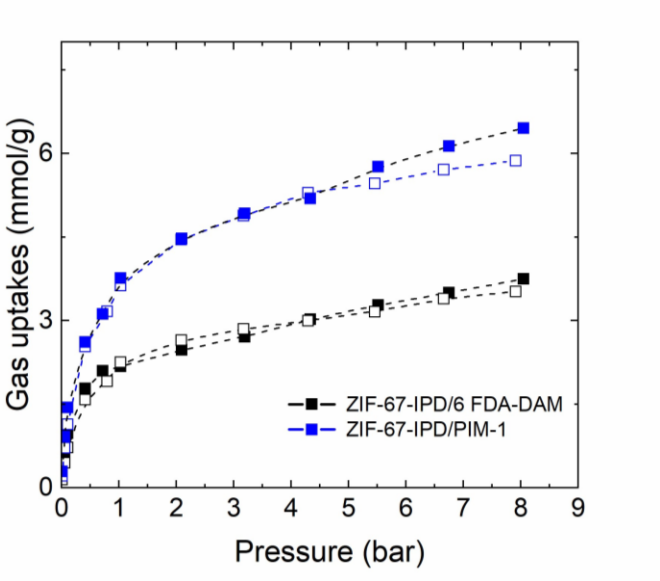

Figure 4.13 : Simulated propane (solid symbols) and propylene (open symbols) sorption isotherms for the composites. 34.5 wt. % ZIF-67-IPD/6FDA-DAM (black) and ZIF-67-IPD/PIM-1 (blue) at 308 K up to 8 bar.

4.3 ZIF67/Polymer MMM Models with MOF Surfaces Terminated by Methanol

4.3.1 ZIF67 surface models

The model for the ZIF-67 NP was created using the same methodology as applied to the pristine ZIF-67 NP with water terminations, by cleaving it from a supercell with (2×2×2) unit cells. The resulting atomistic model, which has a 16 cages of spherical shape, has its outer surface terminated by $–C(H_3)O$ groups and –H, taking into account the dissociative adsorption of methanol. The resulting outer surface of the ZIF-67 NP showing a similar zig-zag shape than the one saturated with water is represented in Figure 4.14.

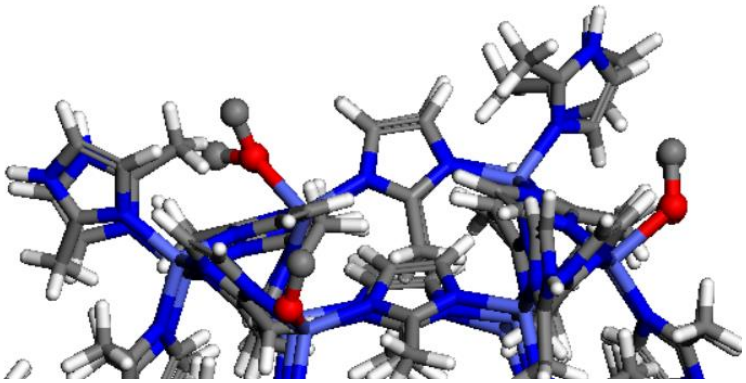

Figure 4.14 : Schematic representation of the ZIF-67 surface terminated by methanol. Color code: C (gray), O (red), N (blue), Co (steel blue), and H (white)

The atomic partial charges for ZIF-67 NP with methanol terminations (Table 4.2) were determined through cluster-based DFT calculations (as shown in Figure 4.15) using the combination of PBE functional and the 6-31G basis set, performed with Gaussian 09 [30]. While in the previous model, the atomic partial charges of ZIF-67 and the force field parameters were taken from the work of Krokidas et al.[32], in this part, the same atomic partial charges were retained with $–C(H_3)O$ terminations, while the charges of the terminal -OCH_3 groups and –H were determined through cluster-based DFT calculations. The electrostatic potentials were obtained using the CHELPG [41] scheme for fitting. The force field parameters for the terminal -OCH_3 groups were taken from the TraPPE united atom force field developed for methanol [42]. Illustrations of the ZIF-67 NP (size of ~59 Å) are presented in Figure 4.16. The intramolecular non-bonded framework interactions were calculated using a scaled 1-4 approach, which included a 0.5 scaling of the Coulombic term and a 0.83 scaling of the van der Waals terms. This strategy is the same than the one described in Chapter 3 for the ZIF-67 NP terminated with –OH.

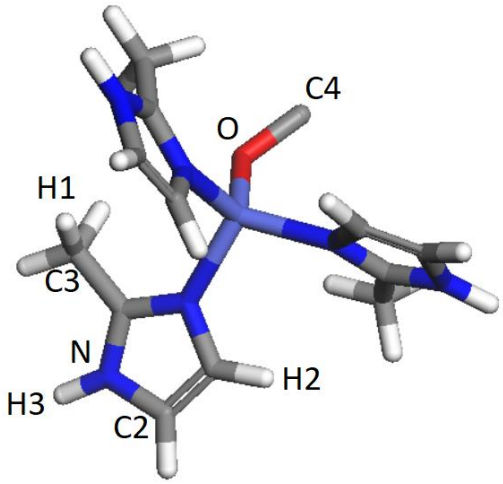

Figure 4.15 : Schematic representation of cluster to obtain charges for ZIF-67 NP terminated by methanol.

Table 4.2 : The atomic partial charges for ZIF-67 NP terminated by methanol.

Atom type	ZIF-67 Partial charges (e)
C1	0.7846
C2	-0.0581
C3	-0.3094
C4	0.2500
H1	0.0584
H2	0.0910
H3	0.2842
N	-0.6956
Co	1.3497
O	-0.5330

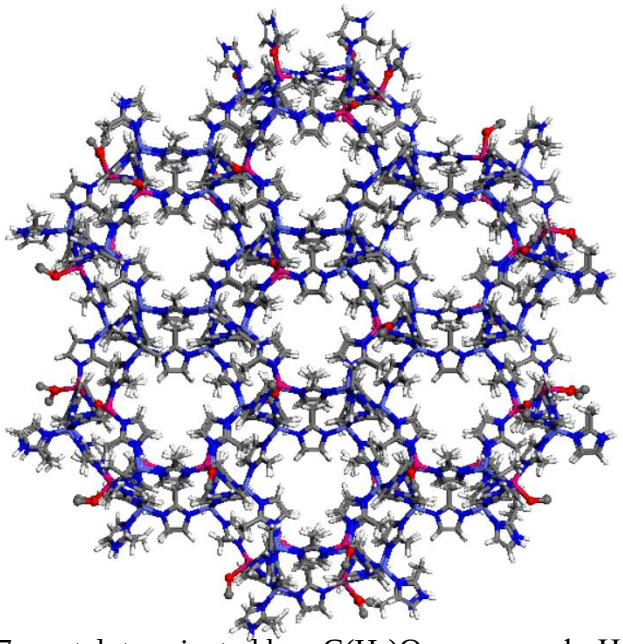

Figure 4.16 : ZIF-67 crystal, terminated by –C(H_3)O groups and −H. Color code: C (gray), O (red), N (blue), Co (steel blue), and H (white).

4.3.2 ZIF-67/6FDA-DAM and ZIF-67/PIM-1 MMM models

The interface models of MOF/polymer with –C(H_3)O terminations were constructed using the same method applied to the MOF/polymers interface models. In constructing the ZIF-67/6FDA-DAM composite with 34.5 wt.% ZIF-67 NP, a typical arrangement involved the packing of four polymer chains around the ZIF-67 NP. Conversely, for the ZIF-67/PIM-1 composite with 34.5 wt.% ZIF-67 NP, five polymer chains were packed around the ZIF-67 NP. The MOF-based composites were simulated within a cubic simulation cell, with a size of approximately ~59 Å for the ZIF-67/6FDA-DAM composite containing 34.5 wt. % ZIF-67, and with a size of ~63 Å for the 34.5 wt. % ZIF-67 NP in the PIM-1 composite.

The equilibration of the so-obtained MOF/polymer composites was accomplished using a 21-step MD decompression-compression method [33] with Pmax equal to 10 kbar employing LAMMPS [34]. The MD simulations were conducted for 1 ns, employing time step of 1 fs and utilizing the Nosé-Hoover thermostat and barostat with relaxation times of 0.1 ps and 1 ps, respectively [35,36]. A 14-Å cut-off was employed for the LJ interactions, with Coulombic contributions evaluated using tail corrections and Ewald summations. As an illustrative example, representative equilibrated atomistic model of the ZIF-67/PIM-1 composite is shown in Figure 4.17.

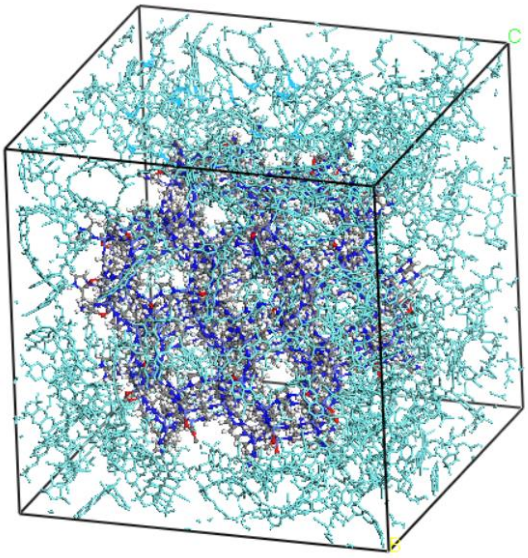

Figure 4.17 : Representative atomistic model for the ZIF-67/ PIM-1 composite with containing 34.5 wt.% ZIF-67 with –C(H_3)O termination. PIM-1 atoms are represented as ball and stick atoms and polymer chains in light blue lines. Color code: O (red), C (grey), H (white), N (blue) and Co (steel blue).

4.3.3 Analysis of the ZIF-67/6FDA-DAM and ZIF-67/PIM-1 MMM interfaces

Figure 4.18a and Figure 4.18b remind the radial atomic density profile of 6FDA-DAM in ZIF-67 composite with water termination, along with representative snapshots already discussed in Chapter 3. Meanwhile, Figure 4.18c and Figure 4.18d present the same set of data for the ZIF-67/6FDA-DAM composites with –C(H_3)O termination. Figure 4.18c reveals that the upper limit of the MOF surface is shifted to a radial value of 12.1 Å. Simultaneously, the radial atomic density of the polymer gradually increases from 9.5 Å to 16.6 Å, resulting in a 7.1 Å interfacial MOF/polymer region length, which is slightly longer than that simulated for the ZIF-67/6FDA-DAM composite with -OH termination. Both interfacial region (blue colored area) and MOF/polymer overlap region (black shaded area) are much longer in the case of ZIF-67/6FDA-DAM composites with –C(H_3)O termination (7.1 Å vs. 5.8 Å and 2.6 Å vs. 0.8 Å respectively) compared to ZIF-67/6FDA-DAM composites with water termination. Figure 4.18b indicates the existence of voids at the MOF/polymer interface, which are associated with micropores up to 6 Å in size. In contrast, Figure 4.18d demonstrates the polymer conform to the pocket created at the MOF surface due to –C(H_3)O termination. Hence, using methanol as a solvent contributes to an improved compatibility

between the MOF and the polymer, allowing for more effective packing of the 6FDA-DAM in the vicinity of the MOF surface.

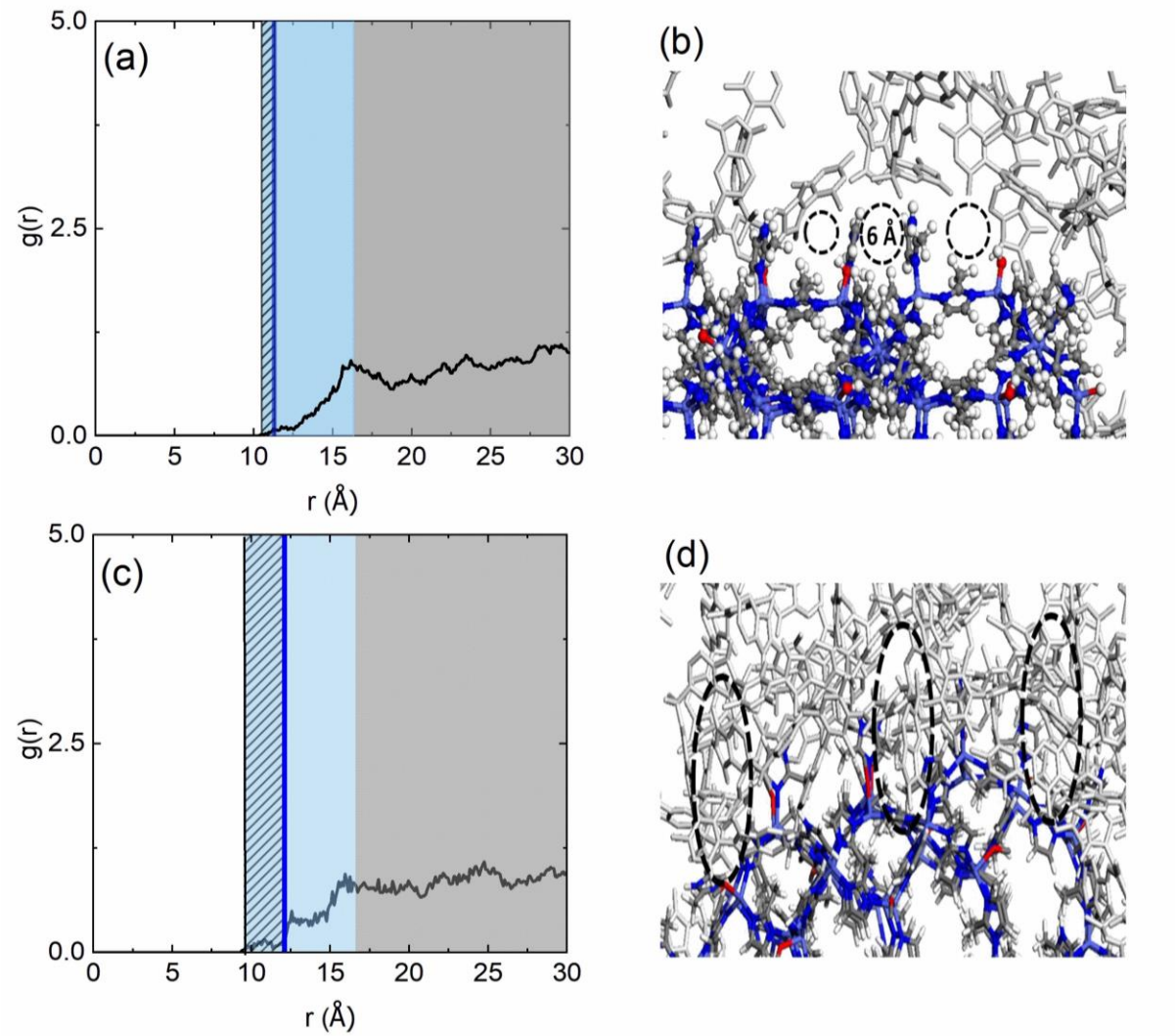

Figure 4.18 : Calculated Radial atomic density distribution of (a) 6FDA-DAM (black) in the ZIF-67/6FDA-DAM composite with –OH termination with respect to the center of the nanoparticle (r = 0), (b) Representative snapshot of the interface of ZIF-67/6FDA-DAM showing the presence of microvoids (c) Radial atomic density distribution of 6FDA-DAM (black) in ZIF-67/6FDA-DAM composite with –C(H_3)O terminations with respect to the center of the nanoparticle (r = 0), (d) Representative snapshot of the interface of ZIF-67/6FDA-DAM with –C(H_3)O terminations where MOF/polymer overlap is marked by a dashed circle. The interfacial MOF/polymer overlap regions are marked by black dashed shaded areas. Color scheme: 6FDA-DAM, grey wireframe; ZIF-67, ball and stick; O, red; C, gray; H, white; Co, blue.

Figure 4.19a displays the RDFs calculated between the oxygen atoms of 6FDA-DAM and the hydrogen atoms of the terminal $–CH_3OH$ and –OH groups of the MOF surfaces with $–C(H_3)O$ and –OH termination in their respective composites. The interfacial MOF/polymer interaction is stronger in ZIF-67/6FDA-DAM with $–C(H_3)O$ terminations, with both shorter associated distance (2.65 Å vs 2.85 Å) and higher intensity of this RDF peak as compared to ZIF-67/6FDA-DAM with –OH termination. Furthermore, similar interactions take place between the CH_3 group of (6FDA-DAM) and the oxygen atom of both methanol and water (characteristic distance of ~3.9 Å) as shown in Figure 4.19b.

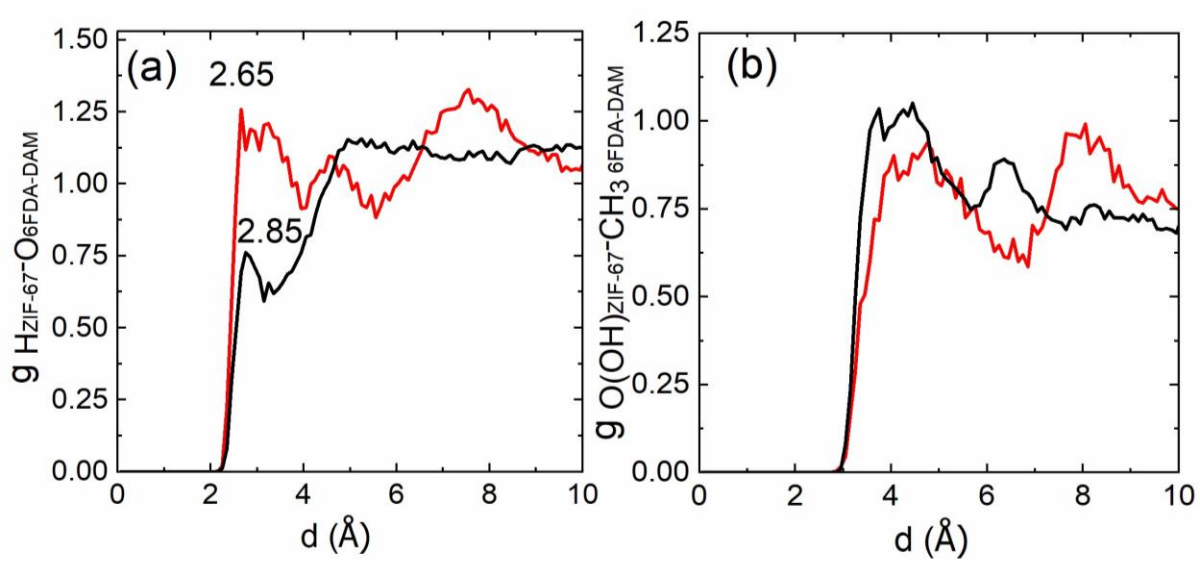

Figure 4.19 : Calculated radial distribution functions in the composites (a) between oxygen atoms of 6FDA-DAM and – H(CH_3O**H**) of the ZIF-67 (red) and –H(O**H**) of the ZIF-67 (black) surface (b) between $–CH_3$ groups of 6FDA-DAM and – O(CH_3**O**H) of the ZIF-67 (red) and –O(**O**H) of the ZIF-67 (black) surface in the corresponding composites.

Figure 4.20 displays the radial atomic density profile of PIM-1 in ZIF-67-based composites with both –OH and $–C(H_3)O$ terminations. The dark blue line representing the upper limit of the ZIF-67 surface, measures at r=11.2 Å and 12.3 Å for PIM-1 with ZIF-67 surfaces terminated by –OH and $–C(H_3)O$, respectively. The termination of the ZIF-67 surface with $–C(H_3)O$ results in an expanded upper limit of the MOF surface due to the presence of the methoxy groups of methanol. The radial atomic density of the polymer exhibits a gradual increase from 9.8 Å to 16.8 Å, leading to an interfacial MOF/polymer region length longer

than that simulated for the pristine ZIF-67/PIM-1 composite (7.0 Å vs. 4.9 Å, respectively). When compared to ZIF-67/PIM-1 with water terminations, a slightly longer MOF/polymer overlap length is observed for ZIF-67/PIM-1 with –C(H_3)O terminations (2.6 Å vs. 1.8 Å). These extended interfacial and overlap lengths follow the same trend observed for the ZIF-67/6FDA-DAM composite, indicating that using methanol as a solvent enhances the compatibility between the MOF and the polymer and promotes more efficient packing of PIM-1 near the MOF surface.

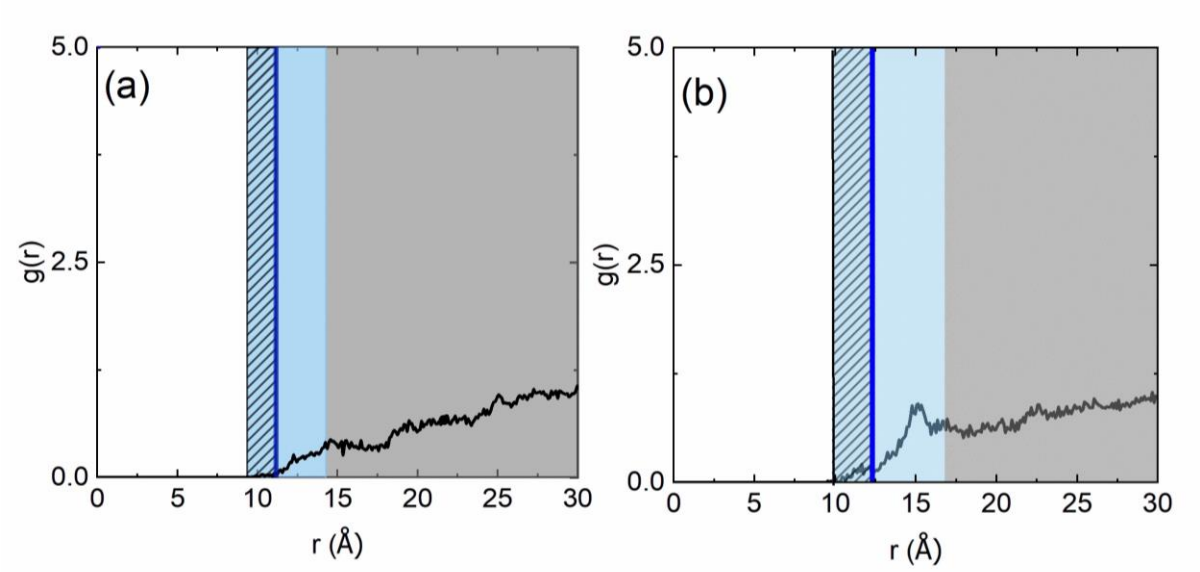

Figure 4.20 : Calculated Radial atomic density distribution of (a) PIM-1 (black) in the ZIF-67/PIM-1 composite with –OH termination with respect to the center of the nanoparticle (r = 0), (b) Radial atomic density distribution of PIM-1 (black) in the ZIF-67/PIM-1 composite with –C(H_3)O termination with respect to the center of the nanoparticle (r = 0), The interfacial MOF/polymer overlap regions are marked by black dashed shaded areas.

Furthermore, when compared to ZIF-67/6FDA-DAM, similar MOF/polymer interfacial and overlap regions (7.0 Å vs. 7.1 Å and 2.5 Å vs. 2.6 Å, respectively) are observed than in the case of ZIF-67/PIM-1 with –C(H_3)O terminations, despite employing a more rigid polymer. In Chapter 3, PIM-1, with its L-shape vertex, was demonstrated to effectively plug into the pocket formed by the "zig-zag" ZIF-67 surface [46], while 6FDA-DAM cannot provide complete coverage on the MOF surface. Here, with –C(H_3)O terminations, 6FDA-DAM can efficiently cover the ZIF-67 surface, as illustrated in Figure 4.21a, while PIM-1 fits into the

pocket created by the "zig-zag" MOF surface, as shown in Figure 4.21b. Interestingly, similar MOF/polymer interfacial and overlap regions were observed.

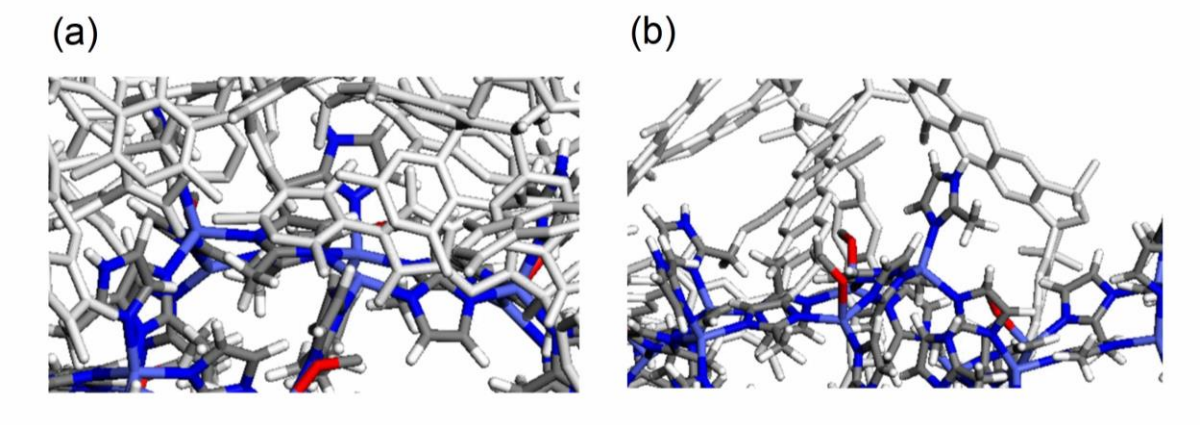

Figure 4.21 : Representative snapshot of the interface of (a) ZIF-67/6FDA-DAM where 6FDA-DAM perfectly covers ZIF-67 surface (b) ZIF-67/PIM-1 where PIM-1 plug into the troughs of MOF surface. Color scheme: 6FDA-DAM and PIM-1, grey wireframe; ZIF-67, wireframe; O, red; C, gray; H, white; Co, blue.

In order to better understand the dynamics of polymer chains at the interface, as opposed to their behavior within the bulk polymer, torsion angle distributions were analyzed in both the ZIF-67/6FDA-DAM and ZIF-67/PIM-1 composites with $–C(H_3)O$ terminations. In the case of ZIF-67/6FDA-DAM, the distributions of the diamine-dianhydride linkage ($\varphi_{C–N–C-C}$) of 6FDA-DAM are presented in Figure 4.22, alongside torsional angle distributions for the –OH terminated composites. The moderate conformational change resulting in a narrower torsional angle distribution for the polymer in the interfacial region can be observed. This change could be attributed to a slightly reduced polymer mobility, leading to an increasing of the polymer rigidity. When compared to the torsional angle distributions of 6FDA-DAM in the –OH terminated composite, a slightly narrower distribution of torsional angles was observed in the $–C(H_3)O$ terminated composite concerning the polymer chains at the interface. Hence, the solvent medium on the MOF surface exerts a significant influence on the dynamics of polymer chains within a short range from the surface.

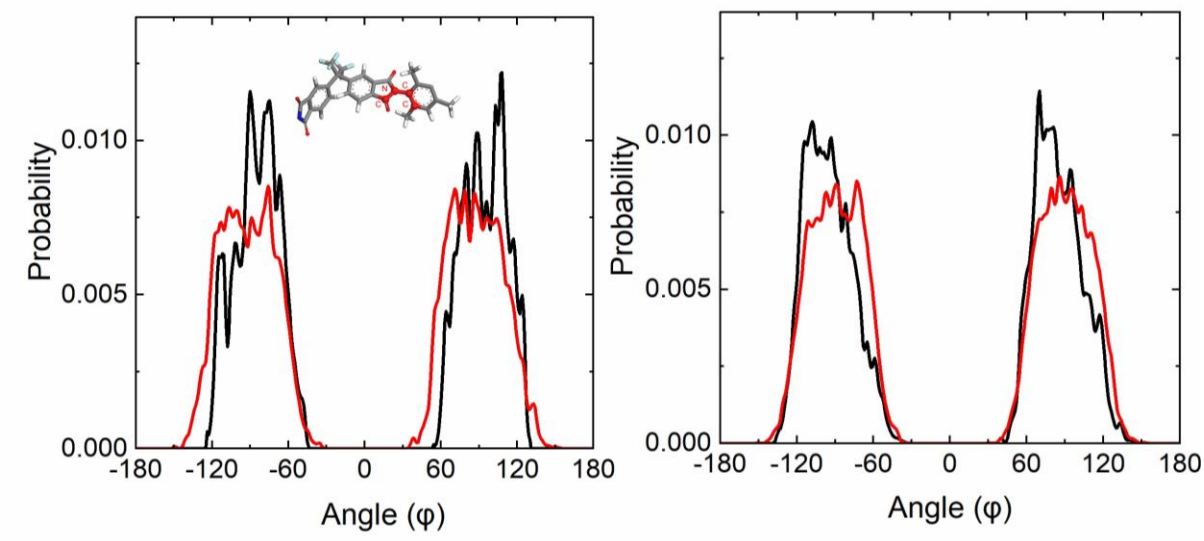

Figure 4.22 : Torsional angle ($\varphi_{C-N-C-C}$) distributions in the 6FDA-DAM for the (a) ZIF-67/6FDA-DAM at the interface (black) and at bulk phase (red) with –C(H_3)O terminated (b) ZIF-67/6FDA-DAM at the interface (black) and at the bulk phase (red) with –OH terminated composites.

The two representative torsional angles $\varphi_{C-C-O-C}$ and $\varphi_{C-C-C-C}$ of PIM-1 in ZIF-67/PIM-1 composite are reported in Figure 4.23. The torsional profiles for $\varphi_{C-C-O-C}$ of PIM-1 in the ZIF-67/PIM-1 composite are nearly identical for the polymer at the interfacial region and the bulk polymer, as observed previously for other functionalized and functionalized composites, indicating a similar polymer planar conformation (Figure 4.23a). However, a slightly different torsional angle distribution for the polymer at the interfacial region compared to the bulk polymer can be observed for the second torsional angle distribution. This observation points to a slight reduction in polymer dynamics at the interfacial region (Figure 4.23b). This information suggests that MOF functionalization enhances the embedding of polymer onto the MOF surface, even though it diminishes the flexibility of the polymer, as demonstrated in Chapter 3 and here for the ZIF-67/PIM-1, ZIF-67-IDip/PIM-1, and ZIF-67-IPD/PIM-1 composites.

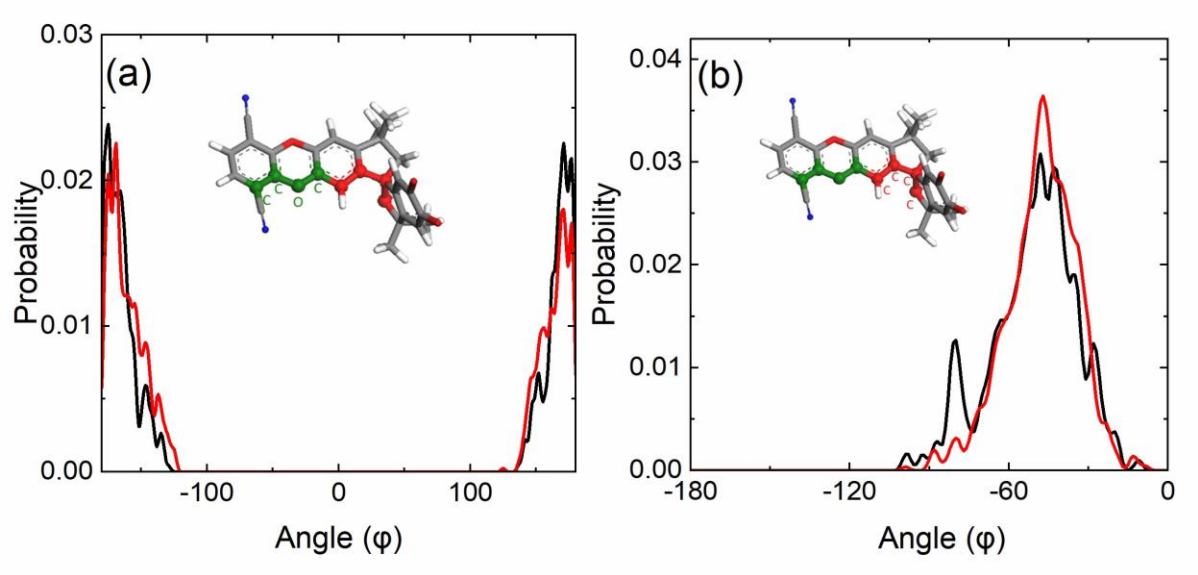

Figure 4.23 : Torsional angle distributions in the PIM-1 for the ZIF-67/PIM-1 composite with –C(H_3)O termination (a) $\varphi_{C-C-O-C}$ angle at the interface (black) and at the bulk phase (red) (b) $\varphi_{C-C-C-C}$ angle at the interface (black) and at the bulk phase (red).

Figure 4.24 reports a summary of the MOF/polymer overlap length and interfacial length between composites with ZIF-67 (–OH terminations), ZIF-67(–C(H_3)O terminations) ZIF-67-IDip and ZIF-67-IPD fillers in 6FDA-DAM and PIM-1 polymer matrices. MOF/polymer compatibility enhanced with MOF surface functionalization with carbene functions or methoxy-group terminations since much longer MOF/polymer overlap or interfacial lengths were obtained in these two scenarios. Hence, for both MOF/6FDA-DAM and MOF/PIM-1, the longest interfacial length is obtained with –C(H_3)O terminations, while longest overlap length is obtained with IPD functionalization.

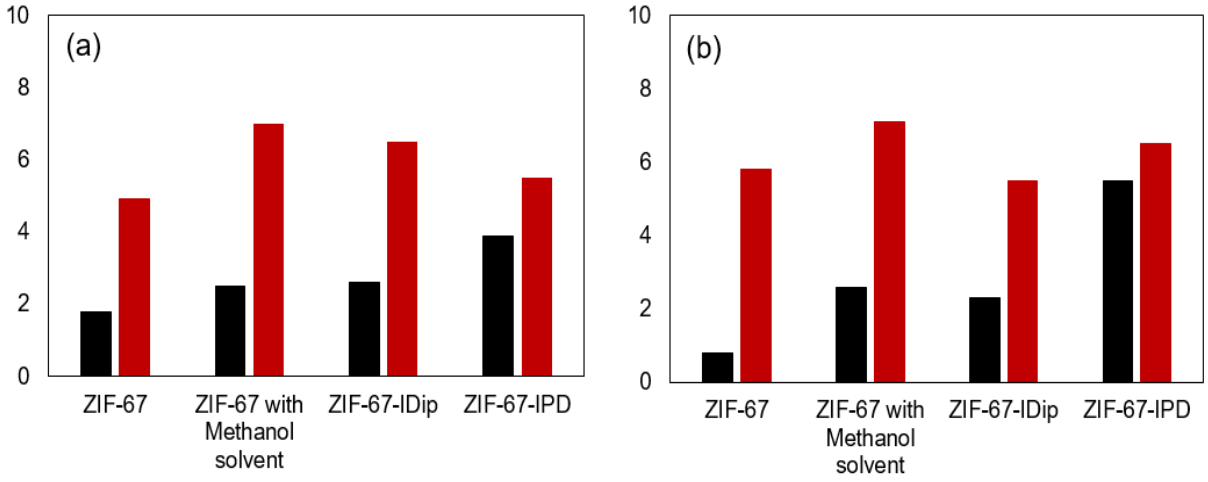

Figure 4.24 : General summary of MOF/polymer overlap (black) and interfacial (red) lengths of composites with ZIF-67 (-OH termination), ZIF-67 (–C(H_3)O termination), ZIF-67-IDip and ZIF-67-IPD fillers in (a) 6FDA-DAM and (b) PIM-1 polymer matrices in bar charts.

Furthermore, evaluation of the interactions between MOF and the polymer through the calculation of binding energies per atoms in the corresponding composites (Figure 4.25), showed that similar higher binding energies were obtained for MOFs with 6FDA-DAM and PIM-1 with –C(H_3)O terminations compared to the systems with water terminations. Hence, employing methanol as the solvent for MOF surface terminations enhances the compatibility between the MOF NP and the polymers.

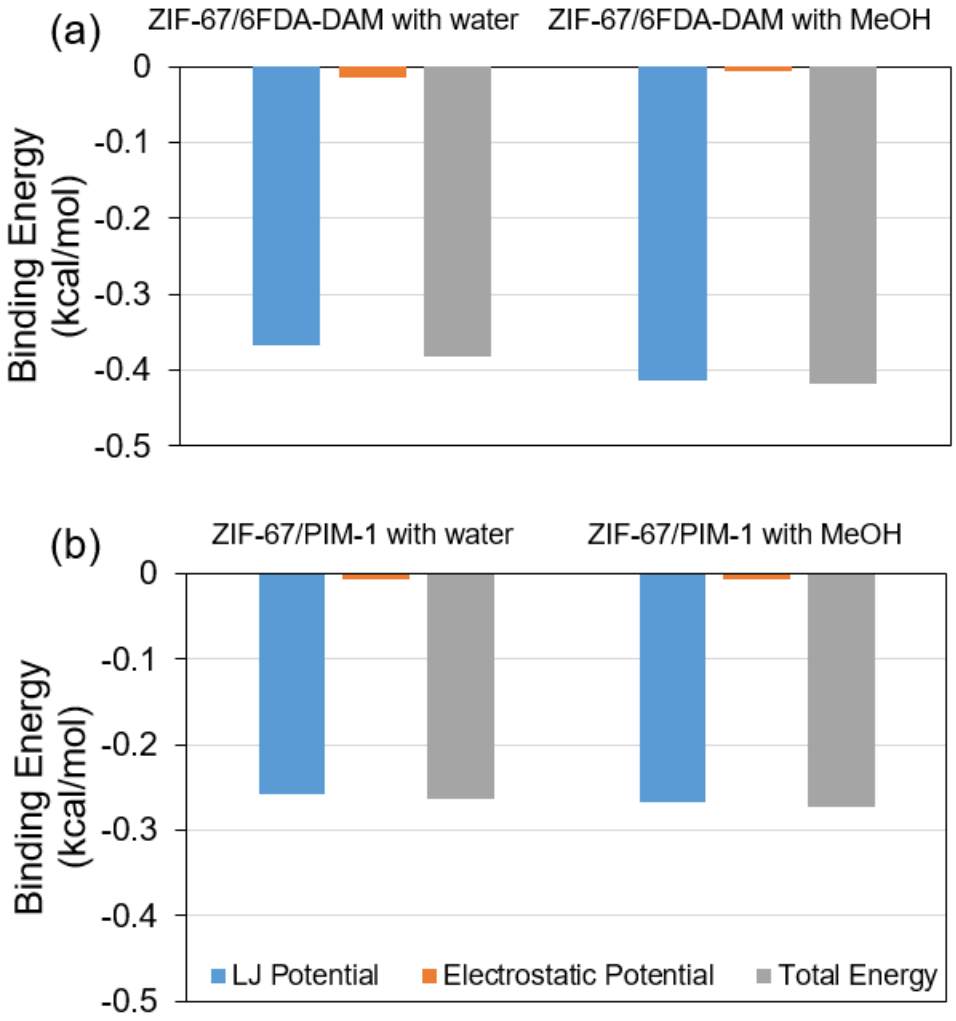

Figure 4.25 : Binding energies per atoms of ZIF-67 with polymers in 34.5 wt. % ZIF-67/6FDA-DAM and 34.5 wt. % ZIF-67/PIM-1 composites with –C(H_3)O (MeOH) and –OH terminations in bar charts.

4.3.4 Adsorption properties of ZIF-67/6FDA-DAM and ZIF-67/PIM-1 MMMs

The single component propane and propylene adsorption isotherms were performed on models for 6FDA-DAM, 34.5 wt. % ZIF-67/6FDA-DAM composites with –OH and –C(H_3)O terminations at 308 K up to 8 bar (Figure 4.26). The solvent medium does not substantially influence the sorption isotherms in terms of shape and amount adsorbed. Figure 4.27 evaluates how the nature of the polymer affects the sorption isotherms for propane and

propylene for the ZIF-67 based composites terminated with $–C(H_3)O$ groups. Compared to the 34.5 wt. % ZIF-67/6FDA-DAM composite, 34.5 wt. % ZIF-67/PIM-1 composite displayed higher propane and propylene uptakes due to the fact that PIM-1 is more porous than 6FDA-DAM.

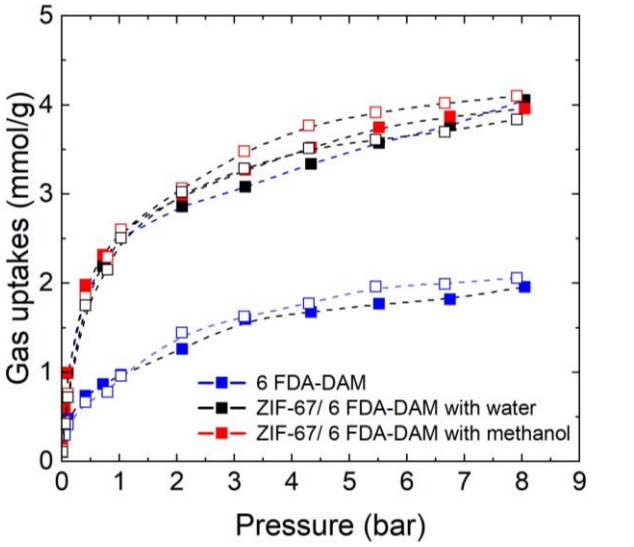

Figure 4.26 : Simulated propane (solid symbols) and propylene (open symbols) sorption isotherms for the composites. 34.5 wt. % ZIF-67/6FDA-DAM (black) with –OH terminations and ZIF-67/6FDA-DAM (red) with $–C(H_3)O$ terminations at 308 K up to 8 bar and comparison with pure 6FDA-DAM (blue).

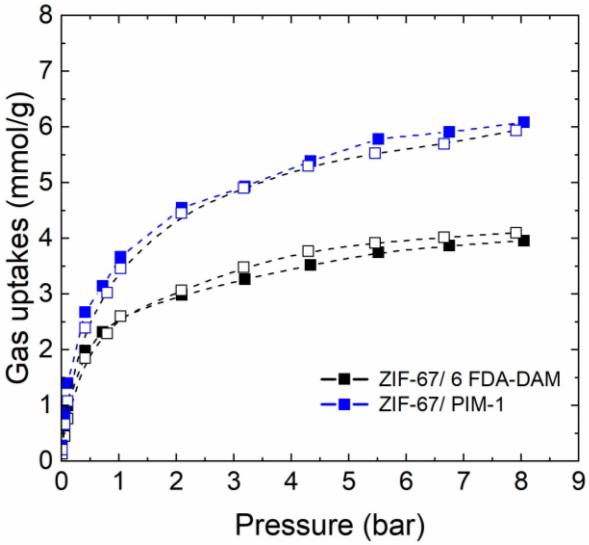

Figure 4.27 : Simulated propane (solid symbols) and propylene (open symbols) sorption isotherms for the composites. 34.5 wt. % ZIF-67/6FDA-DAM (black) and ZIF-67/PIM-1 (blue) with $–C(H_3)O$ terminations at 308 K up to 8 bar.

4.4 Conclusion

In summary, microscopic models for the composites of IPD functionalized ZIF-67 combined with 6FDA-DAM and PIM-1 as well of the unfunctionalized ZIF-67 composites with different terminal solvent functions, were constructed and analyzed with the computational strategy validated in Chapter 3. The existence of two polar sites in IPD plays a role in improving the compatibility between the MOF surface and the 6FDA-DAM polymer by facilitating a more efficient packing of the polymer in the vicinity of the MOF surface. In the case of ZIF-67-IPD/PIM-1, this composite is characterized by a lower compatibility with a reduced overlap and interfacial length as compared to ZIF-67-IPD/6FDA-DAM This is attributed to the fact that the more rigid PIM-1 cannot penetrate the pocket of the ZIF67-IPD surface, unlike the case with ZIF-67-IDip/PIM-1. On the other hand, employing methanol as the solvent to tune the MOF surface termination leads to enhanced compatibility between the MOF surface and 6FDA-DAM, allowing this polymer to effectively cover the ZIF-67 surface, while PIM-1 fits into the pockets created by the "zig-zag" shape of the MOF surface terminated by methoxy-groups. Further, we revealed that tuning the terminal groups by changing the nature of the solvent does not substantially change the single component sorption properties of the composites. The next step is a detailed analysis of the kinetics of propylene/propane in these composites, including the examination of free energy profiles, as presented in Chapter 5.

REFERENCES

[1] H. Zhu, L. Wang, X. Jie, D. Liu, Y. Cao, Improved Interfacial Affinity and CO2 Separation Performance of Asymmetric Mixed Matrix Membranes by Incorporating Postmodified MIL-53(Al), ACS Appl. Mater. Interfaces. 8 (2016) 22696–22704. https://doi.org/10.1021/acsami.6b07686.

[2] M. Kalaj, S.M. Cohen, Postsynthetic Modification: An Enabling Technology for the Advancement of Metal-Organic Frameworks, ACS Cent. Sci. 6 (2020) 1046–1057. https://doi.org/10.1021/acscentsci.0c00690.

[3] B. Liu, D. Li, J. Yao, H. Sun, Improved CO2 separation performance and interfacial

affinity of mixed matrix membrane by incorporating UiO-66-PEI@[bmim][Tf2N] particles, Sep. Purif. Technol. 239 (2020) 116519. https://doi.org/10.1016/j.seppur.2020.116519.

[4] S. Japip, Y. Xiao, T.S. Chung, Particle-Size Effects on Gas Transport Properties of 6FDA-Durene/ZIF-71 Mixed Matrix Membranes, Ind. Eng. Chem. Res. 55 (2016) 9507–9517. https://doi.org/10.1021/acs.iecr.6b02811.

[5] K.G. Liu, F. Bigdeli, A. Panjehpour, S. Hwa Jhung, H.A.J. Al Lawati, A. Morsali, Potential applications of MOF composites as selective membranes for separation of gases, Coord. Chem. Rev. 496 (2023) 215413. https://doi.org/10.1016/j.ccr.2023.215413.

[6] S. Shahid, K. Nijmeijer, S. Nehache, I. Vankelecom, A. Deratani, D. Quemener, MOF-mixed matrix membranes: Precise dispersion of MOF particles with better compatibility via a particle fusion approach for enhanced gas separation properties, J. Memb. Sci. 492 (2015) 21–31. https://doi.org/10.1016/j.memsci.2015.05.015.

[7] W. Chen, Z. Zhang, C. Yang, J. Liu, H. Shen, K. Yang, Z. Wang, PIM-based mixed-matrix membranes containing MOF-801/ionic liquid nanocomposites for enhanced CO2 separation performance, J. Memb. Sci. 636 (2021) 119581. https://doi.org/10.1016/j.memsci.2021.119581.

[8] Y. Shi, S. Wu, Z. Wang, X. Bi, M. Huang, Y. Zhang, J. Jin, Mixed matrix membranes with highly dispersed MOF nanoparticles for improved gas separation, Sep. Purif. Technol. 277 (2021) 119449. https://doi.org/10.1016/j.seppur.2021.119449.

[9] C. Jiao, Z. Li, X. Li, M. Wu, H. Jiang, Improved CO2/N2 separation performance of Pebax composite membrane containing polyethyleneimine functionalized ZIF-8, Sep. Purif. Technol. 259 (2021) 118190. https://doi.org/10.1016/j.seppur.2020.118190.

[10] S. Wang, W. Morris, Y. Liu, C.M. McGuirk, Y. Zhou, J.T. Hupp, O.K. Farha, C.A. Mirkin, Surface-specific functionalization of nanoscale metal-organic frameworks, Angew. Chemie - Int. Ed. 54 (2015) 14738–14742. https://doi.org/10.1002/anie.201506888.

[11] A. Knebel, A. Bavykina, S.J. Datta, L. Sundermann, L. Garzon-Tovar, Y. Lebedev, S. Durini, R. Ahmad, S.M. Kozlov, G. Shterk, M. Karunakaran, I.D. Carja, D. Simic, I. Weilert, M. Klüppel, U. Giese, L. Cavallo, M. Rueping, M. Eddaoudi, J. Caro, J. Gascon, Solution processable metal–organic frameworks for mixed matrix membranes using porous liquids, Nat. Mater. 19 (2020) 1346–1353. https://doi.org/10.1038/s41563-020-0764-y.

[12] A.A. Tezerjani, R. Halladj, S. Askari, Different view of solvent effect on the synthesis methods of zeolitic imidazolate framework-8 to tuning the crystal structure and properties, RSC Adv. 11 (2021) 19914–19923. https://doi.org/10.1039/d1ra02856a.

[13] B. Chen, F. Bai, Y. Zhu, Y. Xia, A cost-effective method for the synthesis of zeolitic imidazolate framework-8 materials from stoichiometric precursors via aqueous

ammonia modulation at room temperature, Microporous Mesoporous Mater. 193 (2014) 7–14. https://doi.org/10.1016/j.micromeso.2014.03.006.

[14] B. Zhang, J. Zhang, C. Liu, X. Sang, L. Peng, X. Ma, T. Wu, B. Han, G. Yang, Solvent determines the formation and properties of metal-organic frameworks, RSC Adv. 5 (2015) 37691–37696. https://doi.org/10.1039/c5ra02440d.

[15] N. Keser Demir, B. Topuz, L. Yilmaz, H. Kalipcilar, Synthesis of ZIF-8 from recycled mother liquors, Microporous Mesoporous Mater. 198 (2014) 291–300. https://doi.org/10.1016/j.micromeso.2014.07.052.

[16] Y. Pan, D. Heryadi, F. Zhou, L. Zhao, G. Lestari, H. Su, Z. Lai, Tuning the crystal morphology and size of zeolitic imidazolate framework-8 in aqueous solution by surfactants, CrystEngComm. 13 (2011) 6937–6940. https://doi.org/10.1039/c1ce05780d.

[17] Y.R. Lee, M.S. Jang, H.Y. Cho, H.J. Kwon, S. Kim, W.S. Ahn, ZIF-8: A comparison of synthesis methods, Chem. Eng. J. 271 (2015) 276–280. https://doi.org/10.1016/j.cej.2015.02.094.

[18] Y. Pan, Y. Liu, G. Zeng, L. Zhao, Z. Lai, Rapid synthesis of zeolitic imidazolate framework-8 (ZIF-8) nanocrystals in an aqueous system, ChemComm. 47 (2011) 2071–2073. https://doi.org/10.1039/c0cc05002d.

[19] J. Gascon, S. Aguado, F. Kapteijn, Manufacture of dense coatings of Cu3(BTC)2 (HKUST-1) on α-alumina, Microporous Mesoporous Mater. 113 (2008) 132–138. https://doi.org/10.1016/j.micromeso.2007.11.014.

[20] O.M. Yaghi, G. Li, H. Li, Selective binding and removal of guests in a microporous metal–organic framework, Nature. 378 (1995) 703–706. https://doi.org/https://doi.org/10.1038/378703a0.

[21] E.L. Bustamante, J.L. Fernández, J.M. Zamaro, Influence of the solvent in the synthesis of zeolitic imidazolate framework-8 (ZIF-8) nanocrystals at room temperature, J. Colloid Interface Sci. 424 (2014) 37–43. https://doi.org/10.1016/j.jcis.2014.03.014.

[22] A. Schejn, L. Balan, V. Falk, L. Aranda, G. Medjahdi, R. Schneider, Controlling ZIF-8 nano- and microcrystal formation and reactivity through zinc salt variations, CrystEngComm. 16 (2014) 4493–4500. https://doi.org/10.1039/c3ce42485e.

[23] X. Yang, T. Song, T. Su, J. Hu, S. Wu, Exploring the Influence of the Reused Methanol Solution for the Structure and Properties of the Synthesized ZIF-8, Processes. 10 (2022) 1705.

[24] J. Cravillon, S. Münzer, S.J. Lohmeier, A. Feldhoff, K. Huber, M. Wiebcke, Rapid room-temperature synthesis and characterization of nanocrystals of a prototypical zeolitic imidazolate framework, Chem. Mater. 21 (2009) 1410–1412. https://doi.org/10.1021/cm900166h.

[25] J. Cravillon, R. Nayuk, S. Springer, A. Feldhoff, K. Huber, M. Wiebcke, Controlling zeolitic imidazolate framework nano- and microcrystal formation: Insight into crystal growth by time-resolved in situ static light scattering, Chem. Mater. 23 (2011) 2130–2141. https://doi.org/10.1021/cm103571y.

[26] H. Bux, F. Liang, Y. Li, J. Cravillon, M. Wiebcke, J. Caro, Zeolitic Imidazolate Framework Membrane with Molecular Sieving Properties by Microwave-Assisted Solvothermal Synthesis Helge, Chem. Mater. 131 (2009) 16000–16001. https://doi.org/10.1021/cm902032y.

[27] F. Tian, A.M. Cerro, A.M. Mosier, H.K. Wayment-Steele, R.S. Shine, A. Park, E.R. Webster, L.E. Johnson, M.S. Johal, L. Benz, Surface and stability characterization of a nanoporous ZIF-8 thin film, J. Phys. Chem. C. 118 (2014) 14449–14456. https://doi.org/10.1021/jp5041053.

[28] C. Chizallet, S. Lazare, D. Bazer-bachi, F. Bonnier, V. Lecocq, E. Soyer, A. Quoineaud, N. Bats, Catalysis of Transesterification by a Nonfunctionalized Metal - Organic Framework : Acido-Basicity at the External Surface of ZIF-8 Probed by FTIR and ab Initio Calculations, J. Am. Chem. Soc. 132 (2010) 12365–12377.

[29] R. Semino, N.A. Ramsahye, A. Ghoufi, G. Maurin, Microscopic Model of the Metal-Organic Framework/Polymer Interface: A First Step toward Understanding the Compatibility in Mixed Matrix Membranes, ACS Appl. Mater. Interfaces. 8 (2016) 809–819. https://doi.org/10.1021/acsami.5b10150.

[30] M.J. Frisch, G.W. Trucks, H.B. Schlegel, G.E. Scuseria, M.A. Robb, J.R. Cheeseman, G. Scalmani, V. Barone, G.A. Petersson, H. Nakatsuji, X. Li, M. Caricato, A. V. Marenich, J. Bloino, B.G. Janesko, R. Gomperts, B. Mennucci, H.P. Hratchian, J. V. Ortiz, D. Izmaylov, A. F. Sonnenberg, J. L. Williams-Young, F. Ding, F. Lipparini, F. Egidi, J. Goings, B. Peng, A. Petrone, V.G. Henderson, T. Ranasinghe, D. Zakrzewski, J. Gao, N. Rega, G. Zheng, W. Liang, M. Hada, M. Ehara, K. Toyota, R. Fukuda, J. Hasegawa, M. Ishida, T. Nakajima, Y. Honda, O. Kitao, H. Nakai, T. Vreven, J.E. Throssell, K. Montgomery, J. A., Jr. Peralta, F. Ogliaro, M.J. Bearpark, J.J. Heyd, E.N. Brothers, K.N. Kudin, V.N. Staroverov, T.A. Keith, R. Kobayashi, A.P. Normand, J. Raghavachari, K.; Rendell, J.C. Burant, S.S. Iyengar, J. Tomasi, M. Cossi, J.M. Millam, M. Klene, C. Adamo, R. Cammi, J.W. Ochterski, R.L. Martin, K. Morokuma, O. Farkas, J.B. Foresman, D.J. Fox, Gaussian 09, Revision E.01, (2009).

[31] J. Wang, R.M. Wolf, J.W. Caldwell, P.A. Kollman, D.A. Case, Development and Testing of a General Amber Force Field, J. Comput. Chem. 56531 (2004) 1157–1174.

[32] P. Krokidas, M. Castier, S. Moncho, D.N. Sredojevic, E.N. Brothers, H.T. Kwon, H.K. Jeong, J.S. Lee, I.G. Economou, ZIF-67 Framework: A Promising New Candidate for Propylene/Propane Separation. Experimental Data and Molecular Simulations, J. Phys. Chem. C. 120 (2016) 8116–8124. https://doi.org/10.1021/acs.jpcc.6b00305.

[33] G.S. Larsen, P. Lin, K.E. Hart, C.M. Colina, Molecular simulations of pim-1-like polymers of intrinsic microporosity, Macromolecules. 44 (2011) 6944–6951.

https://doi.org/10.1021/ma200345v.

[34] S. Plimpton, Fast Parallel Algorithms for Short-Range Molecular Dynamics, J. Comput. Phys. 117 (1995) 1–19. https://doi.org/10.1039/c7sm02429k.

[35] S. Nosé, A unified formulation of the constant temperature molecular dynamics methods, J. Chem. Phys. 81 (1984) 511–519. https://doi.org/10.1063/1.447334.

[36] W.G. Hoover, Canonical dynamics: equilibrium phase-space distributions, 31 (1985) 1695–1697.

[37] R. Semino, J.P. Durholt, R. Schmid, G. Marin, Multiscale modeling of the HKUST-1/polyvinyl alcohol) interface: From an atomistic to a coarse graining approach, J. Phys. Chem. C. 121 (2017) 21491–21496. https://doi.org/10.1021/acs.jpcc.7b07090.

[38] M. Benzaqui, R. Semino, N. Menguy, F. Carn, T. Kundu, J.M. Guigner, N.B. McKeown, K.J. Msayib, M. Carta, R. Malpass-Evans, C. Le Guillouzer, G. Clet, N.A. Ramsahye, C. Serre, G. Maurin, N. Steunou, Toward an Understanding of the Microstructure and Interfacial Properties of PIMs/ZIF-8 Mixed Matrix Membranes, ACS Appl. Mater. Interfaces. 8 (2016) 27311–27321. https://doi.org/10.1021/acsami.6b08954.

[39] R. Semino, N.A. Ramsahye, A. Ghoufi, G. Maurin, Role of MOF surface defects on the microscopic structure of MOF/polymer interfaces: A computational study of the ZIF-8/PIMs systems, Microporous Mesoporous Mater. 254 (2017) 184–191. https://doi.org/10.1016/j.micromeso.2017.02.031.

[40] M.Z. Ahmad, M. Navarro, M. Lhotka, B. Zornoza, C. Téllez, W.M. de Vos, N.E. Benes, N.M. Konnertz, T. Visser, R. Semino, G. Maurin, V. Fila, J. Coronas, Enhanced gas separation performance of 6FDA-DAM based mixed matrix membranes by incorporating MOF UiO-66 and its derivatives, J. Memb. Sci. 558 (2018) 64–77. https://doi.org/10.1016/j.memsci.2018.04.040.

[41] C.M. Breneman, K.B. Wiberg, Determining Atom-Centered Monopoles from Molecular Electrostatic Potentials . The Need for High Sampling Density in Formamide Conformational Analysis, J. Comput. Chem. 11 (1990) 361–373.

[42] M.G. Martin, J.I. Siepmann, Transferable potentials for phase equilibria. 1. United-atom description of n-alkanes, J. Phys. Chem. B. 102 (1998) 2569–2577. https://doi.org/10.1021/jp972543+.

CHAPTER 5

ASSESSMENT OF THE ENERGY BARRIERS FOR PROPYLENE/PROPANE TO CROSS THE WINDOWS

5.1 Introduction

In the previous chapters, several atomistic models of ZIF-67/polymer composites were constructed and evaluated, focusing on their thermodynamic separation properties when exposed to propane/propylene mixtures. The simulation results have consistently indicated that these composites do not exhibit favorable thermodynamic separability.

The subtle differences in size and shape between propane and propene pose a challenge when attempting to separate them through a sieving mechanism [1]. ZIFs are recognized for their flexibility, allowing molecules with larger critical diameters than the pore window to diffuse into their pores [2]. Although the aperture size of ZIF-67 is 3.3 Å, the flipping motion of the ligand under pressure or in the presence of guest molecules enables the adsorption of larger molecules, such as propane (kinetic diameter: 4.16 Å) and propylene (kinetic diameter: 4.03 Å), within the structure [3].

Recent experiments focusing on the industrially significant propylene/propane separation have demonstrated a preferential diffusion of propylene over propane through ZIF-8, owing to its slightly smaller effective diameter [4–9]. Experimental studies using membranes have revealed that while both gases display similar sorption affinities within ZIF-8, their diffusion rates differ significantly by two orders of magnitude. This observation highlights a promising diffusion-driven selectivity [7,10]. Due to its slightly smaller kinetic diameter in comparison to propane, propylene exhibits greater ease in passing through the aperture, resulting in significantly faster diffusion when compared to propane. Kwon et al. showed that the stiffer Co-N bond in ZIF-67 makes it more efficient for separating C_3H_6/C_3H_8 in comparison to ZIF-8 [11]. Krokidas et al. further validated the higher efficiency of ZIF-67 for C_3H_6/C_3H_8 separation through their custom developed force fields and subsequent molecular dynamics simulations [12]. The diffusion results demonstrated a distinct correlation between kinetic-driven separation and the flexibility of the various framework apertures. Further, Verploegh et al. examined the self-diffusivity of 15 different adsorbed molecules in ZIF-8 under infinite

dilution conditions using transition-state theory methods, while considering the effects of temperature and loading. Their molecular simulation results exhibited good agreement with experimental findings [13].

Herein in this chapter, the energy barriers associated with the crossing of the pore entrance by propylene and propane for ZIF-67 and its derivatives were explored. For this purpose, MD simulations were carried out to perform potential of mean force (PMF) calculations [14] to achieve accurate calculation of the free energy profile along the reaction coordinate through umbrella sampling technique [15,16]. The obtained results, helps the understanding of the sieving mechanism as a function of the penetrant size and of the MOF aperture size and flexibility.

5.2 Free Energy Profiles for Propylene/Propane in ZIF-67

PMF simulations were performed for propane and propylene, in the modelled ZIF-67 NP presented in the previous chapters, to obtain the free energy profile along a specific Reaction Coordinate (RC). The umbrella sampling was chosen as biased sampling method. In the implementation of umbrella sampling, propane and propylene molecules were individually positioned at a moderate distance of the cage center and pulled from the gate center until they exceeded the last atom of the ZIF-67 NP, moving along nearly 3.5 Å outside of the cage. More specifically, the origin point (r = 0 Å, z = 0 Å) was positioned close to the gate center of ZIF-67. This arrangement ensured that the entrance and exit points for the molecules were positioned near the z = 0 Å and z = 5 Å locations, respectively. Figure 5.1 shows a representation of how umbrella sampling was performed in the simulations.

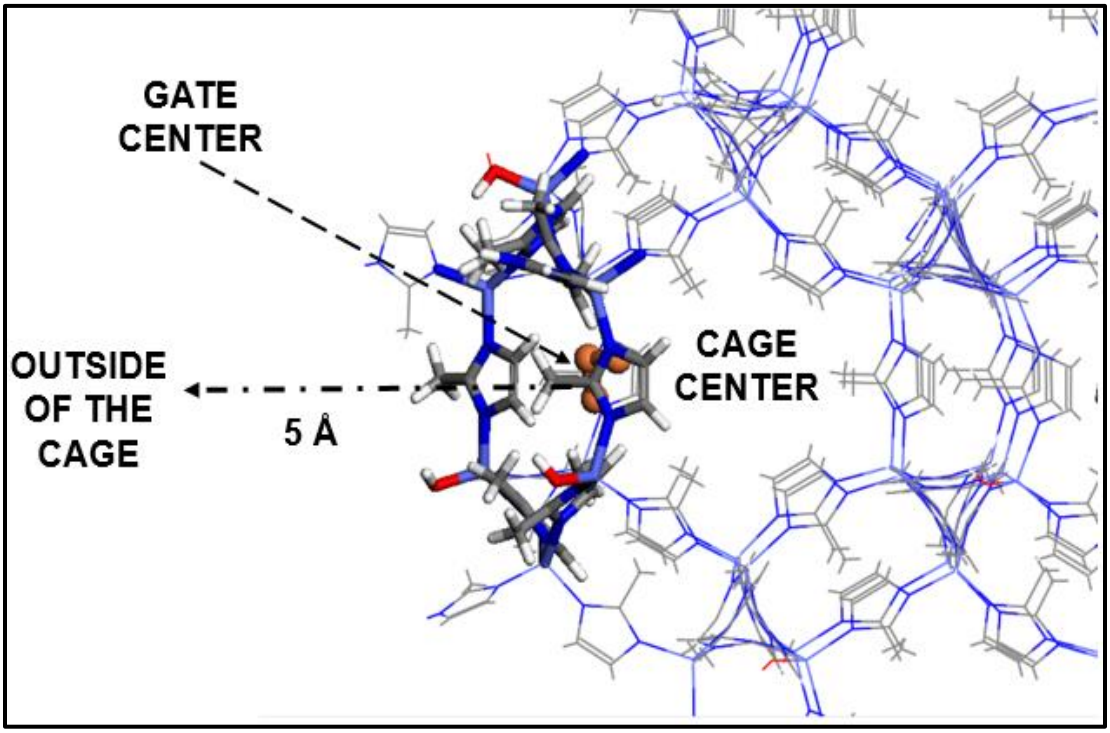

Figure 5.1 : Schematic representation of the computational procedure applied to ZIF-67 NP.

NVT-MD runs were executed using the LAMMPS simulation package [17]. It should be noted that, during this study both MOF framework and guests are treated with flexible force field [4]. Most flexible MOF models are quite responsive to changes in pressure, often exhibiting a tendency to shrink or even collapse the framework during NPT simulations, despite their generally satisfactory performance in NVT calculations. For this reason, the NVT statistical ensemble was chosen for the MD simulations in line with previous computational studies [18]. The velocity-Verlet integration algorithm with a 1 fs time step was employed. In NVT simulations, a Nose−Hoover thermostat was used with a temperature damping parameter of 100.0 fs. The van der Waals interactions were modeled using the Lennard Jones 12−6 potential, and electrostatic interactions were computed using the particle−particle particle−mesh (PPPM) Ewald summation method, with a cutoff of 14.0 Å for both interactions. The NVT-MD were carried out at 308 K.

The umbrella sampling calculations were conducted using the collective variables (colvars) package [19] integrated into LAMMPS. The collective variable chosen here is the axial component of the displacement of either propane or propylene. In umbrella sampling, the

guest is confined to a three-dimensional region along the reaction coordinate using a spring. A spring constant of K_r = 0.2 kcal·mol^{-1} ·Å^{-2} was applied to maintain the guest near r = 0 Å. simultaneously, a second force constant of K_z = 2 kcal·mol^{-1} ·Å^{-2} was applied to pull the guest to the desired position. The spring constant must be carefully selected to ensure overlapping umbrellas, as using inappropriate values can lead to erroneous energy profiles. The path was divided into 15 umbrella sampling windows, each with 0.325 Å width and a harmonic biasing potential (U) in the form of

$$U = \frac{1}{2} K_r(r - r_i)^2 + \frac{1}{2} K_z(z - z_i)^2 \tag{5.1}$$

where the guests were guided to sample around the neutral position (r_i, z_i) was applied following the method carried out by Güvensoy-Morkoyun [20] and Verploegh [13].

For each umbrella sampling window, a NVT-MD simulation was conducted for 600 ps. The first 100 ps are designated for equilibration and are excluded from the subsequent calculations. The remaining 500 ps are used for the production period of each umbrella sampling. For each system and guest, an NVT-MD simulation for umbrella sampling is conducted over a duration of 10 ns. Then, the weighted histogram analysis method (WHAM) is employed, utilizing the code developed by Grossfield, to combine the data from the different umbrella sampling simulations into a free energy profile [21]. Hence, this method is employed to analyze the collection of umbrella samplings and derive PMF profiles.

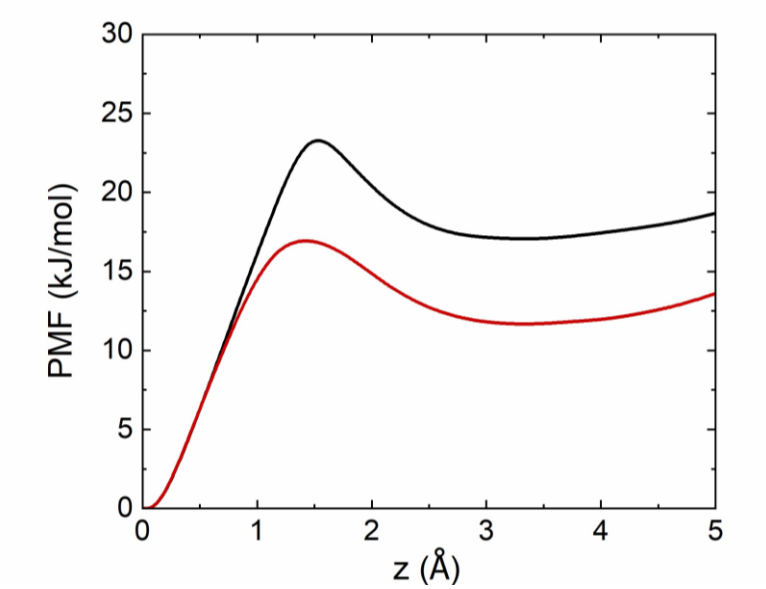

Figure 5.2 : Calculated free energy profile for propane (black line) and propylene (red line) molecules plotted as a function of the distance from the aperture center to the ouside of the cage for ZIF-67 NP.

The PMF calculations reveal free energy profiles for propane and propylene positioned near the gate center of ZIF-67, helping us to understand the energy barriers encountered by guests as they exit the ZIF-67 structure. In Figure 5.2, RC values of 0 and 5 Å represent the center of the gate and the outermost region of the cage, respectively. As shown in the figure, the free energy sharply increases for both guests, resulting in a maximum around 1.5 Å. Subsequently, it decreases to certain energy levels, signifying the weakling of the interaction between the imidazolate linkers and the guests. A relatively higher energy barrier is observed for propane (25 kJ/mol) compared to propylene (17 kJ/mol) Propane exhibits more restricted motion than propylene; therefore, the propane molecules have to overcome a higher energy penalty to enable to diffuse in ZIF-67. Despite their minimal size differences, the energy barriers for the passage of propane and propylene through the pore openings can vary significantly. According to a high-throughput screening study reported by Pramudya and co-workers [1] on MOFs for propane and propylene separation using force-field-based and DFT calculations, the energy barriers for propane were found to be 10 kJ/mol higher than that for propylene. Indeed, they demonstrated that, for a MOF to be effective for the kinetically driven propylene/propane separation, the computed diffusion energy barrier for propane should exceed 35 kJ/mol, whereas for propylene, it should be at least 10 kJ/mol lower than

that for propane to facilitate propylene diffusion [1]. In line with their findings, an energy barrier difference of 8 kJ/mol-energy was found here, which supports that ZIF-67 is effective for a kinetics-driven propylene/propane separation at low pressure.

The flexibility of the aperture is directly linked to the separation efficiency of the framework, as the size and flexibility of the aperture play a crucial role in governing gas permeation and resulting diffusivity. In order to enhance the separation mechanism via a higher energy barrier difference, it is possible to modify the rigidity of ZIF-67 by selectively preserving the rigidity of certain Co-N bonds within the ZIF-67 NP. As the work by Kwon et al. [22] pointed out that the separation enhancement in ZIF-67 is a result of the restricted ligand flipping motion in ZIF-67, which governs the aperture stiffness and the gate fluctuation and opening via Co-N bonds. Further work by Krokidas et al. [23] highlighted that altering the rigidity of metal bonds in the ZIF structures, leads to a reduction in aperture size smaller and stiffer, while the molecule size becomes larger. This interplay between the gas penetrant and the aperture results in an increased energy barrier, leading to a subsequent drop in diffusivity. Hence, another approach of modifying the rigidity of ZIF-67 by selectively preserving the rigidity of certain Co-N bonds within the ZIF-67 NP, considered to facilitate propylene diffusion more effectively. In the second approach, there is a sharp increase in the free energy, leading to energy barriers occurring around 1.46 Å for propylene and ~ 2.11 Å for propane. The diffusion barriers for ZIF-67 are 34.5 kJ/mol for propane and 18.5 kJ/mol for propene, with a difference of more than 10 kJ/mol in energy. This extended distance for propane, as well as the higher energy barrier, could be attributed to the more restricted motion of propane along with the rigidity of the Co-N bonds within the ZIF-67 NP.

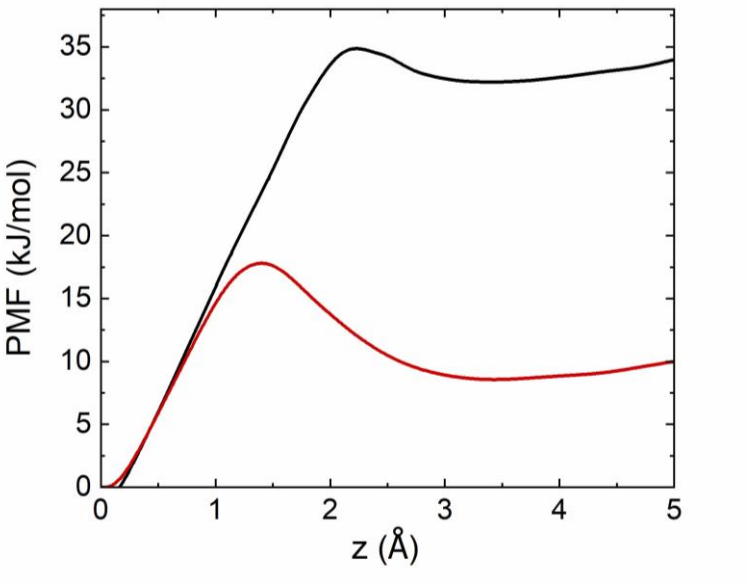

Figure 5.3 : Calculated free energy profile for propane (black line) and propylene (red line) molecules as a function of the distance from the aperture center to the ouside of the cage for ZIF-67 NP along with selectively preserving the rigidity of specific Co-N bonds within the ZIF-67 NP.

Further analysis to understand the separation mechanism of the propylene/propane, the aperture behavior of the ZIF-67 was investigated using MD simulations. The NVT-MD simulations were carried out for 10 ns with a time step of 1 fs using Nosé-Hoover thermostat with relaxation times of 0.1 ps and 1 ps, respectively. The aperture diameter is estimated by measuring the average values of distances between two hydrogen atoms, specifically r_1, r_2 *and* r_3 values as represented in Figure 5.4. In this case, a more accurate approach is to estimate the effective diameter by considering the van der Waals radius of hydrogen atoms. Therefore, the effective diameter is calculated by subtracting the van der Waals radius of hydrogen atoms from the geometric diameter, which in this case is estimated to be 2.4 Å. A value of 1.2 Å for the vdw radius, is a commonly choice in the literature [4]. Hence, time-averaged aperture values were evaluated via calculating the effective diameters (Figure 5.5).

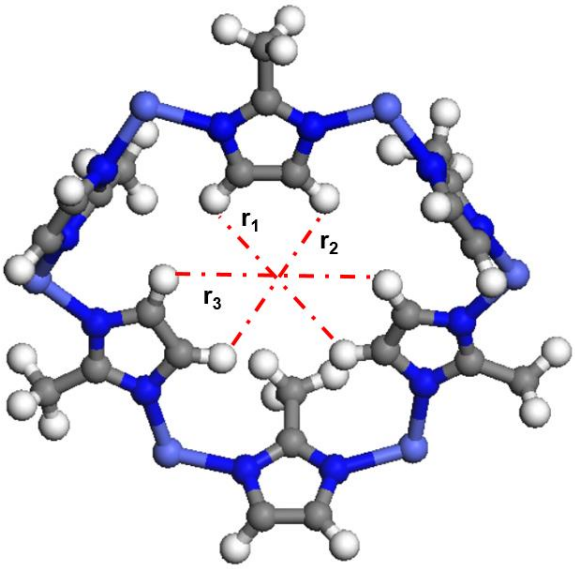

Figure 5.4 : Aperture size calculation of ZIF-67 obtaining from the mean values of distances of r_1 , r_2 and r_3 (red dashed lines).

Figure 5.5 shows the changes in the windows size distribution of the ZIF-67 NP cage once increasing the temperature. It is evident that the framework aperture exhibits fluctuation resembling a swelling-like motion of the MOF windows. This leads to an approximately Gaussian-type distribution of the window sizes with an aperture oscillation. This aperture oscillation correlates with the experimental H NMR results, indicating the oscillation of the ligands [24]. The oscillation of the ZIF-67 aperture at 308 K yields an average aperture diameter of 3.35 Å. This finding is consistent with a recent computational study [25], which reported a diameter of 3.35 Å at 308 K, and closely aligns with experimental measurements [26] (~ 3.3 Å at 153 K). It's important to note that accurately predicting the aperture size can significantly influence the sieving mechanism of ZIF-67 for propane/propylene separation, given the subtle size differences between the two molecules.

Moreover, it appears that the aperture oscillation is influenced by temperature, and as the temperature rises, the extent of oscillation (fluctuation width) also increases. Therefore, as the temperature increases, the aperture diameter also expands to 3.37 Å and 3.40 Å at 500 K and 600 K, respectively. This observation is consistent with the experimental findings of Kolokov et al. [24], where they demonstrated clear oscillations of the ligands forming the

aperture, akin to a "saloon door" motion. These oscillations exhibited a more significant amplitude with rising temperatures [24]. The stiffness of the Co-N bond is the key factor that governs the stiffness of the aperture and the gate's fluctuation and opening. Therefore, the enhancement of separation can be achieved by optimizing the rigidity of the flipping motion of the ligands.

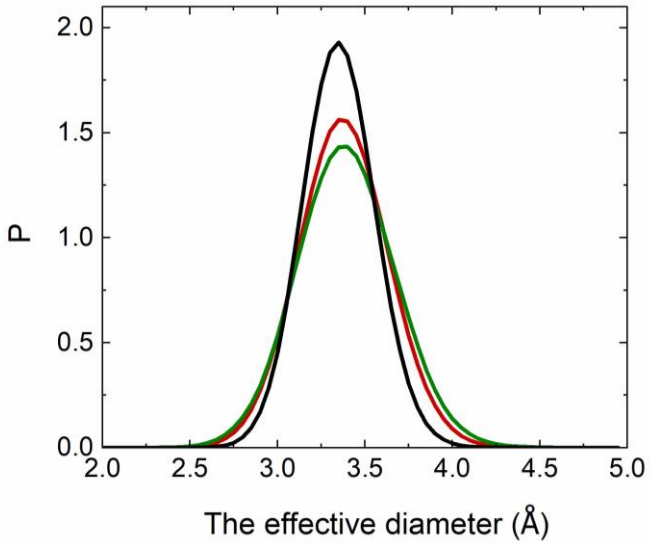

Figure 5.5 : Distribution of ZIF-67 aperture sizes upon heating (black line, 308 K; red line, 500 K; green line, 600 K).

5.3 Free Energy Profiles for Propylene/Propane in ZIF67-IDip

To enhance the compatibility between ZIF-67 and polymers and strengthen the interfacial interactions in MOF/polymer composites, the surface of ZIF-67 was modified with NHC-based IDip groups, as discussed in Chapter 3. Atomistic-scale investigations revealed that while the IDip functionalization of the ZIF-67 surface improved the packing of the polymers at the MOF surface, it had minimal impact on the adsorption properties of the composites. Since surface modification did not significantly influence the thermodynamic separation mechanism, the focus of this section is on the kinetic-driven separation ability of ZIF-67-IDip.

PMF simulations were conducted for propane and propylene within the ZIF-67-IDip NP, aiming to obtain the free energy profile along a 12 Å RC. Compared to the ZIF-67 NP RC of

6 Å, the RC for ZIF-67-IDip was determined as 12 Å. The presence of IDips on the ZIF-67 surface influences the selection of RC based on distances exceeding beyond the upper limit of the MOF cage from the gate center. Hence, due to the bulky IDip atom modifications on the ZIF-67 surface, the RC distance for the PMF simulations was extended compared to the RC distance of unfunctionalized ZIF-67 NP. The previously generated ZIF-67-IDip NP model described in Chapter 3 was used for these PMF simulations. Within the umbrella sampling, both propane and propylene molecules were individually positioned near the gate center and pulled from that point until they exceeded the exit of the ZIF-67-IDip NP. In this context, 0 Å corresponds to the center of the gate near to the cage center, while 12 Å represents the distance more than the upper limit of MOF cage. Figure 5.6 shows a representation of how umbrella sampling is performed in ZIF-67-IDip NP. In the umbrella sampling simulations, a spring constant of $K_r = 0.2$ kcal·mol^{-1} ·Å^{-2} was used to maintain the guest near r = 0 Å, while a second force constant of $K_z = 2$ kcal·mol^{-1} ·Å^{-2} was applied to pull the guest to its target position. In the umbrella sampling process, the path was divided into 36 umbrella sampling windows, each having a width of 0.325 Å.

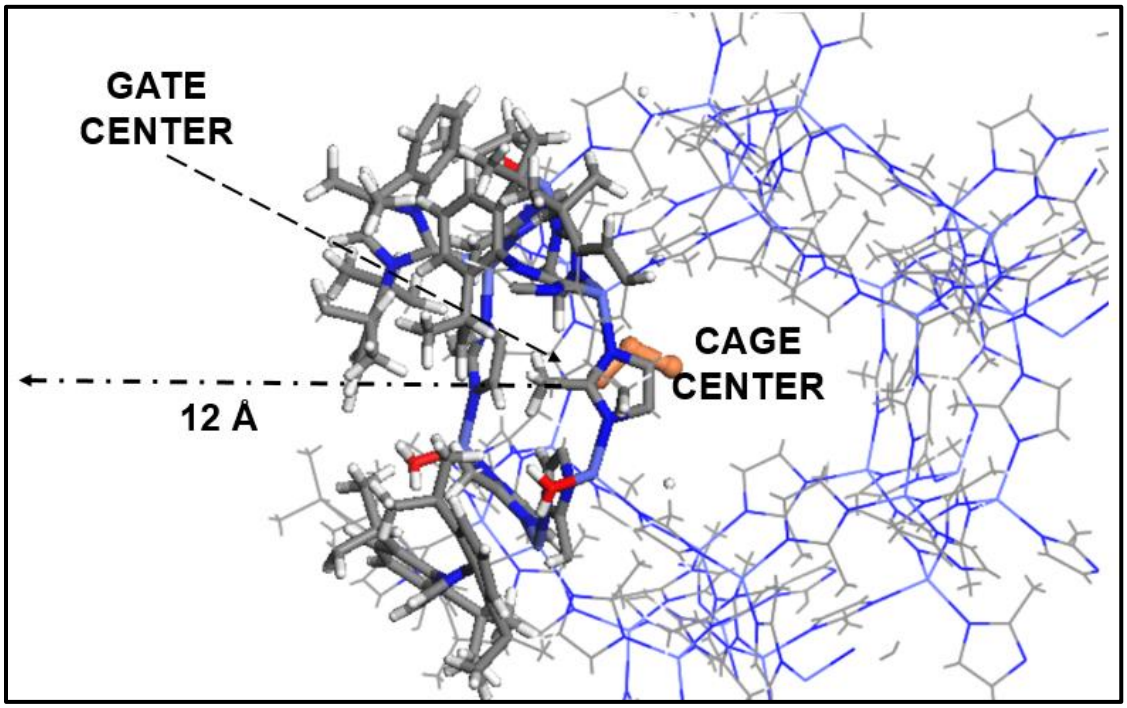

Figure 5.6 : Schematic representation of the computational procedure applied to ZIF-67-IDip NP.

Figure 5.7 shows the PMF calculations for propane and propylene along a 12.0 Å distance as RC values of 0 and 12 Å represent the center of the gate and the outermost region of the cage, respectively. For both guests, the free energy rises to a high energy level at approximately 7.3 Å, followed by a decrease to certain energy levels. The ~7.3 Å distance corresponds to the distance from the gate center to the near to the outermost atom of ZIF-67-IDip cage which ultimately results in the highest energy level. As the guests exceed the MOF cage, the free energy decreases due to the weakening of interactions between the imidazolate linkers of MOF atoms and the guests. The diffusion barriers within ZIF-67-IDip are 153.5 kJ/mol for propane and 126.9 kJ/mol for propylene, with an energy difference of ~ 27 kJ/mol.

In comparison to unfunctionalized ZIF-67, the energy barriers for guests were observed at 1.46 Å, while this distance increased to 7.28 Å with ZIF-67 functionalization, as the upper limit of the functionalized MOF surface shifted to a longer distance due to the presence of the functional IDip groups, which significantly influences the location of the energy barriers. Furthermore, significantly higher energy barriers for both guests were observed with ZIF-67-IDip NPs. In comparison to unfunctionalized ZIF-67 NPs, a much higher energy barrier difference also occurred, indicating a higher kinetics-driven separation ability of this functional ZIF-67 vs pristine ZIF-67 (27 kJ/mol vs. 8 kj/mol). The strong bonding between the carbene molecule and the metals of the outermost atoms of MOF cage (C-Co bonds)[27] is responsible for the higher energy barrier difference, demonstrating that IDip functionalization not only enhances compatibility between ZIF-67 and polymers along with strengthening interfacial interactions in MOF/polymer composites but also improves the propylene/propane separation mechanism.

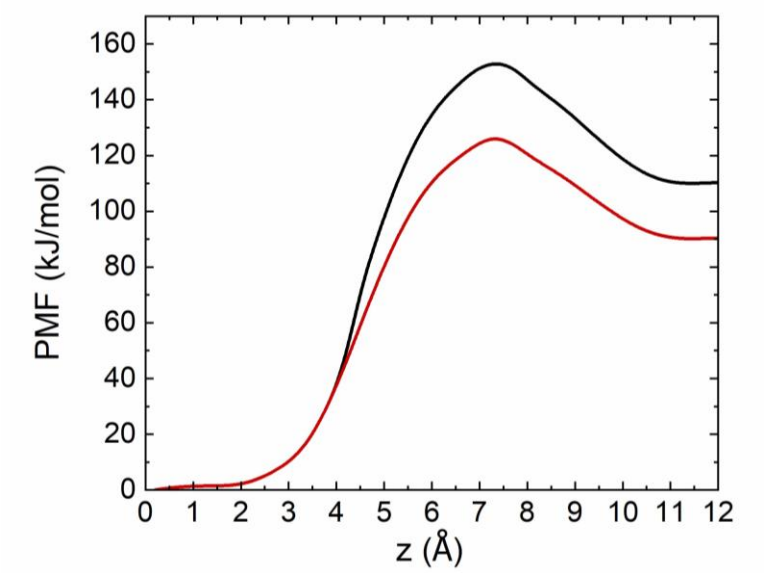

Figure 5.7 : Calculated free energy profile of propane (black line) and propylene (red line) molecules plotted as a function of the distance from the aperture center to the outside of the cage for ZIF-67-IDip NP.

The behavior of the ZIF-67-IDip aperture gate was also examined. Figure 5.8a illustrates the windows size distribution of the ZIF-67-IDip NP cage in comparison to that of ZIF-67 NP. Similar to the ZIF-67 aperture, the ZIF67-IDip aperture exhibits fluctuating behavior reminiscent of a Gaussian size distribution. The ZIF-67-IDip NP demonstrates a broader aperture distribution with an aperture diameter of 3.55 Å, while the ZIF-67 NP has a slightly smaller aperture diameter of 3.35 Å. This suggests that ZIF-67-IDip features a more flexible window, indicating that the effective aperture size of ZIF-67-IDip windows are much larger compared to ZIF-67, providing greater diffusion in the ZIF-67-IDip NP, as supported by the work of Parkes et al. [28]. The presence of bulky IDips on the ZIF-67 surface appears to influence the separation mechanism, as ZIFs are governed by the orientation of the imidazolate-based linkers that forms the windows.

Figure 5.8b shows the changes in the ZIF-67-IDip framework aperture as it undergoes heating. It appears that the aperture oscillation is influenced by temperature, and as the temperature rises, the fluctuation width also slightly increases, but aperture diameter remained same in this case at 500 K and 600 K.

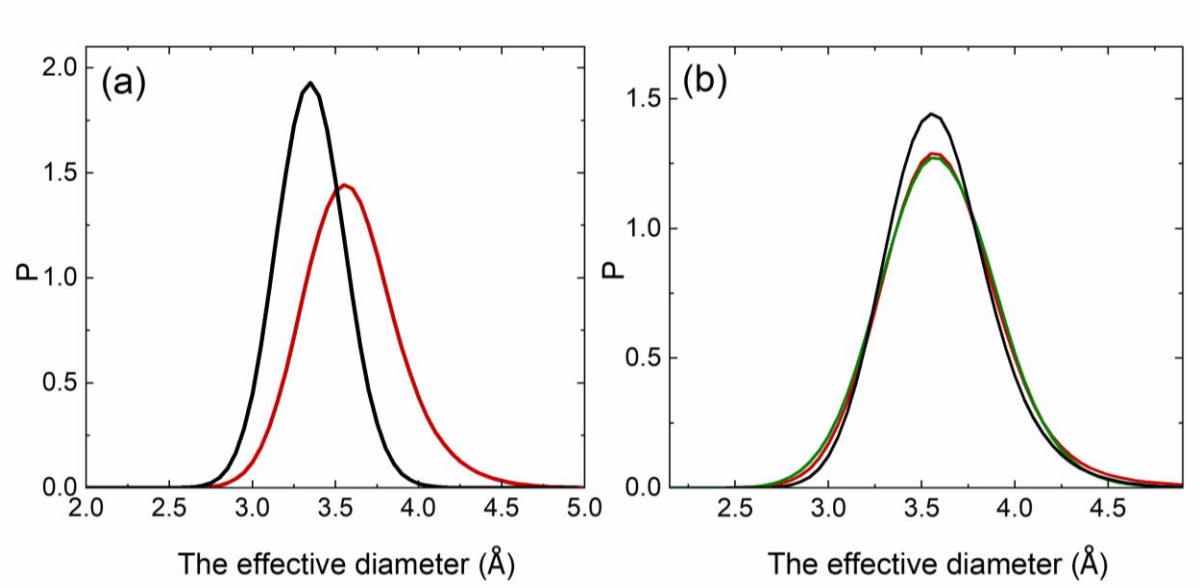

Figure 5.8 : The effective diameter for (a) ZIF-67 aperture size (black line) and ZIF-67-IDip aperture size (red line) (b) ZIF-67-IDip aperture sizes upon heating (black line, 308 K; red line, 500 K; green line, 600 K).

5.4 Free Energy Profiles for Propylene/Propane in ZIF67-IPD

A different surface modification agent, IPD, was utilized to explore interfacial interactions between the MOF and polymers in Chapter 4. It was observed that IPD functionalization of the ZIF-67 surface improved the packing of the polymers at the MOF surface compared to IDip, owing to its two polar sides facilitating adsorption on the MOF surface and creating additional binding forces between MOFs and polymer chains. However, the adsorption properties of the composites remained minimally affected. Herein, the focus of this section is kinetic separation of ZIF-67-IPD to gain insights into the propylene/propane separation mechanism.

PMF simulations were calculated within the ZIF-67-IPD NP for propane and propylene, with the aim of generating the free energy profiles along a 6 Å RC. The ~6 Å distance corresponds to the distance from the gate center to the near to the outermost atom of ZIF-67-IPD cage. Because of the IPD atom modifications on the ZIF-67 surface, the RC distance for the PMF simulations was increased to 6 Å, compared to the unfunctionalized ZIF-67 RC distance.

The previously generated ZIF-67-IPD NP model was employed for these PMF simulations. In the umbrella sampling, both propane and propylene molecules were individually positioned near the gate center and pulled from that point until exceeding the exit of the ZIF-67-IPD NP. Figure 5.9 provides a representation of how umbrella sampling is performed in ZIF-67-IPD NP. In the umbrella sampling simulations, a spring constant of K_r = 0.2 kcal·mol^{-1} ·Å^{-2} was employed to keep the guest near r = 0 Å, while a second force constant of K_z = 2 kcal·mol^{-1} ·Å^{-2} was applied to pull the guest to z = 6 Å with 18 umbrella sampling windows along the path, each having a width of 0.325 Å.

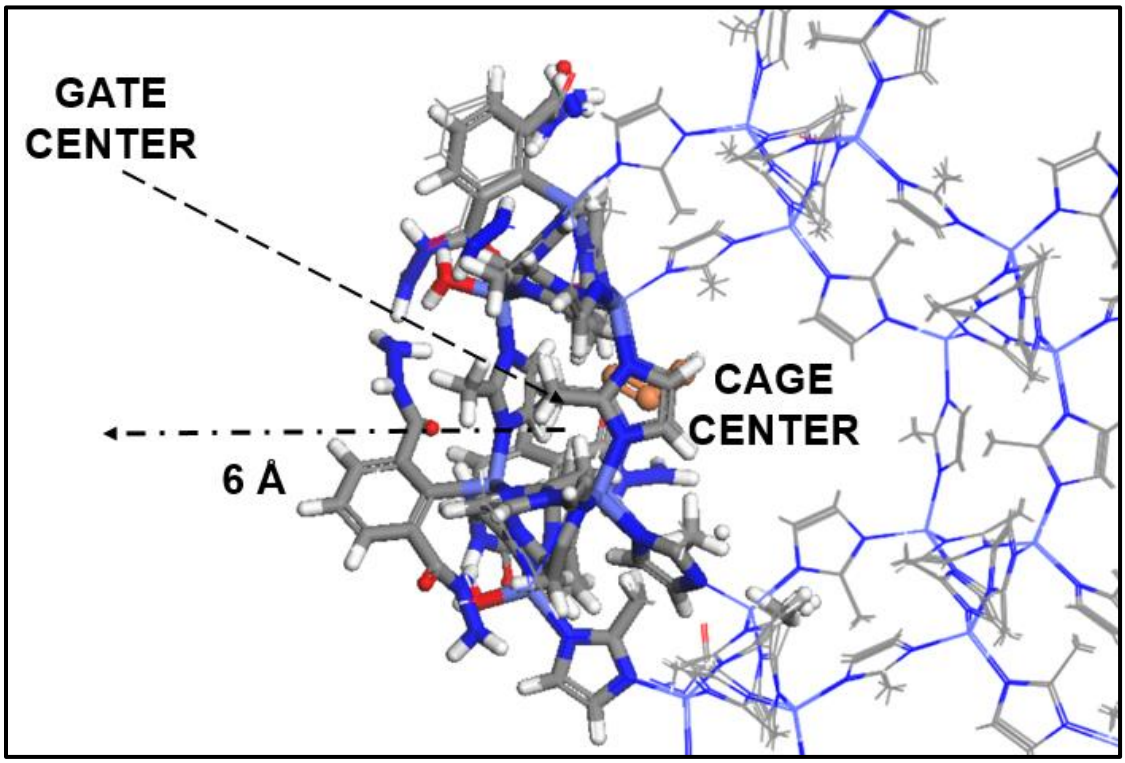

Figure 5.9 : Schematic representation of how umbrella sampling is performed in ZIF-67-IPD cage.

PMF calculations were performed to assess the behavior of propane and propylene over a 6.0 Å distance in Figure 5.10. The results indicate that for propylene, a sharp increase in free energy is observed, resulting in the emergence of energy barriers at around 1.15 Å distance while, for propane, these barriers appear at a longer distance of 3.62 Å. As the guests exceed the MOF cage, the presence of IPD atoms on ZIF-67-IPD surface creates steric hindrance. The abundance of amino and amide groups on the ZIF-67-IPD surface inhibits the passage of

the propane molecule (see Figure 5.11a), whereas for the case of propylene (Figure 5.11b), there is an absence of such hindrance. Consequently, the energy barriers at around 1.15 Å distance for propylene are attributed to the distance between the gate center and the innermost atoms of the "zig-zag" ZIF-67 surface. Meanwhile, the energy barriers at 3.62 Å for propane arise from the distance between the gate center and the outermost atoms of the "zig-zag" ZIF-67 surface. Hence, the extended distance observed for propane, along with the slightly higher energy barrier, can be attributed to the more restricted motion of propane, coupled with steric hindrance caused by the functional groups. The diffusion barriers within ZIF-67-IPD are 8 kJ/mol for propane and 7.3 kJ/mol for propylene. It appears that the calculated energy barriers for both guests are respectively low (~10 kJ/mol) compared to other systems. Considering the relatively small ~1 kJ/mol energy barrier difference, this functionalized material is not expected to show any kinetics-driven separation of the two guests.

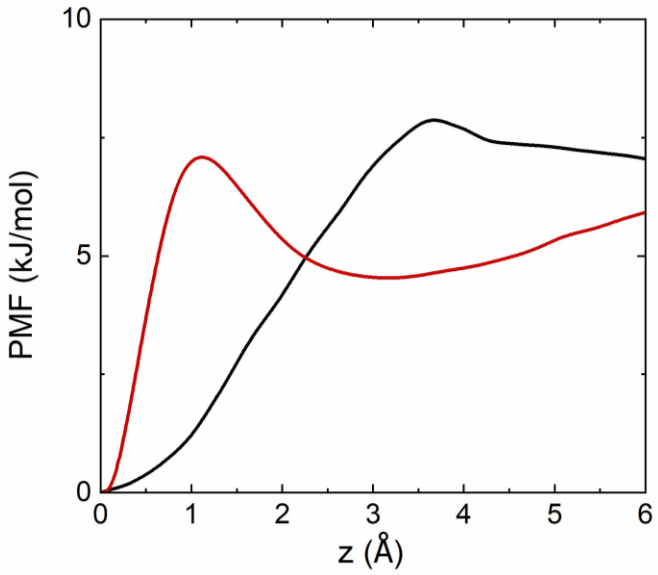

Figure 5.10 : Calculated Free energy profile of propane (black line) and propylene (red line) molecules plotted as a function of the distance from the aperture center to the outside of the cage for ZIF-67-IPD NP.

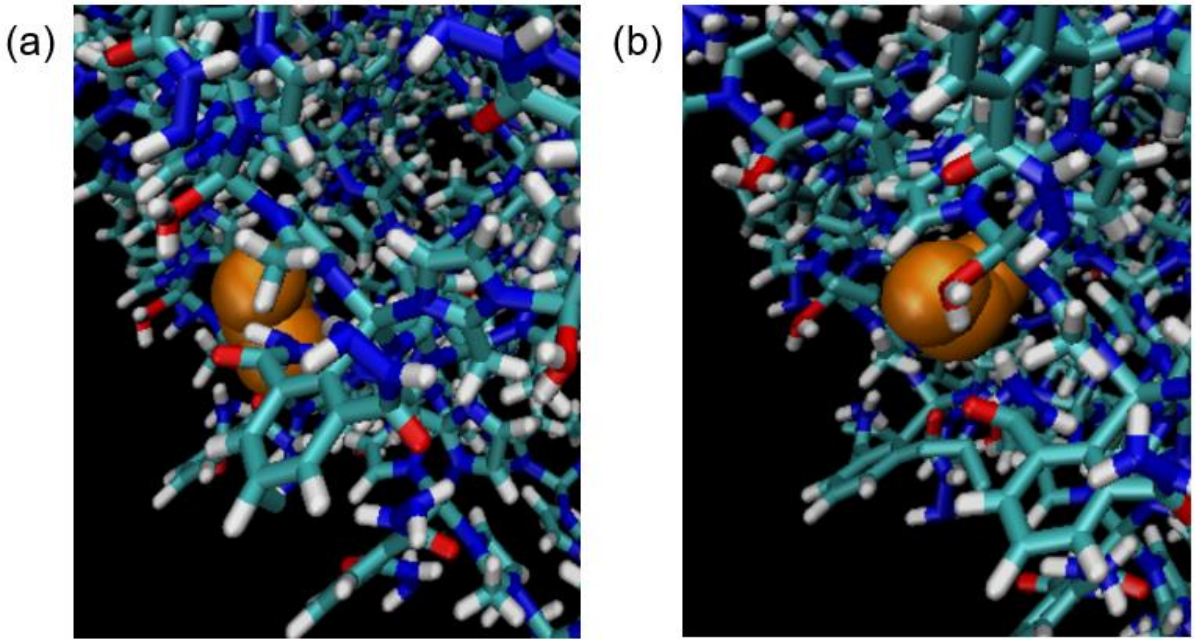

Figure 5.11 : Schematic representation of (a) propane and (b)propylene passage through the gate of ZIF-67-IPD cage. ZIF-67-IPD atoms are represented as stick atoms and guests in orange CPK atoms. Color code: O (red), C (grey), H (white), N (blue) and Co (steel blue).

5.5 Free Energy Profiles for Propylene/Propane in ZIF67 with MOF Surfaces Terminated by Methanol

In the previous chapter, atomistic-scale investigation was performed to explore how the selection of a new solvent, methanol, impacts the adhesion between ZIF-67 and the polymers in the composites. It was demonstrated that these composites lack significant potential for thermodynamic separation. Therefore, in this section, MD simulations were employed to conduct PMF calculations, allowing for the calculation of the free energy profile along the reaction coordinate, as explained in the previous parts.

In Figure 5.12, the PMF calculations illustrate the free energy profiles for propane and propylene over a 5.0 Å RC distance. In this context, 0 Å corresponds to the center of the exiting cage, while 5.0 Å represents the outermost region of the cage. In the umbrella sampling simulations, a spring constant of K_r = 0.2 kcal·mol^{-1} ·Å^{-2} was employed to keep the guest near r = 0 Å while, a second force constant of K_z = 2 kcal·mol^{-1} ·Å^{-2} was applied to pull the guest to its intended position. In the umbrella sampling process, the path was divided

into 15 umbrella sampling windows, each having a width of 0.325 Å, consistent with the previous calculations. For both guests, the free energy shows a sharp increase, resulting in energy barriers at around 4.06 Å, followed by a decrease to specific energy levels, indicating the disruption of interaction forces between the imidazolate linkers and the guests. The relatively higher energy barrier for propane can be attributed to its hindered motion, requiring it to overcome a higher barrier for diffusion within ZIF-67. The diffusion barriers within ZIF-67 are 40.8 kJ/mol for propane and 34 kJ/mol for propylene, with an energy difference of ~ 7 kJ/mol. In comparison to ZIF-67 with water terminations, the energy barriers for guests were observed at 1.46 Å, while this distance increased to 4.06 Å with methanol terminations. This extended distance of 2.6 Å could be attributed to the interaction forces between the $C(H_3)OH$ termination groups and the guests. It appears that the charge of the hydrogen atoms on the imidazolate linkers (–H atoms of the dissociative adsorption of methanol) at the outer surface of the cage influences the passage of guests through the gate. Indeed, the charge of the hydrogen in methanol is notably higher compared to the hydrogen involved in the dissociative adsorption of water (0.2842 vs. 0.133). Greater charges on the hydrogen atoms influence the hydrogen bonding between imidazolate linkers and guests, thereby increasing the electrostatic interaction. Hence, the higher energy barrier along with a longer distance passage through the gate occurs for ZIF-67 with methanol terminations.

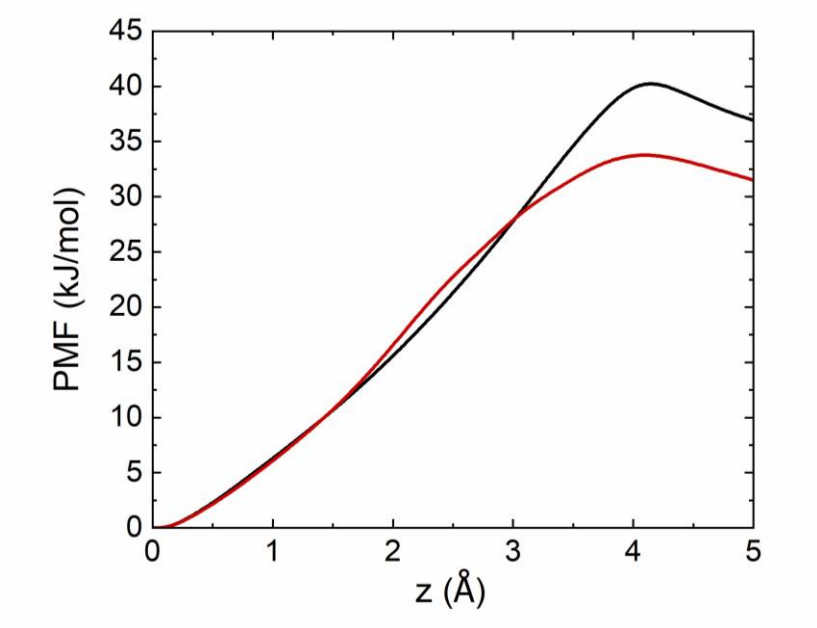

Figure 5.12 : Calculated free energy profile of propane (black line) and propylene (red line) molecules plotted as a function of the distance from the aperture center to the outside of the cage for ZIF-67 NP NP with $–C(H_3)O$ terminations.

To further investigate the impact of solvent selection on the separation mechanism of propylene and propane, the behavior of the ZIF-67's aperture was analyzed. It is well-established that aperture size plays a crucial role in influencing the sieving mechanism of ZIF-67. Figure 5.13 illustrates the alterations in the ZIF-67 framework's aperture as guest molecules pass through the gate. It is clear that the framework's aperture undergoes a swelling motion characterized by a Gaussian size distribution. Further analysis indicates that the ZIF-67 NP with methanol terminations in the presence of guests, exhibits an aperture diameter of approximately 2.97 Å, whereas this diameter is 3.92 Å for the water-terminated ZIF-67 NP. Hence, the less flexible windows of ZIF-67 NP along with the higher electrostatic interaction that comes from the greater charges of –H atoms of the dissociative adsorption of methanol affects the energy barriers for guests.

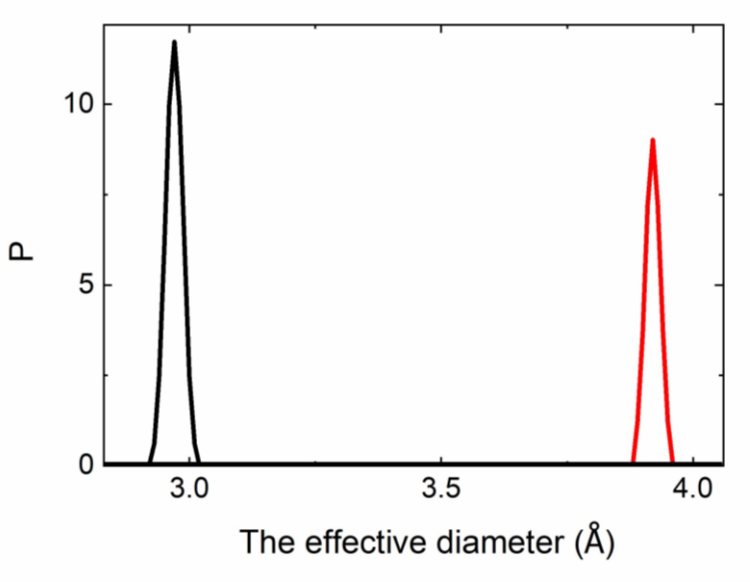

Figure 5.13 : Distribution of ZIF-67 aperture sizes with methanol (black line) and water (red line) terminations at 308 K.

5.6 Conclusion

In the previous chapters, the separation mechanism was demonstrated to be not thermodynamically driven. Therefore, here kinetic studies focused on evaluating the energy barriers in ZIF-67 related to propylene and propane diffusion. ZIF-67 NPs with different surface functionalization were analyzed using PMF simulations through the umbrella sampling technique. The analyses were further extended to a ZIF-67 NP mimicking the synthesis with methanol as an alternative solvent. The results contribute to a deeper understanding of the sieving mechanism of the ZIF-67 surface in relation to penetrant size, aperture size, and flexibility.

The calculated free energy profiles of ZIF-67 confirmed that the separation mechanism is kinetic-driven. This is supported by the differences in energy barriers observed for propane and propylene, which can be attributed to the restricted motion of propane along with the rigidity of the Co-N bonds. Likewise, the IDip functionalization of the ZIF-67 surface, leads to a higher energy barrier difference due to the strong bonding between the carbene molecule and the metals of the outermost atoms of MOF cage. However, in the case of functionalization of ZIF-67-IPD NP, the diffusion barriers are quite low with a relatively small ~1 kJ/mol energy barrier difference, making this material inapplicable for this

separation. On the other hand, the use of methanol as the solvent for MOF surface terminations enhances the compatibility between the MOF nanoparticles and the polymer. The less flexible windows of ZIF-67 NP with methanol terminations influences the opening of the gate, along with the charges of the dissociative hydrogen atoms on the imidazolate linkers at the outer surface. Particularly, the charge of the hydrogen in methanol is higher compared to the hydrogen involved in the dissociative adsorption of water, which influences the hydrogen bonding between imidazolate linkers and guests, thereby increasing the electrostatic interaction.

REFERENCES

[1] Y. Pramudya, S. Bonakala, D. Antypov, P.M. Bhatt, A. Shkurenko, M. Eddaoudi, M.J. Rosseinsky, M.S. Dyer, High-throughput screening of metal-organic frameworks for kinetic separation of propane and propene, Phys. Chem. Chem. Phys. 22 (2020) 23073–23082. https://doi.org/10.1039/d0cp03790g.

[2] A. Schneemann, V. Bon, I. Schwedler, I. Senkovska, S. Kaskel, R.A. Fischer, Flexible metal-organic frameworks, Chem. Soc. Rev. 43 (2014) 6062–6096. https://doi.org/10.1039/c4cs00101j.

[3] X. Ma, D. Liu, Zeolitic imidazolate framework membranes for light olefin/paraffin separation, Crystals. 9 (2019) 1–26. https://doi.org/10.3390/cryst9010014.

[4] C. Zhang, R.P. Lively, K. Zhang, J.R. Johnson, O. Karvan, W.J. Koros, Unexpected Molecular Sieving Properties of Zeolitic Imidazolate Framework-8, J. Phys. Chem. Lett. (2012) 8–12. https://doi.org/10.1021/jz300855a.

[5] N. Hara, M. Yoshimune, H. Negishi, K. Haraya, S. Hara, T. Yamaguchi, Diffusive separation of propylene/propane with ZIF-8 membranes, J. Memb. Sci. 450 (2014) 215–223. https://doi.org/10.1016/j.memsci.2013.09.012.

[6] H.T. Kwon, H.K. Jeong, In situ synthesis of thin zeolitic-imidazolate framework ZIF-8 membranes exhibiting exceptionally high propylene/propane separation, J. Am. Chem. Soc. 135 (2013) 10763–10768. https://doi.org/10.1021/ja403849c.

[7] H.T. Kwon, H.K. Jeong, Highly propylene-selective supported zeolite-imidazolate

framework (ZIF-8) membranes synthesized by rapid microwave-assisted seeding and secondary growth, Chem. Commun. 49 (2013) 3854–3856. https://doi.org/10.1039/c3cc41039k.

[8] P. Bernardo, E. Drioli, G. Golemme, Membrane Gas Separation:A Review/State of the Art, Ind. Eng. Chem. 48 (2009) 4638–4663.

[9] D. Liu, X. Ma, H. Xi, Y.S. Lin, Gas transport properties and propylene/propane separation characteristics of ZIF-8 membranes, J. Memb. Sci. 451 (2014) 85–93. https://doi.org/10.1016/j.memsci.2013.09.029.

[10] H.T. Kwon, H.K. Jeong, Improving propylene/propane separation performance of Zeolitic-imidazolate framework ZIF-8 membranes, Chem. Eng. Sci. 124 (2015) 20–26. https://doi.org/10.1016/j.ces.2014.06.021.

[11] H.T. Kwon, H.K. Jeong, A.S. Lee, H.S. An, J.S. Lee, Heteroepitaxially Grown Zeolitic Imidazolate Framework Membranes with Unprecedented Propylene/Propane Separation Performances, J. Am. Chem. Soc. 137 (2015) 12304–12311. https://doi.org/10.1021/jacs.5b06730.

[12] P. Krokidas, M. Castier, S. Moncho, D.N. Sredojevic, N. Edward, H.T. Kwon, H. Jeong, J.S. Lee, I.G. Economou, ZIF-67 Framework : A Promising New Candidate for Propylene / Propane Separations - Experimental Data and Molecular Simulations ZIF-67 Framework : a Promising New Candidate for Propylene / Propane Separation Experimental Data and Molecular Simulations, (2016). https://doi.org/10.1021/acs.jpcc.6b00305.

[13] R.J. Verploegh, S. Nair, D.S. Sholl, Temperature and Loading-Dependent Diffusion of Light Hydrocarbons in ZIF-8 as Predicted Through Fully Flexible Molecular Simulations, J. Am. Chem. Soc. 137 (2015) 15760–15771. https://doi.org/10.1021/jacs.5b08746.

[14] W. You, Z. Tang, C.E.A. Chang, Potential Mean Force from Umbrella Sampling Simulations: What Can We Learn and What Is Missed?, J. Chem. Theory Comput. 15 (2019) 2433–2443. https://doi.org/10.1021/acs.jctc.8b01142.

[15] G.M. Torrie, J.P. Valleau, Nonphysical Sampling Distributions in Monte Carlo Free-Energy Estimation: Umbrella Sampling, J. Comput. Phys. 23 (1977) 187–199.

[16] J. Kästner, Umbrella Sampling, Wiley Interdisciplinary Reviews-Computational Molecular Science, 2011.

[17] S. Plimpton, Fast Parallel Algorithms for Short-Range Molecular Dynamics, J.

Comput. Phys. 117 (1995) 1–19. https://doi.org/10.1039/c7sm02429k.

[18] P. Krokidas, M. Castier, S. Moncho, E. Brothers, I.G. Economou, Molecular Simulation Studies of the Diffusion of Methane, Ethane, Propane, and Propylene in ZIF-8, J. Phys. Chem. C. 119 (2015) 27028–27037. https://doi.org/10.1021/acs.jpcc.5b08554.

[19] G. Fiorin, M.L. Klein, J. Hénin, Using collective variables to drive molecular dynamics simulations, Mol. Phys. 111 (2013) 3345–3362. https://doi.org/10.1080/00268976.2013.813594.

[20] A. Güvensoy-Morkoyun, S. Velioğlu, M.G. Ahunbay, S.B. Tantekin-Ersolmaz, Desalination Potential of Aquaporin-Inspired Functionalization of Carbon Nanotubes: Bridging between Simulation and Experiment, ACS Appl. Mater. Interfaces. 14 (2022) 28174–28185. https://doi.org/10.1021/acsami.2c03700.

[21] A. Grossfield, An implementation of WHAM : the Weighted Histogram Analysis Method Version 2.0.9, Department, Biophysics, University of Rochester Medical Center, Rochester, NY, 2013. https://doi.org/http://membrane.urmc.rochester.edu/content/wham/.

[22] H.T. Kwon, H. Jeong, A.S. Lee, H.S. An, J.S. Lee, H.T. Kwon, H. Jeong, A.S. Lee, H.S. An, J.S. Lee, Heteroepitaxially-grown Zeolitic Imidazolate Framework Membranes with Unprecedented Propylene / Propane Separation Performances, J. Am. Chem. Soc. (2015). https://doi.org/10.1021/jacs.5b06730.

[23] P. Krokidas, S. Moncho, E.N. Brothers, I.G. Economou, Defining New Limits in Gas Separations Using Modified ZIF Systems, ACS Appl. Mater. Interfaces. 12 (2020) 20536–20547. https://doi.org/10.1021/acsami.0c02886.

[24] D.I. Kolokolov, A.G. Stepanov, H. Jobic, Mobility of the 2-Methylimidazolate Linkers in ZIF-8 Probed by 2H NMR: Saloon Doors for the Guests, J. Phys. Chem. C. 119 (2015) 27512–27520. https://doi.org/10.1021/acs.jpcc.5b09312.

[25] P. Krokidas, M. Castier, I.G. Economou, Computational Study of ZIF-8 and ZIF-67 Performance for Separation of Gas Mixtures, J. Phys. Chem. C. 121 (2017) 17999–18011. https://doi.org/10.1021/acs.jpcc.7b05700.

[26] R. Banerjee, A. Phan, B. Wang, C. Knobler, H. Furukawa, M. O'Keeffe, O.M. Yaghi, High-throughput synthesis of zeolitic imidazolate frameworks and application to CO2 capture, Science (80-.). 319 (2008) 939–943. https://doi.org/10.1126/science.1152516.

[27] M.N. Hopkinson, C. Richter, M. Schedler, F. Glorius, An overview of N-heterocyclic carbenes, Nature. 510 (2014) 485–496. https://doi.org/10.1038/nature13384.

[28] M. V Parkes, H. Demir, S.L. Teich-mcgoldrick, D.S. Sholl, J.A. Greathouse, M.D. Allendorf, Molecular dynamics simulation of framework flexibility effects on noble gas diffusion in HKUST-1 and ZIF-8, Microporous Mesoporous Mater. 194 (2014) 190–199. https://doi.org/10.1016/j.micromeso.2014.03.027.

CONCLUSIONS AND PERSPECTIVES

This PhD work focused on employing a combination of force field and quantum-based calculations to gain microscopic insight into the separation performances of MOF mixed matrix membranes (MMMs) designed for olefin/paraffin separation. The considered model MOF, ZIF-67 was selected based on its exceptional performance for this gas mixture along with its remarkable stability and flexible framework that enables the diffusion of molecules larger than the dimension of the cage apertures. On the other hand, three different polymers were considered for this study, each with unique physical properties: 6FDA-DAM with its inhibited polymer chain packing, 6FDA-DABA with its plasticizing control capability and PIM-1 with its rigid contorted molecular backbone and relatively high porosity. The overall objective was to combine ZIF-67 with these polymers to design MMMs with expected good interfacial adhesion between MOF and polymers that drives the homogenous dispersion of MOF nanoparticles within the polymer matrices. In this context, a systematic computational study was conducted to model reliable atomistic models for polymers, MOFs, and MOF/polymer composites. A special attention was devoted to characterize finely the MOF/polymer interfaces in terms of MOF/polymer overlap region, polymer organization and pore structuring/dimension prior to explore the sorption behavior of these composites.

In the first part of the project, a computational methodology was applied for modeling MOFs, polymers and their resulting composites to reveal the microscopic origin of the improved adhesion between ZIF-67 and 6FDA-DAM in the resulting composites through MOF surface functionalization with carbene groups. It was further demonstrated how MOF functionalization affects the propane and propylene adsorption performance in these composites while systematically assessing the impact of the nature of the polymers on the ZIF-67/polymer adhesion in the corresponding composites and their subsequent effects on adsorption properties. IDip functionalization of the ZIF-67 surface was revealed to facilitate a more efficient polymer packing at the MOF surface, leading to a significantly better MOF/polymer compatibility to prevent MOF filler agglomeration as experimentally observed. The ZIF-67/PIM-1 composite was further shown to exhibit a better compatibility compared to the ZIF-67/6FDA-DAM composite since the conformation of PIM-1 better accommodates its backbone at the MOF surface. The sorption simulations evidenced that the

propylene/propane separation by these composites is not thermodynamically-driven confirming the experimental findings.

As a further step, the microscopic models of the composites made of IPD functionalized ZIF-67 and both 6FDA-DAM and PIM-1 polymers were examined, along with the exploration of the impact of the terminal functions of the outer surface of ZIF-67 that can be tuned by the nature of the solvent on the ZIF-67/polymer adhesion in the corresponding composites. This comprehensive approach allowed for an in-depth characterization of the resulting interfaces. It appeared that the presence of two polar sites in the IPD function (vs a single polar site for IDip function) plays a key role in enhancing compatibility between ZIF-67 surfaces and the polymer. This enhancement occurs by enabling a more efficient packing of 6FDA-DAM in the vicinity of the MOF surface. On the other hand, employing methanol as the solvent for controlling the MOF surface termination leads to an enhancement of the compatibility between the ZIF-67 surface and the polymer, enabling 6FDA-DAM to efficiently cover the ZIF-67 surface, while PIM-1 fits into the pockets formed by the 'zig-zag' shape of the MOF surface.

As a final step kinetics of propane and propylene were explored in ZIF-67 and its functionalized forms with the evaluation of the energy barriers required to cross the windows of the corresponding MOFs. These studies employed PMF simulations, conducted through the umbrella sampling technique. The free energy profiles of ZIF-67 confirmed that the separation mechanism is kinetically driven, with an energy barrier difference between propane and propylene. Likewise, the IDip and IPD functionalization of the ZIF-67 surface resulted in a larger and smaller energy barrier difference, respectively. This results emphasizes that the functionalization of the MOF surface should be carefully selected if one wants to enhance the kinetically driven separation performance of ZIF-67.

Overall, among the studied strategies to enhance the compatibility between ZIF-67 and the polymer, that surface functionalization with IDip gave the best results. This is evident from the resulting long MOF/polymer overlap and interfacial lengths. Interestingly this functionalization also enables to enhance the energy barrier difference between propylene and propane to cross the gate entrance that is expected to lead to a more effective kinetics-driven separation.

Future direction of this work involves the exploration of alternative MOF/Polymer composites, combining the ultra-small pore MOF UTSA-280 highly selective for ethylene/ethane (Figure 1a) and the 6FDA-DAM:DABA polymer (Figure 1b). In this context, the constructed atomistic model of 6FDA-DAM: DABA (3:2) was combined with a UTSA-280 surface model to build the corresponding composite illustrated in Figure 1.c with the atomic density profile plotted along the z-direction in Figure 1.d. We can observe that the interfacial region, denoted as region A exhibits a significant overlap length of ~2.5 Å, the main MOF/polymer interactions implying a closest contact of ~2.65 Å between O(6FDA-DAM:DABA) and H(OH) of the UTSA-280 surface. Figure 1.f. further shows that interfacial pores (highlighted in the grey area) extend up to ~8 Å. These newly generated interfacial microvoids are anticipated to play a significant role in governing the thermodynamics and dynamics of the ethylene/ethane adsorption within the overall composite. Therefore, this preliminary exploration of UTSA-280/6FDA-DAM:DABA will be followed by thermodynamic and kinetic studies of ethylene/ethane gas mixtures through a combination of MC and MD simulation techniques.

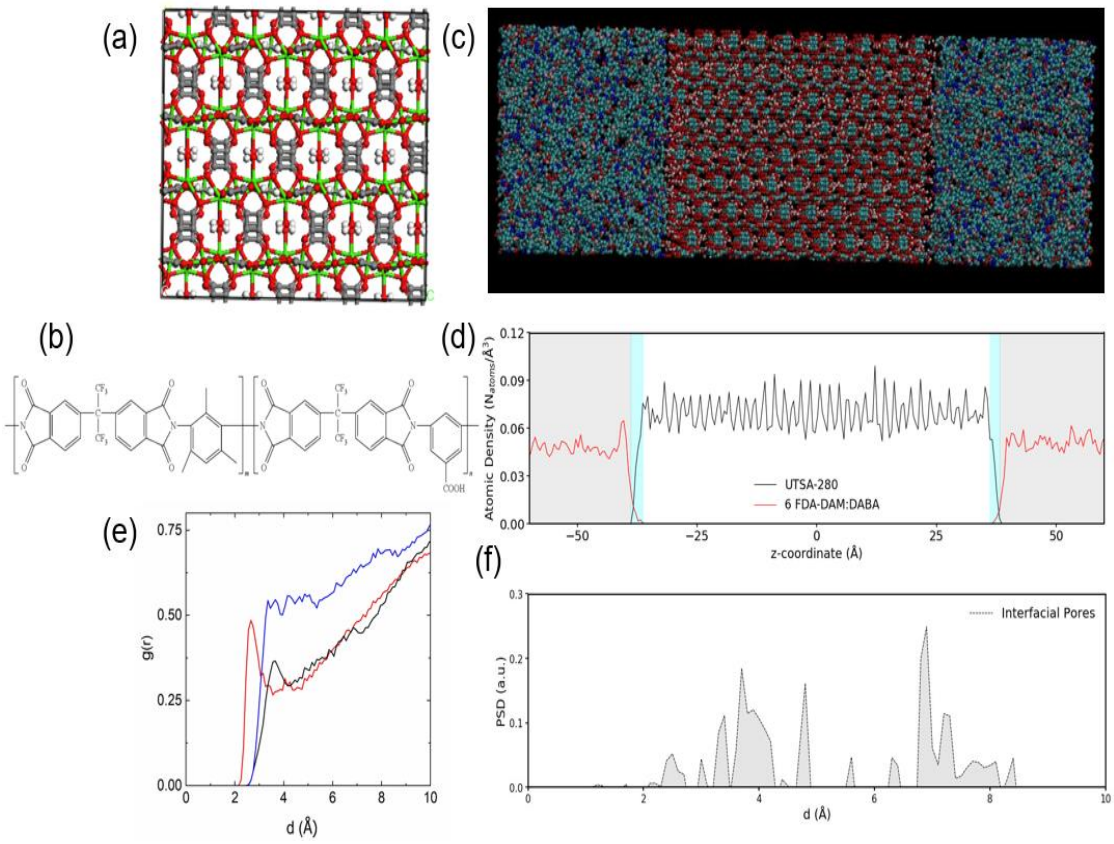

Figure 1. UTSA-280 crystal, terminated by OH and H groups, (b) Representation of 6FDA-DAM:DABA(3:2) structure, (c) Illustration of the constructed UTSA-280/6FDA-DAM:DABA model, (d) Atomic density profile for the UTSA-280/6FDA-DAM:DABA in the direction perpendicular to the surface slab (i.e. along the z direction), (e) Calculated radial distribution functions in the UTSA-280/6FDA-DAM:DABA between O (red curve), $-CH_3$ groups (blue curve) and C (black curve) of 6FDA-DAM:DABA and H(OH) of the UTSA-280, (f) Pore size distribution of UTSA-280/6FDA-DAM:DABA. UTSA-280 atoms are represented as ball and stick atoms. Color code: O (red), C (grey), H (white) and Ca (green).

Abstract

Membranes, due to their low cost, high energy efficiency and ease of processing, have aroused great interest in the field of gas separation. Polymer membranes currently occupy a dominant position in the commercial market, despite the existing tradeoff between permeability and selectivity associated with their use. Over the past decade a novel class of inorganic-organic porous materials, Metal-Organic Frameworks (MOFs), has emerged as a new research domain in solid state materials. These hybrid nanoporous materials formed by the self-assembly of metal ions or clusters, linked together via a variety of bridging ligands, creating stable open structures with sufficiently large pores for industrially-important applications, such as in gas adsorption, storage and separation. Indeed, a number of recent studies have demonstrated that MOFs could be optimal candidates for membrane-based gas separation processes. In addition, owing to the remarkable properties of MOFs, an alternative strategy to overcome the selectivity/permeability trade-off limits of polymer membranes is to make mixed-matrix membranes (MMMs), in which MOF particles are incorporated into polymer matrices. Typically, the alkane/alkene separation is highly topical since it was identified recently as one of the "7 chemical separation to change the world". Propylene (C_3H_6) is with ethylene (C_2H_4), the largest feedstock in petrochemical industries with a global production that exceeds 200 million tons per year, with these chemicals mostly used to produce polymer-grade and plastic products, particularly the widely utilized polypropylene.

The objective of the PhD will be to predict the separation performances of a series of MMMs for diverse olefin/paraffin separation based on atomistic models constructed for the corresponding MMMs using a combination of force field and quantum calculations. More specifically, we will implement an MC/MD simulation scheme to perform simulations of membrane permeation processes. This prediction will pave the way towards the development of the corresponding MMM and their separation testing by collaborators.

Keywords: Molecular simulation, membrane, Hydrocarbon separation, MOF, polymer

Résume

Les membranes, de par leur faible coût, leur haute efficacité énergétique et leur facilité de traitement, ont suscité un vif intérêt dans le domaine de la séparation des gaz. Les membranes polymères occupent actuellement une position dominante sur le marché commercial, malgré le compromis existant entre perméabilité et sélectivité liée à leur utilisation. Au cours de la dernière décennie, une nouvelle classe de matériaux poreux inorganiques-organiques, les Métal Organique Framework (MOFs), est devenue un nouveau domaine de recherche sur les matériaux à l'état solide. Ces matériaux nanoporeux hybrides formés par auto-assemblage d'ions métalliques ou d'agrégats, reliés entre eux par une variété de ligands de pontage, créent des structures ouvertes stables avec des pores suffisamment grands pour des applications importantes sur le plan industriel, telles que l'adsorption, le stockage et la séparation de gaz. En effet, un certain nombre d'études récentes ont démontré que les MOFs pourraient être des candidats optimaux pour les procédés de séparation des gaz à base de membranes. De plus, en raison des propriétés remarquables des MOFs, une autre stratégie pour surmonter les limites de sélectivité / perméabilité des membranes polymères consiste à fabriquer des membranes à matrice mixte (MMMs), dans lesquelles des particules de MOFs sont incorporées dans des matrices polymères. Typiquement, la séparation alcane / alcène est une question d'actualité puisqu'elle a été récemment identifiée comme l'une des «7 séparations chimiques pour changer le monde». Le propylène (C_3H_6) et l'éthylène (C_2H_4), constituent la plus grande matière première des industries pétrochimiques, avec une production mondiale supérieure à 200 millions de tonnes par an. Ces produits chimiques sont principalement utilisés pour la fabrication de produits de qualité polymère et en plastique, en particulier le polypropylène largement utilisé.

L'objectif de la thèse sera de prédire les performances de séparation d'une série de MMM pour différentes séparations oléfines/paraffines sur la base de modèles atomistiques construits pour les MMM correspondants en utilisant une combinaison de calcul quantique et de calcul de champs de force. Cette prédiction ouvrira la voie au développement du MMM correspondant et à ses tests de séparation par des collaborateurs.

Mots-clés : Simulation moléculaire, membrane, séparation d'hydrocarbures, MOF, polymèr

Özet

Membranlar düşük maliyetleri, yüksek enerji verimliliği ve işlenme kolaylıkları nedeniyle gaz ayırma proseslerinde büyük ilgi uyandırmıştır. Polimerik membranlar, gaz geçirgenliği ve seçiciliği arasındaki zıt ilişkiye rağmen, ticari pazarda baskın bir konuma sahiptir. Son on yılda, inorganik-organik gözenekli malzemelerin nispeten yeni bir sınıfı olan Metal organik kafesler (MOF'ların), katı hal malzemeleri alanında yeni bir araştırma alanı olarak ortaya çıktı. Metal organik kafesler, metal iyonlarının poli-fonksiyonel organik moleküllere bağlanmasıyla kendiliğinden bir araya gelerek oluşur ve gaz adsorpsiyonu, depolama ve ayırma gibi endüstriyel açıdan önemli uygulamalar için yeterince büyük gözeneklere sahip stabil açık yapılar oluşturur. Aslında, son zamanlarda yapılan birçok çalışma, MOF'ların membran bazlı gaz ayırma prosesleri için en uygun adaylardan biri olabileceğini göstermiştir. Karışık matrisli membranlar (MMM' ler), MOF' ların (dikkat çekici özellikleri) ve polimerik membranların (seçicilik/geçirgenlik denge sınırlarını aşmak için alternatif bir strateji oluşturması) bir araya geldiği malzemelerdir. Günümüzde alken/alkan ayırımı hala son derece günceldir ve yakın zamanda "dünyayı değiştirecek 7 kimyasal ayırma"'dan biri olarak da tanımlanmıştır. Yılda 200 milyon tonu aşan küresel üretime sahip, propilen (C_3H_6) ve etilen (C_2H_4), petrokimya endüstrilerinin en büyük hammaddesi olma niteliğindedir ve çoğunlukla polimer, plastik ve özellikle de polipropilen üretiminde yaygın olarak kullanılır.

Bu doktora programının amacı, kuvvet alanı ve kuantum hesaplamalarının bir arada kullanılarak çeşitli olefin/parafin ayrımı için bir dizi karışık matrisli membranların ayırma performanslarının atomistik modellere dayalı olarak tahmin edilmesidir. Bu bağlamda, membran geçirgenlik süreçlerinin simülasyonlarını gerçekleştirmek için bir dizi moleküler dinamilk ve Monte Carlo simülasyonları uygulanmıştır. Bu yaklaşım ile ilgili MMM'nin geliştirilmesi ve ortak araştırmacıların deneysel ayırma testlerini başarılı bir şekilde gerçekleştirmeleri için öngörü sağlanacaktır.

Anahtar kelimeler: Moleküler simülasyon, membran, gaz ayırma, MOF, polimer